

DRAGHEAD ANALYSIS

AN ANALYSIS OF THE
DRAGHEAD'S PHYSICAL PROCESSES
TO DETERMINE THE TRAILING
FORCES AND THE PRODUCTION

Draghead analysis

An analysis of the draghead's physical processes
to determine the trailing forces and the production

By

G.H. ter Meulen

Version 1.3

in partial fulfilment of the requirements for the degree of

Master of Science

in Offshore & Dredging Engineering

at the Delft University of Technology

Supervisors:

Prof. dr. ir. S.A. Miedema,
Prof dr. ir. C. van Rhee,
Ir. M. Winkelman,

TU Delft
TU Delft
Damen Dredging Equipment

This thesis is confidential and cannot be made public until November, 2020.

An electronic version of the final version will be made available at <http://repository.tudelft.nl/>.

Preface

Over the years the dredging industry has increasingly caught my interest. During high school I often watched the engineering documentaries on Discovery Channel where they explained in detail how the reclamations of the airport in Hong Kong and the Palm Islands in Dubai were constructed. This had a big influence on my choice to study Mechanical Engineering at the TU Delft and eventually to follow the master in Offshore & Dredging Engineering with a specialisation in dredging. For an internship I stayed in Singapore in 2016 where I was responsible for the logistics of the repair and modification of the 'Volvox Terranova'. This is a trailing suction hopper dredger in the 'jumbo' category which can transport over 30.000 tons of sand. The internship was an extremely informative experience which motivated me even more to start my career in the dredging industry after my graduation.

This research is performed because of the willingness within Damen Dredging Equipment and the entire dredging industry to better determine the trailing forces of a trailing suction hopper dredger and to find a relation between the production and the trailing velocity. The report is therefore useful for shipbuilders but also for contractors. At the moment, one is able to determine forces on the draghead by use of conservative formula's or field measurement data, which gives an acceptable estimation. The trailing velocity and position of the suction pipe is adjusted real time by looking at the density measurement sensors. High experienced dredgers are able to push the production of the vessel to the maximum, where inexperienced dredgers need years of practice to reach high mixture densities.

This is the final report of the extensive research that is performed by me in the previous months. During my research I was located at Damen Dredging Equipment in Nijkerk which is part of Damen Shipyards Group, with a head office located in Gorinchem. In cooperation with the experienced research and development team of Damen and under the supervision of Professor Sape Miedema, TU Delft, I performed this research which is part of my graduation to obtain the Msc. degree in Offshore & Dredging Engineering.

I have had a great time at Damen Dredging Equipment in Nijkerk and I would like to thank everybody for their support and willingness to answer all my questions. I would like to thank Ewout van Duursen and Mark Winkelman in particular. I am impressed about the knowledge they have gained over the years. Compared to fellow students, graduating at different companies, the amount of feedback and guidance from Ewout and Mark was incredible. Therefore, I would highly recommend graduating at Damen Dredging Equipment.

Looking back on my graduating time, I am very glad that the cooperation with Sape Miedema was very constructive. My graduation subject is in the research area in which Sape has been working for years. I have therefore used many of his theories to solve the problems. The spar sessions at Sape's office were not only amusing but also helpful to come up with good ideas and insights. Also, I would like to thank several friends that have read my report and gave useful feedback to improve the legibility of the report.

My knowledge about dredging has improved significantly and hopefully my results have added new insights for the dredging industry and institutions. I am very eager to start working in the field and use my theoretical knowledge to make the dredging operations more efficient.

*G.H. ter Meulen
Nijkerk, October 2018*

Abstract

In dredging there are a lot of opportunities to improve the production processes and to make the production cycle more efficient, especially the excavation process of the draghead. The aim of this research is to determine the trailing forces and to estimate the production of the draghead. Besides that, the goal is to get more insight into how the draghead behaves, depending on the trailing velocities. The variations in the trailing velocities, soil characteristics, control settings and draghead and suction pipe geometries that can occur do not make it easy to determine the trailing forces on the draghead and suction pipe. Because of this complexity, it is also hard to define how to estimate the production. Therefore, the scope of this research is limited to just one sand type with specific soil characteristics.

An analysis of the draghead and the suction pipe, with a freely suspended visor, showed the physical processes in and around the whole suction pipe system. Because the draghead is fixed to the suction pipe, the influence of suction pipe on the draghead is analysed first. After that, the draghead is divided into two parts, the visor and the visor house. With the use of force and moment balances the trailing forces are determined for every trailing velocity. In addition, the production and its production limits are defined.

The calculations show that the increase of the trailing velocity results in higher trailing forces on the suction pipe and draghead. For a velocity of around 2 m/s the draghead, for a Damen SLK600 used in the case study, will lift off from the bed. It should be notified that, among other variables, the dredging depth has an effect on this 'floating' point. Moreover, the results showed that the drag forces at common trailing velocities of 1-2 m/s are relatively low compared to the soil excavation forces and therefore have a small share in the total trailing forces. When the suction pipe system is trailed against the current the dragforce becomes more significant.

The interaction of the draghead with the bed causes several processes to take place. The resulting relevant trailing forces are mapped and determined. The settlement of the draghead causes a hump of sand to be pushed forwards which result in a sled force and a friction force. Besides that, the flow through the pipes will cause impulse forces in the bends and at the end of the jet pipe out of the nozzle. The jets fluidize the sand which results in the largest production contribution. Furthermore, it can be seen that the penetration depth and cavity width of the jets depend on the trailing velocity and determine the amount of sand that is loosened. The cavities can overlap at low trailing velocities, resulting in a jet production limit.

The jets have a significant influence on the behaviour of the visor. The freely suspended visor will drop until a solid bed layer is reached. The cutting force and vacuum force are the dominant forces working on the visor. Application of the equilibrium-moment method showed that the visor is slowly moving upwards when the trailing velocity is increased. However, the cutting layer thickness remains almost constant for an increasing trailing velocity which results in a linear increase of the cutting production. The cutting production contributes, 20-25%, to the total situ production. The total jet and cutting production lead, together with the jet water inserted and ambient water flow, to the total production and mixture density. When the capacity of the dredging pump is insufficient, spillage will occur.

This research shows the best possible estimate of the draghead production and corresponding trailing forces. It should be kept in mind that the calculations are based on a simplification of the suction pipe system and the geometries of the suction pipe system of Damen. Nevertheless, a lot of research can be performed into the processes that occur, to improve the results of the calculations. Suggestions for further research would be to determine the magnitude of the vacuum force, the erosion production which is not considered in this research or the on velocity depending cavity width. Validations of the results is another point of consideration. Thus, to determine trailing forces and production, the new approach used in this study contributes to a better understanding of the draghead.

KEYWORDS:

Draghead, suction pipe, freely suspended visor, trailing velocity, trailing force, drag force, jet production, penetration depth, cavity width, cutting forces, cutting layer thickness, cutting production, production mixture density

Contents

Contents	9
1 Introduction	13
1.1 Trailing suction hopper dredger	14
1.1.1 Draghead	14
1.1.2 The suction tube and dredge pump.....	15
1.1.3 Hopper loading and unloading.....	16
1.1.4 Propulsion and ship	16
1.2 Fields of research	17
1.3 Problem description	18
1.4 Research goals and scope	18
1.5 Research questions	19
1.6 Report structure	20
1.6.1 Model structure	20
1.6.2 Chapter structure	21
2 Force analysis of the suction pipe	23
2.1 Literature.....	25
2.1.1 Gravity force.....	25
2.1.2 Drag force	26
2.2 Model description.....	30
2.2.1 Geometry suction pipe.....	30
2.2.2 Moment and force balances	32
2.3 Model results & Discussion.....	39
2.3.1 Forces working on the suction pipe	39
2.3.2 Results of the trailing force without soil excavation forces	40
2.3.3 Results of the trailing force with soil excavation forces	41
2.3.4 Total trailing force	43
2.4 Verification	44
2.4.1 Verification of the drag force coefficient	44
2.4.2 Influence current velocity.....	45
2.4.3 Verification of the dredging depth influence	46
2.4.4 Verification trailing forces.....	47
2.5 Conclusion	47
3 Force analysis of the draghead	49
3.1 Literature.....	50
3.2 Model description.....	51
3.2.1 Forces on the draghead.....	51
3.2.2 Soil characteristics.....	53
3.2.3 Calculating the trailing forces on the draghead	56
3.3 Model results & Discussion.....	66
3.3.1 Forces on the draghead.....	68

3.3.2	<i>Total force balance</i>	74
3.4	Optimization & Verification.....	76
3.4.1	<i>Accuracy cutting forces</i>	76
3.4.2	<i>Verification soil compaction force</i>	76
3.5	Conclusion	78
4	Jetting production	79
4.1	Literature.....	81
4.2	Model description.....	82
4.2.1	<i>Calculation of the pump pressure, jet- velocity and discharge</i>	82
4.2.2	<i>Jet production</i>	85
4.3	Model results & Discussion.....	95
4.3.1	<i>Jet geometry</i>	95
4.3.2	<i>Pump pressure, jet- velocity and discharge</i>	95
4.3.3	<i>Jet production</i>	96
4.4	Optimization & Verification.....	99
4.4.1	<i>Optimizing the jet settings</i>	99
4.4.2	<i>Vlasblom's coefficient: alfa</i>	99
4.5	Conclusion	101
5	Cutting production	103
5.1	Literature.....	105
5.2	Model description.....	106
5.2.1	<i>Visor geometry</i>	106
5.2.2	<i>Visor equilibrium-moment method</i>	110
5.2.3	<i>Soil excavation forces of the visor</i>	111
5.2.4	<i>Cutting production & jet dependency</i>	111
5.3	Model results & discussion	112
5.3.1	<i>Visor forces</i>	113
5.3.2	<i>Visor equilibrium with variable layer thicknesses</i>	117
5.3.3	<i>Soil excavation forces of the visor</i>	118
5.3.4	<i>Cutting production</i>	119
5.4	Optimization & Verification.....	120
5.4.1	<i>Narrowing of the wearing pieces</i>	120
5.4.2	<i>Cutting production for an optimized visor</i>	121
5.4.3	<i>Vacuum force dominance</i>	122
5.4.4	<i>Spillage</i>	122
5.4.5	<i>Cutting teeth holders and negative blade angle</i>	125
5.5	Conclusion	126
6	Conclusion & Recommendations	127
7	References	129
8	Appendices	131
8.1	Appendices chapter 1	131
8.1.1	<i>Detailed flow chart of the trailing force and production model</i>	131
8.2	Appendices chapter 2	132
8.2.1	<i>Naming explanation of the suction pipe segments</i>	132

8.2.2	<i>Lengths suction pipe TSP600</i>	133
8.2.3	<i>Skin friction of the suction pipe</i>	134
8.3	<i>Appendices chapter 4</i>	135
8.3.1	<i>Jetting theory</i>	135
8.3.2	<i>Jet discharge (Bernoulli)</i>	136
8.3.3	<i>Cavitation</i>	137
8.3.4	<i>Dilatation and Erosion (high speed erosion)</i>	138
8.3.5	<i>Moody diagram</i>	139
8.3.6	<i>Results traversing jet experiment Wegenaar</i>	140
8.3.7	<i>Maximum jet power</i>	140
8.4	<i>Appendices chapter 5</i>	141
8.4.1	<i>Resolution of forces working on the visor</i>	141
8.4.2	<i>Pore pressure distribution shear plane and blade</i>	141
8.4.3	<i>Moment balance around the visor hinge</i>	142

1 Introduction

Dredging is the excavating of soils from an area under water, as for example rivers, lakes and seas, with a dredge. In the past, canals and harbours have been dug by hand but in the industrial revolution machine powered tools have been designed to accelerate the process, ease the work and reduce the costs. In the middle of the 20th century the trailing suction hopper dredger (TSHD) has been invented. A trailing suction hopper dredger can be compared with a large vacuum cleaner that is dragged behind a vessel over the seabed and sucks up the soil (see Figure 1). The main function of a trailing suction hopper dredger is to maintain the depth of canals, rivers and harbours by removing sand and silt. Another major function is to reclaim land from the sea by dumping soil in coastal areas.

A hopper is able to dredge and store soil while sailing and is therefore not an obstruction for the ship traffic in rivers and harbours. Stationary dredgers often use anchors in order to maintain their position and therefore can create dangerous situations. Another advantage of the TSHD is that the excavated soil can be transported over larger distances. The excavated soil can temporarily be stored inside of the vessel, in the storage area, which is called the hopper. And last but not least, trailing suction hopper dredgers are also quite suitable to work under offshore conditions which extends the working area and put them in a unique position in comparison to other type of dredgers.

In the first paragraph of this chapter, the working principle of a trailing suction hopper dredger is further explained. Afterwards, it will be clear that a hopper is not just a vessel but more a floating sand production factory. Aboard the vessel are various tools that all help with excavating, transporting and storing the sand. In the second paragraph, the different fields of research are discussed which is an introduction to the scope and the need for this research which can be found in the problem description in the third paragraph. Although a lot of research has been done by academic institutions, shipbuilders and dredging contractors, many questions remain to be answered.

In the fourth paragraph, the research goals are formulated. These goals delivered the research questions as stated in the fifth paragraph. The report structure is described in the last paragraph and is a guideline to understand the method used throughout the report to solve the problem.



Figure 1: Trailing suction hopper dredger manufactured by Damen Shipyards

1.1 Trailing suction hopper dredger

In this paragraph, the working principle of a trailing suction hopper dredger will be explained in more detail. The dredging vessel is divided into segments which will be explained separately (see Figure 2). To start with the draghead and the suction tube which are positioned on the side of the vessel. First, the draghead loosens the soil which is then hydraulically brought up to the surface. By use of multiple gantries, the suction pipe is lowered by cables to the bed. The suction pipe is attached to the hull where it is connected to the pump system which transports the fluid mixture. The centrifugal pumps which are typically used, convert rotational energy into movement of the fluid. Because the pressure rises, an under pressure is created at the inlet which “pushes” the mixture into the pump. After the mixture has passed the pump, it is loaded into the hopper where the soil settles and the water flows off. Offloading can be performed in different ways which is explained in the last segment of this paragraph.

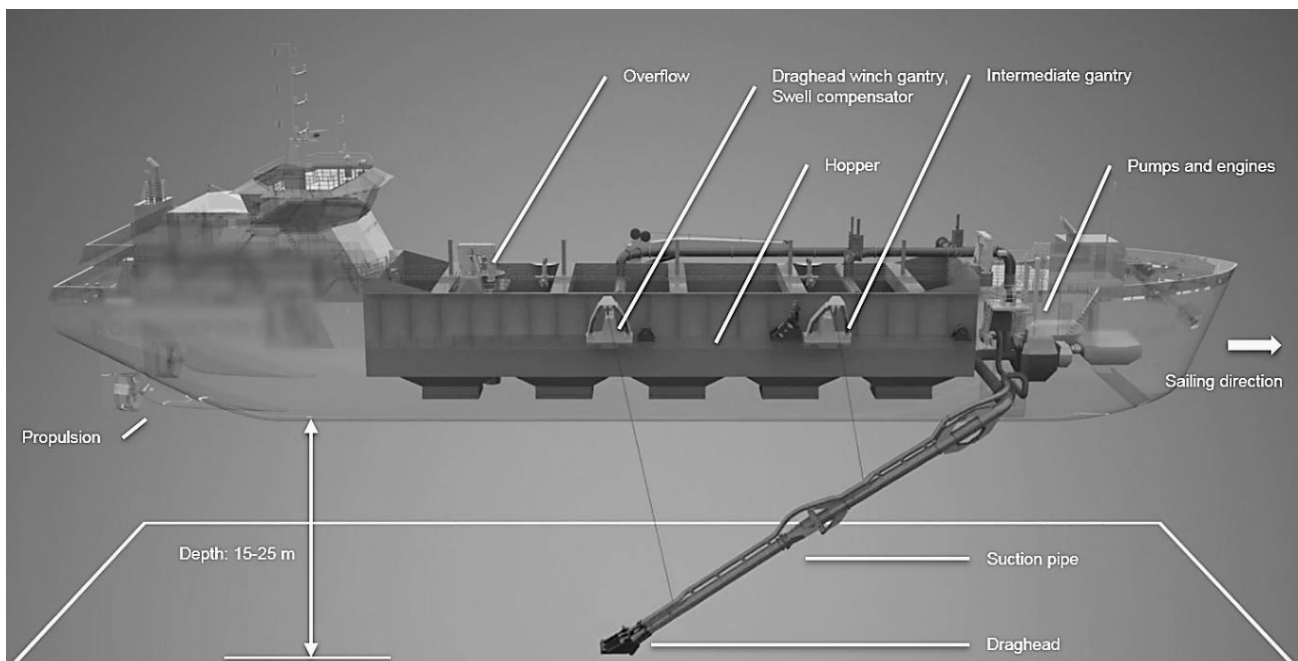


Figure 2: Naming different segments TSHD 2000

The materials that are mostly excavated by a TSHD are sand and silt. Other materials, like clay and rock, are possible to be excavated but could cause several problems. The cohesive clay often sticks inside the draghead and suction pipe where it blocks the supply of the soil mixture. Inside of the suction pipe, clay can form clay balls that can grow to the size of a football. In the pipe bends or dredging pump, these balls could get stuck and then cause blockage of the flow. Also, the draghead often slides into the old trails while dredging clay, which is called 'rutting'. During rock trailing the draghead faces several problems. The draghead needs to be incredibly heavy to scratch and cut the rock. The production remains very low and, consequently, is therefore often not economical.

1.1.1 Draghead

During dredging a large steel structure is dragged behind the vessel over the seafloor. This enormous heavy 'box' is called the draghead. It is attached to the tip of the suction tube. The draghead cuts a layer of soil with the cutting teeth, attached to the visor. The visor can move up and down by use of a hinge, placed in the heel of the visor house. The visor can be supported in three different ways. First, the layer thickness can be regulated by fixing the visor to the visor house in order to realize a solid layer thickness. Another way to vary the layer thickness is by regulating a certain pressure in the cylinders. The cylinders are placed between the visor and visor house, see Figure 4. Or, what is done most often, the visor is not supported and is able to move, around 70 degrees, up and down. The draghead will find an equilibrium position depending on the forces it encounters.

During cutting the shear forces causes the grains to move out of their structure. The enlargement of the pores leads to entrainment of water. As a result the narrow channels between the grains cause resistance for the

inflowing water. The resulting pressure difference pushes the grains even harder together which increases the soil stresses and cutting force (chapter 3). The solution for reducing the cutting forces is to install waterjets in front of the draghead opening. A jet hose, which runs from the jet pump, inboard the vessel, over the suction pipe to the draghead is attached to the jet chamber inside the draghead. Here, the water flow is divided into several jets with a smaller diameter placed in a row. The jets penetrate water under high pressure between the grains of the soil into the pores. In this way, the soil is dislocated from its densely packed structure. The soil is stirred up by the turbulence of the water and by means of an under pressure created by the pump the soil is transported into the suction tube, which runs from the draghead to the hull of the vessel. The soil is transported with the surrounding water by means of erosion. Erosion is the transport of soil with the use of a fluid.

The draghead will endure heavily in the harsh environment where it is working in. To protect the draghead against damage and to extend its lifetime, there are wear pieces attached to sensitive areas as for example around the hinge, the visor and in front of the draghead. Here, the draghead will push a hump of sand in front of the draghead because of the uneven bottom floor and because the draghead will sink a little bit into the sand bed due to its weight. The wear pieces are fabricated out of special metal alloys.

Over the years, the draghead design has not changed that much. The two main designs used are the Californian draghead and the Holland model. The difference between the two designs is that the Californian draghead is divided into two separate visors. The philosophy behind this design is that there is larger area where entrainment of water can take place which leads to a higher erosion production.

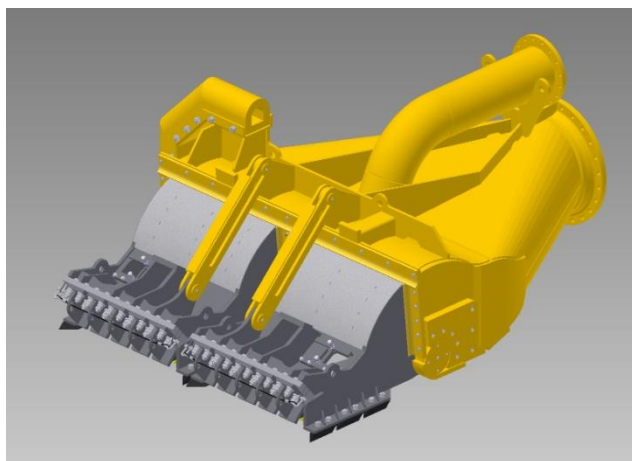


Figure 3: Californian model

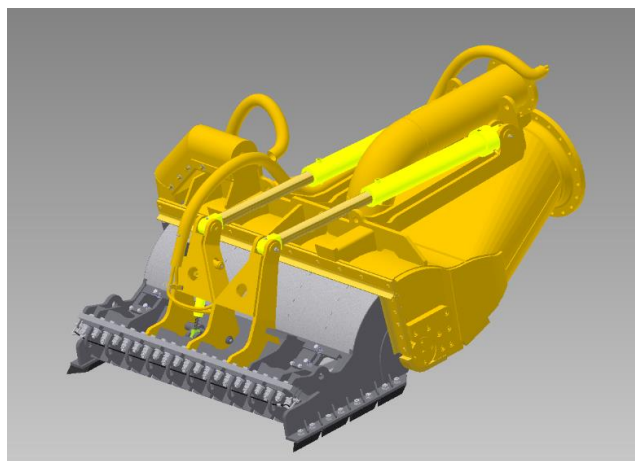


Figure 4: Holland model equipped with hydraulic cylinders

1.1.2 The suction tube and dredge pump

The suction tube is a long pipe equipped with cardan hinges and turning glands to compensate the movements that arise between the draghead and the sea bed due to the motion of the vessel. The main function of the suction tube is to transport the soil mixture into the vessel and the jet water in the opposite direction to the nozzles. For larger vessels with long suction tubes dredging at large depths an underwater pump is needed to avoid cavitation in the main dredging pump. The underwater pump is usually positioned halfway the suction pipe. The benefit of this pump is that the absolute pressure is lower, and cavitation will less likely occur.

The biggest part of the vessels motion is compensated by use of a swell compensator. The swell compensator makes use of a large hydraulic cylinder which can move up- and downwards. The cable which is attached to the suction pipe runs over a pulley and when the draghead is lowered onto the seabed this hydraulic cylinder moves upwards and secures that a certain tension is maintained on the cable. The opposite of this situation happens when the hopper is moved upwards by the motion of the waves and the draghead is released from the bottom. The dynamic force caused by the weight of the suction pipe and draghead will push the cylinder downwards in this case. This system avoids that the draghead starts bouncing on the bed by the motions and makes sure the production is not interrupted. A significant wave height of three meters can be conquered with the swell compensating system of Damen's TSHD 2000.

1.1.3 Hopper loading and unloading

The soil mixture is temporarily stored in the hopper of the vessel. This large tank also functions as a settlement area where the soil is separated from the water. The soil settles to the bottom and water flows off through the overflow. The overflow is a large tube which is positioned vertically in the centre of the hopper. The overflow can be adjusted in height to ensure that even in the beginning of the loading cycle water can be drained off. When the sand bed is rising the overflow is slowly moved upwards. By lowering the overflow in the end of the hopper loading, often a denser sand mixture can be reached.

The inflowing sand mixture will slowly settle in the hopper. Near the inlet, a high density flow sinks directly to the bottom. Due to these density waves, there are large flow velocities which causes turbulence and disrupt the particles from settling. Also, the different particle sizes disturb the settling process. This is called hindered settling. Because not every particle settles at the same speed, in the wake of the faster, bigger particles, the smaller particles are pushed upwards. By use of multiple inlets, the sand mixture can be equally distributed over the hopper. The loading continues till the dredge mark is reached. The dredge mark is the maximum allowed draught of the vessel. The stability and maximum draught of the vessel depends, amongst other things, on water temperature and salinity. This is the reason why there are multiple dredging marks, each for a different situation.

After the hopper is filled, the pumps will continue to run with fresh water for a while. The reason for this is to clean the pipes to remove all the particles in the pipes and between the closures. Cleaning will prevent wearing of the closures, blockage due to settling of particles in the pipeline and ensures that less weight is present inside the suction pipe while hoisting the pipe on board.

When the discharge area is reached, the hopper content needs to be dumped. During loading most of the water is drained off so the soil needs to be fluidized again. Therefore, jets are installed, in the bottom floor. The fluidized sand- water mixture is discharged out of the hopper in several ways. Often, the way the soil will be dumped depends on the purpose the soil has been dredged for. The excavated soil can be dumped in three different ways:

- *Rain bowing*
- *Discharge pipeline*
- *Quick discharge (Bottom doors/ Split hopper)*

Rain bowing is spraying of the soil mixture, under high pressure, over large distances from the vessel to the dumping area. The sandy brown arc that can be seen during rain bowing is the reason for the naming. Hoppers can approach the beach closely and deliver the sand directly onto the right spot. Rain bowing is mainly used for land reclamation and beach strengthening.

When rain bowing is not an option, because of the distance that needs to be covered, a floating pipeline can be connected to the bow of the ship to press the sand mixture through hoses to the dumping site. At site the soil will settle and the water flows off. The settled soil will be distributed by bulldozers over the dumping area.

The bottom doors are large doors in the bottom of the vessel which are hydraulically driven and can dump the load within a few minutes. It is the fastest way to unload the hopper. A disadvantage of this type of discharging the load, is that the depth needs to be sufficient enough for the draught of a loaded hopper to open the bottom doors. Dumping for reclamation purposes is therefore possible until a certain depth. A split hopper works in a similar way, the difference is that a split hopper separates the hopper in two over the whole length of the vessel. The split hopper and bottom doors can both be used for covering and supporting pipelines. In harbors there are special dumping facilities where contaminated sand can be pumped to shore where it is cleaned on land.

1.1.4 Propulsion and ship

When the vessel needs to move from the harbour to the dredging site, it is able to sail with a maximum speed, at dredging depth, of around 10-12 knots (11.5 knots; 21.2 km/h, Damen's TSHD 2000 m³). The vessel is powered with large engines which power the propellers, and also the pumps and other tools onboard. The average trailing speed of a TSHD is around 2-3 knots (4.5 km/h). The hull of the hopper is optimized for a large storage area, but also the manoeuvrability and resistance of the vessel should not be forgotten. A trend of the last few decades is the increase in hopper size. Large hoppers can dredge cheaper and are therefore more competitive. They are especially used for land reclamation where manoeuvrability is not the biggest issue.

1.2 Fields of research

To remain a leading shipbuilder, there is a constant desire for Damen to build innovative and competitive vessels for their customers. Shipbuilding for the dredging industry means designing vessels which can excavate the soil in an efficient way for the lowest price. This can be managed by continuing to improve the total dredging process.

The research of Braaksma is focussed on how to model a TSHD so that the total process can be controlled automatically (Braaksma, 2008). As introduced in paragraph 1.1 and showed in the control model of Braaksma in Figure 5, the trailing suction hopper dredger can be divided into different segments. The segments mentioned in the figure (the power train, ship design, hopper, pump- and pipeline and draghead), are modelled as 'black boxes'. This simplified model shows the working of the TSHD in a schematic way and the strong relation between the different processes that take place during dredging.

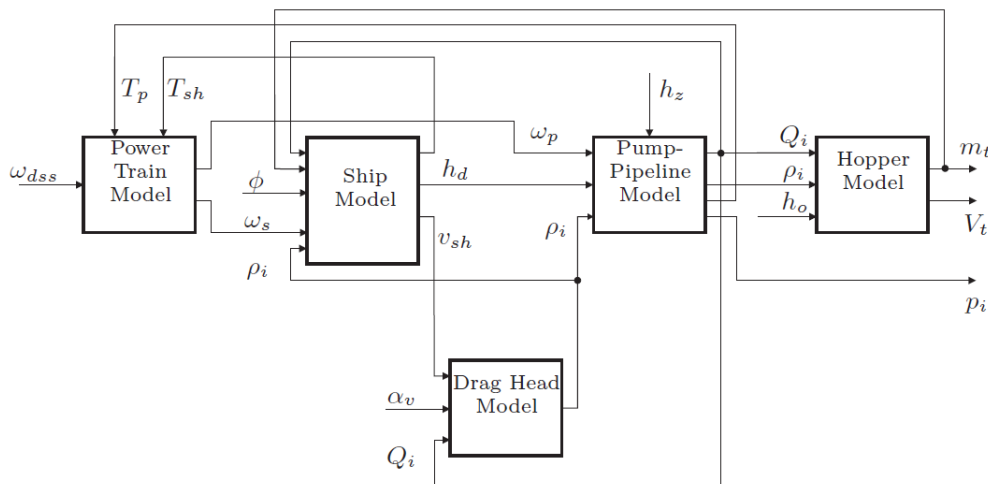


Figure 5: Control model dredging process (Braaksma, 2008)

The power train model powers the vessel and the pumps. The vessels trailing velocity, determined by the ship model, controls the speed in which the draghead is dragged through the soil. The draghead excavates the soil and creates a mixture with a certain flow and density. Thereafter it is transported upwards by the pump into the hopper, which is described by the pump and hopper model respectively. The different variables in the figure are not important at this moment. What is important is: how well described are these models yet?

Damen Shipyards has its own team of naval architects and CFD engineers which are specialized in designing hydrodynamic hulls and efficient propulsion systems. The power train model describes the power needed to overcome the total resistance from the vessel and its tools. The resistance of the vessel is included in the ship's model. The residual resistance is mainly caused by the resistance of the suction pipe and draghead and partly by the draghead model. Another recent collaboration between Damen Dredging Equipment and the TU Delft has given a lot of insight on hopper loading. A CFD model, designed in Openfoam by B. Sloof, can determine the settling behaviour of a certain particle size in the hopper (Sloof, 2017). With this model, the overflow losses can be determined, and thanks to the visualisations of the CFD simulations it shows where there is room for improvements for future hopper designs.

The pump system has been the focus of Damen Dredging Equipment over the last years. A specialized team of engineers is continuously improving the dredge pumps geometry and specifications. Also, a lot research has been done about the transport of mixture flows in pipes at the Technical university of Delft.

Miedema, van Rhee, Vlasblom and many others have described the different processes around the draghead and the interaction with the soil (Miedema, The Delft Sand, Clay and Rock Cutting Model, 2014), (Rhee, Lecture notes Dredging Processes 2 [OE4727], 2016). **However, the draghead model, as a whole, is under investigated. In literature the processes have never been integrated to see the interaction. A perfect described draghead model can give accurate feedback to the power train- and pump and pipeline model.** Like the resistance the draghead face and what the mixture density and flow is, immediately after it leaves the draghead. The drag head model of Braaksma was focused on the control properties and the physics is very simplified.

1.3 Problem description

The previous paragraph already gave an impetus to the problem description which is the need for an accurate and completely described draghead model. The more detailed problem description is defined in the end of this paragraph but the need for the model will first be explained from a more theoretical and practical point of view.

The behaviour of the draghead depends on a lot of processes. ***The behaviour refers to how the draghead is moving depending on the trailing forces which act on the draghead. When the trailing velocity changes, the force distribution also changes and the draghead will find a new equilibrium position.*** The variations in trailing velocities, soil characteristics and draghead and suction pipe geometries do not make it easier to determine the trailing forces on the draghead and suction pipe. Because of this complexity it is hard to define how to handle the equipment to gain and estimate the optimal production. Furthermore, the expected trailing forces are needed for engineering of the equipment and choosing the required propulsion system.

Because the excavating of the soil takes place at the bottom of the sea at large water depths, it is difficult to see what is actually happening. For the operators, the production is a mystery until the moment the mixture is on board, they can read on the measuring systems and see in the hopper what there has been excavated. Moreover, every vessel is manned with a different crew. Practice shows that they all dredge in their own manner which result in divergent productions. It would be valuable to advise the operators in how to dredge in an optimal way with the equipment. This could lead to a more consistent- and optimal production. The next step could be to fully automate the production process so that no human differences or failures can occur. This is in the trend of the whole maritime industry that moves to fully automated ships. Only when something goes wrong, there needs to be intervened by the small crew that is still present on board.

The practical problems above show the need for a draghead model so that every process in the draghead model and the interactions are understood. This leads to the following problem description:

- ***There is a lack of knowledge about the interaction of the draghead's physical processes to understand what is happening inside and around the draghead.***
- ***The relation of the behaviour of the draghead depending on the trailing velocity is unknown.***
- ***The total production of the draghead cannot yet be accurately determined.***

1.4 Research goals and scope

The aim of this research is to get more insight about what is happening around the draghead. By integrating the excavation processes into a model and using that expertise to determine the forces and predict the production. First all the knowledge and theory about the draghead needs to be collected and analysed what is already available. Subsequently, a draghead force- and production model can be designed that integrates the different processes. Eventually, the draghead model should be integrated in a production (control) model, comparable to the model shown in paragraph 1.2, to give the answer on the total force and production estimation. The integration itself is not included in the scope of this project. In summary, the design process of the model can be defined in four research goals:

- *Acquiring knowledge about which physical processes take place during the interaction of the draghead, soil and water.*
- *Determining the forces on the draghead as a function of the trailing velocity.*
- *Determining the behaviour of the draghead as a function of the trailing velocity.*
- *To find the production as a function of the trailing velocity.*

There are many types of soil that can be encountered, all with different excavating techniques. Because of limited time for this research, the focus in this research is on the soil composition sand. This is the type of soil that is most often excavated by trailing suction hopper dredgers.

To verify the model, a case study will be performed throughout the research. The suction pipe system of Damen Shipyards will be used for the different test cases.

1.5 Research questions

The problem description and research goals lead to the following main research question:

“How can the physical processes around the draghead be integrated into a model and used to determine the trailing forces and the production?”

For convenience the main research question is divided into several sub questions and are arranged per chapter. The report is divided into two parts, A and B. The explanation of the two parts, is explained in the next paragraph, 'Report structure'.

Part A:

Chapter 2 (Force analysis of the suction pipe):

- What is the magnitude of the drag forces caused by the suction tube?
- What is the influence of the suction pipe to the behaviour of the draghead?
- At which trailing speed will the draghead lift off from the seabed?

Chapter 3 (Force analysis of the draghead):

- Which physical processes take place in and around the draghead?
- What is the magnitude of the trail forces caused by the draghead?
- What are the dominant parameters for the trailing forces?

Part B:

Chapter 4 (Jetting production):

- What is the influence of the trailing speed on the jet penetration depth and cavity width?
- What is the jet production depending on the trailing velocity?
- Which parameters influence the jet production and can be changed to optimize the jet design configuration?

Chapter 5 (Cutting production):

- What is the magnitude of the cutting forces?
- What is the equilibrium position of the draghead visor depending on the trailing velocity?
- What is the contribution of the cut production to the total production?
- What is the volume production rate of the total production?
- What are the limitations of the draghead for the total production?

1.6 Report structure

In this paragraph is explained in which sequence the problem has been analysed and tackled. A visualisation of the model structure will substantiate the choice for this sequence. Additionally, explained is how each chapter is structured and the choice to do so.

1.6.1 Model structure

The research can be divided in two parts, A and B:

- **Part A:** The force analysis -> determines the behaviour of the draghead
- **Part B:** The production analysis -> follows from the behaviour of the draghead

It appears that the forces are the input for the production. The first step in researching the main goal of the research is determining the behaviour of the draghead by analysing and calculating all relevant forces. And subsequently the production can be determined with the calculated equilibrium positions of the suction system. The structure of the different parts in chapters are visualized in Figure 6.

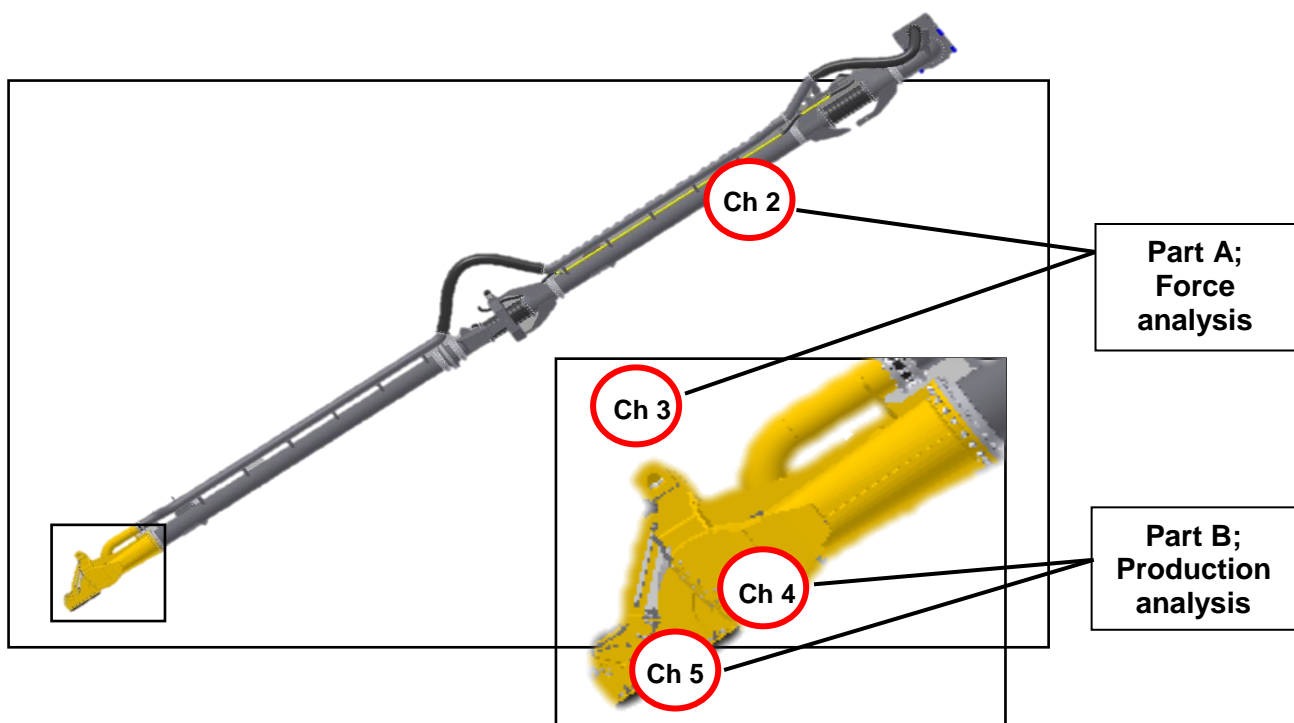


Figure 6: Model structure

Part A: Analysis of the draghead and suction pipe

Chapter 2 and chapter 3 are mainly about the trailing forces. In chapter 2 the behaviour of the suction pipe is described. The suction pipe transfers all the forces encountered by the draghead towards the hull of the vessel. The suction pipe is also dragged through the water which causes drag forces. The force balance of the suction tube, the influence of the suction tube on the draghead and its equilibrium position will be described in this chapter.

Chapter 3 is about the forces on the draghead caused by the many processes that occur around the draghead. The forces follow mostly from the interaction between the draghead and the seabed. That is the reason the first paragraph of this chapter defines the soil characteristics of sand, which are also used in the rest of the report. The remainder of this chapter describes in detail which forces act on the draghead. Most of the forces are determined by the end of this chapter and the total force balance of the draghead can be made up. Except for the jet- and visor forces which are described more fully in chapter 4 and 5 but they are used already for the force balance in chapter 3.

Part B: Production draghead

Now it is known what the behaviour of the draghead is. With that the first production contribution can be determined. Jetting, described in chapter 4, is the loosening of soil by fluidizing the sand. In this way the soil can be pumped upwards more easily and, it contributes to the total production. Not to mention that another purpose of jetting is reducing the cutting forces. Jetting fluidizes the sand until a certain depth causing a reduction of the bearing capacity of the soil. In this way the visor sinks further down the soil. The cutting force, friction force, vacuum force and gravitation onto the visor now determine the equilibrium position of the visor, this is described in chapter 5. The production model takes the position of the visor into account and determines the cutting layer thickness for the 'cutting production'. Furthermore, the situ production contributions are merged and with the aid of a mass balance the remaining production contributions are calculated. In the end of this chapter, the total production and mixture density are calculated. In the remaining chapter of the report the final results are presented in the conclusion.

1.6.2 Chapter structure

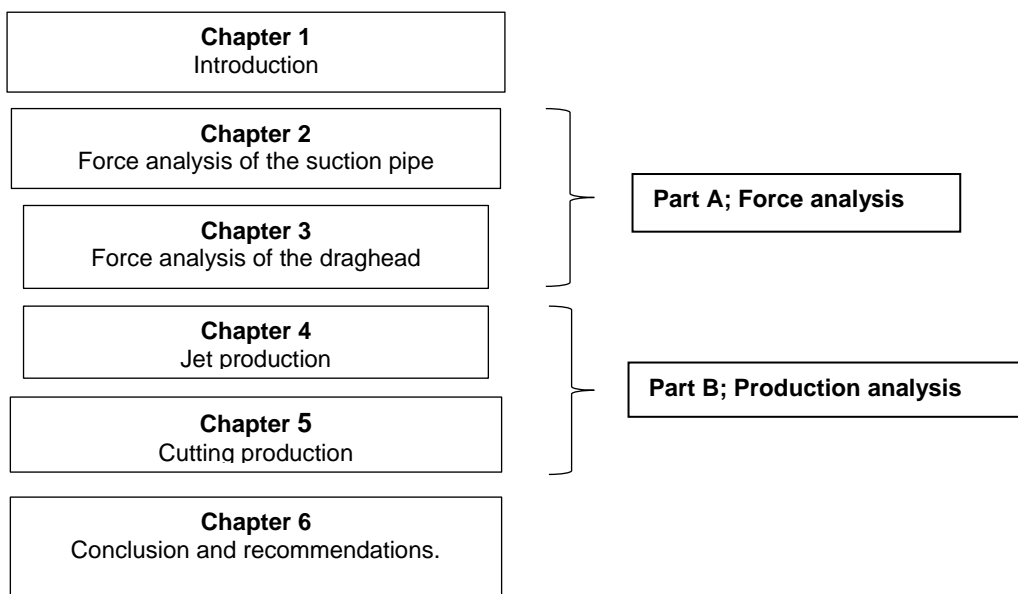


Figure 7: Report structure

The structure from chapter 2 to 5 is equal. In the beginning of each chapter the main topic is introduced, and all used literature is summarized briefly. Thereafter is shown how the theory is used and implemented into the model, in the 'Model description'. For every 'chapter' of the model, in paragraph 'Model results & Discussion', a case study is used to verify whether the model shows recognizable behaviour seen in practice. The results and observations are also directly discussed and concluded in the end of each chapter. The chapter structure is visualized in Figure 7 and Figure 8.

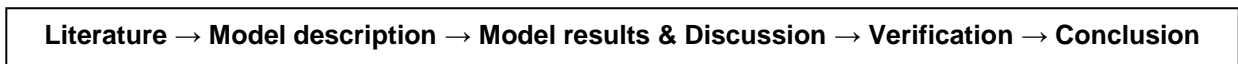
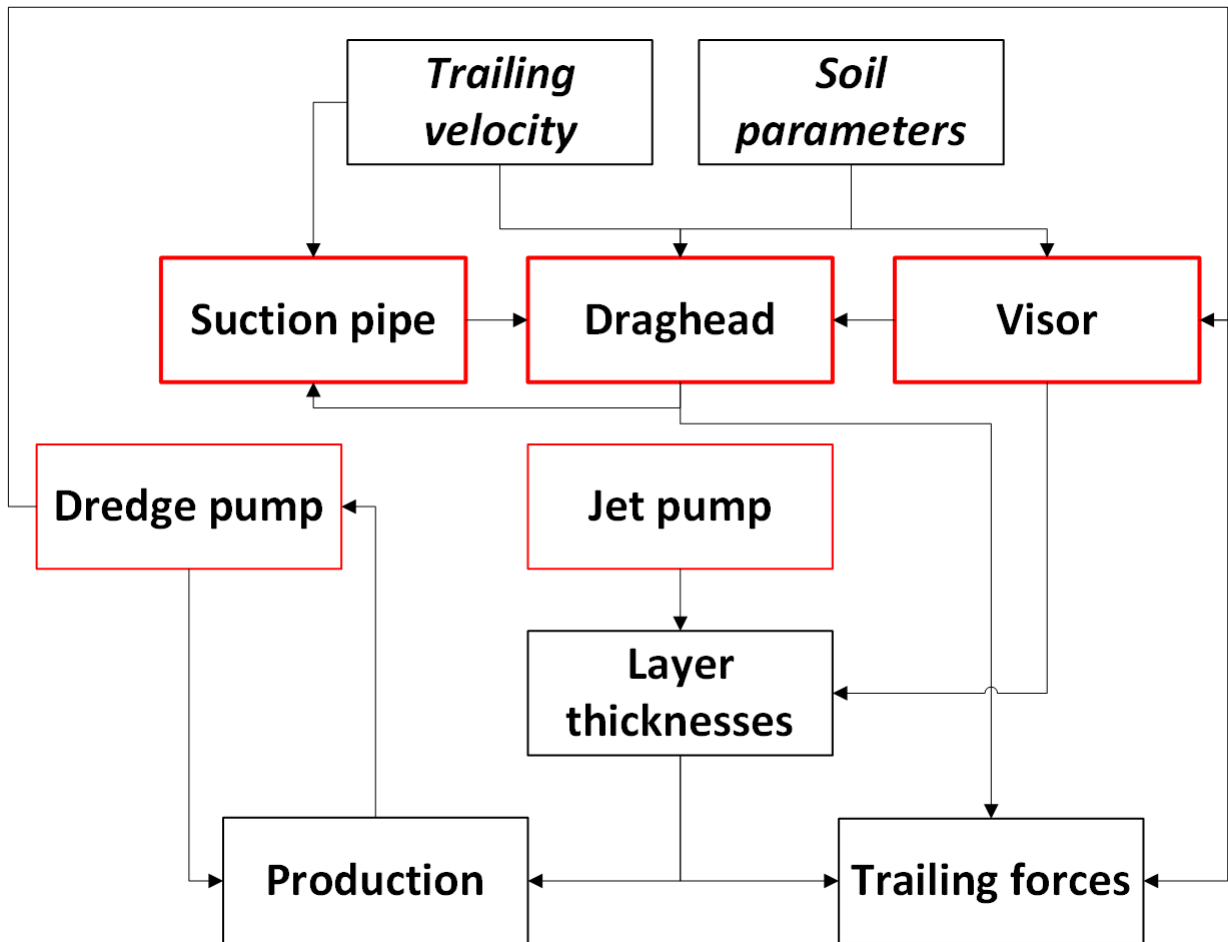


Figure 8: Structure of each chapter

On the next page a flow chart of the total model is shown. The chart shows the connection between the different parts and the importance to start with analysing the suction pipe first. The red lined boxes can be seen as the chapters in this report which together give an answer to the main research question. A more detailed version of the flow chart can be found in appendix 8.1.1.



2 Force analysis of the suction pipe

The suction pipe is attached to the hull of the vessel and is supported by two cables and the sliding piece rails. The cable length can be adjusted to lower the draghead to the seabed. The suction pipe is divided in three segments which makes it possible to change the angle between the pipes to work at different water depths.

There are two reasons why is started with analysing the suction pipe. The first reason is to determine the influence of the suction pipe's weight on the draghead's force balance. The gravity force working on the heavy structure should keep the draghead on the bed. For the calculation of the trailing forces, the resulting vertical force from the draghead and suction pipe on the bed is needed, abbreviated with $F_{c,v}$. The vertical force balance of the draghead depends on the distribution of the forces of the draghead and suction pipe over the bed, cables and sliding piece construction and will be calculated in this chapter (illustrated in Figure 9 and Figure 10).

The second reason is that when the suction pipe is trailed through the water, it experiences drag forces. As soon as the trailing velocity increases the drag forces will also increase. There might be a trailing speed where the trailing forces become so large that the draghead will lift off from the bed. When the draghead loses contact with the bed, sand production will stop. This moment can be seen as a trailing velocity production limit. Finally, for the total trailing forces, not only the forces on the draghead are included, but also the drag forces on the suction pipe.

In the literature, in the first paragraph, the drag force experienced by the suction pipe system is described in detail. In the past, multiple researches have been performed to find the drag coefficient for a cylindrical pipe. The results of previous research will be used to estimate the drag coefficient of the suction tube. In the model description, paragraph 2.2, the geometry of the suction pipe is shown. Besides that, is focused on how to determine the trailing forces and how the reaction forces of the suction pipe change when the trailing velocity is increased. For the case study, the geometries and dimensions of Damen's TSP600 are used. The abbreviation TSP600 means a trailing suction pipe with an inner diameter of 600 mm. These results are crucial for the rest of the report.

The suction pipe is simplified so it can only move in the vertical plane, in the length of the vessel. Dynamic motions will not be taken into account. It is assumed that the swell compensator takes away all the motions of the ship, the waves and slopes of the bed. Also, rotations of the turning glands are ignored and the two upper pipe pieces are seen as one fixed upper pipe. The simplification is further explained in 2.2.1. In paragraph 2.3 the total trailing force of the suction pipe and draghead is calculated.

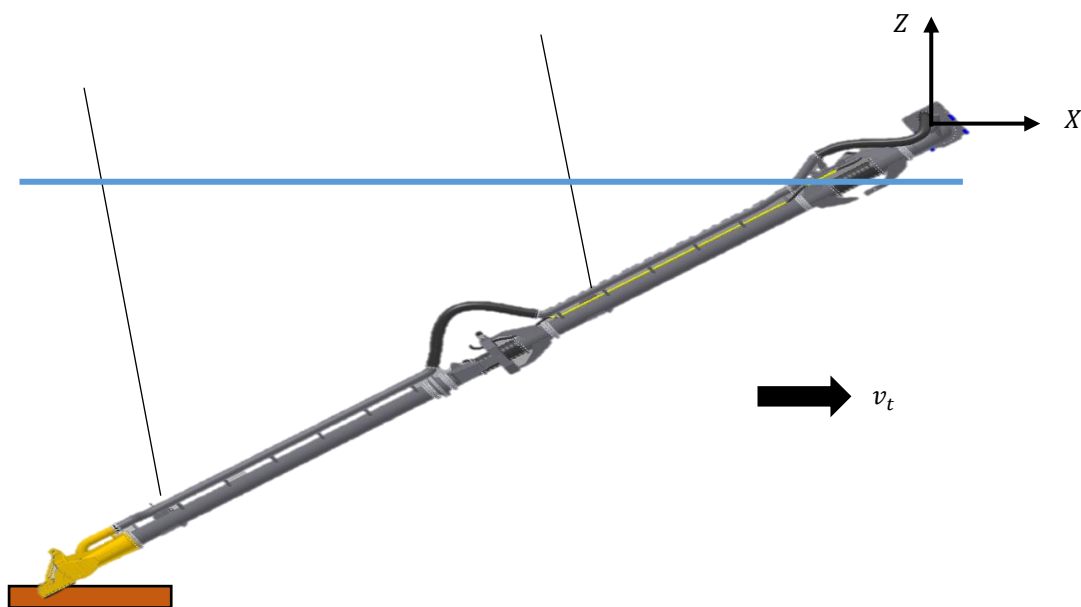


Figure 9: Side view X-Z plane, Damen suction pipe system: TSP600

Notation

Latin		
C	Compensation factor swell compensator	%
C_d	Drag coefficient	-
D_{pipe}	Pipe diameter	m
$F_{A,h}$	Horizontal reaction force in A (sliding piece)	kN
$F_{A,v}$	Vertical reaction force in A (sliding piece)	kN
$F_{B,h}$	Horizontal reaction force in B (cardan hinge)	kN
$F_{B,v}$	Vertical reaction force in B (cardan hinge)	kN
$F_{C,h}$	Horizontal reaction force in C (draghead)	kN
$F_{C,v}$	Vertical reaction force in C (draghead)	kN
$F_{cable,1}$	Cable force in upper pipe	kN
$F_{cable,2}$	Cable force in lower pipe	kN
$F_{drag,1}$	Drag forces on upper pipe	kN
$F_{drag,2}$	Drag forces on lower pipe	kN
F_g	Gravity force	kN
m	Mass	kg
n	Porosity	-
V	Volume	m ³
v_f	Flow velocity along the pipe	m/s
v_t	Trailing velocity (ground speed/ cutting velocity)	m/s
Greek		
α_1	Suction pipe angle upper pipe	°
α_2	Suction pipe angle lower pipe	°
β_1	Cable gantry angle upper pipe	°
β_2	Cable gantry angle lower pipe	°
ν	Kinematic viscosity	m ² /s

2.1 Literature

The forces working on the suction pipe are drag forces from the fluid that flows along the pipe and the gravity working on the heavy steel structure. Both forces are studied and explained in this paragraph. The forces result in reaction forces in points A, B and C and the cables force in the upper and lower pipe. Point C is where all the excavation forces on the draghead apply. These forces are described in chapter 3, 4 and 5 but are used already in this chapter for the calculation of the total trailing forces and behaviour of the suction pipe system. Below, in Figure 10, the simplified suction pipe system with the drag-, gravity- and reaction forces is shown.

Other research on the suction pipe system has been performed by L. Zhi. She researched the dynamic behaviour of the suction pipe due to the ship motions, bed slopes and the swell compensator stiffness (Zhi, 2002). Her report suggested that to make the dynamic behaviour more accurate, attention must be paid to the force analysis of specifically the forces on the draghead. The research has been used for the analysis of the suction pipe in 2.2, but is simplified as stated in the introduction, because this report focusses on the forces and production of the draghead, rather than the complex dynamic movements of the suction pipe.

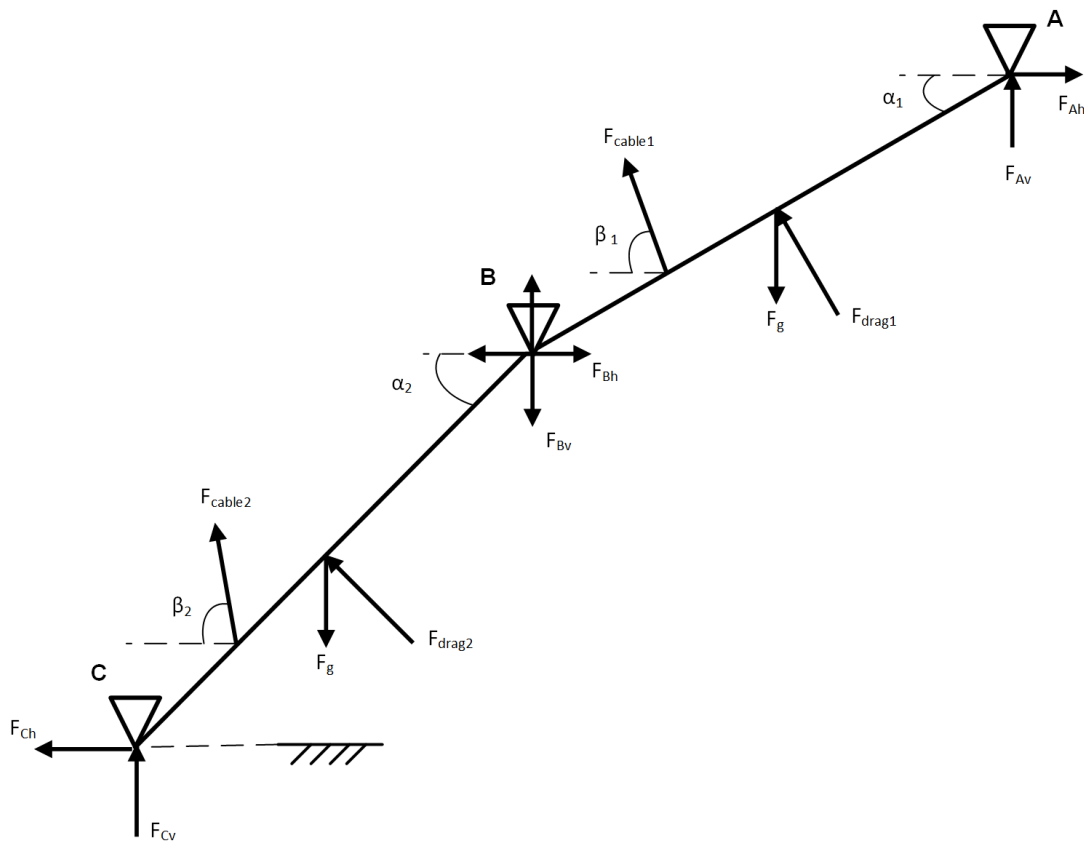


Figure 10: Force diagram of the suction pipe system

2.1.1 Gravity force

The buoyant force is equal to the displaced volume of the liquid by the object. Because of these buoyant forces, the weight of the suction pipe system submerged in water will be lower. The submerged weight of the suction pipe system can be calculated with:

$$m = (\rho_{steel} - \rho_w) * V \quad (\text{eq. 1})$$

$$F_{g,submerged} = m * g \quad (\text{eq. 2})$$

In which V is the volume of the steel structure and ρ_{steel} is the density of the suction pipe and draghead material.

Not only the structure itself, but also the mixture pumped upwards has a significant contribution to the gravity force. Assuming the mixture flow is distributed homogeneously over the pipe, this force can be expressed by the internal volume of the draghead and suction pipe times ρ_m , which is the density of the sand mixture that is transported to the hopper. The mixture density can be calculated with the porosity in case of fully saturated sand, n . The density of sand is $\approx 2650 \text{ kg/m}^3$ and the density of sea water is $\approx 1025 \text{ kg/m}^3$. The mixture density follows from:

$$\rho_m = \rho_s * (1 - n) + \rho_w * n \quad (\text{eq. 3})$$

2.1.2 Drag force

The immersed suction tube and draghead will face fluid resistance during trawling. The motion of the object through the water column causes drag forces. The magnitude of the drag force depends on the magnitude of the flow velocity. The flow velocity (v_f) can be divided in a sailing- (v_t) and current velocity (v_c). The current velocity can increase or decrease the flow speed along the pipe. This depends on the direction of the current velocity. The flow angle from the sailing velocity is almost similar to the sailing direction. However, the current velocity can flow from a different direction than the sailing direction which then changes the flow velocity and flow direction. This can either strengthen or weaken the drag forces on the body. Because the suction pipe and draghead are analysed in two dimensions in the vertical plane, different angles of the current velocity are not taken into account. The current velocity is directed in the direction of the sailing velocity or the opposite.

The drag forces consist of form drag and skin friction. The drag force coefficient depends on the laminar-turbulent regime the body is moving in. With the Reynolds formula (R_e) shown in eq. 4, the Reynolds number can be calculated which then indicates in which regime the fluid is. For a smooth cylinder the boundary layer is in the laminar regime for a Reynolds number up to $3 \cdot 10^5$. Despite that in the wake of the cylinder the situation can already be turbulent. When the Reynolds number increases and is in between $3 \cdot 10^5 < Re < 3 \cdot 10^6$, the boundary layer changes slowly to the turbulent regime which results in a smaller wake because the boundary layer separates at a larger angle. This is visualized in Figure 11 (Dowling, 2015). The effect results in a drop in the drag coefficient from 1.2, for Reynolds of $1 \cdot 10^5$, to 0.4 for $1 \cdot 10^6$, indicated in Figure 14.

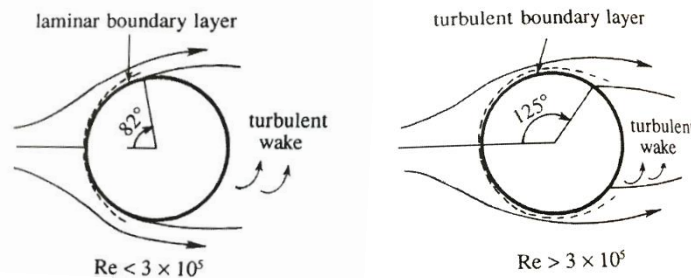


Figure 11: Laminar - turbulent boundary layer (Dowling, 2015)

The calculation of the Reynolds number for the suction pipe and draghead are stated below. The Reynolds number is depending on the width of the body and is therefore different for the suction pipe and the draghead.

$$R_e = \frac{v_f * D_{pipe}}{\nu} \quad (\text{eq. 4})$$

Assuming for the pipe ($v_f = 0.5144 \text{ m/s}$ (1 knots), $D_{pipe} = 0.625 \text{ m}$):

$$R_{e_{pipe}} = \frac{v_f * D_{pipe}}{\nu} = \frac{0.5144 * 0.625}{1.05 * 10^{-6}} = 3.06 * 10^5 [-] \quad (\text{eq. 5})$$

For the draghead (0.5144 m/s, 2.507 m):

$$Re_{draghead} = \frac{v_f * w_{draghead}}{\nu} = \frac{0.5144 * 2.507}{1.05 * 10^{-6}} = 12.28 * 10^5 [-] \quad (\text{eq. 6})$$

This indicates that the flow is in both cases in the turbulent regime. Here, the velocity is that of the pipe relative to the fluid [m/s] which is multiplied by the diameter of the suction tube [m] or width of the draghead [m] and divided by the kinematic viscosity of the sea water ([m²/s]; 20 degrees Celsius, salt water).

In turbulent flows the drag force to the suction tube is quadratically depending on the velocity and can be described by the formula below. Where ρ_w is the seawater density, C_d is the drag coefficient, l_{pipe} the length over which the fluid is flowing and D_{pipe} the diameter of the pipe.

$$F_D = \frac{1}{2} * \rho_w * v_f^2 * C_d * l_{pipe} * D_{pipe} \quad (\text{eq. 7})$$

The suction tube will move through the water column under an angle and will hold this position because it is hung up by the gantry cables and supported by the bed. The inclined pipe will experience a force perpendicular and parallel to the pipe, as shown in Figure 12. The suction tube and draghead can move freely around the hinges and will find a balance with the forces exerted onto the suction pipe and draghead. When the drag force onto the suction pipe becomes too large the draghead might not be able to stay on the ground. The velocity can be decomposed in a perpendicular- and parallel component, see Figure 12, eq. 8 and eq. 9. Where the velocity component perpendicular to the pipe mainly causes form drag, the velocity parallel to the suction pipe causes skin friction. The skin friction is however negligible at high Reynolds numbers and can therefore be ignored. In trigonometric functions the velocity components can be written as:

$$v_{f,\perp} = v_f * \sin(\alpha) \quad (\text{eq. 8})$$

$$v_{f,\parallel} = v_f * \cos(\alpha) \quad (\text{eq. 9})$$

The velocity perpendicular to the pipe determines the Reynolds number, so when the pipe is positioned under a different angle the number needs to be recalculated. Assuming a situation with a velocity of 1 knots [0.5144 m/s] and a pipe angle of 45 degrees, the Reynolds number then becomes:

$$Re_{\perp} = \frac{v_{f,\perp} * D_{pipe}}{\nu} = \frac{0.5144 * \sin(45) * 0.625}{1.05 * 10^{-6}} = 2.27 * 10^5 [-] \quad (\text{eq. 10})$$

The dragforce for the perpendicular contribution can be determined and decomposed in two components, a vertical and a horizontal direction.

$$F_{D,\perp} = \frac{1}{2} * \rho_w * (v_f * \sin(\alpha))^2 * C_d * l_{pipe} * D_{pipe} \quad (\text{eq. 11})$$

$$F_{D,\perp,H} = F_{D,\perp} * \sin(\alpha) \quad (\text{eq. 12})$$

$$F_{D,\perp,V} = F_{D,\perp} * \cos(\alpha) \quad (\text{eq. 13})$$

Now the only unknown variable is the drag coefficient which depends on three factors namely, the Reynolds number, the shape of the body and the skin roughness.

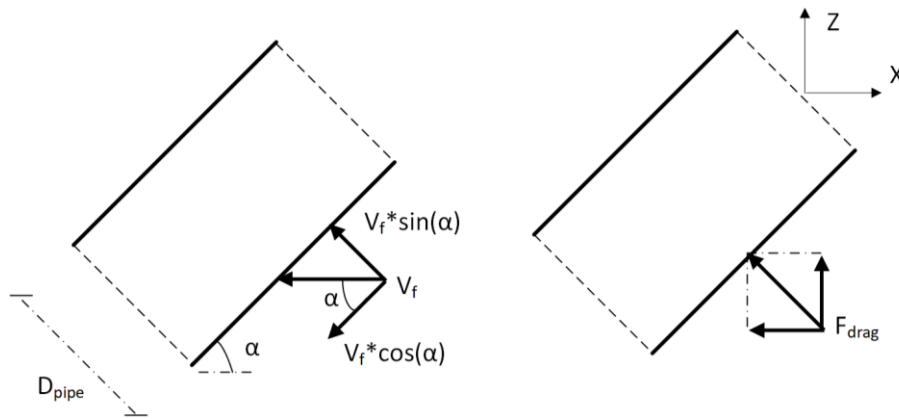


Figure 12: Form drag force diagram on the suction pipe

When the Reynolds number is plotted against the flow velocity, the transition value of $3 \cdot 10^5$ is already reached at very low speeds (Figure 13). The critical flow regime starts for a Reynolds number of $3 \cdot 10^5$ as was shown in Figure 11. This means the suction pipe will always be in the turbulent regime during common trailing velocities. This also applies for the draghead, indicated by the orange line in Figure 13.

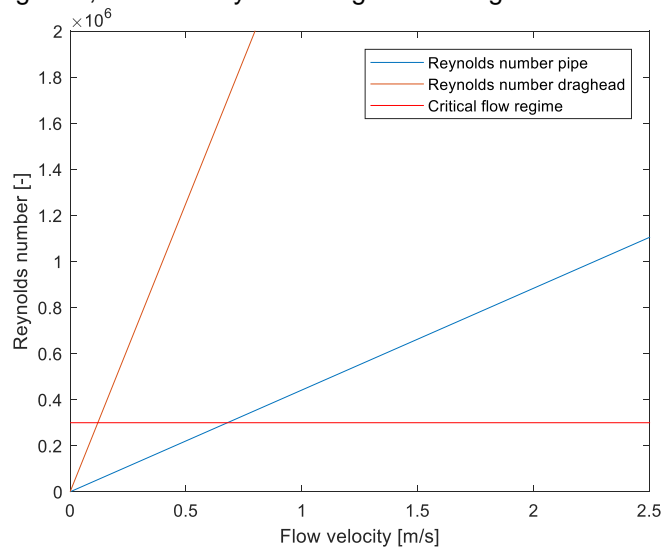


Figure 13: Critical flow regime calculation

In the graph of Figure 14, the drag coefficient is plotted against the Reynolds number (White, 2011). This graph indicates that for a Reynolds number larger than $3 \cdot 10^5$ a sudden drop of the drag coefficient can be observed. This theory is only valid for cylindrical and spherical shapes but not for a rectangular shape like the draghead. For shapes different than cylindrical and spherical shapes, the drag coefficient stays almost constant for Reynolds number above $1 \cdot 10^3$.

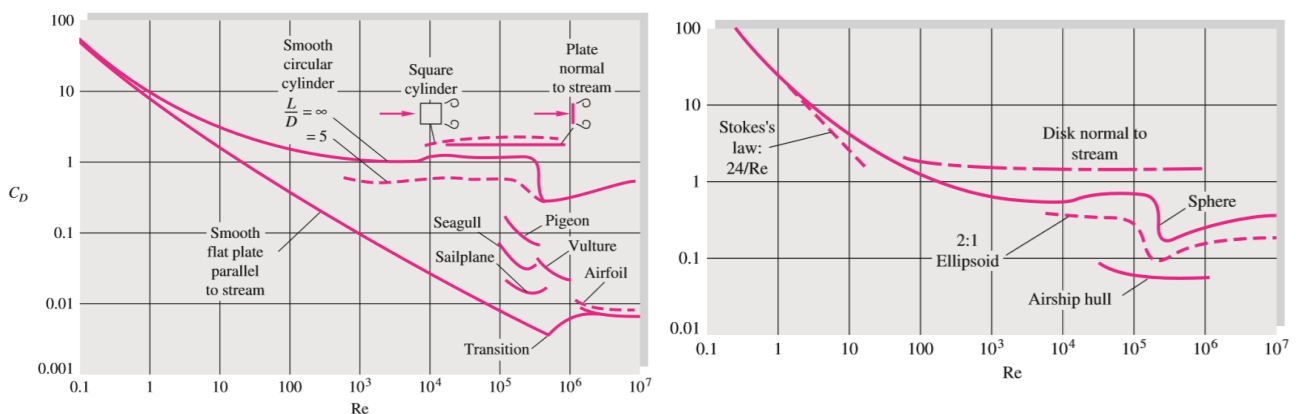


Figure 14: Drag coefficient plotted against the Reynolds number for different shapes; left side 2D bodies, right side 3D

For a cylindrical pipe in literature a C_d value of 1.2 is given for a Reynolds number of $1 \cdot 10^5$ and 0.4 for a Reynolds number of $1 \cdot 10^6$ (VOUW, 2010). The suction pipe will work in the area between these two Reynolds number and therefore in the range of the drop seen in Figure 14. Despite the drag coefficient will decrease for increasing velocities, the drag force will still increase because it is quadratic dependent on the velocity, eq. 7.

Nevertheless the suction pipe does not have a perfect cylindrical shape because of all the pipe, bends, hinges and other items attached to it. Therefore the drag coefficient could be slightly higher. Another hypothesis is that the drag coefficient is lower because of the jet pipe that is positioned in the wake of the suction tube. The shape of the suction tube changes towards a more streamlined ellipse shown in Figure 15, (White, 2011).

In Liu Zhi's report is stated that from practical experiments performed by Royal IHC a drag coefficient of 0.9-1.0 is found (Zhi, 2002). Here the drag coefficient is measured for a flow perpendicular to the cylinder (flow velocities and pipe diameter are unknown). For the calculations in the report a drag coefficient of 0.9 will be used for the suction pipe and 1.2 for the draghead (flat plate). The on trailing velocity depending drag coefficient is not accurate to define with a formula because the theory is not unequivocal enough. Further research should be performed to find this relation.

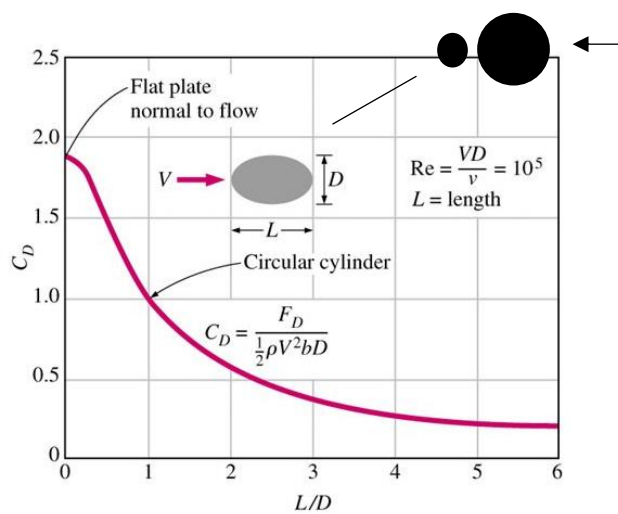


Figure 15: Change of the drag coefficient due to length/diameter aspect ratio

2.2 Model description

2.2.1 Geometry suction pipe

The geometry of **the simplified** suction pipe is shown in Figure 16. The system boundaries are chosen around the entire suction pipe and draghead where they cut the cables and sliding piece so the suction pipe system gets isolated from the vessel. The sliding piece fixes the pipe in horizontal direction, in point A, to the hull of the vessel and in vertical direction by the weight of the pipe. The suction pipe system is divided into three stiff segments to realize a realistic representation and can be distinguished as the upper pipe, the lower pipe and the visor. The upper pipe is supported by a cable that runs over the intermediate gantry. The lower pipe is supported by the draghead gantry where also the swell compensator is installed. The visor is not analysed in this chapter but will be described in chapter 5.

These segments are normally able to rotate from each other, in the x-z plane indicated, using the hinges located in point A, B and C. In this report, the turning glands, hinges in the axis of the pipe that allow rotational movement of the suction pipe around its axis, in A and B are fixed. The hinges, that normally allow the suction pipe to move out of the x-z plane are also restricted (the single hinge). The simplification adds some extra restrictions to the movement of the suction pipe which results in a 2D projection below. The names and angles are listed in the legend (Table 1).

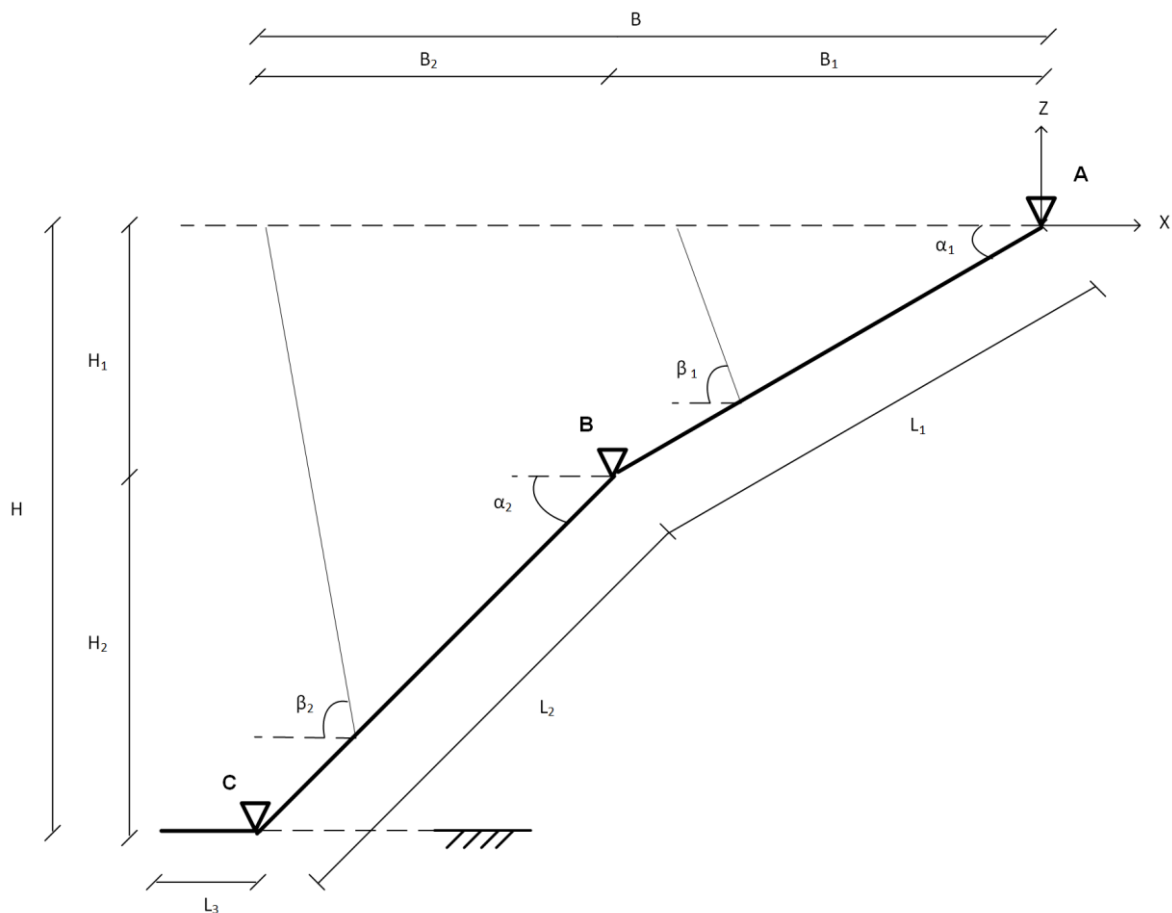


Figure 16: Geometry, simplified suction pipe system

Table 1: Legend Figure 16

Name	Symbol	Value
Upper suction pipe length	L1	15.560 m
Lower suction pipe + draghead length	L2	14.904 m
Lower suction pipe length	L2a	12.895 m
Draghead length	L2b	2.009 m
Visor length	L3	1.200 m
Pipe outer diameter	D_{pipe}	0.650 m
Upper suction pipe angle	α_1	30°
Lower suction pipe angle	α_2	45°
Intermediate gantry cable angle	β_1	70°
Draghead gantry cable angle	β_2	80°
Dredging depth	H	18.32 m

The draghead is attached to the lower suction pipe without any hinges but with a fixed rigid connection, this means the submerged weight of the suction pipe and drag forces on the suction pipe have a significant contribution to the behaviour of the draghead.

The suction pipe is a dynamic system, when the forces change due to increasing trailing velocities, the resulting force distribution needs to be reevaluated. Fixed point A (0,0) is located in the origin of the coordinate system which is the heart of the suction opening in the sliding piece. The coordinate system is chosen to be positive to the right, sailing direction, and positive in upward direction. In this research only the static situation when the draghead is still resting on the bed is of interest because of the reason when the draghead is lifted from the bed production stops.

The maximum dredging depth is restricted by the length of the suction pipe. In practice the upper and lower suction pipe have a slightly different pipe angle because it is preferred to dredge with a upper corner. This prevents the upper suction pipe to move under the sliding piece. When the vessel is lifted by the motion of the waves and the upper suction pipe is positioned under the sliding piece, the entire weight of the vessel will be supported by the suction pipe and the construction can get seriously damaged. The maximum dredging depth that is normally handled in practice, is reached when both suction pipes are under an angle of 45°. In this case the maximum dredging depth is 25.92 m ($H_{\text{max}} = (L_1 + L_2) * \sin(45)$).

Another option is to keep the upper suction pipe under a fixed angle of for example 30°. When is dredged at other depths, the lower suction pipe angle changes. Until the point the upper corner is gone, then the upper suction pipe needs to be pulled upwards. The lowest achievable dredging depth is when the upper suction pipe is horizontal and the lower suction pipe is under an angle of not more than 30°. In this report the pipe angles are fixed and the upper suction pipe angle is chosen to be 30° and the lower suction pipe angle 45°. In this case the dredging depth becomes 18.32 m.

Assumptions:

Not yet indicated assumptions for the simplification of the suction pipe are stated here. Also assumptions which were already mentioned are repeated:

- skin friction over the suction pipe and draghead is neglected. Also form drag that arises from the parallel velocity component along the pipe and draghead is neglected.
- The seabed boundary effects will be neglected in this research. The main reason is that the flow speed will not be influenced by the seabed. Only the current flow will be slightly smaller closer to the bed. The situation is simplified and there is assumed that the velocity is constant over the total water column (Journee, 2001).
- Because the suction pipe is not always fully immersed in the fluid, the pipe moves through the free water surface. This means drag forces arise due to wave forming. This is not included in this research because it will have a small effect on the positioning of the suction pipe because the force engage closely to the sliding piece and therefore create a relatively small moment.

- The draghead and suction pipe are analysed in two dimensions in the vertical plane, in the length of the vessel, by fixing the hinges that make it possible for the suction pipe to rotate around its axis and to other planes than the x-z plane.
- Dynamic movements of the vessel will not be taken into account because it is assumed that the swell compensator takes away the motions of the ship and the waves.
- The stiffness of the cable is assumed infinite. This means the cable length will not adjust when tension in the cable increases or decreases.
- The suction pipe angles and gantry cable angles are fixed.
- The drag coefficient is assumed constant although it will slightly change depending on the flow velocity along the pipe. Besides that is the shape of the suction pipe assumed cylindrical.

2.2.2 Moment and force balances

Using a step-by-step plan, the resultant forces can be calculated by use of the force- and moment equations to finally find the balance of the suction pipe system and trailing forces depending on the trailing velocity. First, to determine the compensation force by the swell compensator, the static force in the cables have to be determined at standstill. For this calculation only the gravitational forces are included, the trailing velocity is still zero and therefore the drag forces too. At this moment the suction pipe hangs completely in the cables at a fixed angle and is not yet supported by the bed. From the equilibrium also the static forces in point A are determined, which are necessary for the final trailing force calculation. This will be discussed later

Secondly, can be controlled by the compensation factor of the swell compensator, what the constant tension force in the cable of the lower suction pipe is. And which part should be supported by the bed in point C in order to keep the pipe in balance and under an angle of 45 degrees. First, in a static situation, then at increasing trailing velocity whereby the drag forces will increase. From this result will appear whether the lower pipe or upper pipe will move earlier. Important to mention is that the swell compensator can thus control how much of the vertical force is compensated. In this way the pressure of the draghead on the soil can be regulated. For every type of soil the bearing capacity is different so the compensation factor must be adjusted accordingly.

Finally, with the vertical soil reaction force on the draghead the force balance of the draghead can be determined. The draghead analysis is performed in chapter 3, 4 and 5, but the effect of the resulting soil excavation forces are substituted into this chapter to see effect to the equilibrium of the suction pipes. Last but not least can the resulting soil excavation forces and drag forces be used to calculate the total trailing forces in point A.

2.2.2.1 Static situation at standstill without soil forces

The external forces that work on the free hanging suction pipe system at standstill are the gravity force, the cables forces and the forces in point A. The suction pipe is divided in different parts with its own centre of gravity. The COG of the segments bigger than 30 kg are determined by use of an 3D-model in Inventor. This should give a realistic representation of the weight distribution. The different force contribution and where they apply on the pipe are indicated in Figure 17. The corresponding names are indicated in 2.3.1.1.

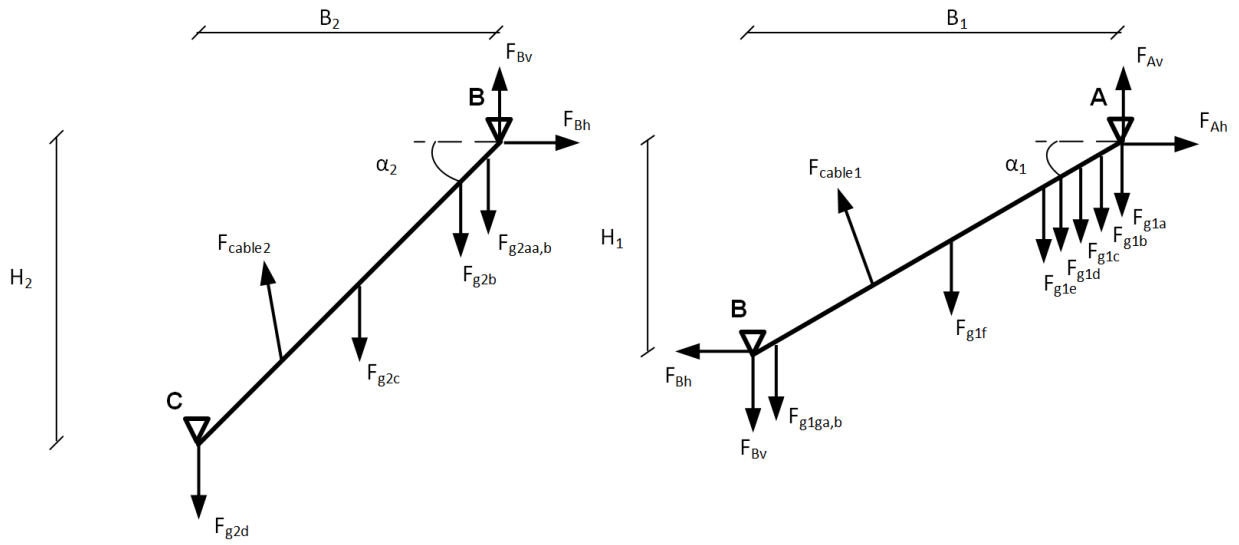


Figure 17: Force overview of the lower- and upper suction pipe for a free hanging situation at standstill

Now the resultant force of the lower- and upper suction pipe can be calculated, but first is referred to the 8.2.1 for a more detailed overview of the suction pipe system where the names for the moment arms are indicated. The horizontal- and vertical arm projection names are shortened for simplicity in the equations following in the rest of this chapter.

Lower suction pipe

The moment balance around point B is used to determine the unknown cable force of the lower pipe. The drag force is zero at this moment and indicated in the equation with $F_{drag,zero}$. The counter-clockwise rotation around point B is the positive moment direction!

$$\sum M_{B,lowerpipe} = B_{2a} * (F_{g2ab} + F_{g2aa}) + B_{2b} * F_{g2b} + B_{2c} * F_{g2c} + B_{2d} * F_{g2d} - L_{d2} * F_{drag,zero} - B_{c3} * \mathbf{F}_{cable,2} * \sin(\beta_2) - H_{c3} * \mathbf{F}_{cable,2} * \cos(\beta_2) = 0 \quad (\text{eq. 14})$$

$$\sum F_{v,lowerpipe} = \mathbf{F}_{Bv} + F_{drag,zero} * \cos(\alpha_2) + \mathbf{F}_{cable,2} * \sin(\beta_2) - F_{g2ab} - F_{g2aa} - F_{g2b} - F_{g2c} - F_{g2d} = 0 \quad (\text{eq. 15})$$

$$\sum F_{h,lowerpipe} = \mathbf{F}_{Bh} - F_{drag,zero} * \sin(\alpha_2) - \mathbf{F}_{cable,2} * \cos(\beta_2) = 0 \quad (\text{eq. 16})$$

There are three equations and three unknown variables ($\mathbf{F}_{cable,2}$, \mathbf{F}_{Bv} , \mathbf{F}_{Bh}) so the forces can be calculated.

$$\mathbf{F}_{cable,2} = \frac{B_{2a} * (F_{g2ab} + F_{g2aa}) + B_{2b} * F_{g2b} + B_{2c} * F_{g2c} + B_{2d} * F_{g2d} - L_{d2} * F_{drag,zero}}{B_{c3} * \sin(\beta_2) + H_{c3} * \cos(\beta_2)} \quad (\text{eq. 17})$$

$$\mathbf{F}_{Bv} = -F_{drag,zero} * \cos(\alpha_2) - \mathbf{F}_{cable,2} * \sin(\beta_2) + F_{g2ab} + F_{g2aa} + F_{g2b} + F_{g2c} + F_{g2d} \quad (\text{eq. 18})$$

$$\mathbf{F}_{Bh} = F_{drag,zero} * \sin(\alpha_2) + \mathbf{F}_{cable,2} * \cos(\beta_2) \quad (\text{eq. 19})$$

2.2.2.2 Static situation with compensated vertical soil force at standstill

The cable force can be adjusted by changing the pressure in the swell compensator by using a different compensation factor. In this way the force with which the head rests on the bed can be adjusted. In equation 20, c is the compensation factor for the initial cable force of the lower pipe. Because of the swell compensation, the force in the cable remains constant. On a sandy bed, the swell compensator is usually set to a compensation factor of 50% of the maximum compensation capacity available. On different soils, as for example silt with a lower bearing capacity, a compensation factor of 80%.

Now the vertical soil reaction force onto the draghead (F_{C_v}) can be calculated.

$$F_{\text{cable},2,v,c} = F_{\text{cable},2} * \sin(\beta_2) * c \quad (\text{eq. 20})$$

$$F_{\text{cable},2,h,c} = F_{\text{cable},2} * \cos(\beta_2) * c \quad (\text{eq. 21})$$

$$F_{\text{cable},2,c} = \sqrt{F_{\text{cable},2,v,c}^2 + F_{\text{cable},2,h,c}^2} \quad (\text{eq. 22})$$

$$\sum M_{B,\text{lowerpipe},c} = B_{2a} * (F_{g2ab} + F_{g2aa}) + B_{2b} * F_{g2b} + B_{2c} * F_{g2c} + B_{2d} * F_{g2d} - L_{d2} * F_{\text{drag},zero} - B_{c3} * F_{\text{cable},2,v,c} - H_{c3} * F_{\text{cable},2,h,c} - B_2 * F_{C_v} = 0 \quad (\text{eq. 23})$$

$$F_{C_v} = \frac{B_{2a} * (F_{g2ab} + F_{g2aa}) + B_{2b} * F_{g2b} + B_{2c} * F_{g2c} + B_{2d} * F_{g2d} - L_{d2} * F_{\text{drag},zero} - B_{c3} * F_{\text{cable},2,v,c} - H_{c3} * F_{\text{cable},2,h,c}}{B_2} \quad (\text{eq. 24})$$

$$F_{C_v} = F_{C_v,\text{draghead}} \quad (\text{eq. 25})$$

The reaction forces in the lower suction pipe have to be recalculated because of the new force distribution. The subscript c means that the force is resulting from the new compensated force distribution. The red highlighted forces in Figure 18 will change because of the new force distribution.

Lower suction pipe

$$\sum F_{v,\text{lowerpipe},c} = F_{C_v} + \mathbf{F}_{Bv,c} + F_{\text{drag},zero} * \cos(\alpha_2) + \mathbf{F}_{\text{cable},2,v,c} - F_{g2ab} - F_{g2aa} - F_{g2b} - F_{g2c} - F_{g2d} = 0 \quad (\text{eq. 26})$$

$$\sum F_{h,\text{lowerpipe},c} = \mathbf{F}_{Bh,c} - F_{\text{drag},zero} * \sin(\alpha_2) - \mathbf{F}_{\text{cable},2,h,c} = 0 \quad (\text{eq. 27})$$

There are two equations and two unknown variables ($\mathbf{F}_{Bv,c}$, $\mathbf{F}_{Bh,c}$) so the forces can be calculated.

$$\mathbf{F}_{Bv,c} = -F_{C_v} - F_{\text{drag},zero} * \cos(\alpha_2) - \mathbf{F}_{\text{cable},2,v,c} + F_{g2ab} + F_{g2aa} + F_{g2b} + F_{g2c} + F_{g2d} \quad (\text{eq. 28})$$

$$\mathbf{F}_{Bh,c} = F_{\text{drag},zero} * \sin(\alpha_2) + \mathbf{F}_{\text{cable},2,h,c} \quad (\text{eq. 29})$$

Upper suction pipe

$$\sum M_{A,\text{upperpipe},c} = B_{1a} * F_{g1a} + B_{1b} * F_{g1b} + B_{1c} * F_{g1c} + B_{1d} * F_{g1d} + B_{1e} * F_{g1e} + B_{1f} * F_{g1f} + B_{1g} * (F_{g1ga} + F_{g1gb}) + B_2 * \mathbf{F}_{Bv,c} - H_2 * \mathbf{F}_{Bh,c} - L_{D1} * F_{\text{drag},zero} - B_{c2} * \mathbf{F}_{\text{cable},1,c} * \sin(\beta_1) - H_{c2} * \mathbf{F}_{\text{cable},1,c} * \cos(\beta_1) = 0 \quad (\text{eq. 30})$$

$$\sum F_{v,\text{upperpipe},c} = -\mathbf{F}_{Bv,c} + F_{\text{drag},zero} * \cos(\alpha_1) + \mathbf{F}_{\text{cable},1,c} * \sin(\beta_1) + \mathbf{F}_{Av,c} - F_{g1a} - F_{g1b} - F_{g1c} - F_{g1d} - F_{g1e} - F_{g1f} - F_{g1ga} - F_{g1gb} = 0 \quad (\text{eq. 31})$$

$$\sum F_{h,\text{upperpipe},c} = -\mathbf{F}_{Bh,c} - F_{\text{drag},zero} * \sin(\alpha_1) - \mathbf{F}_{\text{cable},1,c} * \cos(\beta_1) + \mathbf{F}_{Ah,c} = 0 \quad (\text{eq. 32})$$

There are three equations and three unknown variables ($\mathbf{F}_{cable,1,c}$, $\mathbf{F}_{Av,c}$, $\mathbf{F}_{Ah,c}$) so the forces can be calculated.

$$\sum M_{Fg} = B_{1a} * F_{g1a} + B_{1b} * F_{g1b} + B_{1c} * F_{g1c} + B_{1d} * F_{g1d} + B_{1e} * F_{g1e} + B_{1f} * F_{g1f} + B_{1g} * (F_{g1ga} + F_{g1gb}) \quad (\text{eq. 33})$$

$$\mathbf{F}_{cable,1,c} = \frac{\sum M_{Fg} + B_2 * F_{Bv,c} - H_2 * F_{Bh,c} - L_{D1} * F_{drag,zero}}{B_{c2} * \sin(\beta_1) + H_{c2} * \cos(\beta_1)} \quad (\text{eq. 34})$$

$$\mathbf{F}_{Av,c} = F_{Bv,c} - F_{drag,zero} * \cos(\alpha_1) - \mathbf{F}_{cable,1,c} * \sin(\beta_1) + F_{g1a} + F_{g1b} + F_{g1c} + F_{g1d} + F_{g1e} + F_{g1f} + F_{g1ga} + F_{g1gb} \quad (\text{eq. 35})$$

$$\mathbf{F}_{Ah,c} = F_{drag,zero} * \sin(\alpha_1) + \mathbf{F}_{cable,1,c} * \cos(\beta_1) + F_{Bh,c} \quad (\text{eq. 36})$$

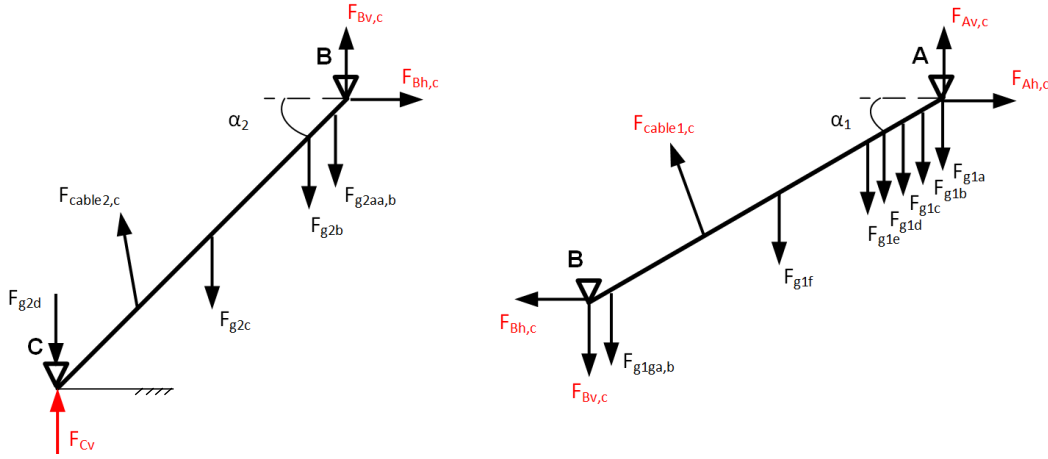


Figure 18: Force overview of the lower- and upper suction pipe with a compensated vertical soil force at standstill

2.2.2.3 Static situation with compensated vertical soil reaction force and increasing trailing velocity

The force distribution changes again when the trailing velocity increases. The dragforce which applies perpendicular, in the middle of the pipes will cause the pipe to move upwards. In the momentum balance around point A and B, the drag force parallel to the pipes and draghead drops out. In the force balance too because this part mainly consists of friction of the drag forces which is negligible small. At a certain trailing velocity the lower pipe and the upper pipe starts to float and the angle of the suction pipe changes. At this moment the suction pipe cannot be approached anymore as a static situation.

The subscript $_{vt}$ means that the force is depending on the trailing velocity resulting from the increasing drag forces.

Lower suction pipe

$$\sum M_{B,lowerpipe,c,vt} = B_{2a} * (F_{g2ab} + F_{g2aa}) + B_{2b} * F_{g2b} + B_{2c} * F_{g2c} + B_{2d} * F_{g2d} - L_{d2} * F_{drag,2} - B_{c3} * F_{cable,2,v,c} - H_{c3} * F_{cable,2,h,c} - B_2 * F_{Cv,vt} = 0 \quad (\text{eq. 37})$$

$$\sum F_{v,lowerpipe,c,vt} = F_{Cv,vt} + F_{Bv,c,vt} + F_{drag,2} * \cos(\alpha_2) + F_{cable,2,v,c} - F_{g2ab} - F_{g2aa} - F_{g2b} - F_{g2c} - F_{g2d} = 0 \quad (\text{eq. 38})$$

$$\sum F_{h,lowerpipe,c,vt} = F_{Bh,c,vt} - F_{drag,2} * \sin(\alpha_2) - F_{cable,2,h,c} = 0 \quad (\text{eq. 39})$$

There are three equations and three unknown variables ($\mathbf{F}_{Cv,vt}$, $\mathbf{F}_{Bv,c,vt}$, $\mathbf{F}_{Bh,c,vt}$) so the forces can be calculated.

$$F_{Cv,vt} = \frac{B_{2a} * (F_{g2ab} + F_{g2aa}) + B_{2b} * F_{g2b} + B_{2c} * F_{g2c} + B_{2d} * F_{g2d} - L_{d2} * F_{drag,2} - B_{c3} * F_{cable,2,v,c} - H_{c3} * F_{cable,2,h,c}}{B_2} \quad (\text{eq. 40})$$

$$F_{Cv,vt} = F_{Cv,draghead,vt} \quad (\text{eq. 41})$$

$$F_{Bv,c,vt} = -F_{Cv,vt} - F_{drag,2} * \cos(\alpha_2) - F_{cable,2,v,c} + F_{g2ab} + F_{g2aa} + F_{g2b} + F_{g2c} + F_{g2d} \quad (\text{eq. 42})$$

$$F_{Bh,c,vt} = F_{drag,2} * \sin(\alpha_2) + F_{cable,2,h,c} \quad (\text{eq. 43})$$

Upper suction pipe

$$\sum M_{A,upperpipe,c,vt} = B_{1a} * F_{g1a} + B_{1b} * F_{g1b} + B_{1c} * F_{g1c} + B_{1d} * F_{g1d} + B_{1e} * F_{g1e} + B_{1f} * F_{g1f} + B_{1g} * (F_{g1ga} + F_{g1gb}) + B_2 * F_{Bv,c,vt} - H_2 * F_{Bh,c,vt} - L_{D1} * F_{drag,1} - B_{c2} * F_{cable,1,c,vt} * \sin(\beta_1) - H_{c2} * F_{cable,1,c,vt} * \cos(\beta_1) = 0 \quad (\text{eq. 44})$$

$$\sum F_{v,upperpipe,c,vt} = -F_{Bv,c,vt} + F_{drag,1} * \cos(\alpha_1) + F_{cable,1,c,vt} * \sin(\beta_1) + F_{Av,c,vt} - F_{g1a} - F_{g1b} - F_{g1c} - F_{g1d} - F_{g1e} - F_{g1f} - F_{g1ga} - F_{g1gb} = 0 \quad (\text{eq. 45})$$

$$\sum F_{h,upperpipe,c,vt} = -F_{Bh,c,vt} - F_{drag,1} * \sin(\alpha_1) - F_{cable,1,c,vt} * \cos(\beta_1) + F_{Ah,c,vt} = 0 \quad (\text{eq. 46})$$

There are three equations and three unknown variables ($F_{cable,1,c,vt}$, $F_{Av,c,vt}$, $F_{Ah,c,vt}$) so the forces can be calculated.

$$\sum M_{Fg} = B_{1a} * F_{g1a} + B_{1b} * F_{g1b} + B_{1c} * F_{g1c} + B_{1d} * F_{g1d} + B_{1e} * F_{g1e} + B_{1f} * F_{g1f} + B_{1g} * (F_{g1ga} + F_{g1gb}) \quad (\text{eq. 47})$$

$$F_{cable,1,c,vt} = \frac{\sum M_{Fg} + B_2 * F_{Bv,c,vt} - H_2 * F_{Bh,c,vt} - L_{D1} * F_{drag,1}}{B_{c2} * \sin(\beta_1) + H_{c2} * \cos(\beta_1)} \quad (\text{eq. 48})$$

$$F_{Av,c,vt} = F_{Bv,c,vt} - F_{drag,1} * \cos(\alpha_1) - F_{cable,1,c,vt} * \sin(\beta_1) + F_{g1a} + F_{g1b} + F_{g1c} + F_{g1d} + F_{g1e} + F_{g1f} + F_{g1ga} + F_{g1gb} \quad (\text{eq. 49})$$

$$F_{Ah,c,vt} = F_{drag,1} * \sin(\alpha_1) + F_{cable,1,c,vt} * \cos(\beta_1) + F_{Bh,c,vt} \quad (\text{eq. 50})$$

Floating pipes

At the moment the ground force $F_{Cv,vt}$, becomes zero, the draghead will lift off from the bed. $F_{Cv,vt} \leq 0$ is the floating point of the lower suction pipe. The cable force of the lower pipe is held constant by the swell compensator. However, the cable force of the upper pipe changes and slowly decrease when the drag force on the upper pipe increases.

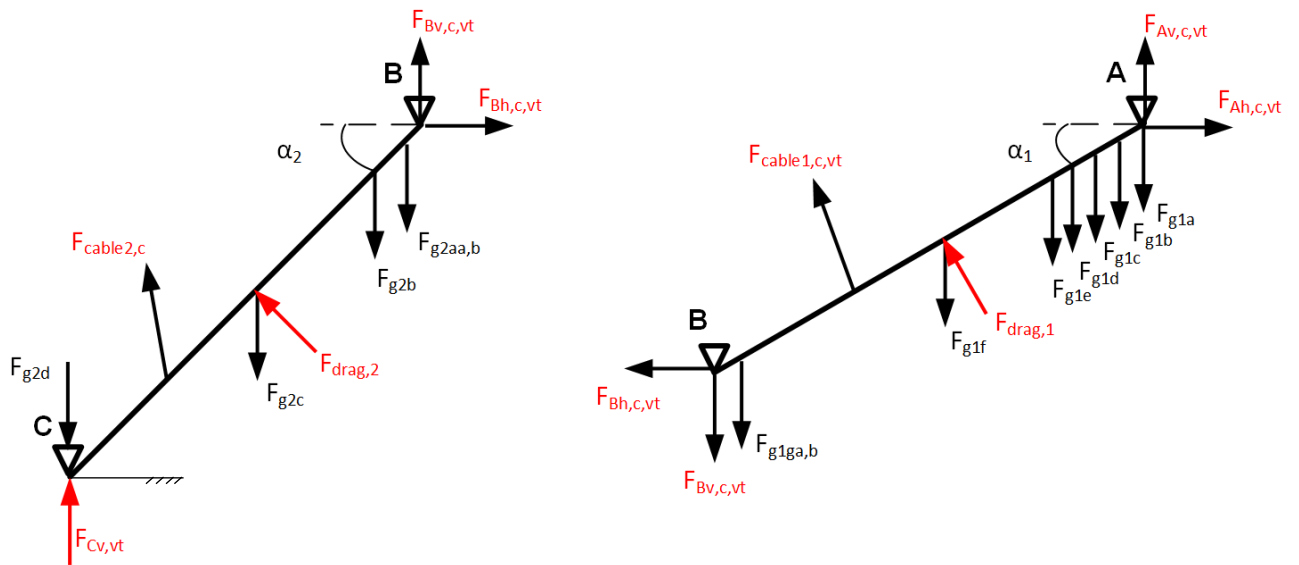


Figure 19: Force overview of the suction pipes with a compensated vertical soil force and increasing trailing velocity

2.2.2.4 Static situation with compensated soil excavation forces and increasing trailing velocity

As previously mentioned will the soil reaction forces on the draghead be treated later on in chapter 3, 4 and 5, but the resultant soil excavation forces are used already in this chapter for the calculation of the total trailing forces and the floating points. Again will the excavation forces on the draghead result in a new distribution of the forces over the suction pipe system. The new soil reaction forces $F_{Cv,soil,vt}$ and $F_{Ch,soil,vt}$ follow from the draghead equilibrium in chapter 3. It consists of the force on the visor, the soil forces of the visor house and the resulting vertical soil force $F_{Cv,vt}$ from the suction pipe system.

Lower suction pipe

$$\sum F_{v,lowerpipe,soil,c,vt} = \mathbf{F}_{Bv,soil,c,vt} - F_{Bv,c,vt} - \mathbf{F}_{Cv,soil,vt} = 0 \quad (\text{eq. 51})$$

$$\sum F_{h,lowerpipe,soil,c,vt} = \mathbf{F}_{Bh,soil,c,vt} - F_{Bh,c,vt} - \mathbf{F}_{Ch,soil,vt} = 0 \quad (\text{eq. 52})$$

$$\mathbf{F}_{Bv,soil,c,vt} = \mathbf{F}_{Cv,soil,vt} + F_{Bv,c,vt} \quad (\text{eq. 53})$$

$$\mathbf{F}_{Bh,soil,c,vt} = \mathbf{F}_{Ch,soil,vt} + F_{Bh,c,vt} \quad (\text{eq. 54})$$

The cable force of the lower pipe is constant and is equal to the force calculated with equation 22.

Upper suction pipe

$$\sum M_{A,upperpipe,soil,c,vt} = B_{1a} * F_{g1a} + B_{1b} * F_{g1b} + B_{1c} * F_{g1c} + B_{1d} * F_{g1d} + B_{1e} * F_{g1e} + B_{1f} * F_{g1f} + B_{1g} * (F_{g1ga} + F_{g1gb}) + B_2 * F_{Bv,soil,c,vt} - H_2 * F_{Bh,soil,c,vt} - L_{D1} * F_{drag,1} - B_{c2} * \mathbf{F}_{cable,1,soil,c,vt} * \sin(\beta_1) - H_{c2} * \mathbf{F}_{cable,1,soil,c,vt} * \cos(\beta_1) = 0 \quad (\text{eq. 55})$$

$$\sum F_{v,upperpipe,soil,c,vt} = -F_{Bv,soil,c,vt} + F_{drag,1} * \cos(\alpha_1) + \mathbf{F}_{cable,1,soil,c,vt} * \sin(\beta_1) + \mathbf{F}_{Av,soil,c,vt} - F_{g1a} - F_{g1b} - F_{g1c} - F_{g1d} - F_{g1e} - F_{g1f} - F_{g1ga} - F_{g1gb} = 0 \quad (\text{eq. 56})$$

$$\sum F_{h,upperpipe,soil,c,vt} = -F_{Bh,soil,c,vt} - F_{drag,1} * \sin(\alpha_1) - \mathbf{F}_{cable,1,soil,c,vt} * \cos(\beta_1) + \mathbf{F}_{Ah,soil,c,vt} = 0 \quad (\text{eq. 57})$$

There are three equations and three unknown variables ($\mathbf{F}_{cable,1,soil,c,vt}$, $\mathbf{F}_{Av,soil,c,vt}$, $\mathbf{F}_{Ah,soil,c,vt}$) so the forces can be calculated.

$$\sum M_{Fg} = B_{1a} * F_{g1a} + B_{1b} * F_{g1b} + B_{1c} * F_{g1c} + B_{1d} * F_{g1d} + B_{1e} * F_{g1e} + B_{1f} * F_{g1f} + B_{1g} * (F_{g1ga} + F_{g1gb}) \quad (\text{eq. 58})$$

$$\mathbf{F}_{cable,1,soil,c,vt} = \frac{\sum M_{Fg} + B_2 * F_{Bv,soil,c,vt} - H_2 * F_{Bh,soil,c,vt} - L_{D1} * F_{drag,1}}{B_{c2} * \sin(\beta_1) + H_{c2} * \cos(\beta_1)} \quad (\text{eq. 59})$$

$$\mathbf{F}_{Av,soil,c,vt} = F_{Bv,soil,c,vt} - F_{drag,1} * \cos(\alpha_1) - \mathbf{F}_{cable,1,soil,c,vt} * \sin(\beta_1) + F_{g1a} + F_{g1b} + F_{g1c} + F_{g1d} + F_{g1e} + F_{g1f} + F_{g1ga} + F_{g1gb} \quad (\text{eq. 60})$$

$$\mathbf{F}_{Ah,soil,c,vt} = F_{drag,1} * \sin(\alpha_1) + \mathbf{F}_{cable,1,soil,c,vt} * \cos(\beta_1) + F_{Bh,soil,c,vt} \quad (\text{eq. 61})$$

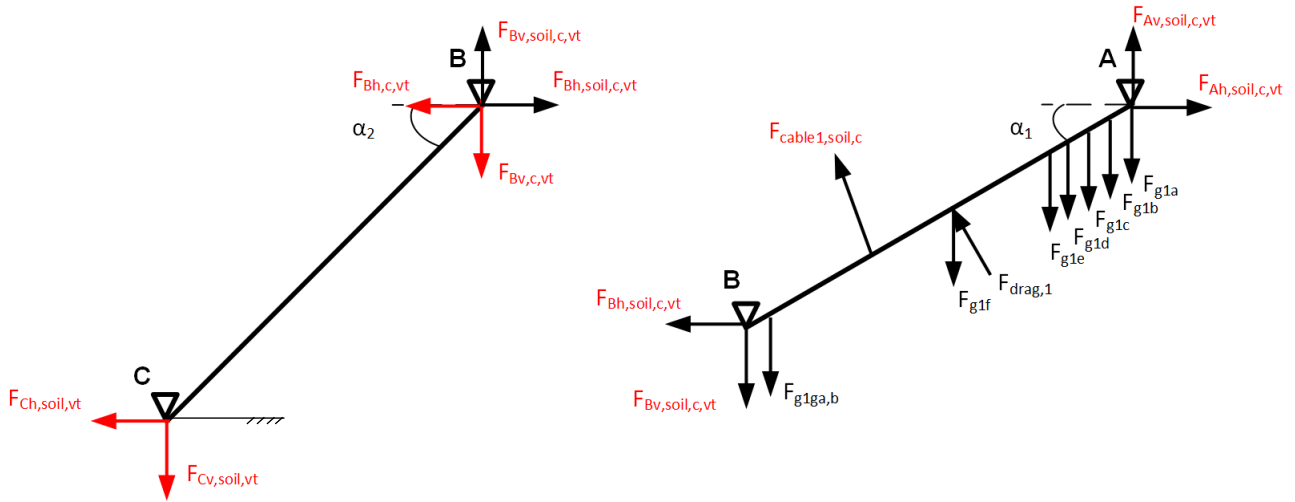


Figure 20: Force overview of the suction pipes with compensated soil excavation forces and increasing trailing velocity

The total trailing force becomes the horizontal component of the force in A minus the horizontal component of the cable forces of the free hanging suction pipe system. The vertical component will not be of influence on the propulsion that needs to be generated. The buoyancy of the vessel will compensate for the vertical resultant trailing force and can therefore be ignored.

$$F_{h,total,trailingforces} = F_{Ah,soil,c,vt} - F_{cable,1,c} * \cos(\beta_1) - F_{cable,2,h,c} = F_{Ah,soil,c,vt} - F_{Ah,c} \quad (\text{eq. 62})$$

In the free hanging system was shown that the cables pull the suction pipe system backwards what results in a resultant force in A. By subtracting this component from the new suction pipe balance in point A with the total drag forces and excavation forces the total trailing force per velocity step is known.

2.3 Model results & Discussion

In this paragraph the case study for the trailing suction pipe TSP600 will be used to determine the trailing forces and the behaviour of the suction pipe system. In the model description is the method to calculate the external forces described in detail already. In this paragraph only the results of the calculations will be shown. The dimensions of the TSP600 where the calculations are performed for are included in appendix 8.2.2.

2.3.1 Forces working on the suction pipe

2.3.1.1 Gravity force

As described in the model description has every segment of the suction pipe its own centre of gravity, mass, volume and internal volume. The resulting force components are listed in the Table 2.

Table 2: Suction pipe and draghead's submerged force components

Force	Naming	Mass [kg]	Volume [m ³]	Volume in [m ³]	Submerged force [kN]
Sliding piece	Fg1a	2233	0.289	-	19
Trunnion bend	Fg1b	881	0.112	0.40	8.79
Jet water hose 1	Fg1c	91	0.106	-	-0.173
Single hinge	Fg1d	2129	0.349	1.02	20.63
Jet water pipe	Fg1e	139	0.018	-	1.18
Suction pipe, upper	Fg1f	2557	0.325	2.52	29.85
Jet water hose 2, upper	Fg1gb	45	0.053	-	-0.09
Jet water hose 2, lower	Fg2ab	45	0.053	-	-0.09
Cardan hinge, upper	Fg1ga	1574	0.260	0.51	14.45
Cardan hinge, lower	Fg2aa	1574	0.260	0.51	14.45
Turning gland	Fg2b	906	0.118	0.18	8.3
Suction pipe, lower	Fg2c	2895	0.369	3.00	34.25
Draghead (minus visor)	Fg2d	3719 (1800)	0.5414 (0.2186)	2.50 (-)	42.26
Total		20,589	2.85	10.6	205.01

2.3.1.2 Drag force

The suction pipe is divided in two pieces. For the calculation of the drag forces is the draghead included in the lower pipe drag force, $F_{drag,1}$. The drag coefficient of the lower and upper pipe is chosen as 0.9 in the case study. The drag coefficient of the draghead, is simplified to the drag coefficient of a flat plate with a value of 1.2 (size draghead; width: 2.51 m, height: 2 m). Because the draghead's surface perpendicular to the flow is not exactly a rectangle a correction factor, c_{rec} , of 0.8 is included to compensate for the surface reduction of these two 'corners'. The drag force equations now become:

$$F_{drag,2} = \frac{1}{2} * \rho_w * (v_t * \sin(\alpha_2))^2 * (c_{d,pipe} * L_{2a} * D_{out} + c_{d,draghead} * L_{2b} * W_{support} * c_{rec}) \quad (\text{eq. 63})$$

$$F_{drag,2} = \frac{1}{2} * 1025 * (v_t * \sin(45))^2 * (0.9 * 12.90 * 0.625 + 1.2 * 2 * 2.51 * 0.8) [N] \quad (\text{eq. 64})$$

$$F_{drag,1} = \frac{1}{2} * \rho_w * (v_t * \sin(\alpha_1))^2 * c_{d,pipe} * L_1 * D_{out} \quad (\text{eq. 65})$$

$$F_{drag,1} = \frac{1}{2} * 1025 * (v_t * \sin(30))^2 * 0.9 * 15.56 * 0.625 [N] \quad (\text{eq. 66})$$

This results in the forces shown in Figure 21, where the drag forces of the lower pipe and draghead and the upper pipe are shown.

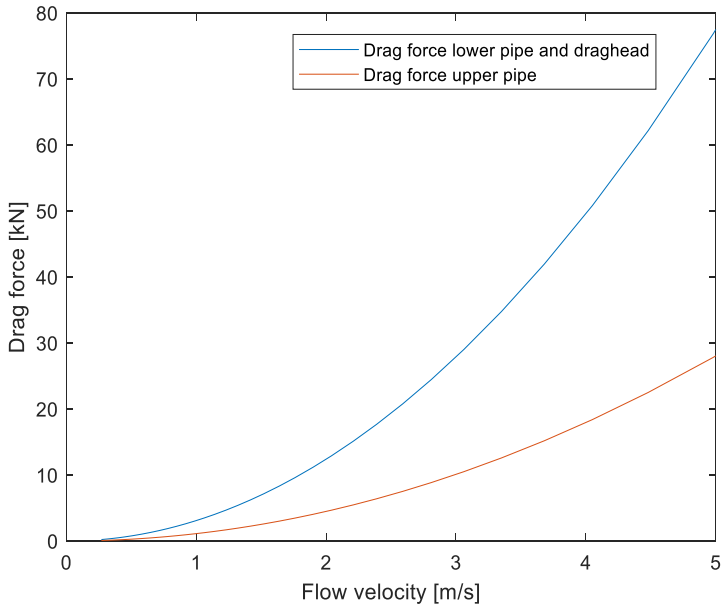


Figure 21: Drag forces, lower and upper pipe ($\alpha_2=45$ degrees, $\alpha_1=30$ degrees)

2.3.2 Results of the trailing force without soil excavation forces

Floating draghead

Below in the left figure the forces on the lower suction pipe are shown together with the compensated soil reaction forces and the compensated cable force (the situation as in 2.2.2.3). The soil excavation forces on the draghead are not yet included. The cable force of the lower pipe is kept at a constant tension by the swell compensator.

The vertical soil force decreases slowly because the drag forces will increase for increasing trailing velocities. Until a speed of 3.57 m/s is reached and the lower pipe will lift off from the bed. The normal force acting on the draghead, $F_{c,vt}$, has decreased to zero. The assumed situation where there is static equilibrium at 45 degrees is no longer valid because the pipe angle will change. Therefore it is also no longer interesting to know what happens at higher trailing velocities because the draghead will lose its main function: the excavation of the sand.

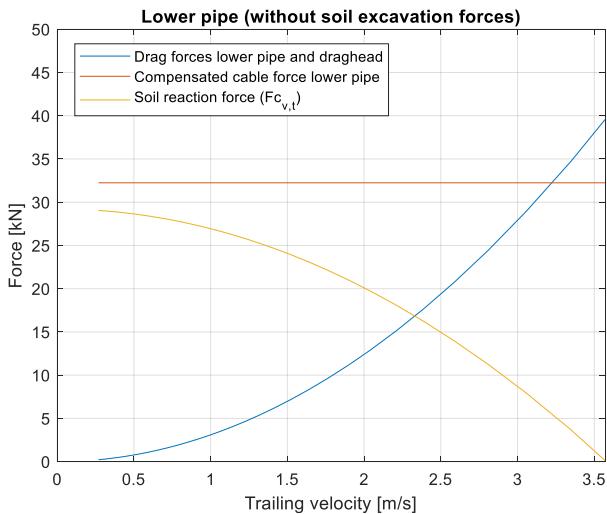


Figure 22: Forces lower pipe versus the trailing velocity

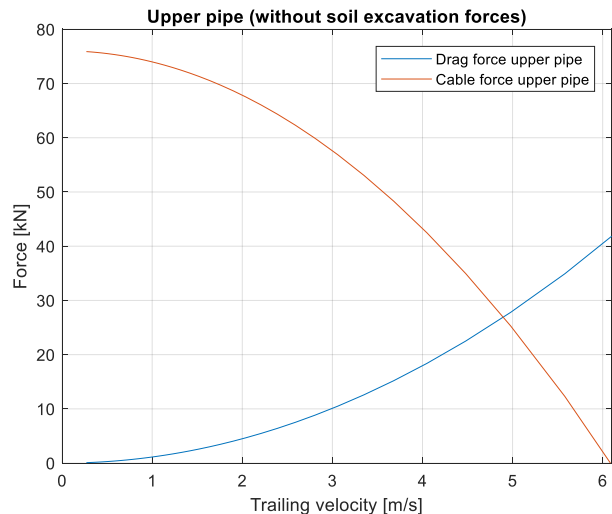


Figure 23: Forces upper pipe versus the trailing velocity

To exclude that the upper pipe will not change position already at a lower velocity, this is checked by plotting the equilibrium of the upper pipe in Figure 23. This graph shows the cable force of the upper pipe together with the drag forces. The upper pipe cable force is not kept under a constant tension but decreases slowly with increasing trailing velocities. It is assumed that the cable length will not change due to the decrease of the cable tension. When the force in the cable becomes zero, the angle of the upper pipe will change, and the equilibrium situation for a pipe angle of 30 degrees is not valid anymore. The results indicate that the upper pipe starts floating at a trailing velocity of around 6 m/s.

Important to mention is that the gap between $x=0-0.27$ m/s is not shown in the graph because the visor is not in equilibrium. This is described in chapter 5, where the equilibrium of the visor is explained in detail.

Trailing forces

The total trailing forces will be known when the excavation forces on the draghead are included into the calculation. Nonetheless, it is also necessary to see how the forces are redistributed without these soil excavation forces. Namely the reaction forces in the cardan hinge (point B) and the sliding piece (point A). Last mentioned are needed to calculate the total trailing force in 2.3.4.

What is striking is that the vertical force in B remains almost constant for increasing trailing velocities, see Figure 24. This can be explained by the fact that the vertical balance is maintained because the vertical soil reaction forces decreases. Again, when the vertical soil reaction force becomes zero at 3.6 m/s, the equilibrium situation no longer applies. The horizontal component of the drag force will lead to a high reaction force in B.

In Figure 25, the forces in point A are plotted which shows that the reaction forces increase with the trailing velocity.

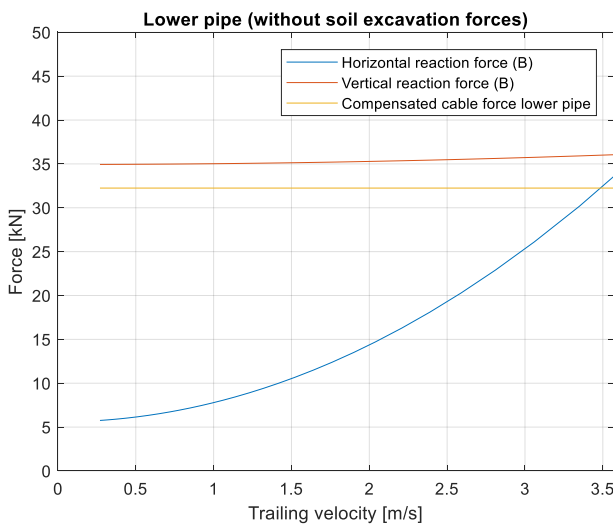


Figure 24: Reaction forces in B versus the trailing velocity

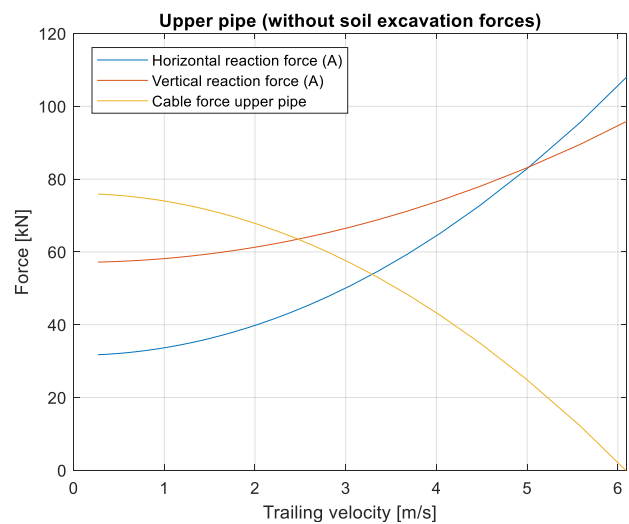


Figure 25: Reaction forces in A versus the trailing velocity

2.3.3 Results of the trailing force with soil excavation forces

When the soil excavation forces (from chapter 3) are taken into account the situation will change. The soil excavation forces on the draghead result in high horizontal and vertical forces in point C. In particular the horizontal excavation forces increase strongly while the vertical excavation forces decrease with increasing trailing velocity. The results are shown in the graphs of Figure 26 and Figure 27, again the left graph shows the force distribution of the lower pipe and in the right graph the upper pipe.

The normal force on the draghead, $F_{sled,head}$, is different compared with the vertical reaction force, $F_{Cv,vt}$ used in the previous subparagraph. This is explained in chapter 3. The principal is the same though, when the normal force decreases to zero the contact between the draghead and the bed will be gone a the lower pipe starts to float. This already happens at a lower trailing velocity than without the excavation forces, namely at 2.3 m/s. The soil excavation forces are the sum of all the resultant forces acting on the draghead. The horizontal and vertical component of the soil excavation force are equal to each other because the angle of the lower pipe is in this case 45 degrees. At different angles the forces will vary.

When the sled force decreases to zero the draghead will lift off from the bed. A hypothesis is that water is sucked in through the narrow gap that is created at the front, the vacuum force on the visor decreases. As the vacuum force gets less dominant the visor will fold up which causes that the excavation force will decrease. The draghead will drop again and the process will repeat itself. This could result in a pounding draghead and a strongly varying production density. This is very undesirable and a lower speed will have to be maintained.

The cable force of the upper pipe decreases again to zero around 6 m/s. The upper pipe will therefore not change its angle sooner than the lower pipe.

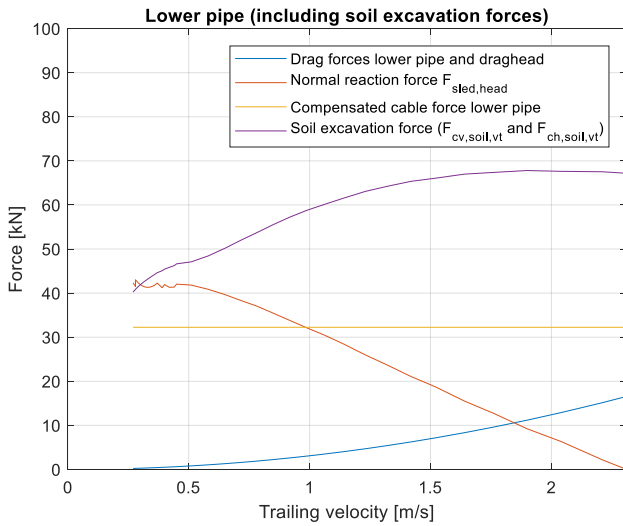


Figure 26: Forces lower pipe versus the trailing velocity

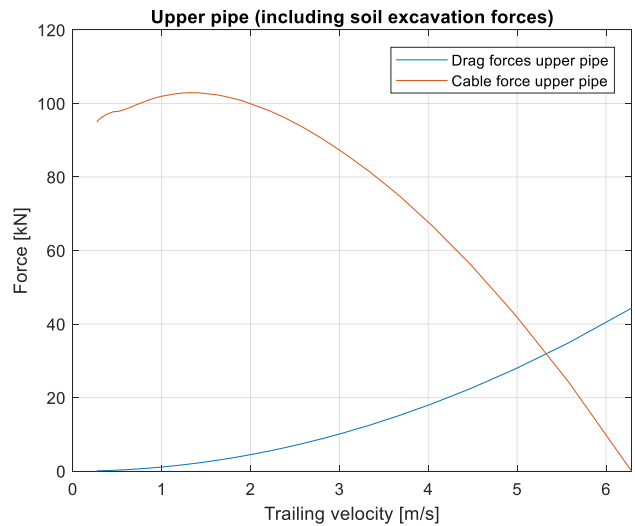


Figure 27: Forces upper pipe versus the trailing velocity

The reaction forces in point A and B are shown in Figure 28 and Figure 29.

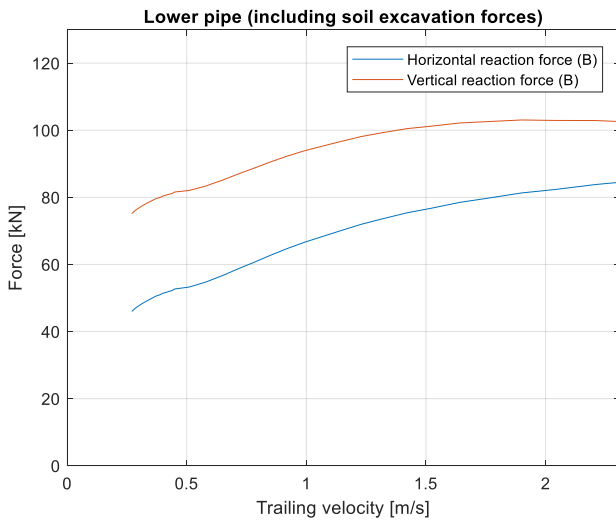


Figure 28: Reaction force in B versus the trailing velocity

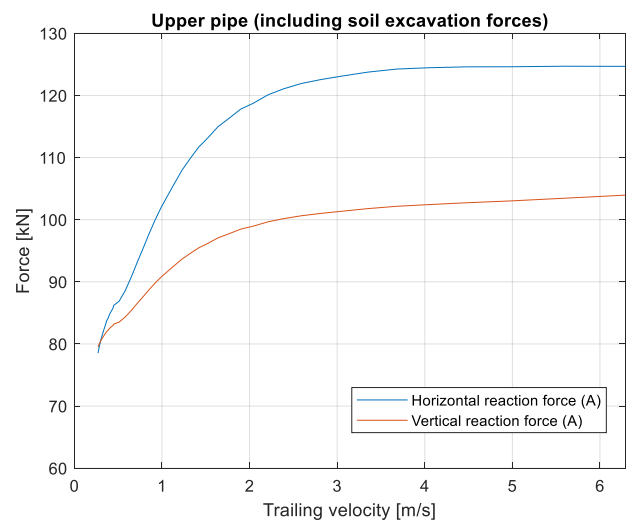


Figure 29: Reaction force in A versus the trailing velocity

2.3.4 Total trailing force

Now that all forces are included in the calculation the total trailing forces can be determined. The pipe is suspended from the ship at three locations. As has been shown previously, there are horizontal reaction forces in the cable in a stationary situation. In order to explicitly show the trailing forces, these resultant forces must be subtracted from the horizontal reaction force in A to determine the total trailing force (eq. 62). For comparison the drag forces are also shown in the graph below.

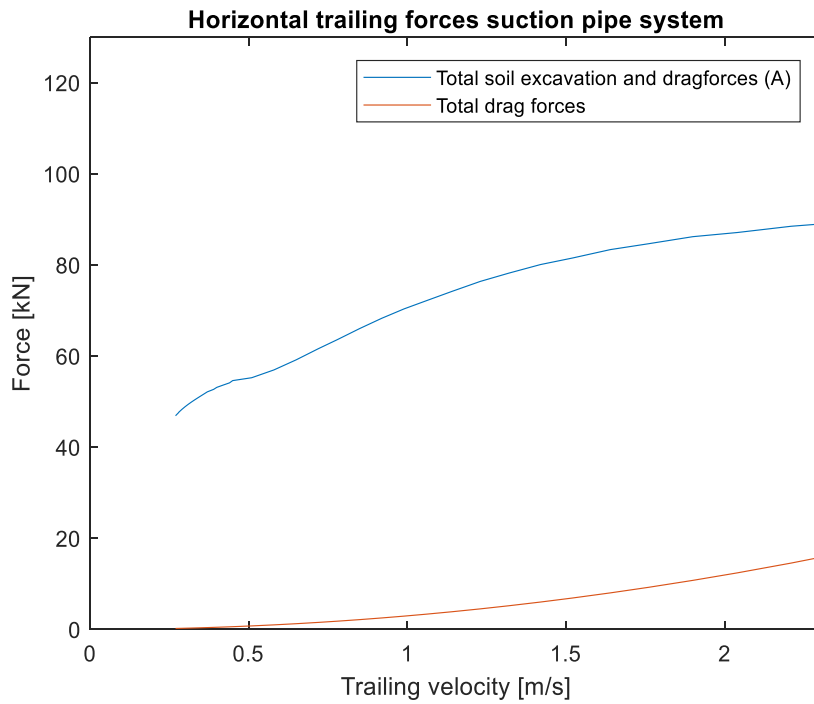


Figure 30: Total horizontal trailing force in point A versus the trailing velocity

2.4 Verification

In this section, variables used in the calculations are verified to see what their influence is on the behaviour of the suction pipe system. In the literature study it was described that there is no clear answer to what the value of the drag force coefficient is. In addition, no current velocity has been included in the case study, therefore this influence will be examined in subsection 2.4.2. Furthermore will be described what the effect of is the reduction of the lower pipe angle for dredging at lower depths. In the end will be verified whether the calculated total trailing forces of the previous paragraph match with trailing forces found in other studies.

2.4.1 Verification of the drag force coefficient

As described in the literature study, there is a lot of division over the value of the drag force coefficient of the suction pipe. The values assigned to the drag coefficient of the suction pipe range from 0.6-1.2 [-]. To see the effect of the coefficient, the total trailing forces are reviewed for the two extreme values. This is done because the drag force on the draghead is only a small percentage of the total drag force on the lower pipe. And for a rectangular shape no drop in the drag coefficient is observed (Figure 14). The results for a drag coefficient of 0.6 are plotted in the figure below. The drag coefficient of the draghead is kept equal to 1.2.

Drag coefficient, $C_d = 0.6$:

This means that the drag forces on the pipes decrease by 33%. At low speeds, however, the drag force is only a small percentage of the total trailing force on the suction pipe system. The soil excavation forces are much more dominant. This is even strengthened by the large lever arm because the soil excavation force applies on the draghead and the drag forces halfway on the pipe.

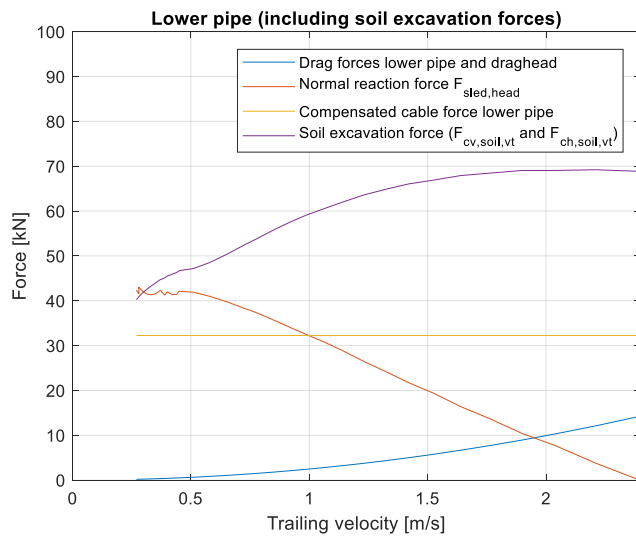


Figure 31: Drag force lower pipe versus the trailing velocity for a drag coefficient of 0.6

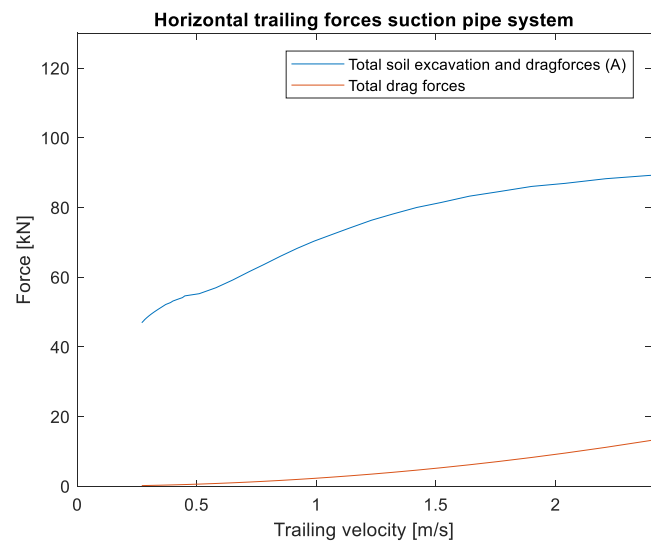


Figure 32: Drag force upper pipe versus the trailing velocity for a drag coefficient of 0.6

Drag coefficient, $C_d = 1.2$:

The results for the coefficient 1.2 are not shown in the report but a comparable result as above is observed. From this can be concluded that for the behaviour of the suction pipe, the drag coefficient is not very important at usual trailing velocities of 1-2 m/s. For the total trailing force, the drag force is becoming more and more dominant with a higher drag coefficient. The percentage of drag forces with respect to the total trailing force at 1 m/s is between 3-6% ($C_d = 0.6 - 1.2$). This percentage increases strongly when the trailing velocity is increased to 2 m/s, 11-18%.

2.4.2 Influence current velocity

A trailing velocity of 2 m/s (=cutting velocity) can be seen as the maximum trail velocity. However, when there is dredged against the current, the flow velocities on the pipe are higher than the cutting velocities. The drag forces become more dominant than shown above because they increase quadratically with the velocity. In Figure 33 the results are shown for an extra current velocity of 2 knots (1m/s) and a drag coefficient of 0.9. In the situation without soil excavation forces, the draghead is then lifted at a trailing speed of 2.5 m/s already. In the case with soil excavation forces the draghead starts floating at 1.9 m/s.

The ratio of the drag force to the total trailing force at 1 m/s increases strongly to 14-22% ($C_d = 0.6 - 1.2$) and at a trailing velocity of 2 m/s, 25-40%.

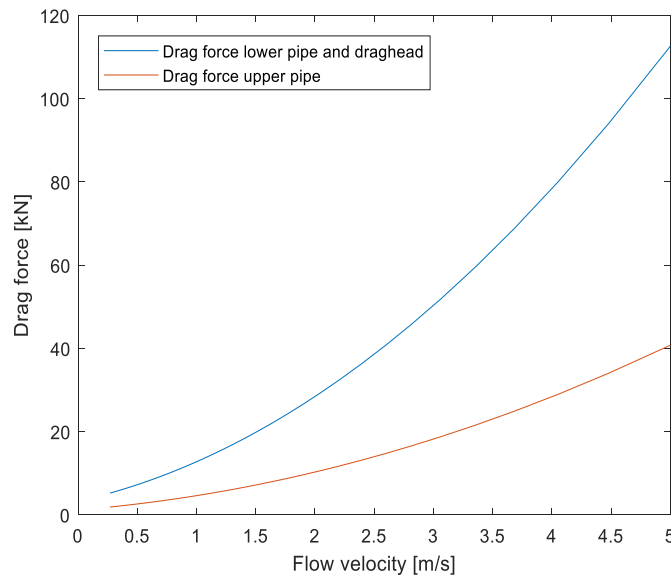


Figure 33: Drag forces, lower and upper pipe ($\alpha_2=45$ degrees, $\alpha_1=30$ degrees)

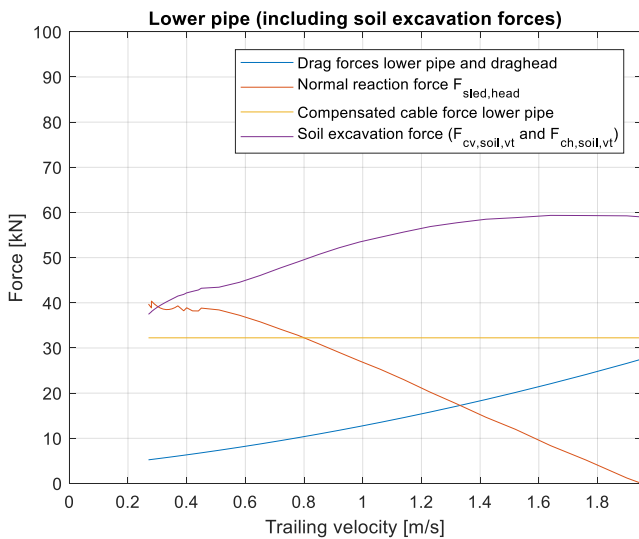


Figure 34: Drag force lower pipe versus the trailing velocity

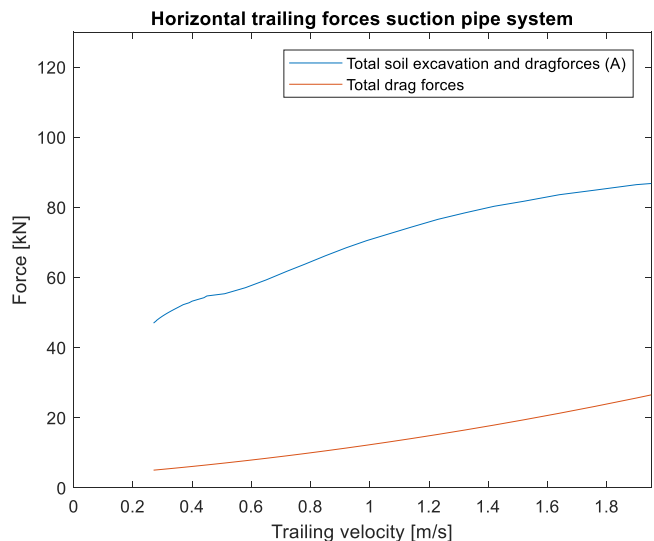


Figure 35: Drag force upper pipe versus the trailing velocity

2.4.3 Verification of the dredging depth influence

Up till now is in the case study a lower suction pipe angle of 45 degrees and a upper suction pipe angle of 30 degrees maintained. However, a trailing suction hopper dredger is also used for shallower waters. Below, two other configurations for different water depths (h) are shown. For simplicity of the calculation is it assumed that the angle of the lower- and upper suction pipe will not change.

Figure 36 and Figure 37 describe the forces for a lower suction pipe angle of 30 degrees and a upper suction pipe angle of 10 degrees. The moment the draghead lifts off is at 4.7 m/s. This is because the resulting vertical force of the submerged weight is lower at this angle. In addition, the effect of the horizontal excavation force is reduced because of the decrease of the vertical lever arm. The result is that the vertical force on the draghead is bigger, and therefore experiences a larger sled force. The total trailing force is consequently higher.

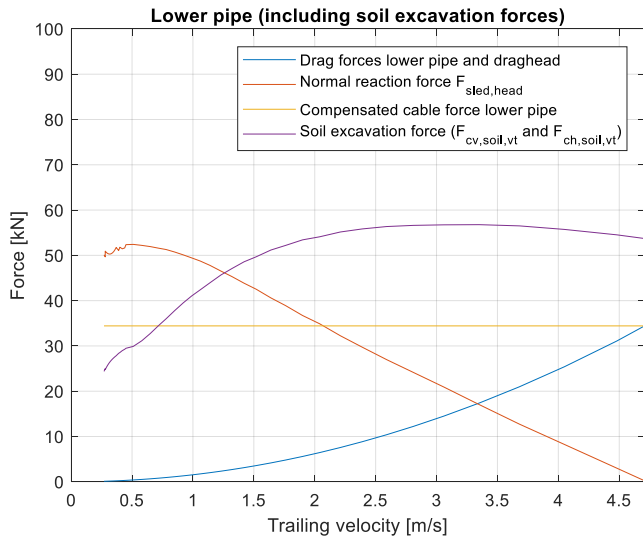


Figure 36: for $\alpha_1=10^\circ$, $\alpha_2=30^\circ$, $h=10.15$ m

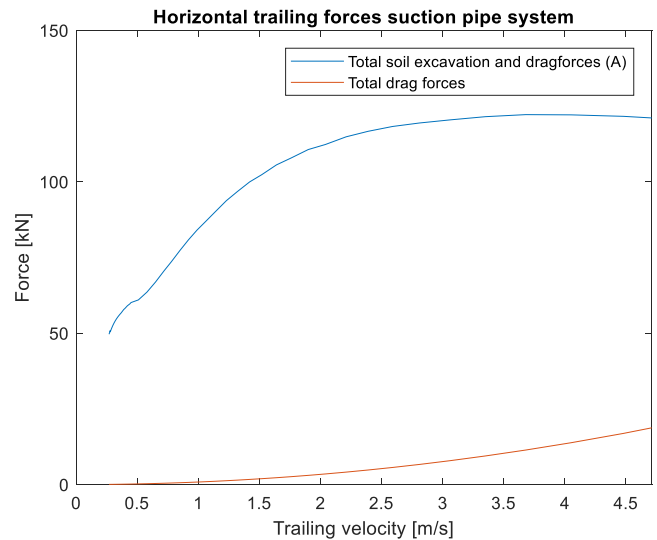


Figure 37: for $\alpha_1=10^\circ$, $\alpha_2=30^\circ$, $h=10.15$ m

In Figure 38 and Figure 39 this effect is amplified even worse because the resultant drag forces are lower and the forces on the draghead are higher.

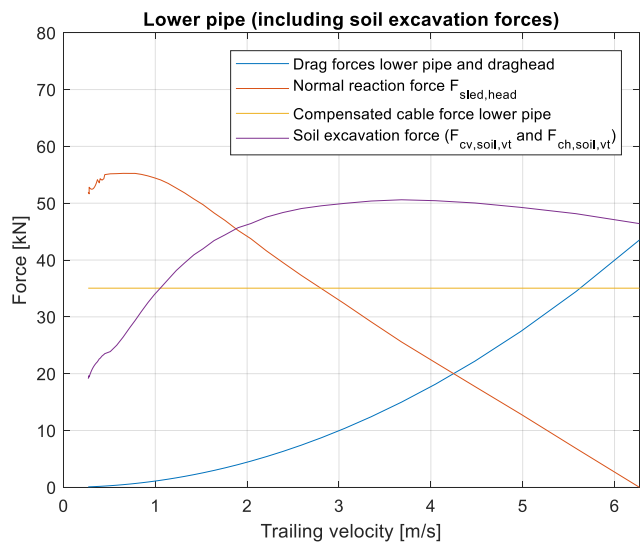


Figure 38: for $\alpha_1=0^\circ$, $\alpha_2=25^\circ$, $h=6.30$ m

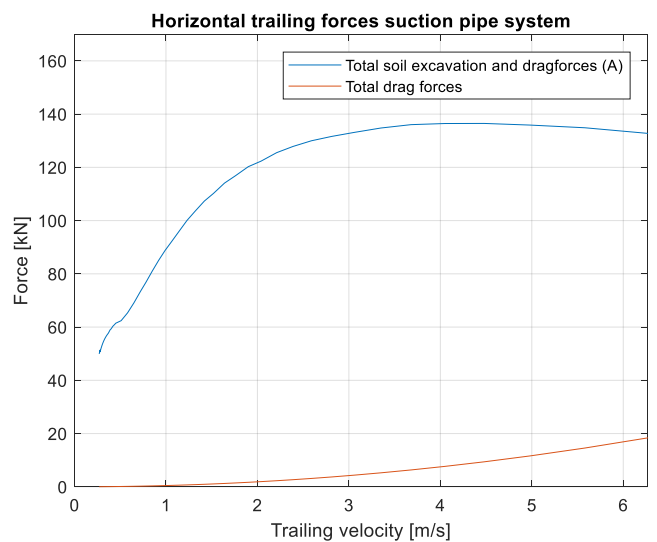


Figure 39: for $\alpha_1=0^\circ$, $\alpha_2=25^\circ$, $h=6.30$ m

The conclusion is that the compensation factor of the swell compensator should be chosen differently in order to obtain the same vertical soil force, $F_{Cv,vt}$, at different velocities. This can be done simply by adjusting the pressure in the swell compensator to the depth and velocity at which is dredged. In the same way the pipe angles can also be used to increase or decrease the soil force temporarily without having to adjust the pressure in the swell compensator.

2.4.4 Verification trailing forces

To check whether the calculated total trailing forces match with results from previous studies, the outcomes are compared. For the comparison of the trailing forces, the research of P. de Jong (Jong, 1988) and the current trailing force calculation of Damen Dredging Equipment are used. In P. de Jong's research, he calculates the forces on the suction tube and draghead while jetting and cutting at the same time. The visor is kept horizontal which results in a constant blade angle and layer thickness. Furthermore is the size of the suction pipe twice as big while the dimensions of the draghead are almost equal. The total horizontal trailing force for cutting and jetting ranges from 100-300 kN (0.5-2 m/s). Again this is a very rough comparison because P. de Jong's assumptions are very different from this research.

The present trailing force estimated by Damen is 124 kN at operational speed (TSP600, depth 20 m, sand (400 kPa), layer thickness 10 cm, swell compensation factor 50%). The trailing forces seems to be on the high side. Because the dimensions and the way in which the trailing forces are calculated vary significantly, the only conclusion that can be drawn, is that the order size of the trailing forces match.

2.5 Conclusion

The aim of this chapter was to determine the trailing forces experienced by the suction pipe. Moreover, to show which influence the trailing forces have on the force distribution over the cables and support by the bed, to see the behaviour of the suction pipe system. By use of the settings of the swell compensator the resulting vertical force on the bed, from the suction pipe and the draghead, can be set. The results indicate that when the swell compensator compensates 50% of the initial cable tension of the lower pipe, and the excavation forces on the draghead are not yet taken into account, the suction pipe will start to float at a trailing velocity of 3.6 m/s. Because of the increasing drag forces, the vertical soil reaction force, $F_{Cv,vt}$, decreases.

With the calculated soil excavation forces resulting from chapters 3, 4 and 5, the total trailing forces are known and the behaviour of the suction pipe system is observed again. The horizontal excavation forces on the draghead and suction pipe are considerable and increase strongly with the trailing velocity. Until the moment the horizontal excavation forces on the draghead and drag force on the pipe gets too dominant. The draghead is lifted from the bed at a trailing velocity of 2.3 m/s.

The drag forces at common trailing velocities of 1-2 m/s are relatively low compared to the soil excavation forces and therefore have a small share in the trailing forces. For trailing velocities of 1 m/s and no current velocity the resulting drag force is negligible compared to the soil excavation forces. For trailing velocities of 2 m/s, which can be seen as the maximum trailing velocity, the drag coefficient gets more dominant. In case there is trailed against the current the drag forces can no longer be ignored and have a significant contribution to the total trailing force.

Results show that the behaviour of the suction pipe system changes when the dredging depth is varied. The different angles cause a change in the direction of the drag forces. However, in particular the influence of the increase in length of the horizontal lever arm, at lower water dredging depths, has a big influence on the draghead equilibrium. In addition, will the decrease of the vertical lever arm of the horizontal resultant forces cause a smaller contribution to the sum of the moments. The result is that the draghead will lift off at a higher trailing velocity and the trailing forces are larger.

3 Force analysis of the draghead

This chapter zooms in on the physical processes in and around the draghead, to be able to determine all the relevant forces that are exerted onto the draghead during trailing. It is desirable to position the draghead in the optimal way to gain the maximum efficient production. Part of the trailing forces could perhaps be decreased, which eventually could result in a more economic suction pipe system or even a reduction of the total power of the propulsion system.

Every type of vessel is equipped with a different size of dredging installation. Damen has designed a diverse range of dragheads for pipe diameters from 400-900 mm. The dimensions of the SLK 600 version is chosen to be analysed in this report, because it is the draghead which is most often sold by Damen. However, the designs of the other sized dragheads are almost identical. By adjusting the dimensions, the forces and the behaviour of these dragheads could be calculated and analysed in a similar way.

In the literature in paragraph 3.1, a small overview is given for which researches have already been done on this subject. In the second paragraph, the analysis of the draghead is performed and is shown what the main forces on the draghead are. Video images of a working draghead at different velocities give an impression of what is happening at the bed while the draghead is trailed over the bed. The forces on the draghead are simplified and projected onto the schematization of the 2D model. But before the forces are determined, first the soil parameters are explained and defined. The soil properties have a lot of influence on the behaviour of the draghead. Because of the diverse soil compositions, it is very difficult to determine how the draghead will behave. Therefore, in this research there is chosen for a specific sand composition.

Below a rendering of the draghead is displayed from two different views. The left side of the dashed line in both animations is the visor, the right side is the visor house. The visor is able to rotate around the hinge in the visor house. In the third paragraph the focus is on the determination of the forces on the visor house although the visor cannot be ignored. The visor forces are investigated in more detail in chapter 5 and results are used and therefore substituted into this chapter.



Figure 40: Sideview of a draghead configuration with a hydraulic cylinder

Notation

Latin		
Nozzle surface area	A_n	m ²
Surface area opening visor	$A_{suction}$	m ²
Dimensionless cutting force (non- and cavitating)	c_1, c_2, d_1, d_2	-
Effective size, median grain size	D_{10}, D_{50}	m
Inner diameter suction pipe	D_i	m
Jet pipe diameter	D_j	m
Nozzle diameter	D_n	m
Relative density	D_r	-
Settlement layer thickness	$h_{i, settle}$	m
Blade length	l_b	m
Mass visor	m_{visor}	kg
Porosity	n	-
Number of nozzles	n_n	-
Specific compaction force	q_{soil}	kg/cm ³
Jet pipe velocity	u_2	m/s
Mixture velocity	v_m	m/s
Volume visor	V_{visor}	m ³
Total volume soil, pore volume	V_t, V_p	m ³
Width draghead (outside)	w_{out}	m
Width support draghead	$w_{support}$	m
Width draghead (inside)	w_{in}	m
Width wearing piece	$w_{wearing}$	m
Greek		
Blade angle	α	°
Lower suction pipe angle	α_2	°
Shear plane angle	β_{shear}	°
External friction angle	δ	°
Dilatancy	ε	-
Correction opening visor geometry	ξ	-
Initial, situ density	ρ_i, ρ_{situ}	kg/ m ³
Mixture density	ρ_m	kg/ m ³
Visor angle	γ	°
Visor – blade angle	γ_2	°
Friction coefficient	μ	-
Internal friction angle	φ	°

3.1 Literature

The determination of the trailing forces has been subject to many studies. In the research of Z. Liu, as previously stated, an estimation is made of the forces on the suction tube and the draghead in a very simplified manner (Zhi, 2002). She has not taken into account the trailing velocity dependence of the trailing forces. To improve the motions of the suction pipe and draghead, a better determination of the trailing forces is needed. In the report of P. de Jong, the forces on the draghead have been calculated in a comparable manner. He also tried to model the speed-dependent influence of the forces (Jong, 1988). He assumed the visor was fixed to the visor house, therefore for different trailing velocities a variable jet penetration depth was determined which resulted in a variable cutting layer thickness. However, a clear force overview in his report is missing.

In addition to the researches which included every force on the draghead, research was carried out into specific components that have been validated with lab experiments. Like for example the force on a cutting blade by S.A. Miedema, which resulted in the cutting and wedge theory used in this chapter. More literature has been used in this chapter, but these are appointed and referred to throughout the chapter.

3.2 Model description

In this paragraph the soil excavation forces of the draghead are described and will show that the soil-draghead interaction is important. The soil characteristics are defined in 3.2.2. Subsequently is explained in detail how the forces on the draghead can be calculated in 3.2.3.

3.2.1 Forces on the draghead

During dredging, the draghead is exposed to several different forces. The soil is excavated by the draghead by use of stress enlargement and reduction, which leads to volume changes of the soil. In Figure 41, an animation of the working principle of the draghead is shown. In the animation, the pull direction of the draghead towards the right is described. The process on the right is the first to take place and influences the following excavation processes.

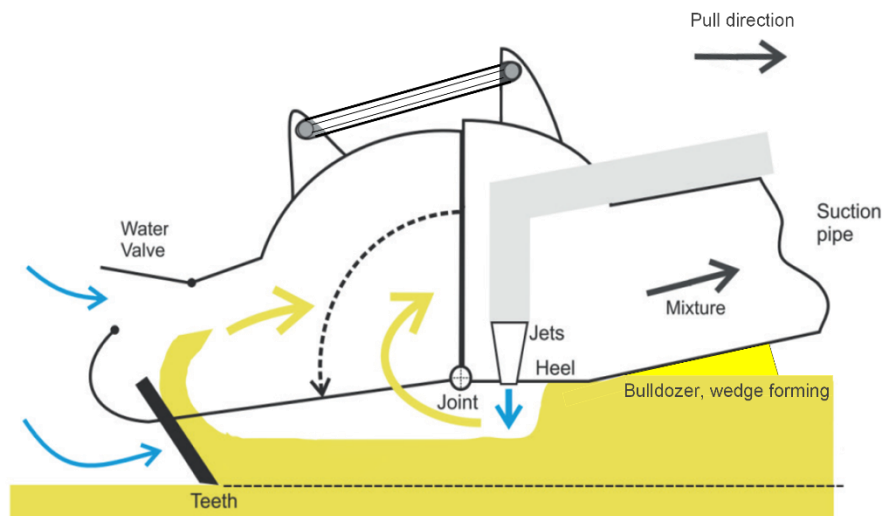


Figure 41: Working principle draghead, source (modified): (Bergh, Osnabrugge, & Keizer, 2015)

With an underwater camera, recordings of a draghead in operation were made to see what is going on around the draghead. Figure 42 shows images of a draghead (type SLK650, width: 2.5 m), trailing at two different velocities at a sand location, north of the Wadden Islands, source: (Spaansen). For low trailing velocities, it can be clearly seen what is happening. Because the draghead slightly settles, it pushes a layer of sand in front of the visor house. This layer slides off and flows away along the draghead.

The heel is the surface area that serves as a foundation for the draghead and ensures that the draghead does not settle too deep. The jet nozzles are placed in the heel just in front of the visor hinge. The nozzles inject water with a high velocity into the sand layer. The soil is fluidized which results in a strength reduction of the soil. The fluidized sand-water mixture is sucked up which facilitates the movable visor to drop deeper to the solid sand layer. The teeth will now make contact with the sand and cut a layer which also contributes to the sand production. The situ soil layer has a high initial density and will be reduced by means of ambient water and jet water to make the mixture easier to pump upwards into the hopper.



Figure 42: A draghead in operation at two different speeds; left-side: 1,25 knts (0,64 m/s) and right-side: 2,5 knts (1,28 m/s)

For a higher trailing velocity, the situation seems to change. The excavation process in front of the visor house looks a lot more turbulent. The hump of sand pushed forwards, blows away because of the higher flow velocities. Furthermore, can be observed that the visor settles less deep compared to lower trailing velocities.

What happens inside of the draghead is a mystery. With insights from previous researches, which were performed for separate processes of the draghead, like cutting with a blade and moving the jets, it is possible to predict what is happening. By simplification of the draghead, a force analysis of the draghead, as shown in Figure 43, is made.

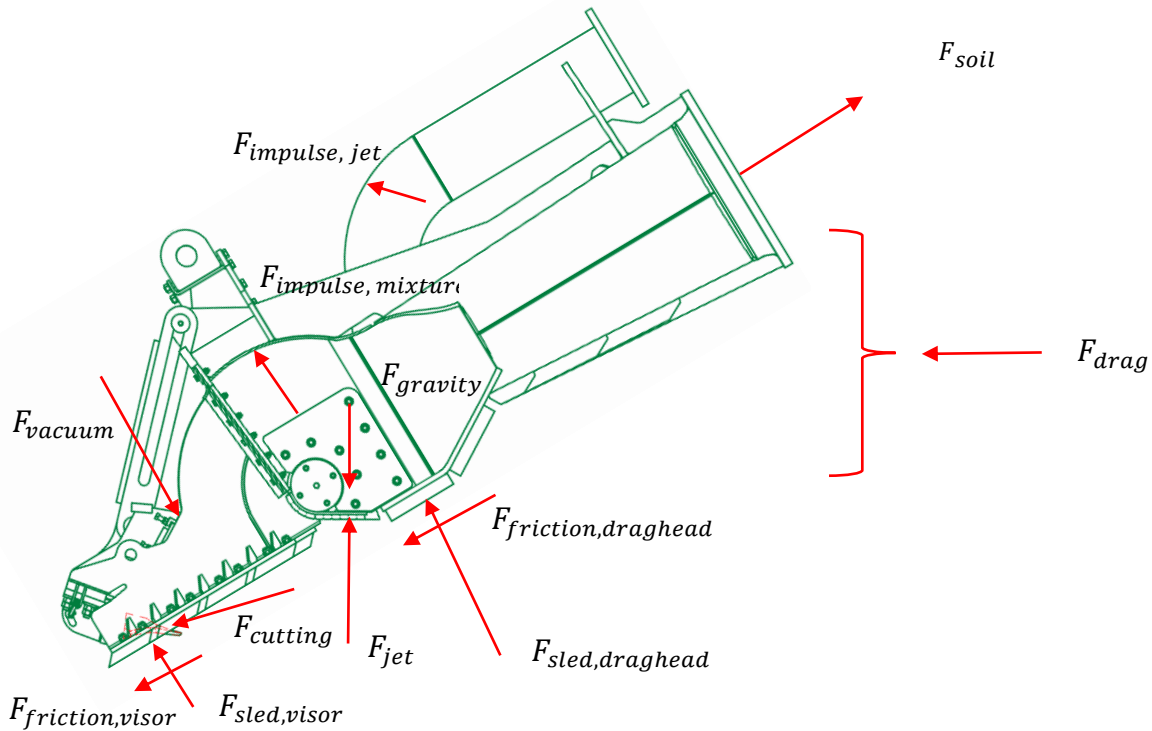


Figure 43: Force overview draghead

The draghead is attached to the suction pipe flange with a fixed connection. The resultant forces of all the soil excavation forces exerted on the draghead are transferred by the suction pipe towards the vessel, indicated with F_{soil} , Figure 43. The drag force, F_{drag} , and gravitation force, $F_{gravity}$, were already calculated in chapter 0. This chapter also showed that the swell compensator partially compensates the weight of the draghead and suction pipe, in that way the normal force on the bed can be regulated. The results indicated that the vertical resultant force, $F_{c,draghead,v}$, slowly decreases when the drag forces increase due to the increasing trailing velocity. The contact with the bed must be maintained to ensure that the distance from the jets to the sand layer is minimal, to minimize entrainment losses. In addition, a certain normal force seems desirable because when the force is too low, the draghead may start bouncing. A bouncing draghead leads to high tensile forces and a strongly fluctuating density, which is very undesirable for the dredging pump.

As has been noted, the draghead pushes a hump of sand in front of the visor house as a result of the settlement of the draghead. This causes a force on the draghead named as: $F_{sled,draghead}$. The shearing of the draghead over the bed results in a friction between the metal surface and the sand particles equal to $F_{friction,draghead}$. The jets inject a large volume of water into the ground. The resulting impulse force, F_{jet} , moves the visor house upwards.

A number of forces also work on the movable visor. The mixture flows towards the pump and the tight seal of the visor with the bed results in an under pressure in the visor and visor house. Due to the pressure difference the visor is pushed downwards with, F_{vacuum} . Loosening of the sand with the aid of the cutting teeth results in cutting force, $F_{cutting}$. And lastly, a similar force as $F_{sled,draghead}$ is working on the tip of the visor, which is named with $F_{sled,visor}$, and follows from the reaction force of the wearing pieces that are pulled through the sand. This force acts perpendicular on the visor wearing pieces and also provides a friction force, equal to $F_{friction,visor}$.

The resulting force due to the redirection of the flow of the mixture, $F_{impulse}$, applies on the inside of the bend in the visor house. The jet water flow also causes an impulse in the bend of the jet pipeline. The forces are described in more detail in 3.2.3. Now the sand properties will first be determined as they are needed for the calculation of the forces

3.2.2 Soil characteristics

Dredging contractors have to deal with an enormous variety of soil compositions. It is hard to design a draghead which works perfectly in every soil type. Soils which are classified in the sand and silt particle size are dredged relatively easy compared to cohesive soils like clay or rock with high compressive- and tensile strengths.

The soil mechanics for dredging differ from the literature found in civil engineering books. It provides a substantial amount of theories but is often not applicable for a moving excavating draghead. The soil is always completely saturated (when gas is neglected) which causes in combination with the short duration of the applied force, for an undrained situation. These theories are often inadequate for the undrained situation. In addition, for dredging, the question is when the soil will fail, while in civil engineering this limit must be prevented.

3.2.2.1 Classification sand:

Sand is classified by grain sizes between 0.063 and 2 mm. The main characteristics of sand are permeability and stiffness, where the stiffness is significant, especially after preloading. The granular particles cannot transfer tensile forces but only compressive forces. An exception is when a negative pore pressure is present which can contribute to large tensile forces in saturated sand. Instead of sand particles moving one by one, chunks of sand could decay because the grains are held together by the negative pore pressure.

The grain size gives a first impression of the soil properties and classification. The shape of the grains for example, has a large influence of the mechanical properties. The grain size distribution gives an indication of the relative proportions of the particle sizes. The cumulative overview of the grain size distribution gives an quick overview of the variety in particle size of a soil sample. Sand with a smooth and wide range of the distribution has a large variety and is called well graded soil. Sand with a narrow range has a small variety and is called uniformly graded.

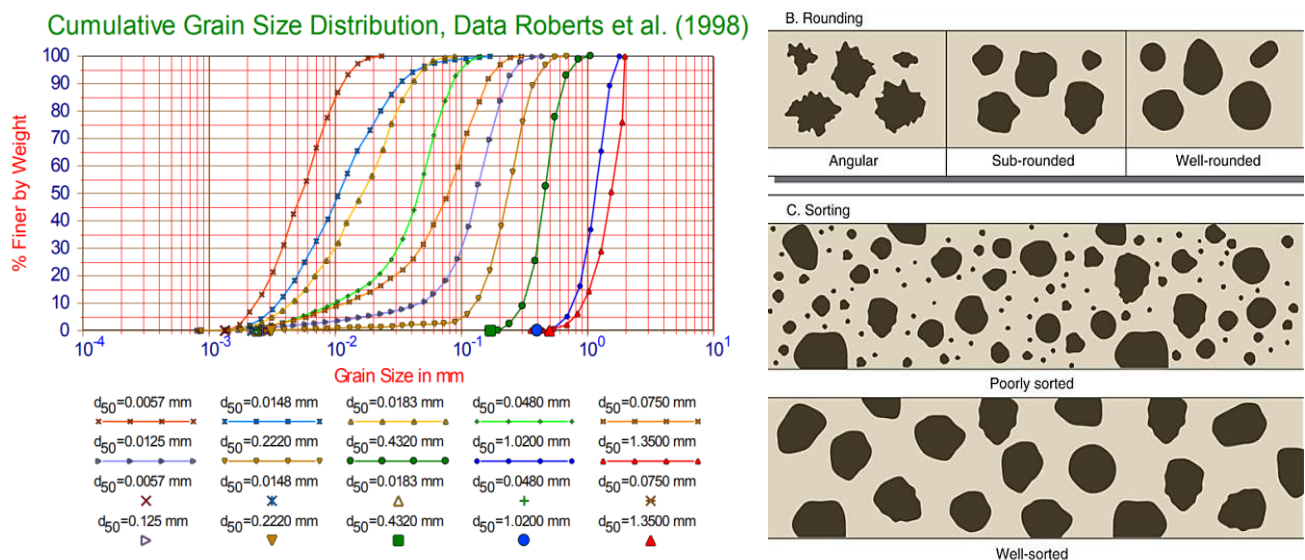


Figure 44: Sand characteristics; grain size distribution and classification, source: (Miedema, *Introduction to Dredging Engineering* [OE4607], 2016)

The median grain size D_{50} indicates that fifty percent of the particle mass is smaller/finer. The grain size distribution can influence the permeability, because for example for a widely distributed grain size, small particles can be trapped in between the pores of larger particles. A well graded particle size distribution increases the stiffness but consequently blocks the water flow and decreases the permeability. The 'effective size' denoted by D_{10} is therefore an important variable for the hydraulic conductivity of the soil. It means, similar to D_{50} that ten percent of the particle mass is smaller than the effective size, D_{10} .

3.2.2.2 Properties sand:

In this research there is chosen to make use of an artificial soil. The name given to the soil is GM-Fine Sand ($D_{50}=0.35$ mm, $D_{15}=0.28$ mm, $D_{10}=0.27$ mm). For the case studies in the rest of the report, this is the only composition used. The composition can be defined as 'dense' packed sand. The model could be extended for other soil compositions in the future but due to huge differences between the soil characteristics this is postponed for now. There is chosen for a dense configuration because trailing suction hopper dredgers work mostly in areas where the soil has consolidated over a long time. Now, the important properties of the sand will be described in this section. An overview of the properties of the composition, which are used in the rest of the report and model, are summarized in Table 5.

Porosity:

The porosity of sand describes the composition of soil, water and air. In case of saturated sand the pores are saturated with water. The *porosity* n is in between 0.29 and 0.46 for fine sands (Das, 2009). This depends on the grading but also on the compaction of the soil. The porosity is the ratio of the volume of the pores and the total volume of the soil.

$$n = V_p/V_t \quad (\text{eq. 67})$$

The porosity of the GM-Fine Sand has a porosity of 0.45 with an maximum of 0.5 and a minimum of 0.44.

Density:

During dredging the in situ soil composition of the sand bed will change completely. The density will drop because the grain structure changes from dense packed soil to loose chunks, and eventually to a homogeneous sand-water mixture. For the solid particles, the density of quartz sand of 2650 kg/m^3 is usually used and a seawater density of around 1025 kg/m^3 . The initial density of completely saturated sand bed with a porosity of 0.45 gives:

$$\rho_i = \rho_{situ} = 0.45 * 1025 + (1 - 0.45) * 2650 = 1918.75 \text{ [kg/m}^3] \quad (\text{eq. 68})$$

In practice, a density of around $1300\text{-}1500 \text{ kg/m}^3$ is strived for during dredging. This decrease of the density is a consequence of an increase of the porosity due to shear stresses, the injection of jet water, the water supply through the voids of the porous soil and erosion-water at the edges of the visor. Higher densities do not act viscous enough, what could cause several problems for the transport of the mixture and the distribution of the mixture in the hopper.

The relative density shows the ratio between the loosest and densest state of the soils. The formula is stated as:

$$D_r = \frac{n_{max} - n}{n_{max} - n_{min}} = \frac{0.5 - 0.45}{0.5 - 0.44} = 83.33 \% \quad (\text{eq. 69})$$

So, the porosity spread determines in what state the soil is. In Table 3, the values of the relative density are appointed.

Table 3: Designation of granular soil based on relative density

D_r (%)	Description
0-20	Very loose
20-40	Loose
40-70	Medium dense
70-85	Dense
85-100	Very dense

Dilatancy:

Densely packed sand has a tendency to expand when it is subjected to shear stress, this is called dilatancy. The volume increase causes entrainment of water into the created space between the grains. Contrarily, when the sand is loosely packed, shear stress can cause the grain structure to contract. The dilatancy can be derived by:

$$\varepsilon = \frac{n_{max} - n_i}{1 - n_{max}} = \frac{0.5 - 0.44}{1 - 0.5} = 0.12 \quad (\text{eq. 70})$$

Permeability:

The permeability can be estimated with different relations. Calculating the permeability with the Hazens equation gives:

$$k = 10^{-2} * D_{10}^2 = 10^{-2} * 0.27^2 = 7.29 * 10^{-4} [m/s] \quad (\text{eq. 71})$$

This is a less accurate relation because of the fact that it only takes into account the effective size. The compaction rate of the soil is also of big influence and therefore the relation of Den Adel should give a better indication. Moreover, this method has been validated by van Rhee and Bezuijen, which gave satisfactory results (Rhee & Bezuijen, The breaching of sand investigated in large-scale model tests, 1998):

$$k = \frac{g}{160\nu} D_{15}^2 \frac{n^3}{(1-n)^2} = \frac{9.81}{160 * 10^{-6}} (0.28 * 10^{-3})^2 \frac{0.45^3}{(1-0.45)^2} = 1.4 * 10^{-3} [m/s] \quad (\text{eq. 72})$$

Nevertheless, the permeability in the case studies in this report are chosen as used in the pore pressure model calculation of Miedema. Here the $k_{max} = 4.5 * 10^{-4}$ m/s and the initial permeability, $k_i = 5 * 10^{-5}$ m/s. This results in a mean permeability of:

$$k_m = \frac{k_i + k_{max}}{2} = \frac{5 * 10^{-5} + 4.5 * 10^{-4}}{2} = 2.5 * 10^{-4} \quad (\text{eq. 73})$$

In Table 4, a small overview is given of the influence of the grading and type of the soil on the permeability.

Table 4: Permeability of different sand type and compositions

Soil	Permeability (m/s)	Degree of permeability
Sandy gravel, clean sand, fine sand	$10^{-3} > k > 10^{-5}$	High to medium
Sand, dirty sand, silty sand	$10^{-5} > k > 10^{-7}$	Low
Material	Permeability (m/s)	d10 (mm)
Uniform coarse sand	0.0036	0.6
Uniform medium sand	0.0009	0.3
Clean, well-graded sand	0.0001	0.1
Uniform fine sand	$36 * 10^{-6}$	0.06
Well graded fine sand	$4 * 10^{-6}$	0.02

Internal friction angle

The internal friction angle can be determined with an triaxial test. The results from multiple tests performed by A. Sitanggang in the lab showed, an internal friction angle, ϕ , of 40° for the DC-Fine Sand which has the same particle size and distribution as the GM-Fine Sand (Sitanggang, 2017).

External friction angle

The external friction angle can be calculated by use of the friction coefficient between the soil and the material, and is a function of the internal friction angle of the soil itself. For a steel sand friction angle in literature the following simplification is used (Miedema, The Delft Sand, Clay and Rock Cutting Model, 2014):

$$\delta = \frac{2}{3} * \phi \quad (\text{eq. 74})$$

$$\delta = \frac{2}{3} * 40 = 27^\circ \quad (\text{eq. 75})$$

In the table below an overview of the different soil parameters is given. With a value spread for a wide range of sand compositions and the dense packed parameters for the GM-Fine sand.

Table 5: Soil parameters; GM-Fine sand

Variable	Symbol	Unit	Value spread; sand	Dense packed – GM-Fine sand
Density	ρ	kg/m ³	1400-1850	1457.5
Density, sat	ρ_{sat}	kg/m ³	1900-2150	1918.8
Median grain size	d ₅₀	mm	-	0.35
Effective grain size	d ₁₅ d ₁₀	mm	-	0.28 0.27
Coefficient of uniformity	C_u	-	-	1.3
Porosity	n	-	0.26-0.46	0.45
	n_{max}	-	-	0.5
	n_{min}	-	-	0.44
Permeability	n_i	-	-	0.44
	k_m	m/s	$3.6 * 10^{-3} - 4 * 10^{-6}$	$2.5 * 10^{-4}$
	k_i	m/s	-	$5 * 10^{-5}$
	k_{max}	m/s	$1 * 10^{-4} - 5 * 10^{-5}$	$4.5 * 10^{-4}$
	Dilatation	ϵ	-	0.12
Cohesion	c	Pa	-	0
Adhesion	a	Pa	-	0
Internal friction angle	φ	°	29-41	40 (36-41)
External friction angle (steel)	δ	°	20-30	27

An overview of other variables used throughout the report are stated in table below:

Table 6: Environmental parameters

Variable	Symbol	Unit	Value
Density sand (quartz)	ρ_s	kg/m ³	2650
Density water	ρ_w	kg/m ³	1025
Water temperature	Degree Celsius	°C	15
Viscosity	ν	m ² /s	0.000001

3.2.3 Calculating the trailing forces on the draghead

3.2.3.1 Gravity- and drag force

In 3.2.1, the need for a certain weight of the draghead is already explained. The gravity force and drag force calculation of the draghead are included in the calculation of, $F_{Cv,draghead,v}$, in chapter 2.

The visor is free to move around the visor hinge when the visor is not fixed to the draghead. So, the weight of the visor itself is important for the force balance and determines its position. The visor needs to have a certain weight to push the cutting teeth into the soil and keep the visor close to bed to create a vacuum. When the soil has little bearing capacity (coherence) the visor will easily sink into the bed. It is clear that a vertical force balance is critical for an optimal working of the draghead and consequently the production. The detailed calculation of the submerged weight and resulting gravity force of the visor is included in chapter 5.

3.2.3.2 Jet force

The jets discharge, with high velocity, a large amount of water out of the nozzles. This creates a jet force which is equal to the impulse force of the jet flow. The impulse force is equal to the mass flow of the fluid times the flow velocity:

$$F_{imp} = \rho_w * Q * v \quad (\text{eq. 76})$$

$$F_j = \rho_w * A_n * u_0^2 * n_n \quad (\text{eq. 77})$$

Where n_n is the number of nozzles installed in the draghead, A_n the nozzle surface area per nozzle ($\frac{\pi}{4} * D_n^2$) and nozzle diameter, D_n . The impulse force is quadratically dependent of the jet nozzle exit velocity, u_0 . The impulse force is directed in the opposite direction of the jet nozzle exit velocity, in the case of the draghead nozzle, upwards, like is shown in the illustration of Figure 45.

Because the jet nozzles are positioned in the visor house heel, it depends on the angle of the lower suction pipe if the jet force is purely vertical directed or has a small horizontal component.

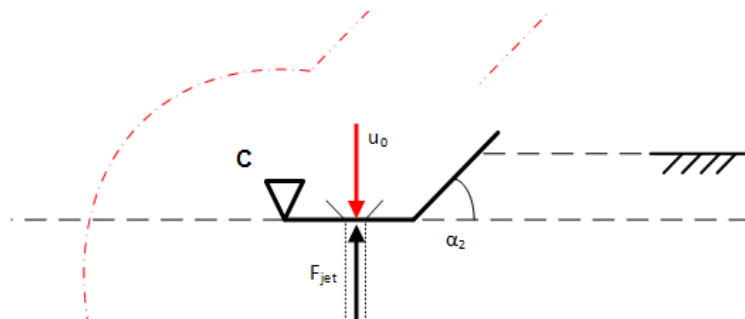


Figure 45: Jet force from impulse of the jet flow

3.2.3.3 Impulse force bends

The excavated sand is turned into a sand mixture in the draghead and from there the mixture is accelerated into the direction of the suction pipe. The sand mixture is accelerated from almost standstill to the speed which the mixture reaches before entering the pump. The sand particles are not directly transported in the right direction. The bends in the draghead and pipe makes it possible to lead the mixture in the direction of the pumps. These bends experience an impulse force for redirecting the mixture flow. The forces caused by redirection of the mixture in the draghead bend are illustrated in Figure 46.

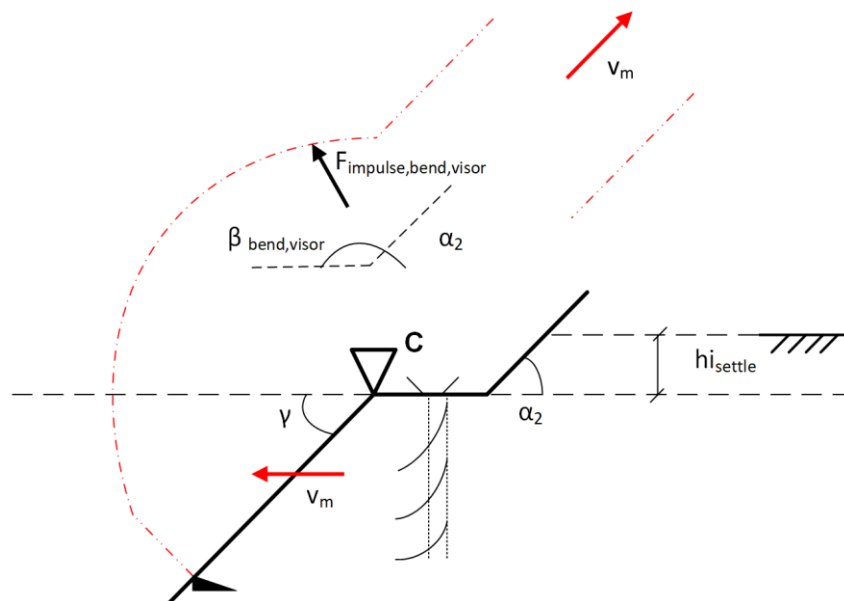


Figure 46: Impulse force in visor house bend due to redirection of the mixture flow

There is assumed that the mixture flow of the jets is directed horizontally to the left and bends of towards the angle of the lower suction pipe. The angle of the pipe bend is then equal to $\beta_{bend,visor} = 180 - \alpha_2$. Another assumption is that the resultant force of the impulse applies on the inside of the visor house of the draghead.

The force can be decomposed in the horizontal and vertical direction:

$$F_{imp,h} = \rho_m * A_{pipe} * v_m^2 * (1 - \cos(\beta_{bend,visor})) = \rho_m * \pi * \left(\frac{D_{pipe}}{2}\right)^2 * v_m^2 * (1 - \cos(\beta_{bend,visor})) \quad (\text{eq. 78})$$

$$F_{imp,v} = \rho_m * A_{pipe} * v_m^2 * \sin(\beta_{bend,visor}) = \rho_m * \pi * \left(\frac{D_{pipe}}{2}\right)^2 * v_m^2 * \sin(\beta_{bend,visor}) \quad (\text{eq. 79})$$

$$F_{imp} = \sqrt{F_{imp,h}^2 + F_{imp,v}^2} \quad (\text{eq. 80})$$

The impulse force due to the redirection of the jet flow can be calculated in the same way. In Figure 47, the angle of the jet bend is shown which is equal to the lower suction pipe angle: $\beta_{bend,jet} = \alpha_2$. The velocity of the jet flow in the pipe is equal to u_2 , the diameter of the jet pipe is D_j and the density of the fluid is the water density, ρ_w .

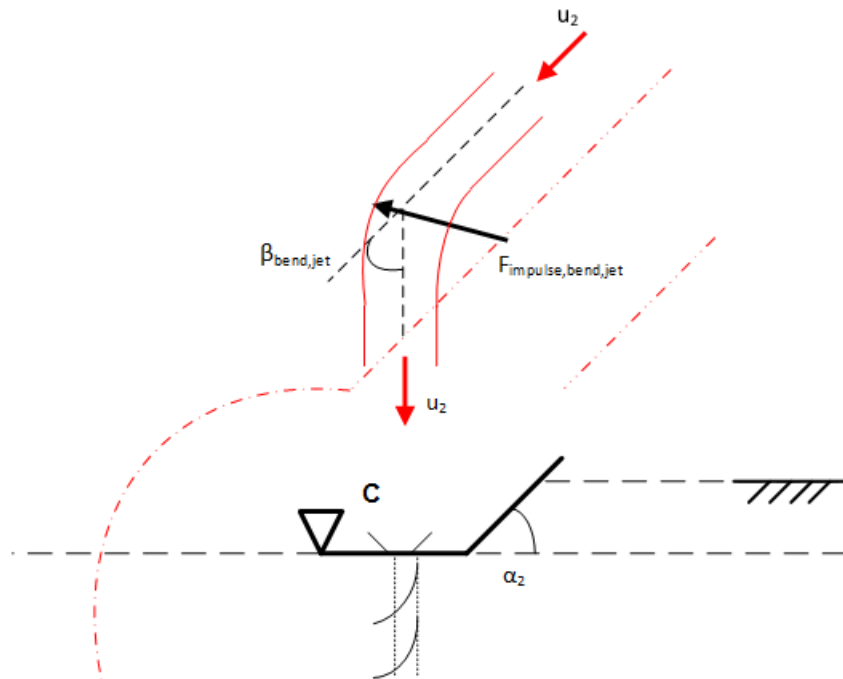


Figure 47: Impulse force jet bend due to redirection of the jet flow

The impulse force in the bend from the small angle differences in de cardan hinge is neglected. Also, the force in the pipe bend close to the sliding piece at the top of the suction pipe is neglected. Here the lever arm is so small that the effect on the behaviour of the draghead is minimal.

3.2.3.4 Vacuum pressure

To accelerate the mixture towards the hopper, there is a vacuum created in the draghead by the centrifugal dredging pump. The force that is exerted on the visor by the resulting force, can be determined with the pressure difference between the inside pressure of the draghead and the hydrostatic pressure outside, times the surface area of the draghead opening:

$$F_{N,vac} = \Delta P * A_{suction} \quad (\text{eq. 81})$$

$$\Delta P = P_{inside} - P_{outside} \quad (\text{eq. 82})$$

$$P_{inside} = P_{neg} + P_{hydrostatic} \quad (\text{eq. 83})$$

$$P_{outside} = P_{hydrostatic} \quad (\text{eq. 84})$$

To calculate P_{neg} the formula used is derived from the Bernoulli equation:

$$P_{neg} = \xi * \frac{1}{2} * \rho_m * v_m^2 \quad (\text{eq. 85})$$

The hydrostatic pressure is calculated with:

$$P_{hydrostatic} = \rho_w * g * h \quad (\text{eq. 86})$$

As can be seen the hydrostatic pressure in the draghead is equal to the surrounding pressure and can be taken out of the equation. The negative pressure can consequently be used to calculate the force that results from the pressure difference between the inside and outside of the draghead visor.

$$F_{N,vac} = \xi * \frac{1}{2} * \rho_m * v_m^2 * l_{visor,opening} * w_{in} = \xi * \frac{1}{2} * \rho_m * v_m^2 * A_{suction} \quad (\text{eq. 87})$$

In which ξ is the dimensionless coefficient for correction of the seal and shape of the suction pipe entrance and inside draghead geometry. The mixture velocity in the pipe is v_m , and the area of the suction mouth draghead opening is equal to $l_{visor,opening} * w_{in}$.

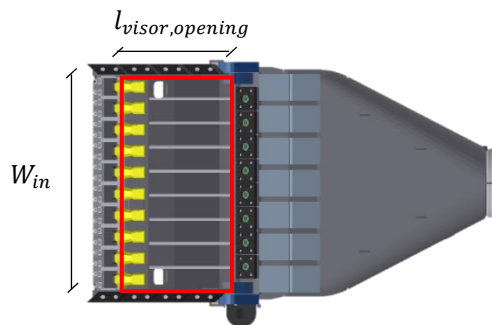


Figure 48: Surface opening visor

3.2.3.5 Sled force

The settlement of the draghead depends on the bearing capacity of the sand and the total load over the contact area between the draghead and the bed. The bearing capacity of the soil indicates at which load there is still no failure of the soil.

The draghead moves with a certain speed over the bed so the consolidation time is just a tenth of a second. If this time is too short, then there is no settlement by consolidation. However elastic compression and deformation by shear can still occur and can cause the draghead to settle.

In Figure 49, the bottom view of the draghead is shown, in which the support area of the visor and visor house are highlighted. Only the visor house provides support for the draghead because the soil is fluidized and eroded by the suction force behind the jets. Here the soil will probably not have a significant bearing capacity anymore. However, the visor will sink through the fluidized layer until it reaches a solid sand layer. The resulting sled force and friction force of the visor are discussed in chapter 0.

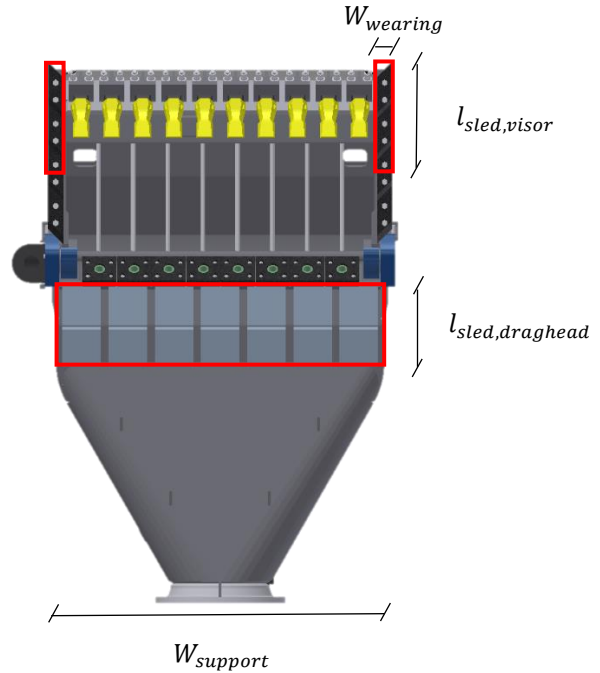


Figure 49: Support area of the visor house and the visor

The visor house can be compared by a sled moving over the sand bed. The settlement of the visor house can be calculated with the specific compaction force method given by Koolen and Kuipers and is illustrated with the side view of the draghead in Figure 50 (Koolen & Kuipers, 1983).

$$F_{sled,N,draghead} = \frac{W_{support} * h_{i,settle}^2 * q_{soil} * g}{2 * \sin(\alpha_2)} = Q \quad (\text{eq. 88})$$

By rewriting the formula the settlement of the draghead by compaction due to the force Q can be calculated:

$$h_{i,settle} = \sqrt{\frac{2 * Q * \sin(\alpha_2)}{W_{support} * q_{soil} * g}} \quad (\text{eq. 89})$$

The specific compaction force, q_{soil} , for a settled heavy soil in this report is set at 6 kg/cm^3 , Bernacki and Haman (1973) (Koolen & Kuipers, 1983). The angle of the sled force with the bed is equal to α_2 , because the wearing pieces on the draghead are in line with the lower suction pipe. The reaction force of the soil, when the settlement is constant, stays equal to $F_{sled,N,draghead}$.

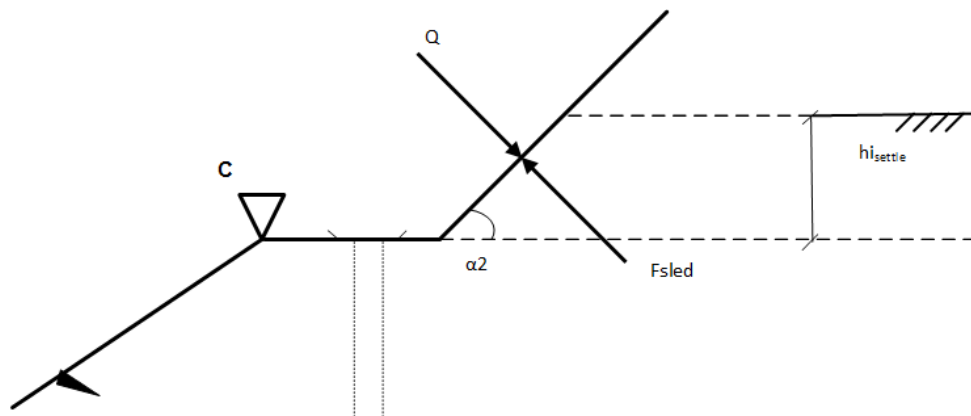


Figure 50: Sled force on the visor house

The resultant force Q of the draghead on the bed can be determined with the force and moment balances. In chapter 2, the resultant reaction force, $F_{Cv,vt}$, of the suction tube on the bed has already been calculated. With a new moment around point B (the cardan hinge), where the soil excavation forces are included, the normal force on the draghead will change and with that the final settlement can be determined (3.3.1.5).

The sled forces can be decomposed in the following way:

$$F_{sled,draghead,h} = F_{sled,N,draghead} * \sin(\alpha_2) \quad (\text{eq. 90})$$

$$F_{sled,draghead,v} = F_{sled,N,draghead} * \cos(\alpha_2) \quad (\text{eq. 91})$$

3.2.3.6 Friction force

The sand bed consists of small grains that are structurally packed together. In case a stress is applied to the soil, the shear stress causes dislocation of the grains by the moving draghead to the top of the bed. The friction force between the draghead and the seafloor is depending of the shear resistance between the soil and the draghead material. The draghead is always moving relative to the bed, even when released at the start of a trail. In case of a moving draghead over the bed there is a dynamic friction coefficient which is usually slightly lower than the static friction.

The surface area which makes contact with the bed causes a friction force. For the draghead this is the lower strip indicated in Figure 49 and for the visor the end of the wearing pieces, the upper strip. The friction caused by the normal stress is area independent but dependent on the force working between the two surfaces.

$$\tau_s = \mu * \sigma_n \quad (\text{eq. 92})$$

$$\mu = \tan(\delta) \quad (\text{eq. 93})$$

Where μ is the friction coefficient, and δ is the external friction angle between the two different materials in this case: sand and steel.

$$\mu = \tan(27) = 0.51 \quad (\text{eq. 94})$$

$$F_{fric} = 0.51 * F_{sled,N,draghead} [kN] \quad (\text{eq. 95})$$

In comparison with 'Agriculture soil mechanics', the previous friction calculated friction coefficient is twice as high. Here a static friction coefficient for steel on dry sand of $\mu = 0.26$ just before movement is given and a dynamic friction coefficient of $\mu = 0.23$ is indicated directly after movement, Nichols (1931). Another research performed by Spoor (1969) found for the friction coefficient of steel over dry soil, $\mu = 0.25$ (Koolen & Kuipers, 1983). The internal friction angles are not given so the values cannot be compared.

The friction force can be decomposed as:

$$F_{fric,h} = F_{fric} * \cos(\alpha_2) \quad (\text{eq. 96})$$

$$F_{fric,v} = F_{fric} * \sin(\alpha_2) \quad (\text{eq. 97})$$

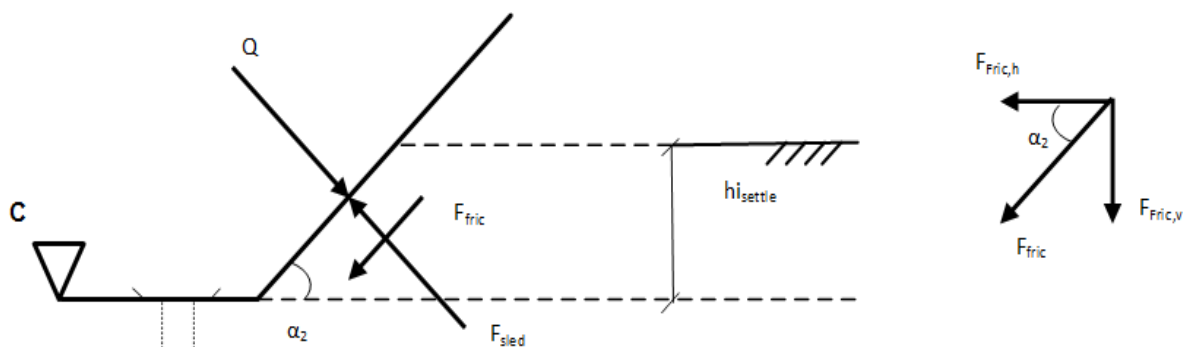


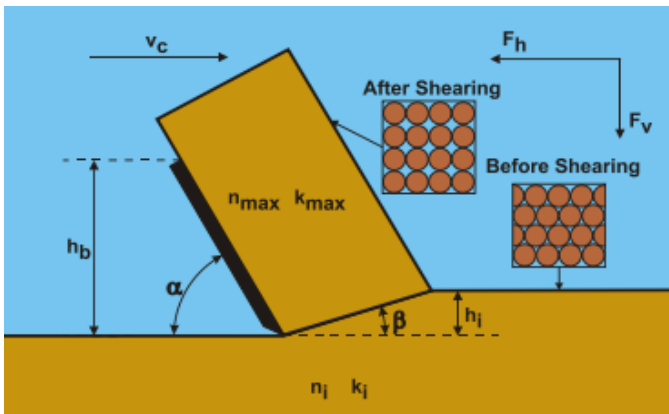
Figure 51: Friction force on the draghead and decomposition of the friction force

Soils with a fine particle size show a higher friction coefficient than coarse sized particles. Packing density is also of influence, where a dense packed sand has a higher friction coefficient than loose packed sand. Butterfield and Andrawes (1972b) found $\mu = 0.17$ for a soil porosity of 43.7% and $\mu = 0.28$ for a porosity of 35.7% (Koolen & Kuipers, 1983) (the friction coefficient values found by Butterfield and Andrawes are for dry sand).

3.2.3.7 Cutting force

The cutting teeth on the visor experience high cutting force while excavating the sand. The cutting forces on a blade, which can be compared with the cutting teeth, are intensively investigated over the years by dr. ir. S.A. Miedema. A summary of the more detailed theory of cutting saturated sand, written by Miedema, is stated here. Derivations are only included when they are necessary to understand the story outline. Otherwise they can be found in the book 'The Delft Sand, Clay & Rock cutting model' (Miedema, The Delft Sand, Clay and Rock Cutting Model, 2014).

In the figure below, the main principle of cutting with a blade is shown. Due to the force applied by the moving blade, the grain particles are dislocated from each other and their grain structure. Hereby the volume of the soil increases (dilatancy). The created space between the grains will be filled up with water, but the grains are still closely packed together, hence the inflowing water experiences resistance. The pressure difference between the pores results in increased grain stresses and consequently higher cutting forces.



1. v_c = cutting velocity
2. h_b = blade height
3. h_i = layer cut thickness
4. α = blade angle
5. β = the shear angle
6. n_i = initial porosity
7. n_{max} = maximum porosity
8. k_i = initial permeability
9. k_{max} = maximum permeability

Figure 52: The cutting process. Source: (Miedema, The Delft Sand, Clay and Rock Cutting Model, 2014)

“The rate of the increase of the pore volume in the dilatancy zone, the volume strain rate, is proportional to the cutting velocity. If the volume strain rate is high, there is a chance that the pore pressure reaches the saturated water vapour pressure and cavitation occurs. This also implies that, with a further increasing cutting velocity, the cutting forces cannot increase as a result of the dilatancy properties of the sand. The cutting forces can, however, still increase with an increasing cutting velocity as a result of the inertia forces and the flow resistance.” (Miedema, The Delft Sand, Clay and Rock Cutting Model, 2014)

For trailing with a draghead at conventional cutting velocities of 0.5 - 2 m/s, dilatancy properties dominate the cutting forces. Due to increasing volume strain rates the cutting forces become higher. Increased volume strain rates can be a reason of increased trailing velocities and therefore the cutting process is depending on the trailing velocity. Inertia forces which play a role at high cutting velocities can be neglected and also gravitation, adhesion and cohesion, present at very low cutting velocities, are neglected.

With the assumptions mentioned above, by only taken into account the dilatancy, the cutting forces on the blade can be calculated with the horizontal and vertical equilibrium of the forces in the shear plane and the force working on the blade, illustrated in Figure 53:

$$\sum F_h = K_1 * \sin(\beta + \varphi) - W_1 * \sin(\beta) + W_2 * \sin(\alpha) - K_2 * \sin(\alpha + \delta) = 0 \quad (\text{eq. 98})$$

$$\sum F_v = -K_1 * \cos(\beta + \varphi) + W_1 * \cos(\beta) + W_2 * \cos(\alpha) - K_2 * \cos(\alpha + \delta) = 0 \quad (\text{eq. 99})$$

Using Darcy's law, as shown by Miedema, the specific flow rate perpendicular to the deformation zone is:

$$q = \frac{\partial Q}{\partial l} = q_1 + q_2 = \varepsilon * v_c * \sin(\beta) \quad (\text{eq. 106})$$

The pressure difference is related with the specific flow rate and can also be expressed using the law of Darcy as:

$$q = k * i = k * \frac{\Delta p}{\rho_w * g * \Delta s} = \varepsilon * v_c * \sin(\beta) \quad (\text{eq. 107})$$

The flow lines are approaching the shear zone from four different directions as shown in Figure 54. The combination of the resistances the flow experiences by the sand package from all directions can be replaced with the parallel resistor method. By replacement follows:

$$R = \frac{\Delta s}{k} \quad (\text{eq. 108})$$

$$\Delta p_{1,i} = \rho_w * g * \varepsilon * v_c * \sin(\beta) * R_{1t,i} \quad (\text{eq. 109})$$

Equation 109 determines the pore vacuum pressure of the cutting layer in each point of the shear zone. The average of the pore vacuum pressure follows by summation of the points (i):

$$P_{1m} = \frac{1}{n} * \sum_{i=0}^n \Delta p_{1,i} \quad (\text{eq. 110})$$

In a similar way the pore pressure on the blade can be derived. For an explanation is referred to the book. The pore vacuum pressure on the blade can be determined with:

$$\Delta p_{2,i} = \rho_w * g * q_i * R_{2t,i} \quad (\text{eq. 111})$$

$$P_{2m} = \frac{1}{n} * \sum_{i=0}^n \Delta p_i \quad (\text{eq. 112})$$

With the calculated pore pressure on the shear plane and the blade, the cutting forces can be determined with the dimensionless cutting force c_i and d_i . For the non-cavitating and the cavitating process respectively:

$$F_{ci} = \frac{c_i * \rho_w * g * v_c * h_i^2 * \varepsilon * w}{k_m} \quad (\text{eq. 113})$$

$$F_{di} = d_i * \rho_w * g * (z + 10) * h_i * w \quad (\text{eq. 114})$$

'The values of the 4 coefficients (c_1 , d_1 , c_2 , d_2) are determined by minimizing the cutting work that is at that shear angle β where the derivative of the horizontal force to the shear angle is zero'. (Miedema, The Delft Sand, Clay and Rock Cutting Model, 2014)

Where the coefficients c_1 and c_2 determine the horizontal and vertical force component respectively for the non-cavitating cutting process. The same notation, d_1 and d_2 applies for the cavitation process.

$$c_1 = \frac{\left(p1m_{dless} * \frac{\sin(\varphi)}{\sin(\beta)} + p2m_{dless} * \frac{h_b}{h_i} * \frac{\sin(\alpha + \beta + \varphi)}{\sin(\alpha)} \right) * \sin(\alpha + \delta)}{\sin(\alpha + \beta + \delta + \varphi)} - p2m_{dless} * \frac{h_b}{h_i} * \frac{\sin(\alpha)}{\sin(\alpha)} \quad (\text{eq. 115})$$

$$c_2 = \frac{\left(p1m_{dless} * \frac{\sin(\varphi)}{\sin(\beta)} + p2m_{dless} * \frac{h_b}{h_i} * \frac{\sin(\alpha + \beta + \varphi)}{\sin(\alpha)} \right) * \cos(\alpha + \delta)}{\sin(\alpha + \beta + \delta + \varphi)} - p2m_{dless} * \frac{h_b}{h_i} * \frac{\cos(\alpha)}{\sin(\alpha)} \quad (\text{eq. 116})$$

$$d_1 = \frac{\left(\frac{\sin(\varphi)}{\sin(\beta)} + \frac{h_b}{h_i} * \frac{\sin(\alpha + \beta + \varphi)}{\sin(\alpha)}\right) * \sin(\alpha + \delta)}{\sin(\alpha + \beta + \delta + \varphi)} - \frac{h_b}{h_i} * \frac{\sin(\alpha)}{\sin(\alpha)} \quad (\text{eq. 117})$$

$$d_2 = \frac{\left(\frac{\sin(\varphi)}{\sin(\beta)} + \frac{h_b}{h_i} * \frac{\sin(\alpha + \beta + \varphi)}{\sin(\alpha)}\right) * \cos(\alpha + \delta)}{\sin(\alpha + \beta + \delta + \varphi)} - \frac{h_b}{h_i} * \frac{\cos(\alpha)}{\sin(\alpha)} \quad (\text{eq. 118})$$

The average dimensionless pressure of the shear plane is $p1m_{dless}$ and the average dimensionless pressure of the blade is $p2m_{dless}$ and can be determined with:

$$p1,2m_{dless} = \frac{1}{n} * \sum_{i=0}^n \left(\frac{\Delta p_i * k_{max}}{\rho_w * g * v_c * e * h_i} \right) \quad (\text{eq. 119})$$

The transition value between the non-cavitating and cavitating cutting process is stated as: if the non-cavitating cutting force is bigger than the cavitating cutting force, the cavitating force applies else the non-cavitating force.

In (Miedema, The Delft Sand, Clay and Rock Cutting Model, 2014) is described with a theory how the shear angle can be determined. It is assumed that for failure of soil a minimum shear energy is needed. At the moment the soil collapses, the soil will shear under an certain angle. When cutting sand, a comparable situation takes place. When the minimum force is known under which the soil will shear the corresponding angle can be determined.

An approximation of the shear angle beta (β) can be determined in the iterative way with the formula:

$$\beta = 61.29^\circ + 0.345 * \frac{h_b}{h_i} - 0.3068 * \alpha - 0.4736 * \delta - 0.248 * \varphi \quad (\text{eq. 120})$$

3.3 Model results & Discussion

The theory and simplifications explained in the model description are used for the calculation of the trailing forces of the SLK600. All the needed dimensions of the SLK600 are listed in Table 7. In the first subsection the forces on the visor house are calculated. The forces on the visor are calculated in chapter 5, but the resultant force in the visor hinge are substituted in the total horizontal and vertical force balance in the end of this chapter to be able to calculate the total soil excavation forces. All the forces working on the visor house are shown in Figure 55.

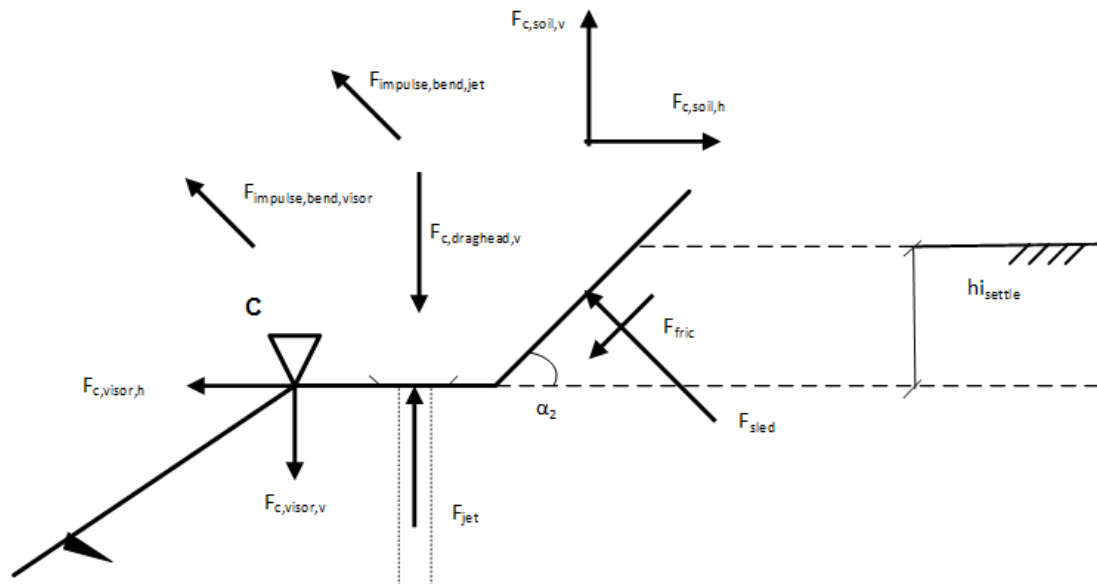


Figure 55: Soil excavation forces on the draghead and resulting forces, $F_{c,soil,h}$ and $F_{c,soil,v}$

Table 7: Draghead dimensions and other variables used in the case study

Variable	Symbol	Value	Unit
Jet pipe surface area	A_j	0.075	m ²
Nozzle surface area	A_n	0.048	m ²
Surface area opening visor	$A_{suction}$	0.867	m ²
Inner diameter	D_i	0.6	m
Nozzle diameter	D_n	0.048	m
Cutting layer thickness	$h_{i,cut}$	0.1 (in this chapter)	m
Mass visor	m_{visor}	1800	kg
Number of nozzles	n_n	8	-
Number of cutting teeth	n_{teeth}	10	-
Blade length	l_b	0.128	m
Specific compaction force	q_{soil}	6	kg/cm ³
Jet discharge	Q_j	0.4793	m ³
Jet exit velocity	u_0	38.95	m/s
Mixture velocity	v_m	5	m/s
Volume visor	V_{visor}	0.2186	m ³
Width draghead (outside)	w_{out}	2.272	m
Width support draghead	$w_{support}$	2.090	m
Width draghead (inside)	w_{in}	2.037	m
Cutting teeth width	w_{teeth}	0.109	m
Width wearing piece	$w_{wearing}$	0.1	m
Blade angle	α	20 (in this chapter)	°
Lower suction pipe angle	α_2	45	°
Shear plane angle	β_{shear}	20	°
Mixture flow redirection angle draghead	$\beta_{bend,visor}$	135	°
Jet flow redirection angle draghead	$\beta_{bend,jet}$	45	°
External friction angle	δ	27	°
Correction opening visor geometry	ξ	3	-
Visor angle	γ	20 (in this chapter)	°
Visor – blade angle	γ_2	45	°
Mixture density	ρ_m	1350	kg/m ³
Internal friction angle	φ	40	°

3.3.1 Forces on the draghead

3.3.1.1 Gravity- and drag force

The gravity- and drag force working on the draghead are determined in chapter 2 and are included in the resultant force $F_{c,v,draghead}$. The influence of the gravity force on the visor is included in the force balance of the visor in chapter 5. The results will be used in the total force balance in the end of this paragraph. The drag force on the visor house is depending of the trailing velocity. Here the gravity forces are shown for an indication of their magnitude:

$$F_{g,visorhouse} = 39.01 [kN] \quad (\text{eq. 121})$$

$$F_{g,visor} = 15.46 [kN] \quad (\text{eq. 122})$$

3.3.1.2 Jet force

The jet force can be calculated with the results from chapter 4. There, the working point of the jet pump is determined which results in a jet exit velocity needed for the calculation of the jet force. In the case of a Damen draghead, the jet force is directed purely vertical upwards when the lower suction pipe angle is 45 degrees.

$$F_j = \rho_w * A_n * u_0^2 * n_n \quad (\text{eq. 123})$$

In the SLK600 there are 8 nozzles installed with a diameter of 48 mm. The jet exit velocity, u_0 is equal to:

$$F_j = 1025 * \frac{\pi}{4} * 0.048^2 * 38.95^2 * 8 = 22.51 [kN] \quad (\text{eq. 124})$$

3.3.1.3 Impulse force bends

The impulse force in the bend of the draghead visor house results from the mixture flow in the pipe. So far, the production of the draghead is not exactly known yet but will be determined in chapter 5. A first estimate is used for the calculation of the impulse force. The mixture flow speed, v_m , is set to 5 m/s and the mixture density is 1350 kg/m³. The inner pipe diameter of the suction tube, D_i , is 0.6 m. The angle of redirection of the flow (see Figure 46) is equal to:

$$\beta_{bend,visor} = 180 - \alpha_2 = 180 - 45 = 135^\circ \quad (\text{eq. 125})$$

The impulse forces in the **draghead bend** becomes:

$$\begin{aligned} F_{imp,bend,visor,h} &= \rho_m * A_{pipe} * v_m^2 * (1 - \cos(\beta_{bend,visor})) \\ &= 1350 * \pi * \left(\frac{0.6}{2}\right)^2 * 5^2 * (1 - \cos(135)) = 16.29 [kN] \end{aligned} \quad (\text{eq. 126})$$

$$\begin{aligned} F_{imp,bend,visor,v} &= \rho_m * A_{pipe} * v_m^2 * \sin(\beta_{bend,visor}) = 1350 * \pi * \left(\frac{0.6}{2}\right)^2 * 5^2 * \sin(135) \\ &= 6.75 [kN] \end{aligned} \quad (\text{eq. 127})$$

$$F_{imp,bend,visor} = \sqrt{F_{imp,bend,visor,h}^2 + F_{imp,bend,visor,v}^2} = \sqrt{16.29^2 + 6.75^2} = 17.63 [kN] \quad (\text{eq. 128})$$

The angle of the direction of the impulse force on the visor is:

$$\tan^{-1}\left(\frac{F_{imp,bend,visor,v}}{F_{imp,bend,visor,h}}\right) = \tan^{-1}\left(\frac{6.75}{16.29}\right) = 22.51^\circ \quad (\text{eq. 129})$$

The impulse force in the **jet pipe bend** results from the jet flow in the jet pipe. The jet flow, u_2 , in the working point is equal to the jet discharge, Q_j , divided by the jet pipe surface area:

$$u_2 = \frac{Q_j}{A_{jet,pipe}} = \frac{0.4793}{0.0755} = 6.35 \text{ [m/s]} \quad (\text{eq. 130})$$

$$\beta_{bend,jet} = \alpha_2 = 45^\circ \quad (\text{eq. 131})$$

$$\begin{aligned} F_{imp,bend,jet,h} &= \rho_w * A_{jetpipe} * u_2^2 * (1 - \cos(\beta_{bend,jet})) \\ &= 1025 * \pi * \left(\frac{0.31}{2}\right)^2 * 6.35^2 * (1 - \cos(45)) = 0.91 \text{ [kN]} \end{aligned} \quad (\text{eq. 132})$$

$$F_{imp,bend,jet,v} = \rho_w * A_{jetpipe} * u_2^2 * \sin(\beta_{bend,jet}) = 1025 * \left(\frac{0.31}{2}\right)^2 * 6.35^2 * \sin(45) = 2.21 \text{ [kN]} \quad (\text{eq. 133})$$

$$F_{imp,bend,jet} = \sqrt{F_{imp,bend,jet,h}^2 + F_{imp,bend,jet,v}^2} = \sqrt{0.91^2 + 2.21^2} = 2.39 \text{ [kN]} \quad (\text{eq. 134})$$

The angle of the direction of the impulse force in the jet pipe bend is:

$$\tan^{-1}\left(\frac{F_{imp,bend,jet,v}}{F_{imp,bend,jet,h}}\right) = \tan^{-1}\left(\frac{2.21}{0.91}\right) = 67.62^\circ \quad (\text{eq. 135})$$

3.3.1.4 Vacuum force

The vacuum force is working on the visor and its relation with the trailing velocity will be described in chapter 5 in subsection 5.3.1.2. The vacuum force is assumed constant:

$$F_{N,vac} = 89.41 \text{ [kN]} \quad (\text{eq. 136})$$

3.3.1.5 Sled force

When the draghead is in equilibrium, the draghead will not settle any further. In that case, the normal force on the draghead, $F_{sled,N,draghead}$, equals the resultant force Q which can be derived from the draghead equilibrium. The moment around point B can be used to derive the sled force on the draghead. Except for $F_{fric,draghead}$ and $F_{c,soil}$, all the forces indicated in Figure 55 are included in the moment equation. The friction force is not included because it is in line with the lever arm. Because the length of the lower suction pipe is long, relative to the distances where the forces apply on the draghead, assumed is that all the forces working on the draghead apply in the same point, C.

By using the resultant force of the suction pipe equilibrium without soil reaction forces, the dragforces, gravity force and cable force of the suction pipe and draghead can be replaced by $F_{c,draghead,v}$ (calculated in chapter 2). The new moment around B becomes (see Figure 56):

$$\begin{aligned} \sum M_B = 0 &= -F_{sled,N,draghead} * l_2 - (F_{c,visor,h} + F_{imp,bend,visor,h} + F_{imp,bend,jet,h}) * l_2 * \sin(\alpha_2) \\ &+ (F_{c,draghead,v} - F_{jet} + F_{c,visor,v} - F_{imp,bend,visor,v} - F_{imp,bend,jet,v}) * l_2 * \cos(\alpha_2) \end{aligned} \quad (\text{eq. 137})$$

By rewriting follows:

$$\begin{aligned} F_{sled,N,draghead} &= -(F_{c,visor,h} + F_{imp,bend,visor,h} + F_{imp,bend,jet,h}) * \sin(\alpha_2) \\ &+ (F_{c,draghead,v} - F_{jet} + F_{c,visor,v} - F_{imp,bend,visor,v} - F_{imp,bend,jet,v}) * \cos(\alpha_2) = Q \end{aligned} \quad (\text{eq. 138})$$

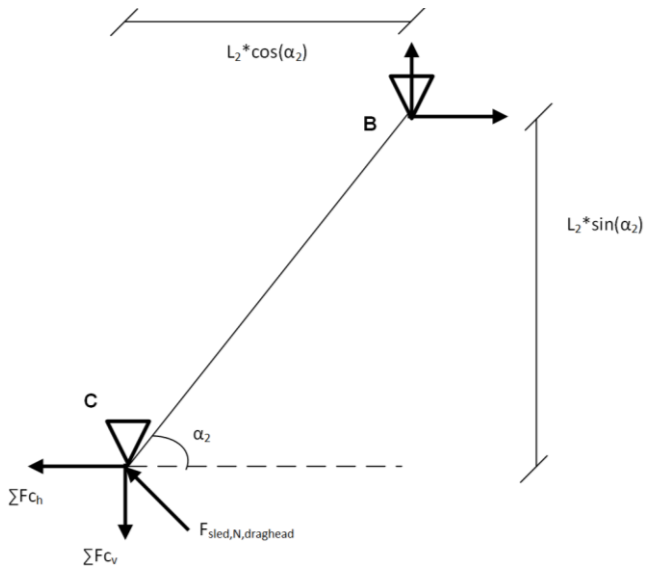


Figure 56: Moment around B for determination of F_{sled}

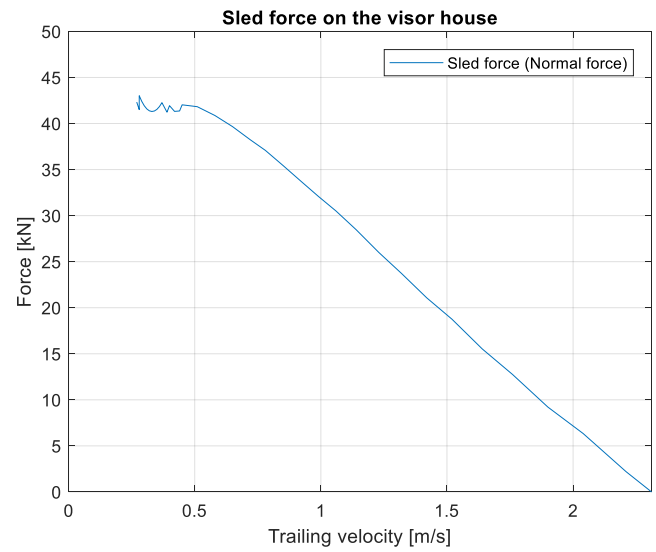


Figure 57: Sled force versus the trailing velocity

In the graph of Figure 57, the sled force is plotted against the trailing velocity. The sled force becomes zero, because of the reason that the drag forces and soil excavation force rise for increasing trailing velocities. The draghead is lifted upwards for a trailing velocity of 2.3 m/s, as seen earlier in chapter 2.

The settlement of the draghead can now be determined with:

$$h_{i, \text{settle}} = \sqrt{\frac{2 * Q * \sin(\alpha_2)}{W_{\text{support}} * q_{\text{soil}} * g}} = \sqrt{\frac{2 * Q * \sin(45)}{2.09 * 6 * 9.81}} \text{ [m]} \quad (\text{eq. 139})$$

The settlement of the draghead versus the trailing velocity is shown in Figure 58.

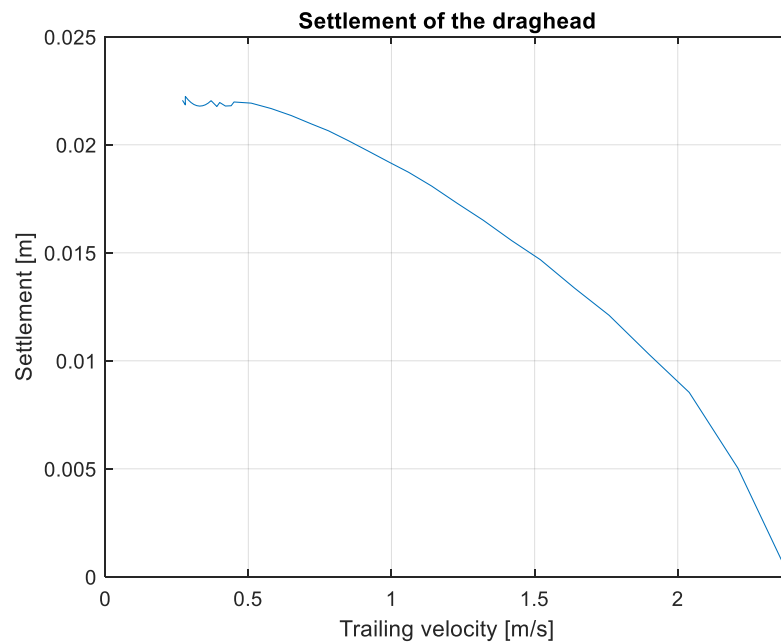


Figure 58: Settlement of the draghead versus the trailing velocity

Wedge forming:

From an image, taken out of a video recording during trailing, can be seen that in front of the draghead a hump of sand is present. This phenomenon is called bulldozing and is present because, wedge forming occurs due to settlement of the draghead and because the draghead is moving forwards. This results in a continuous supply of sand that is pushed forwards. In the calculations of the sled force, this effect is neglected because there is assumed that the soil is compacted and therefore no wedge forming and bulldozing occurs. The reason why there is chosen for the compaction method is because no iteration has to be performed which leads to a simplification of the calculation.



Figure 59: Image of a video recording of working draghead at 1.3 knots (0.67 m/s), lower suction pipe angle 45°

Like the pore pressure model for cutting with small blade angles, Miedema also developed a pore pressure model for the calculation of cutting with large blade angles. In the case of cutting with large blade angles wedge forming occurs. Here the wedge acts as a pseudo blade (Miedema, The Delft Sand, Clay and Rock Cutting Model, 2014). The forces on the blade, so in this case: the draghead housing, can again be determined by the change in pore water pressure in the shear zones. However, to be able to determine the forces with the wedge pore pressure model, the thickness of the cutting layer (in this case $h_{i, \text{settle}}$) needs to be known.

The force, $F_{\text{sled}, N, \text{draghead}}$, to keep the draghead in equilibrium, is known from the previous calculation. So, by equating the wedge cutting force to the sled force, the thickness of the cutting layer can be found by iteration. The settlement of the draghead will then be equal to the cutting layer. A recommendation is to implement this method into an improved version of the calculations in future research.

Saturated sand will shear as the shear type shown in Figure 60. In Figure 61 is the top view of the draghead shown where the flow of sand towards the sides is indicated. The video analysis shows that for low trailing velocities the forward moving 'hump' of sand is collapsing when approximately the internal friction angle is reached.

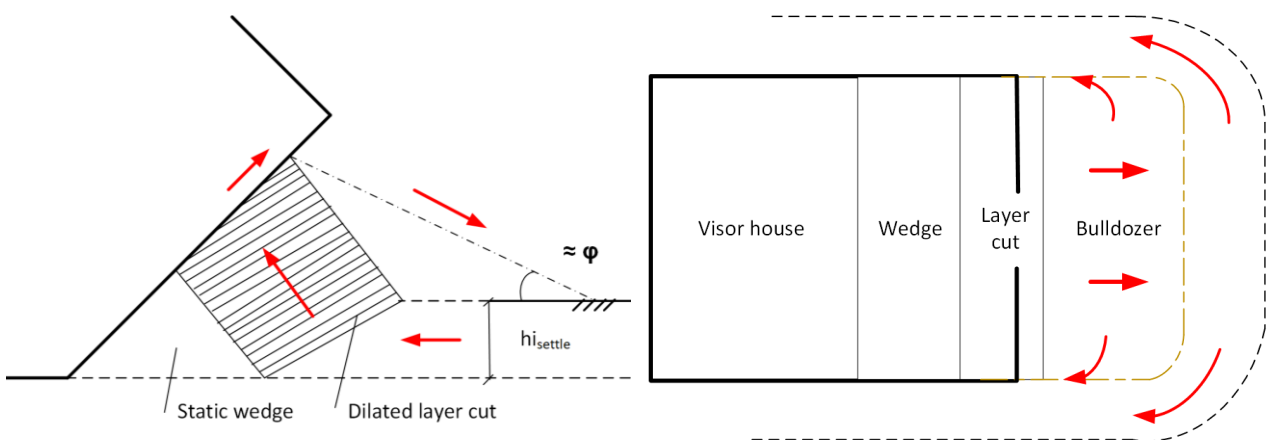


Figure 60: Wedge cutting process with flow lines; side view Figure 61: Wedge cutting process with flow lines; top view

3.3.1.6 Friction force

The friction force arises from the friction between the visor house and the bed. The friction force is dependent of the external friction angle as shown below:

$$\mu = \tan(27) = 0.51 \quad (\text{eq. 140})$$

$$F_{fric} = 0.51 * F_{sled,N,draghead} [kN] \quad (\text{eq. 141})$$

The friction force can be decomposed in:

$$F_{fric,h} = F_{fric} * \cos(\alpha_2) = F_{fric} * \cos(45) [kN] \quad (\text{eq. 142})$$

$$F_{fric,v} = F_{fric} * \sin(\alpha_2) = F_{fric} * \sin(45) [kN] \quad (\text{eq. 143})$$

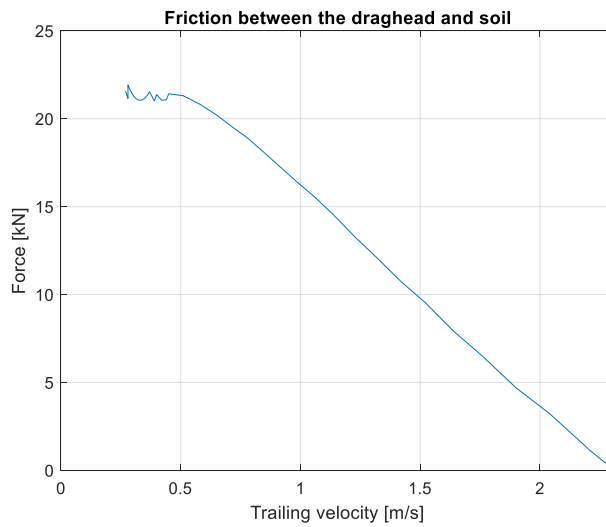


Figure 62: Friction force visor house versus the trailing velocity

3.3.1.7 Cutting force

In the case study, the visor is freely suspended so the visor angle, γ , changes constantly due to the changing forces on the visor. The cutting teeth are positioned under a fixed angle, γ_2 , in the visor so the blade angle changes too. When the visor is allowed to move, the cutting layer thickness, $h_{i,cut}$ can be determined iteratively with the momentum balance around the visor hinge. This is shown in chapter 5. But first, the cutting force for a fixed visor is explained with the pore pressure model of Miedema. The schematisation of the fixed visor is shown in Figure 63 below.

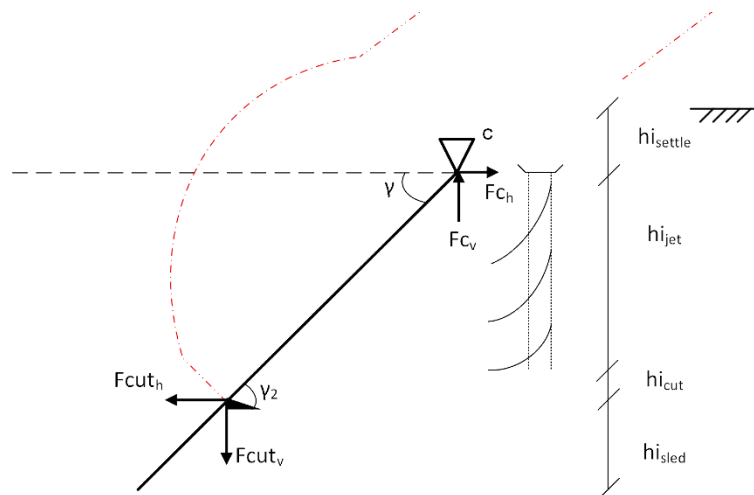


Figure 63: Visor under a fixed visor angle, γ

The issue with a fixed visor is easy to explain with the aid of Figure 63. The jets are positioned in front of the visor and fluidize the sand to a thickness, $h_{i,jet}$. The jet layer thickness is strongly dependent on factors such as the trailing velocity, soil characteristics and jet configurations (Wegenaar, 2014). This is explained in detail in chapter 4. When the jets penetrate to deep, they will spray underneath the visor. Because the visor is fixed, it cannot adjust the visor angle to be able to bring the cutting teeth into the solid sand layer again. The consequence may be that no layer is cut and a lot of jet production spillage and pressure loss occurs. When the jets do not penetrate deeper than the cutting teeth, the teeth will excavate a cutting layer equal to, $h_{i,cut}$. This cutting layer thickness is then dependent on the variable jet layer.

To simplify the cutting force calculation with the pore pressure model, here, it is assumed that the jets do not have an effect on the cutting layer thickness so the cutting layer thickness is assumed constant and equal to $h_b = 0.1 \text{ m}$, with a visor angle fixed under an angle of, $\gamma = 20^\circ$. The blade height, h_b , is dependent on the blade angle, $\alpha_{blade} = \gamma_2 - \gamma$, and blade length, $l_b = 0.128 \text{ m}$. When the cutting teeth in the SLK600 are positioned under an angle of $\gamma_2 = 45^\circ$. The blade height becomes:

$$h_b = l_b * \sin(\alpha_{blade}) = l_b * \sin(\gamma_2 - \gamma) = 0.128 * \sin(45 - 20) = 0.054 \text{ [m]} \quad (\text{eq. 144})$$

With the pore pressure model described in 3.2.3.7, the pore pressure and dimensionless pore pressure in the shear plane and on the blade can be calculated. The results are shown in Figure 64 and Figure 65.

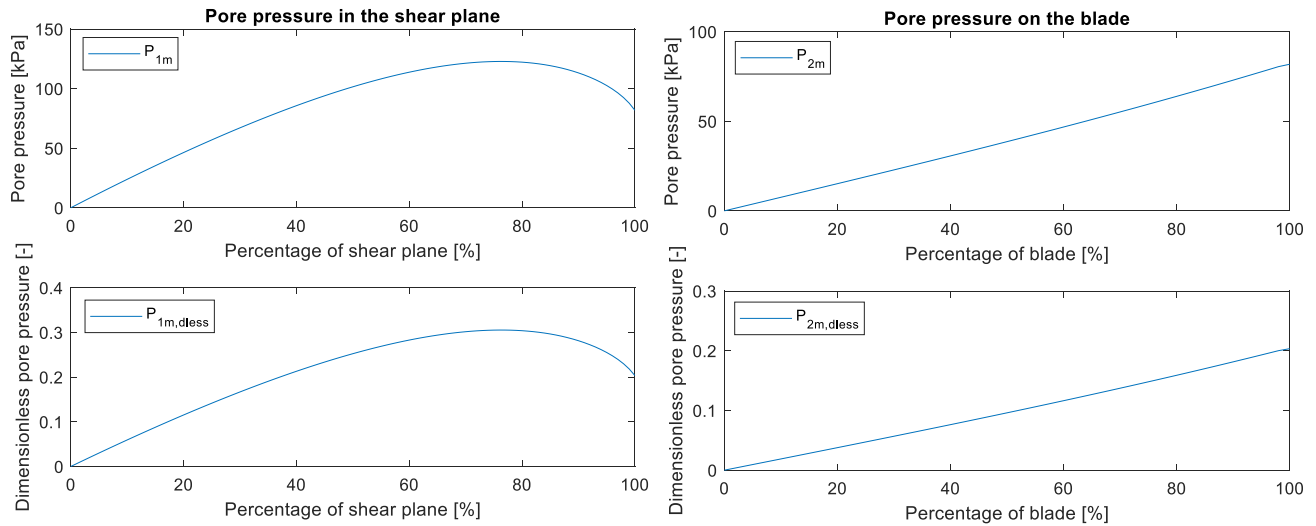


Figure 64: The pore pressure and dimensionless pore pressure **in the shear plane** for a trailing velocity of 1.5 m/s

Figure 65: The pore pressure and dimensionless pore pressure **on the blade** for a trailing velocity of 1.5 m/s

The dimensionless cutting forces, c_1 , c_2 , d_1 and d_2 , can now be determined with equations 115 - 118. The results show that the dimensionless pore pressure is constant with the trailing velocity. This means the dimensionless cutting force is also independent of the trailing velocity and constant:

$$c_1 = 0.2283, c_2 = 0.1379, d_1 = 2.7010, d_2 = 1.8441$$

The cutting force can now be calculated with equation 113 and 114 and the results are shown in Figure 76 and Figure 77. Where w is the total width of the cutting teeth which is equal to $w = w_{teeth} * n_{teeth} = 0.109 * 10 = 1.09 \text{ m}$. This shows that the cutting force increases linear with the trailing velocity, until a certain trailing velocity is reached where the cutting process switches from non-cavitating to cavitating cutting. The cavitating cutting velocity can be calculated with the equation below, derived by Miedema (Miedema, The Delft Sand, Clay and Rock Cutting Model, 2014):

$$v_c = \frac{d_1 * (z + 10) * k_m}{c_1 * h_i * \varepsilon} = \frac{2.7010 * (18.32 + 10) * 2.5 * 10^{-4}}{0.2283 * 0.1 * 0.12} = 7 \text{ [m/s]} \quad (\text{eq. 145})$$

In this case the cavitating cutting process is far beyond common trailing velocities. As soon as the horizontal- or vertical cutting process starts cavitating, the cavitating cutting velocity is set. Here, the horizontal cutting force

starts cavitating at a lower trailing velocity, so the vertical cutting force actually has to be adjusted and will be constant from 6.7 m/s as shown in Figure 66.

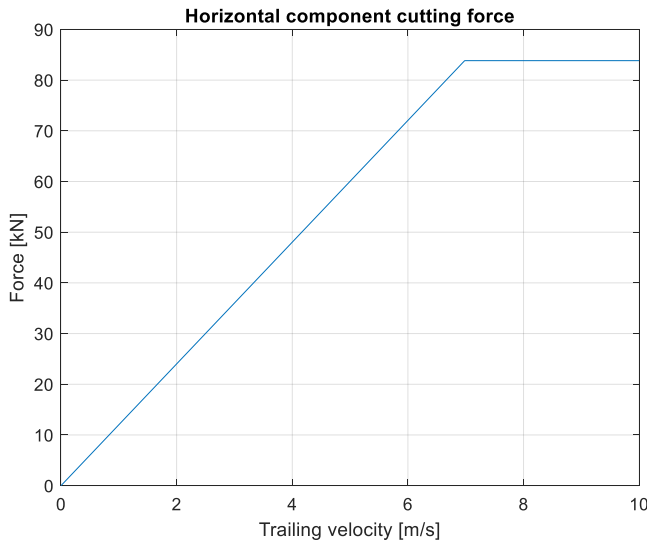


Figure 66: The horizontal cutting force versus the trailing velocity for a fixed cutting layer of 0.1 m

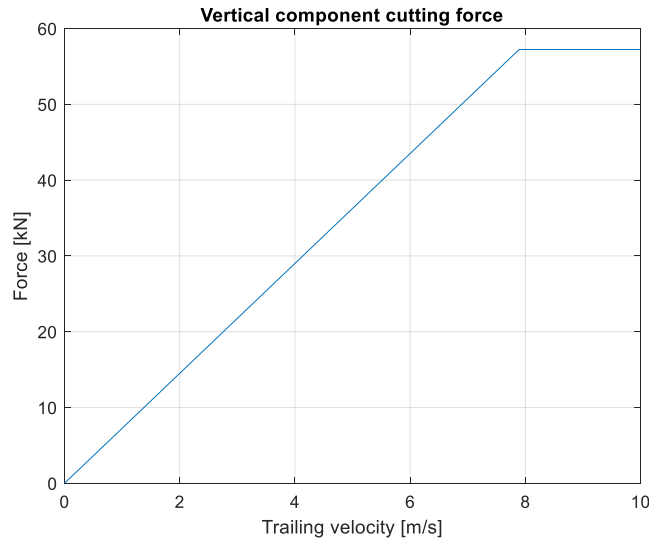


Figure 67: The vertical cutting force versus the trailing velocity for a fixed cutting layer of 0.1 m

3.3.2 Total force balance

All the forces on the visor house are now determined, except for the variable visor forces, $F_{c,visor,h}$ and $F_{c,visor,v}$ which will be substituted in here from chapter 5. With that the resulting force which ‘transfers’ the soil excavation forces, $F_{c,soil,h}$ and $F_{c,soil,v}$ can be calculated. This force was already illustrated in Figure 55. As was assumed in chapter 2 do all forces on the draghead apply in point C. In Figure 68 the directions of the forces are given which results in the equations 146 - 149.

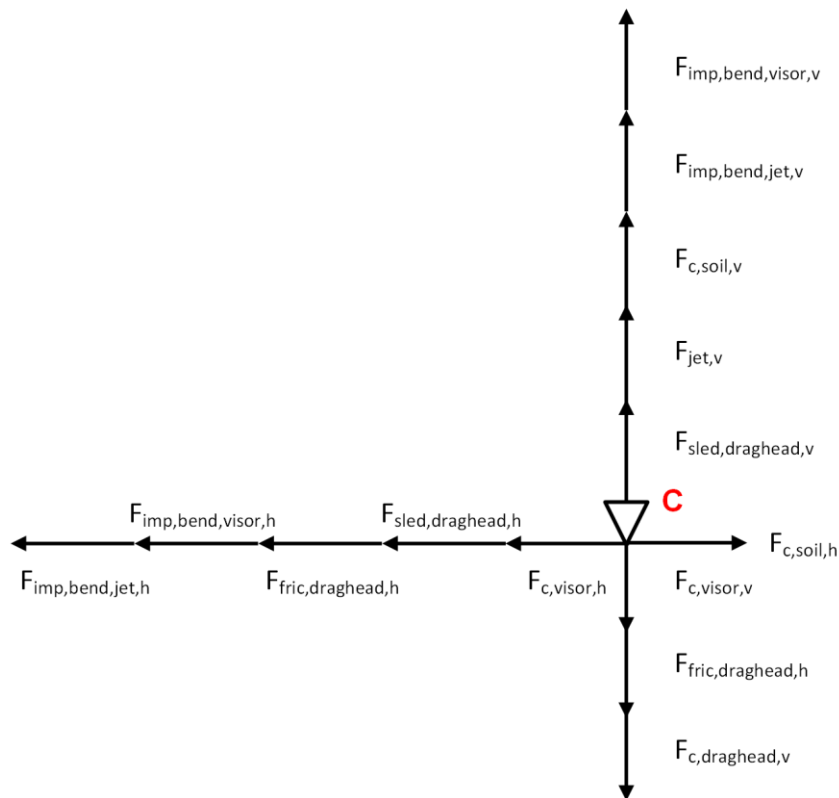


Figure 68: Force direction overview of the draghead

Here, the resultant force of the soil forces in point C are given from the new force equilibrium of the draghead which includes the soil reaction forces:

$$\sum F_{h,draghead} = -F_{c,visor,h} - F_{fric,draghead,h} - F_{sled,draghead,h} + F_{c,soil,h} - F_{imp,bend,visor,h} - F_{imp,bend,jet,h} \quad (\text{eq. 146})$$

$$\sum F_{v,draghead} = 0 = F_{jet} - F_{c,visor,v} - F_{fric,draghead,v} + F_{sled,draghead,v} + F_{c,soil,v} + F_{imp,bend,visor,v} + F_{imp,bend,jet,v} - F_{c,draghead,v} \quad (\text{eq. 147})$$

$$F_{c,soil,h} = F_{c,visor,h} + F_{fric,draghead,h} + F_{sled,draghead,h} + F_{imp,bend,visor,h} + F_{imp,bend,jet,h} \quad (\text{eq. 148})$$

$$F_{c,soil,v} = -F_{jet} + F_{c,visor,v} + F_{fric,draghead,v} - F_{sled,draghead,v} - F_{imp,bend,visor,v} - F_{imp,bend,jet,v} + F_{c,draghead,v} \quad (\text{eq. 149})$$

The results for the soil excavation forces are shown in Figure 69. The figure shows that the soil excavation forces increase with the trailing velocity. For a trailing velocity larger than 2.3 m/s the draghead will lift off and the above described situation is not valid anymore because the angle of the suction pipe will change and new equilibrium conditions have to be determined.

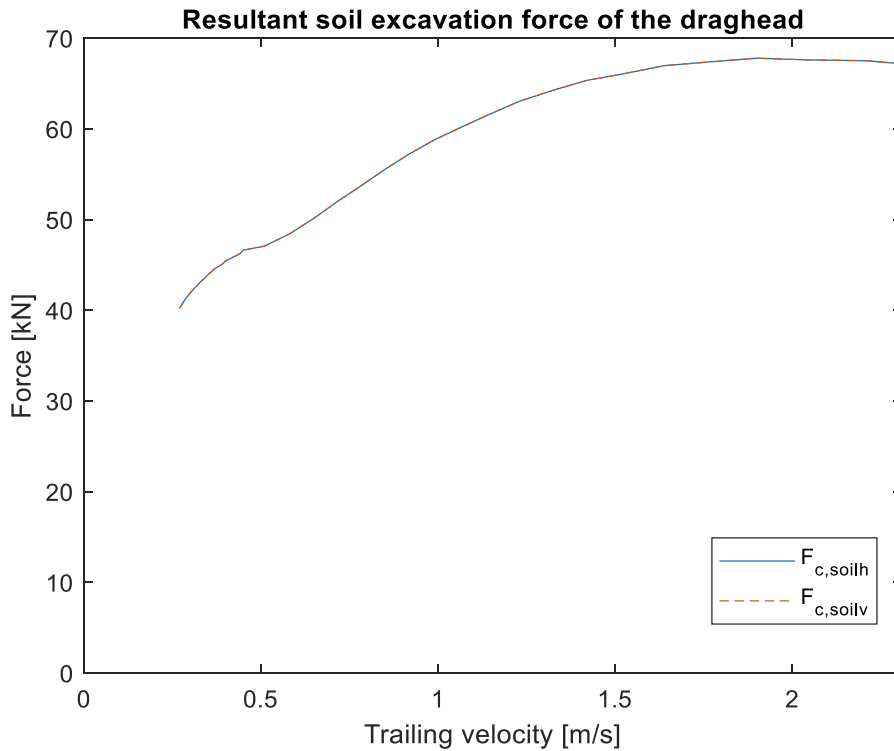


Figure 69: Soil excavation force versus the trailing velocity for a free hanging visor with variable layer thicknesses

Important to mention is that for the calculation of the total soil excavation forces on the draghead, the free hanging visor determined in chapter 5 is used with variable layer thicknesses, with its corresponding excavation forces, and not the previous cutting forces calculated with a fixed layer thickness in 3.3.1.7. The results for trailing velocities of 0 – 0.27 m/s are missing due to the angle of the visor that is limited to 60 degrees and at this trailing velocity, the jet penetration depth is so deep, the jet underneath the visor. This is described in more detail in chapter 5.

3.4 Optimization & Verification

3.4.1 Accuracy cutting forces

In the 'Delft Sand, Clay & Rock Cutting model', Miedema describes the accuracy of the analytical/numerical pore pressure model. The accuracy of the output of a model is strongly dependent on the input. Because the sand properties often vary and are difficult to determine, the input can be inaccurate. *"The accuracy of less than 10% of the analytical method described here is small with regard to the accuracy of the input. This does not mean however that the accuracy is not important, but this method can be applied for a quick first estimate."*

More detailed verification and validation of the pore pressure model is stated in: (Miedema, The Delft Sand, Clay and Rock Cutting Model, 2014).

3.4.2 Verification soil compaction force

To determine the sled forces and settlement of the draghead, the sled compaction method was applied. In the case study a heavy settled soil was used with a specific compaction force, q_{soil} , of 6 kg/cm^3 , but this is a very inaccurate assumption. In 'Agriculture Soil Mechanics' is the soil compaction force for different soils given (Koolen & Kuipers, 1983). The typical values for the different compactions are stated in Table 8. To verify if the specific compaction force has a big influence on the trailing forces and the settlement of the draghead, a small study is performed for two extreme values.

Table 8: Values for the specific compaction force, q_{soil} , [kg/cm^3]. Source: (Koolen & Kuipers, 1983)

Loose soil	Settled medium soil	Settled heavy soil
0.5-1.5 kg/cm^3	3-8 kg/cm^3	6-10 kg/cm^3

For a value of 4 and 8 kg/cm^3 the trailing forces and settlement are reviewed. The results are shown in figure Figure 70 to Figure 73.

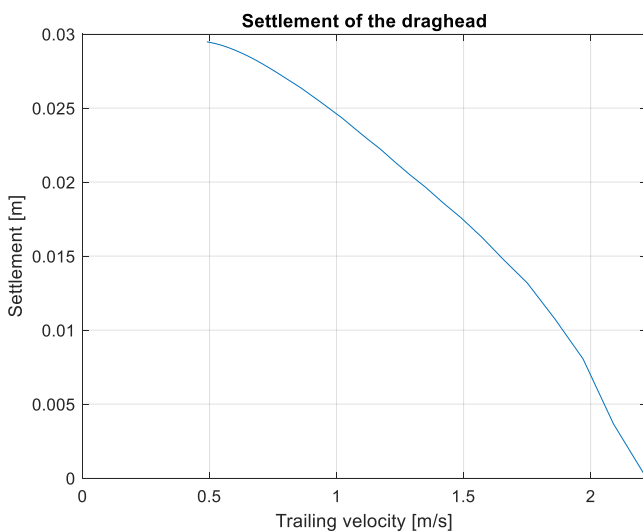


Figure 70: Settlement of the draghead versus the trailing velocity, $q_{soil} = 4 \text{ kg/cm}^3$

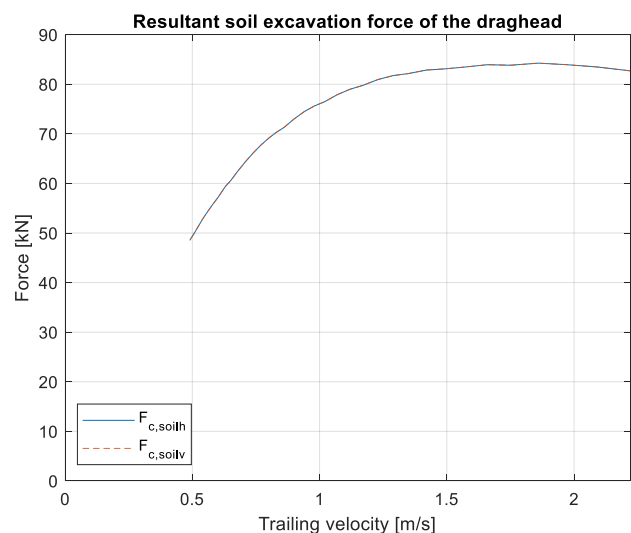


Figure 71: Soil excavation force versus the trailing velocity, $q_{soil} = 4 \text{ kg/cm}^3$

For a specific compaction force of 4 kg/cm^3 the settlement is deeper, relative to the settlement of 6 kg/cm^3 , because the bearing capacity of the soil is lower. As a result the soil excavation force increases significantly. Not only the visor house will settle deeper, the free hanging visor will also find another, deeper equilibrium position. Another observation is that the draghead will lift off from the bed at a lower trailing velocity because especially the horizontal component causes a large moment around B (cardan hinge) pushing the draghead upwards.

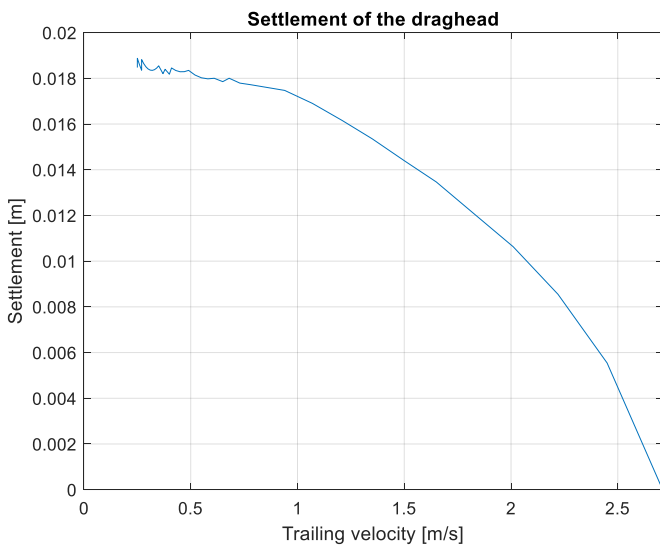


Figure 72: Settlement of the draghead versus the trailing velocity, $q_{soil} = 8 \text{ kg/cm}^3$

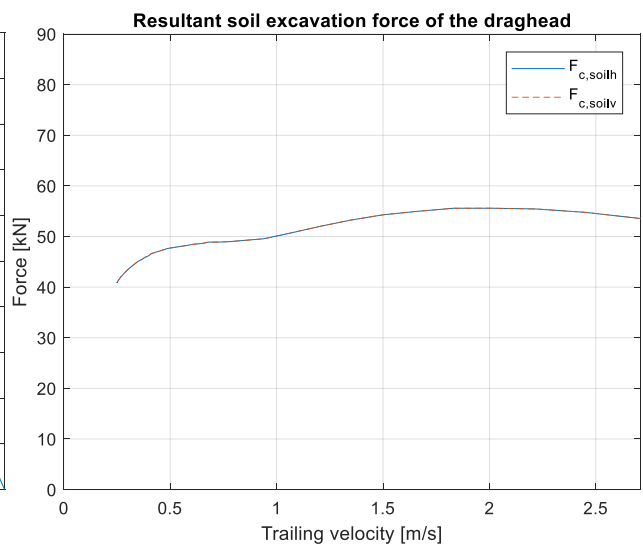


Figure 73: Soil excavation force versus the trailing velocity, $q_{soil} = 8 \text{ kg/cm}^3$

For a specific compaction force of 8 kg/cm^3 the opposite can be observed, the settlement is less deep, and the soil excavation forces decreases relative to the results of 6 kg/cm^3 . And because the soil excavation forces are lower, the draghead is lifting off at a higher trailing velocity.

Decreasing the bulldozer angle

The results for the different soil compaction values show large differences in the settlement and soil excavating forces. It can be stated that the sled forces are dominant in the excavating process. As is written in 3.3.1.5, the soil compaction method is a simplification of what is actually happening at the bed. A recommendation is to improve the sled theory and validate the observations of this model with scale tests.

If the trend observed in the results is plausible, the sled forces could potentially be decreased in different ways:

- Lowering the bulldozer angle; this could result in a smaller horizontal sled force component. The sled force will cause a smaller moment around point B.
- Increase the support area of the visor house; a larger support area could result in a smaller settlement of the visor house and so again smaller resulting horizontal sled forces. The draghead will probably be trailed more over the bed instead of through the bed.

3.5 Conclusion

The purpose of this chapter was to analyse the draghead and to map all the relevant forces working on the draghead. Because the draghead settles, due to the weight of the suction pipe and the draghead itself, it pushes a hump of sand in front of the visor house at a forward speed. This results in a sled force and a friction force on the draghead's visor house. The jet flow and production flow through the pipes result in an impulse force in the bends and at the end of the jet pipe out of the nozzles. The freely suspended visor will sink into the fluidised jet layer until a balance is found. The vacuum force and gravitational force push the visor against the bed while the cutting forces and sled forces push the visor upwards.

Due to strongly increasing trailing forces on the draghead for increasing trailing velocities, mainly due to the cutting force, the force distribution on the draghead changes continuously. The sled and friction force therefore decreases. Furthermore, the results show that the soil reaction forces due to direct contact with the soil and the vacuum force, are the dominant forces at conventional trailing velocities of 0.5 – 2 m/s. The other forces working on the draghead remain almost constant and are not, or to a lesser extent, dependent on the soil characteristics and trailing velocity.

The difference in the magnitude of the sled force, calculated by varying the specific compaction force, changes the total soil excavation force tremendously. This shows the influence of the soil characteristics. Therefore, more extensive research into the sled force must determine whether the specific compaction method gives a good approximation.

4 Jetting production

Jetting is a technique that is used to loosen the compact structure of the sand layer. By forcing water under high pressure and flow velocity into the bed, the sand structure is broken, and the density of the situ soil is lowered. In this way, the diluted mixture can be transported upwards by the dredge pump more easily. This process is visualized schematically in Figure 74. Secondly, jetting reduces the trailing forces while cutting (Jong, 1988). The cutting forces on the draghead are lowered by decreasing the under pressure in the shear zone of the cutting teeth. While cavitating cutting forces are dependent on depth, jet pressure is not. Therefore, dredging with jets can be more energy efficient than dredging with solely cutters, especially at higher depths (Miedema, The Delft Sand, Clay and Rock Cutting Model, 2014). Ideally, the jet penetration depth is equal to the cutting depth, because spillage of jet momentum and situ soil production occurs at lower depths.

The purpose of this chapter is to investigate the influence of the jets on the draghead forces and the production. The jets are the first contribution to the total production, being placed in front of the draghead. Also, the jets will change the composition of the soil and therefore change the behaviour of the visor, which is placed behind the jets. All the calculations are integrated into a jet model to investigate the influence of all involved variables on the jet production. The model is used to perform an optimization to find the most productive jet draghead design.

The subjects related to jetting are described step by step in the literature, which can be found in the first paragraph. The theory is used and extended throughout the rest of the chapter. Some formulas are assumed to be known, others will be explained shortly or a reference is made to the appendix. In the dredging industry a lot of research about jetting has been performed but less is published by the contractors. Nevertheless, some valuable theory is available and gathered from research at academic institutions over the years.

In the second paragraph the model description is explained and starts with the working principle of the jet pump. This is integrated into the model to find realistic operating values for the jet pressure and jet discharge. In the end of this chapter, this relation is used to see the effect of the nozzle diameter on the jet production and the mixture density. With the operating values for the jet pressure and jet discharge the calculation for the penetration depth and cavity width are performed. These variables are the input for the final jet production estimation.

The jet production is simply the product of the penetration depth, the cavity width and the trailing velocity. The penetration depth and cavity width depend on several variables which makes them complex to predict. Different theories to estimate the penetration depth are compared with each other to find the most precise estimation. As in the rest of the report is the relation with the trailing velocity extra highlighted. The trail velocity is an important factor for the duration the jet flow is able to penetrate the soil, because a higher trailing velocity results in a lower jet momentum per travelled distance (Rhee, Lecture notes Dredging Processes 2 [OE4727], 2016). The penetration depth will decrease when the trail velocity increases and so certainly has an effect (Miedema, Introduction to Dredging Engineering [OE4607], 2016). A similar relation should be found for the cavity width.

The total jet volume flux which exist of the jet water discharge and the excavated situ soil by the jets is a substantial part of the total production flux for the final determination of the mixture density and total production. Therefore, this chapter will be used as input for the total production determination in chapter 5.

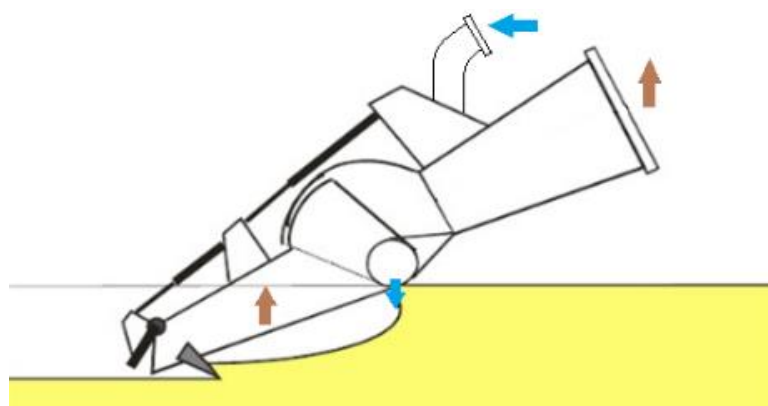


Figure 74: Jetting flow visualization. The blue arrows indicate the jet flow, brown arrows the soil mixture flow. Source: (Vlasblom, 2006) modified.

Notation

Latin		
A_j	Jet pipe surface	m ²
A_n	Nozzle surface	m ²
c_1	Dimensionless cutting force	-
c_d	Jet discharge coefficient	-
D_j	Jet diameter	m
D_n	Nozzle diameter	m
E_{sp}	Specific energy	Pa
f	Approximation factor	-
f_d	Friction factor	-
F_j	Jet force	N
g	Gravity constant	m/s ²
H, H_D	Head, Design head	Pa
Δh_1	Geodetic height difference jet pressure sensor and water level	m
Δh_2	Geodetic height difference jet chamber and nozzle exit	m
$h_{i,jet}$	Layer thickness excavated by jet	m
I_f	Hydraulic gradient	-
I	Jet momentum	kg/s
k_1, k_2	Entrainment coefficient	-
k_i, k_m, k	Initial permeability, mean permeability, permeability	m/s
L	Jet pipe length	m
M_s	Mass flux	kg/s
n_n	Number of nozzles	-
n_o, n_{max}	Initial porosity, maximum porosity	-
Δp	Jet pressure over nozzle	Pa
p_0	Relative ambient fluid pressure	Pa
p_1	Jet chamber pressure	Pa
p_2, p_j	Jet pressure	Pa
P_j	Jet power	W
$P_{nozzle,loss}$	Pressure loss due to contraction	Pa
$P_{pipe,loss}$	Pressure loss due to friction	Pa
$Q, Q_D, Q_s, Q_j, Q_w, Q_{tot}$	Discharge, design jet discharge, sand production, Jet discharge, Water production, total production	m ³ /s
Re	Reynolds number	-
R_{rel}	Relative roughness	-
r	Radial distance from the centreline	m
s	Distance from the nozzle	m
u_0	Nozzle exit velocity	m/s
u_1	Jet chamber velocity	m/s
u_2	Jet pipe velocity	m/s
$u_{s,r}$	Jet velocity in axial direction	m/s
v_c	Cutting velocity	m/s
v_t	Trailing velocity	m/s
w, w_{in}, w_{out}, w_e	Width draghead, Inside width visor, outside width visor, width outer nozzle to visor edge	m
$w_c, w_{c,max}$	Cavity width, maximum cavity width	m
Greek		
α	Suction pipe angle	°
ε	Surface roughness, dilatancy	m, -
ρ_m	Mixture density	kg/m ³
ρ_w	Water density	kg/m ³
ν	Kinematic viscosity	m ² /s

4.1 Literature

A lot of research has been done into the working principle of the jet and the interaction between a jet and the sand bed. In this paragraph, an overview is made of used literature and reference studies where in particular the studies of (Wegenaar, 2014) and (Jong, 1988), as last described in this paragraph, are important references and good comparison material for the jetting model in this chapter.

To start with van Rhee's lecture notes (Rhee, Lecture notes Dredging Processes 2 [OE4727], 2016) in which he bundled the basic theory about jetting. In this lecture note, he describes the working principle of the jet (appendix 8.3.1). Besides that, he shows in a simplistic way how the nozzle discharge and jet velocity depend on the jet pressure with the help of the law of Bernoulli. The derivations and the assumption that are made are summarized in appendix 8.3.2.

Cavitation plays a role when the jet pressure drops to below the vapor pressure. Nobel found experimentally found a cavitation number to calculate the turning point from a non-cavitating jet to a cavitating jet (appendix: 8.3.3) (Nobel, 2013). Jet cavitation occurs at small scale laboratory setups more often but is less of an issue for jetting in practice, at larger water depths. Nevertheless, a calculation check has been built into the model to detect whether cavitation will occur during excavation with jetting.

During jetting in sand, not only water but also sand particles are entrained in the flow. The jet flow diverges in a same way as in water, but the entrainment of sand is more difficult because of the small permeability (appendix: 8.3.4). Especially with low porosity sands where, due to the effect of high speed erosion, jetting becomes less effective (Rhee, Lecture notes Dredging Processes 2 [OE4727], 2016). This shows that the soil type has an effect on the performance of the jet.

To determine the penetration depth, in this research, two different approaches are used. The first one is van Rhee's derivation who is making use of the mass flux of the eroded sand production derived by Vlasblom. The jet production from Vlasblom is based on the momentum of the jet (Rhee, Lecture notes Dredging Processes 2 [OE4727], 2016). Miedema found a similar relation but, instead of the jet momentum, he uses the specific energy that is needed to excavate the soil by cutting, to determine the production of the jet and how deep the jets penetrate. For both formulas the cavity width is an unknown, where Miedema assumes a constant cavity width for a specific case.

There are two relevant studies which looked at the behaviour of a traversing jet over a sand bed using a scaled test set-up. Both studies tried to find a relation between the jet profile and a forward traversing velocity of the jet. Both studies and their methods are summarized here. Yeh performed practical tests with traversing jets, with the aim to find the influence of the outflow of cooling water beneath a ship on the bed (Yeh, 2008). They have worked with relatively large nozzle diameters and low flow velocities compared to the values used during jetting for dredging. The tests are performed with a jet velocity (u_0) of 1-2 m/s, a jet discharge (Q_j) of 0.013 m³/s and a traversing velocity (v_t) varying between 0-0.51 m/s. Therefore, this research is not that useful for verification but nevertheless gives some knowledge of traversing vertical jet streams. A result of their research is a relation for the penetration depth as a function of the velocity ratio between the jet velocity and the traversing velocity of the ship. Another result were derivations for hyperbolic functions to estimate the scour profiles of the jet. The findings were measured for the final scour profile after all the particles had settled. This is also less useful because the loosened particles will probably not settle but disappear straight into the suction pipe.

A research which was totally focused on the behaviour of a moving jet over a sand bed during dredging is performed by (Wegenaar, 2014). This research is very realistic because the values for the trail velocities and jet pressure are similar to those used in practice. Only the jet discharge and logically the nozzle diameter are downscaled to lower values to make the model test executable in a lab. The influence of the sand characteristics are observed by using different sand types. The variation in grain diameter of the sand types causes a difference in the porosity and permeability of the soil which resulted in other jet profiles. Below the input parameters are summed:

- Trail velocity 0.25, 0.5, 1 m/s
- Pressure 4, 6 and 8 bar
- Nozzle exit velocity 30-40 m/s
- Nozzle diameter 5, 7, 9 and 11 mm
- Different sand types (D50 of 0.28 and 0.14 mm, n of 0.4)

For this experiment Wegenaar has also written a model to estimate the penetration depth and the jet profile beforehand and without the settling of the particles. The model makes use of jet- and erosion theory and the calculations are based on a mass- and momentum flux balance for small consecutive elements. The model has also taking into account some sand characteristics like the particle size, the porosity and the permeability and is consequently a more realistic estimation than the penetration depth theory of Miedema (with the exception of the permeability) and Vlasblom who do not take any variation in soil type into account.

Last, but not least, P. de Jong used experimental jet profile data of van Rhee to find a relation between the penetration depth and the cavity width depending on the trailing velocity. He also estimated the jet production based on of the experimental results of van Rhee (Jong, 1988).

4.2 Model description

In this paragraph, the jet model is described. The model description is written in the same sequence as the model is build up. It is subdivided into three parts, where in the first part the jet pressure, jet discharge and jet velocity are calculated using the working principle of the pump. With these outcomes, the jet impulse for the force balance of the draghead can be determined. In the last part the penetration depth and cavity width are calculated, followed by the production and finally the density mixture of the jet production. The calculations are supported with theory from the literature and some extra formulas are added.

4.2.1 Calculation of the pump pressure, jet- velocity and discharge

The jet pump in a trailing suction hopper dredger is often a centrifugal pump. A centrifugal pump accelerates water by means of rotating movement of the impeller. Without going into too much detail on the working principle of the pump, it is important to mention what the output is of the pump is, to calculate the jet discharge and pressure over the nozzle.

A jet pump delivers for a certain number of rotations, a pressure and a belonging discharge. Assumed is that the pump system is in a steady state. This means that the concentration and the velocity of the jets are constant over time. When the pump curve is unknown, it can be determined by finding a few working points (Q,H). The working points can be found by slowly squeezing the discharge side of the pump (jet discharge will decrease). By connecting these working points in a curve fit, the pump curve is found. The pump curve can also be approached with eq. 150 to eq. 152 given by Miedema (Miedema, Introduction to Dredging Engineering [OE4607], 2016).

$$H = A + C * Q^2 \quad (\text{eq. 150})$$

$$A = f * H_D \quad (\text{eq. 151})$$

$$C = \frac{(1 - f) * H_D}{Q_D^2} \quad (\text{eq. 152})$$

Where H is the head of the pump in Pascal and Q is the jet discharge in m³/s. The values for the coefficients A and C can be found with the factor f times or divided by the design values for the head and discharge respectively. The factor f in this formula is typically between 1-1.5 [-]. A common value for the jet pressure is between 5-20 bar. The jet discharge differs more because it should be matched with the size of the draghead, the hopper volume and the dredge pump. In Figure 75, the pump curve is shown for a pressure design value of 8 bar, a jet discharge of 0.5 m³/s and a factor f of 1.05.

If it is also known what the dimensions and shape of the components behind the pump are, the working point of the pump can be determined. Before the fluid accelerates out of the nozzle, it is transported downwards by the jet pipe. The friction of the fluid with the inside of the pipe wall cause losses which can be expressed in a pressure drop. In addition to this friction, there are also losses due to constrictions and pipe bends in the jet system. These losses can also be expressed by a pressure loss and plotted in the same graph as Figure 75.

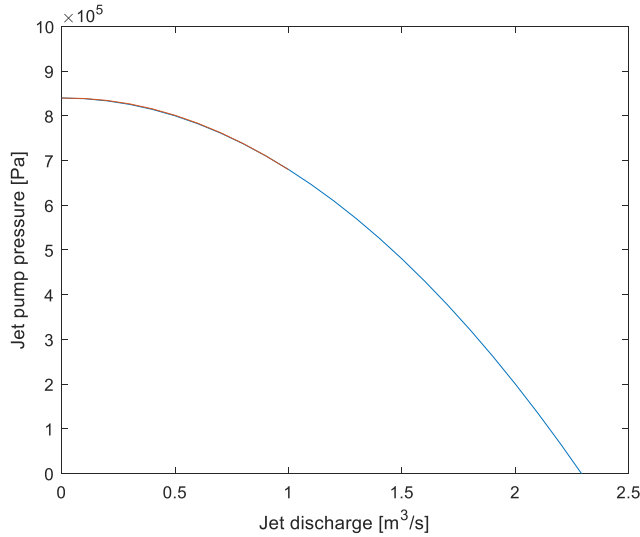


Figure 75: Pump head curve

The friction loss, caused by the friction between the water and the wall, can be calculated with Darcy-Weisbach and Moody. For this, in addition to the Reynolds number, the relative roughness is also required:

$$u_0 = \frac{Q_j}{A_j} \quad (\text{eq. 153})$$

$$Re = \frac{u_0 * D_j}{\nu} \quad (\text{eq. 154})$$

$$R_{rel} = \varepsilon / (D_j * 1000) \quad (\text{eq. 155})$$

By use of eq. 154 and eq. 155, a friction coefficient (f_d) can then be read in the Moody diagram (appendix 8.3.5). As indicated in the table in the appendix, for steel the relative roughness $\varepsilon \approx 0.025$ mm. This allows a loss coefficient to be determined and also what the hydraulic gradient is over a meter of pipe length and ultimately the total pressure drop over the jet pipe.

$$I_f = \frac{f_d * u_0^2}{2 * D_j * g} \quad (\text{eq. 156})$$

$$P_{pipe,loss} = I_f * \rho_w * g * L \quad (\text{eq. 157})$$

The pressure loss caused by pipe bends and constrictions in the jet pipe are not taken into account in the calculations because it differs much per design. To make the calculation more precise this could be considered. In the jet chamber the velocity state is turbulent. There will be some losses but with the assumption that u_1 is small compared to the nozzle exit velocity, the losses in the jet chamber are neglected in this case (Rhee, Lecture notes Dredging Processes 2 [OE4727], 2016). The shape and size of the nozzle determine how the flow develops through the nozzle. This results in a contraction coefficient, c_d . The theory of Bernoulli and some other assumptions are used to calculate the pressure drop over the nozzle. The assumption and derivation are included in the appendix 8.3.2 and result in eq. 158.

$$P_{nozzle,loss} = \frac{1}{2} * \rho_w * \left(\frac{4 * Q_j}{c_d * \pi * D_n^2 * n_n} \right)^2 \quad (\text{eq. 158})$$

When the pipe and nozzle pressure loss are added together, the total pressure loss is known. Now the equations for the pressure loss can be plotted in the same graph as the pump head plot, as is shown in Figure 76. The working point found by the intersection between the two graphs, delivers the pump pressure just behind the pump. The discharge belonging to the working point is now used to calculate the nozzle pressure (Δp). This is done with the same formula as eq. 158 where Q_j should be replaced with the specific jet working point discharge ($Q_{j,wp}$).

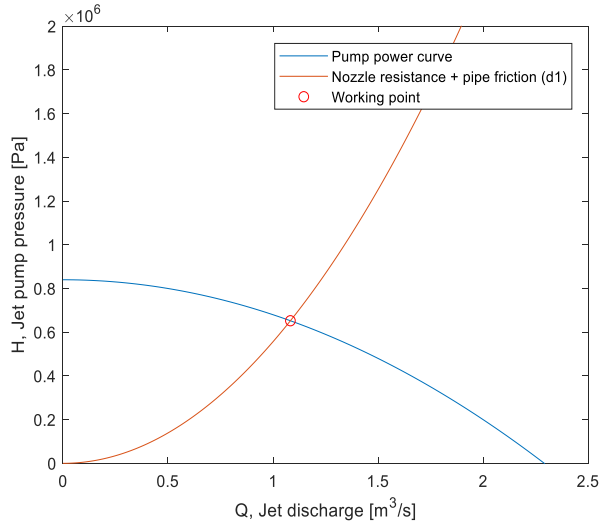


Figure 76: Working point jet pump

The nozzle pressure can now be used to calculate the nozzle exit velocity with eq. 159 as has been explained in the appendix.

$$u_0 = \sqrt{\frac{2 * \Delta p}{\rho_w}} \quad (\text{eq. 159})$$

Jet pump behaviour

The pump does not always behave in the same way. Adjustments can be made to the design and the control of the pump to change the output. This is useful because the soil types can differ per area and therefore the jet control can be optimized for the soil that is dredged. One way is to change the power of the pump by lowering or increasing the rpm. Another way is to lower the discharge by squeezing the flow with a smaller nozzle diameter or reducing the number of nozzles. Or the opposite direction by enlarging the discharge by using a bigger nozzle or increasing the number of nozzles.

When the jet power decreases, by reducing the number of rotations, the centrifugal force and thus the pressure and discharge also decrease. In practice, the jet pressure is used to set the power of the jets. But the jet pump runs almost constantly at maximum power in practice so there is less variation. By changing the nozzle size, the jet discharge will vary and to a lesser extent the jet pressure over the nozzle. The effect is shown in Figure 77. When the nozzle surface enlarges, the resistance which the fluid encounters by contraction, reduces. The pressure decreases and the discharge increases. The jet discharge and the pump head scale in the following manner given by the affinity laws:

$$\frac{H_1}{H_2} = \frac{n_{n,1}^2}{n_{n,2}^2} = \frac{D_{j,1}^2}{D_{j,2}^2}, \quad \frac{Q_{j,1}}{Q_{j,2}} = \frac{n_{n,1}}{n_{n,2}} = \frac{D_{j,1}^2}{D_{j,2}^2} \quad (\text{eq. 160})$$

The nozzle diameter and, with that, the amount of water that is pumped cannot increase unlimited. When the discharge increases the velocity in the jet pipe also increases. The resistance which the water encounters increases quadratic, eq. 156. So, when the pipe resistance is equal to the power which the pump can deliver the fluid will not flow anymore.

There is also a working area, where the nozzle diameter is so small, that the pressure gets high and the discharge drops to approximately zero. At such a high pressure, the nozzle velocity is theoretically at its maximum. However, when the discharge is zero there is also no flow velocity. This could be clarified by the property that water will mist in this case. Therefore, in the model the values for the velocity and pressure for the lower jet discharge area will not be completely realistic. These low discharges should also be avoided because then the pump cannot cool itself anymore, which eventually reduces the lifetime of the pump. In practice, the jets will never work in this area and the pump will work around its best efficiency point (BEP) so that is why there is not gone any deeper into this theory.

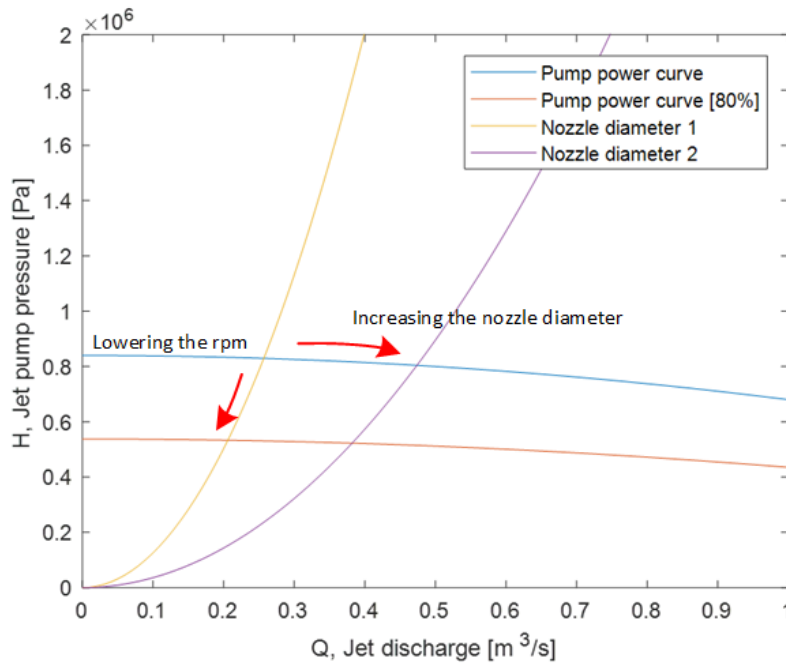


Figure 77: Pump behaviour

4.2.2 Jet production

A traversing jet moving over a bed leaves a trench behind. The eroding working of the jet brings the sand in suspension and pushes the sand up to the sides of the jet trench. For low trailing velocities it first starts with the union shaped profile shown in Figure 78. The jet flow penetrates the sand straight and erodes the sand. The flow bends towards the sides and brings up the sand on the edges. When the jets have moved forward the unstable steep bed slope will collapse and the trench is partly filled again. The walls of the trench will find an equilibrium depending on the internal friction angle of the sand. The final shape of a cross section of a jet is similar to half a circle.

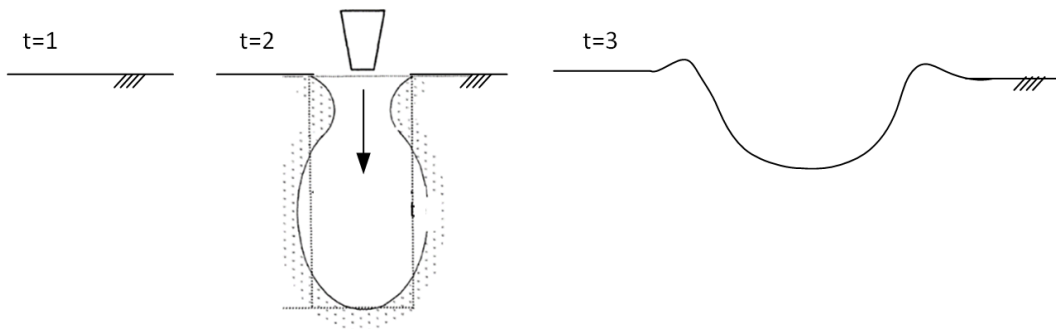


Figure 78: Jet trench process for low trailing velocities < 1 m/s

However, if there is a suction force of the dredge pump, which is strong enough, the eroded sand mixture will be pumped upwards straight. This suggests that the trench profile, after all the particles have settled, is not important but the initial fluidised profile. The flow starts with the nozzle diameter when it leaves the nozzle. Due to entrainment of water and sand into the flow, the jet enlarges till the point where the flow is not powerful enough anymore to penetrate any deeper into the bed. This profile defines the penetration depth and maximum cavity width.

Below is a simple version of the effective jet production stated. In here the situ jet production is the product of the penetration depth [m], the cavity width [m], the trail velocity [m/s] and the number of nozzles.

$$Q_s = h_{i,jet} * w_c * v_t * n_n \quad (\text{eq. 161})$$

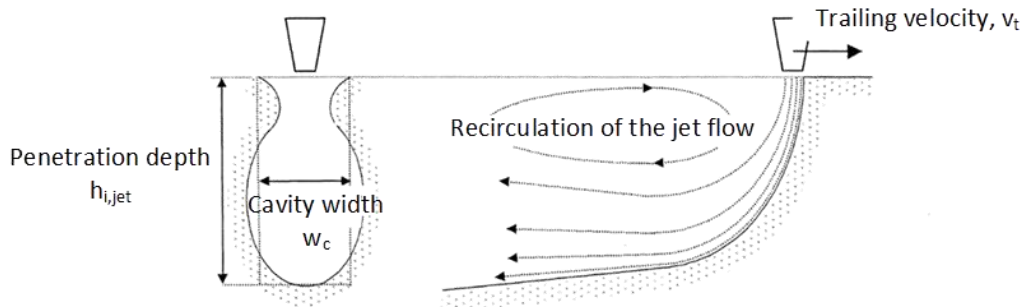


Figure 79: Jet profile cross sections

The in situ jet production is related to the trailing speed, because of the simple reason that when the trailing speed is zero, there will not be any supply of soil and subsequently no production. The faster is trailed, the less deep the jets penetrate because the penetration time decreases and so the jet momentum per travelled distance. On the other hand, the distance travelled is longer and so the supply of sand is higher because of the increased trailing speed. Assuming the penetration depth is linearly depending on the trailing velocity and the cavity width stays constant, the jet production will not change when the trailing velocity is increased.

The penetration depth depends, amongst other variables, on the soil characteristics. Therefore, it is hard to define a formula which is valid for every soil. When the soil characteristics are taken into account, this will result in a more accurate estimation of the penetration depth and eventually of the jet production. Besides the soil parameters, the penetration depth depends on the jet pressure which determines the jet flow velocity as well as the jet discharge like was shown in 4.2.1.

Another method to determine the jet production of eroded sand (in situ sand) is given by Vlasblom. The formula is based on the momentum of the jet times a non-dimensionless empirical parameter α [-]. The jet production of eroded sand, the mass flux [kg/s], is according to Vlasblom given by:

$$M_s = \alpha * I = \alpha * \rho_w * Q_j * u_0 = \alpha * \rho_w * Q_j * \sqrt{\frac{2 * p_j}{\rho_w}} \quad (\text{eq. 162})$$

Vlasblom's formula is a simple approach and does not consider different soil characteristics or the trailing velocity. Instead, he probably used field data to find a value for the coefficient α , to find an acceptable prediction for the jet production. The value 0.1 is typically used by Vlasblom for the variable α . A hypothesis is that the value α depends, amongst other things, on the soil characteristics. Wegenaar compared the production results of his research with Vlasblom's equation (Wegenaar, 2014). For the experiments Wegenaar found a value α of 0.14 ± 0.034 (d_{50} : 284 μm) and 0.13 ± 0.037 (d_{50} : 142 μm). The conclusion is that Vlasblom overestimates the coefficient with an average factor of 1.3-1.4 depending on the soil type. Despite the values found by Wegenaar seem fairly close to the value given by Vlasblom, they result in a production difference of $\approx 30\text{-}40\%$.

The jet power is equal to the jet discharge times the jet pressure. When eq. 163 is substituted in eq. 162, eq. 162 can be rewritten as follows:

$$P_j = p_j * Q_j \quad [W] \quad (\text{eq. 163})$$

$$M_s = \alpha * \rho_w * P_j * \sqrt{\frac{2}{\rho_w * p_j}} \quad \left[\frac{kg}{s} \right] \quad (\text{eq. 164})$$

As suggested by van Rhee, a lower jet pressure and a higher discharge will lead to a higher in situ production according to eq. 164 (Rhee, Lecture notes Dredging Processes 2 [OE4727], 2016).

4.2.2.1 Penetration depth:

Vlasblom – Van Rhee

One way to estimate the penetration depth, is by deriving it from the total mass flux estimated by Vlasblom (Rhee, Lecture notes Dredging Processes 2 [OE4727], 2016). By multiplying the basic production with the soil density and the porosity, the in situ sand production is calculated:

$$M_s = \rho_s * (1 - n_0) * h_{i,jet} * w_c * v_t * n_n \quad (\text{eq. 165})$$

By rewriting the formula, one will find eq. 166. Now the mass flux is determined by Vlasblom and can be substituted into the equation.

$$h_{i,jet} = \frac{M_s}{\rho_s * (1 - n_0) * w_c * v_t * n_n} \quad (\text{eq. 166})$$

In a draghead, multiple nozzles are lined up in a row to cover the whole visor width. For an optimal use of the jet momentum, the jets should not overlap each other. The opposite, when a wall of sand between the jets stays untouched, is also not preferred because then the cutting teeth have to excavate the soil which could result in higher trailing forces. The cavity width has to be determined, to make sure the jets are positioned with the right distance in between them.

Miedema

Since the penetration depth of Vlasblom and van Rhee does not depend on any soil characteristics, except for an empirical coefficient, other production approaches are observed. Miedema described the situ jet production by use of substituting the needed jet power to fluidize the soil layer divided by the specific energy, into the basic production of eq. 161 (Miedema, Introduction to Dredging Engineering [OE4607], 2016). In his penetration depth prediction, the permeability and porosity (dilatancy factor) are included. The production starts with the following equation:

$$Q_s = \frac{P_j}{E_{sp}} \quad (\text{eq. 167})$$

The upper part of the equation, the jet power, can be replaced by eq. 163, written out this results in:

$$P_j = \Delta p_j * Q_j = \Delta p_j * n_n * \left(\frac{2 * \Delta p_j}{\rho_w} \right)^{\frac{1}{2}} * \frac{\pi}{4} * (c_d * D_n)^2 \quad (\text{eq. 168})$$

The lower part of the equation is the specific energy to excavate the soil. Miedema assumes that the specific energy, to jet the soil layer, is the same as for the non-cavitating cutting energy with a blade. Which suggests that the penetration depth reached by excavating with jets is equal to the cutting depth of the blade. The formula for determining the specific cutting energy is stated below.

$$E_{sp} = c_1 * \frac{\rho_w * g * h_i * v_c * \varepsilon}{k_m} \quad (\text{eq. 169})$$

By substituting eq. 168 and eq. 169, this gives for the situ production and the penetration depth estimation:

$$Q_s = \frac{\Delta p_j * n_n * \left(\frac{2 * \Delta p_j}{\rho_w} \right)^{\frac{1}{2}} * \frac{\pi}{4} * (c_d * D_n)^2}{c_1 * \rho_w * g * h_i * v_c} * \frac{k_m}{\varepsilon} \quad (\text{eq. 170})$$

$$h_i = \frac{\Delta p_j * n_n * \left(\frac{2 * \Delta p_j}{\rho_w} \right)^{\frac{1}{2}} * \frac{\pi}{4} * (c_d * D_n)^2}{c_1 * \rho_w * g * h_i * v_c^2 * w} * \frac{k_m}{\varepsilon} \quad (\text{eq. 171})$$

Using Kozeny Carman for determining the mean permeability, the mean permeability and dilatation can be illuminated from the equation and is replaced by the initial permeability of the soil (Miedema, Production estimation of water jets in drag heads, 2019).

$$\frac{k_m}{\varepsilon} \approx 10 * k_i \quad (\text{eq. 172})$$

By rewriting the formula and using the following values for the known variables, eq. 170 is shortened. Assuming that the cavities of the jets are perfectly connected to each other. The cavity width can then be equated to the ratio between the width of the draghead and the number of nozzles ($\frac{w}{n_n}$). Miedema uses the value 0.2 m. For a draghead of 3 meters wide, this means 15 nozzles which connect perfectly to each other. For the blade angle coefficient and the jet nozzle contraction coefficient he chose a value of: c_1 of 0.12 [-] and a contraction coefficient, α , of 0.85 [-]. Be aware that the formula uses SI units so the pressure is filled in with Pa and the water density is 1025 kg/m³. This is the reason the coefficient on the left of the formula diverges slightly from Miedema's coefficient. Miedema used kPa and tonnage/m³ which results in a coefficient for the penetration depth of 5.73 instead of 0.032.

$$Q_s = 0.032 * \Delta p_j^{\frac{3}{4}} * D_n * k_i^{\frac{1}{2}} * w \left[\frac{m^3}{s} \right] \quad (\text{eq. 173})$$

$$h_i = \frac{0.032 * \Delta p_j^{\frac{3}{4}} * D_n * k_i^{\frac{1}{2}}}{v_c} [m] \quad (\text{eq. 174})$$

The assumption Miedema made for the different variables is calibrated for a specific working point. Because the cavity width probably depends on a lot of different variables, the prediction is that the cavity width changes for other cases. A more general relation has to be found to use the relation for different circumstances.

Wegenaar

The last penetration depth estimation that is introduced is the one determined by Wegenaar. His 2D penetration profile can also be used as a production model when the penetration depth, at a chosen distance behind the jet, is multiplied by the width of the draghead. Again, assuming the jet's cavities connect perfectly to each other, and the upright edges in the channel are loose enough such that there is no cohesion between the particles anymore and will collapse. Wegenaar used the jet theory in combination with an erosion theory to see how the jet profile develops in the bed (Wegenaar, 2014). Because the jet has a forward velocity (in the figure to the right), it looks like the profile bends of until a maximum penetration is reached. The trailing velocity direction is indicated in the figure to the right (Figure 80).

By using the same assumption for the cavity width in van Rhee's/ Vlasblom's and Miedema's penetration formulas and by using the penetration depth model of Wegenaar (100 cm behind the jet) the three penetration depths approaches can be compared. The result is shown in Figure 81. It is clear that the penetration depths determined are almost equal for the working point ($P_j \approx 6$ bar, $Q_j = 0.31$ m³/s, $D_n = 0.03$ m, $k_i = 1*10^{-4}$ m/s (calibrated result for Miedema's theory)).

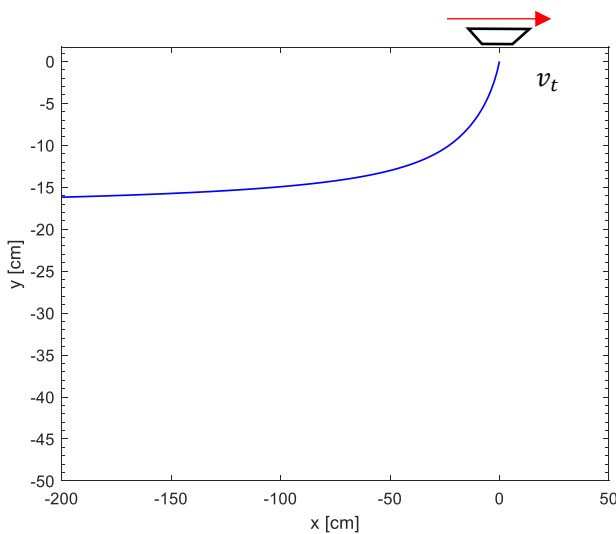


Figure 80: Jet profile by Wegenaar

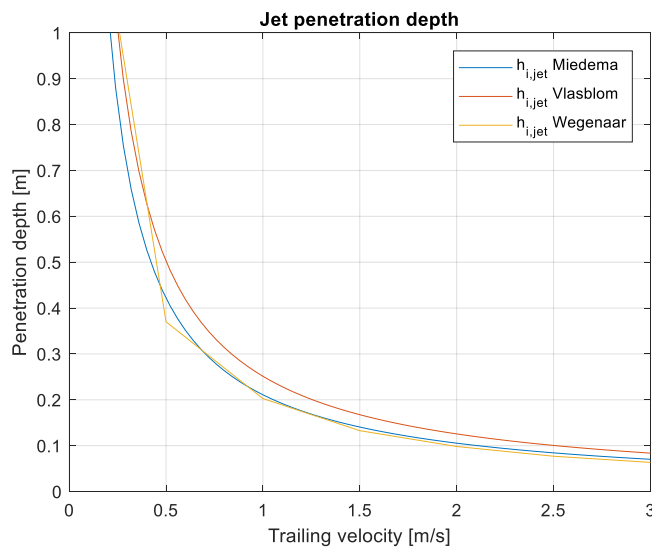


Figure 81: Penetration depth vs. trailing velocity comparison

Wegenaar concluded that the sand characteristics, the trail velocity and the jet pressure have an influence on the penetration depth. He did not come up with a clear relation but his findings from the experiment are shown in appendix 8.3.6. The penetration depth was 1.35 times higher for sand type 2 than type 1. With a trail velocity of 0.25 m/s instead of 0.5 m/s the penetration increases with 1.65 to 1.88, depending on the sand type. And by doubling the pressure the penetration depth increases by 1.5.

In addition Wegenaar predicted a cross-sectional profile of the traversing jet with his jet erosion model. The red line in Figure 82, represents a trail velocity of 0.25 m/s ($w_c \approx 20$ cm, $h_{i,jet} \approx 21$ cm). The green line represents a trail velocity of 1 m/s ($w_c \approx 10$ cm, $h_{i,jet} \approx 9$ cm). Wegenaar indicates that the penetration depth was slightly overestimated with the results found in the experiment. The pump was capable to deliver up to 13 m³/h of water at 8 bar pressure. The discharge was around 0.0036 m³/s.

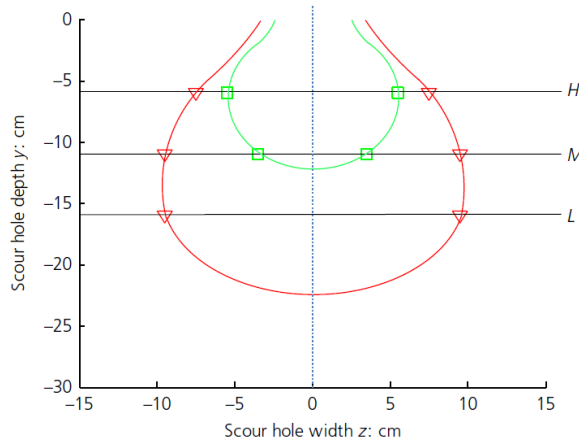


Figure 82: Scour profile prediction Wegenaar

4.2.2.2 Cavity width:

As already indicated during the determination of the penetration depth, a similar relation as the penetration depth, needs to be found for the cavity width. The problem is that when the penetration depth and the cavity width are calculated from the jet production, either way with the jet momentum (Vlasblom) or the specific energy (Miedema), there is only one equation and two unknowns. To make a good estimate the influence of the trailing velocity, nozzle diameter, jet pressure and soil characteristics have to be included into the cavity width relation. The predicted scour profile of Wegenaar can be used for an indication of the shape and the ratio between the penetration depth and cavity width. The predicted profile is for the situation where the edges have not collapsed yet. The union shaped profile in Figure 82 shows that the ratio between the penetration depth and cavity width is $\approx 1:1$ (Wegenaar, 2014). This ratio follows also from the calibrated results from Miedema with the assumption for the cavity width, $w_c = \frac{w}{n_n} (h_{i,jet} = 0.2 \text{ m}, w_c = 0.2 \text{ m}, \Delta p = 6 \text{ bar}, D_n = 3 \text{ cm}, k = 1.10^{-4} \text{ m/s})$.

Because of this, three different relations are discussed. Starting with the cavity width equal to the nozzle diameter, $w_c = D_n$. This is indeed the case for penetrating in cohesive soils as clay (Nobel, 2013). From the test results of Wegenaar can be concluded that this is not the case for sandy soils. A coefficient times the nozzle diameter could give better results, but the question what the value of the coefficient will be, remains. For every case with different jet pressures, different traversing velocities and different soils the coefficient should be determined and thus a relation is needed. The second option is to equal the cavity width to the penetration depth. As can be concluded from the test results above, Vlasblom/v. Rhee's and Miedema's theories can be used to determine the penetration depth as well as the cavity width with the same equations:

$$w_c = h_{i,jet} \quad (\text{eq. 175})$$

Vlasblom's penetration depth, eq. 166, can be rewritten to:

$$w_c = h_{i,jet} = \sqrt{\frac{M_s}{\rho_s * (1 - n_0) * v_t * n_n}} \quad (\text{eq. 176})$$

Miedema's derivation for the penetration depth, eq. 174, can be rewritten to:

$$h_{i,jet}^2 * w_c = h_{i,jet}^3 = \frac{10 * \left(\frac{2}{\rho_w}\right)^{\frac{1}{2}} * \frac{\pi}{4} * c_d^2}{c_1 * \rho_w * g} * \frac{\Delta p_j^{\frac{3}{2}} * D_n^2 * k_i}{v_c^2} [m] \quad (\text{eq. 177})$$

$$w_c = h_{i,jet} = \frac{0.059 * \Delta p_j^{\frac{1}{2}} * D_n^{\frac{2}{3}} * k_i^{\frac{1}{3}}}{v_c^{\frac{2}{3}}} [m] \quad (\text{eq. 178})$$

The cavity width now depends on the trailing velocity, nozzle diameter, jet pressure and for the formula of Miedema also on the permeability (soil characteristics). In a first comparison with test results this looks plausible. Further investigation needs to be done to confirm this relation in order to find a more precise cavity width relation.

When the production is calculated with eq. 176 the production is independent of the trailing velocity. The penetration depth and cavity width scale proportional with the trailing velocity. The production calculated with eq. 178 does not scale proportional with the trailing velocity anymore and the production now depends on the trailing velocity.

The third option is to set the cavitation width equal to the penetration depth times the length/width ratio, α , of the jet scour hole surface area, as indicated by Miedema, based on an analysis by P. de Jong (Jong, 1988). P. de Jong used the results from an extensive jet research performed by van Rhee (Rhee, De invloed van een waterstraal op een zandpakket, april 1986). Miedema concluded from those results that the value of α , which is in this case the ratio between the penetration depth and the cavity width, is almost equal to the trailing velocity (Miedema, Production estimation of water jets in drag heads, 2019).

$$\alpha \approx v_t \quad (\text{eq. 179})$$

$$w_c = h_{i,jet} * \alpha = h_{i,jet} * v_t \quad (\text{eq. 180})$$

By substitution of the above assumption, in the previous relation for the penetration depth, eq. 166, follows:

$$w_c = h_{i,jet} * v_t = \sqrt{\frac{M_s}{\rho_s * (1 - n_0) * v_t^2 * n_n}} * v_t = \sqrt{\frac{M_s}{\rho_s * (1 - n_0) * n_n}} * \sqrt{\frac{1}{v_t^2}} * v_t = \sqrt{\frac{M_s}{\rho_s * (1 - n_0) * n_n}} \quad (\text{eq. 181})$$

The equation of Miedema, for the cavity width, eq. 174, then changes to ($v_c = v_t$):

$$h_{i,jet} = \frac{0.059 * \Delta p_j^{\frac{1}{2}} * D_n^{\frac{2}{3}} * k_i^{\frac{1}{3}}}{v_c} [m] \quad (\text{eq. 182})$$

$$w_c = h_{i,jet} * v_t = \frac{0.059 * \Delta p_j^{\frac{1}{2}} * D_n^{\frac{2}{3}} * k_i^{\frac{1}{3}}}{v_c} * v_c = 0.059 * \Delta p_j^{\frac{1}{2}} * D_n^{\frac{2}{3}} * k_i^{\frac{1}{3}} \quad (\text{eq. 183})$$

This results, in both cases, in a non-trailing velocity depending cavity width. The results of P. de Jong show that the cavity width is not constant but will slowly decrease for increasing trailing velocities (Jong, 1988). Just as was seen already in Figure 82, and the aforementioned assumption that the cavity width is equal to the jet penetration depth $w_c = h_i$. For a trailing velocity of 1 m/s, the ratio α is almost equal to 1 and the assumption that $w_c = h_i$ is valid. For trailing velocities higher or lower than 1 m/s, the cavity width the values diverge and the relation, eq. 179, is not valid anymore. Relation eq. 180, is therefore unusable and needs to be analysed more accurately in order to be applied.

According to P. de Jong and van Rhee the scour profile changes shape at different trailing velocities. For low velocities the scour has an onion-shaped shape, where at higher velocities the shape becomes more like a bowl (semi-circle), Figure 83. Due to this characteristic, it is plausible that the cavity width is less wide than the length of penetration depth at low trailing velocities.

Low trailing velocity

High trailing velocity

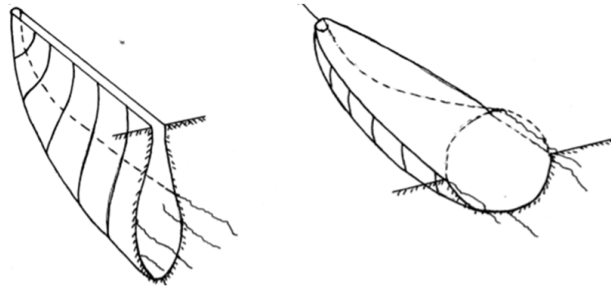


Figure 83: Scour profile for different low- and high trailing velocities

The penetration depth will gradually become more equal to the cavity width for an increasing velocity, and at a higher velocity the penetration depth will eventually be lower. This is shown in the graph of Figure 87 from the jet experiments of P. de Jong, Table 9.

Table 9: Jet profile data from an analysis of P. de Jong

d50=150µm, nozzle pressure=7.5bar, nozzle diameter =14mm				
v_t [m/s]	α [-]	Q_s [m ³ /s]	$h_{i,jet}$ [m]	$w = \alpha * d$ [m]
0.5	0.7	0.0132	0.1940	0.1350
1	1.2	0.0113	0.0970	0.1160
1.5	1.6	0.0100	0.0640	0.0130
2	2	0.0094	0.0480	0.0960

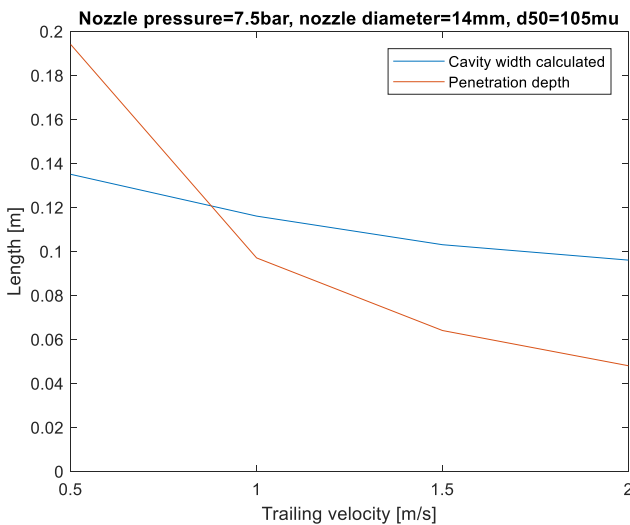


Figure 84: Jet penetration depth and calculated cavity width versus the trailing velocity

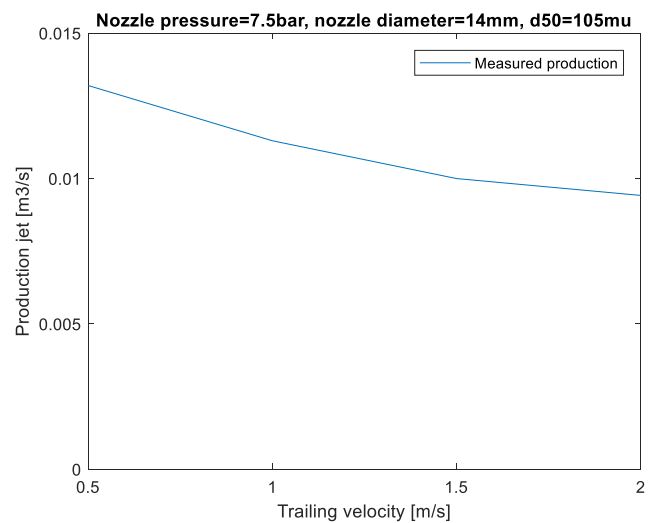


Figure 85: Jet production from experiments

The results from the experiment used in the report of P. de Jong state that the width and penetration depth of the jets are measured after the jet has passed, the walls have collapsed and all the particles have settled again. This gives a completely different value for the cavity width at low- trailing velocities and high trailing velocities. At a high velocity, the bowl-shaped width, may be the same during and after settling, but probably not at a low trailing velocity. This makes the measured production and subsequent coefficients uncertain.

What is even more apparent from the tables, is that the production decreases for increasing trailing velocities. What causes the production to decrease? Is this the result of the difference in measuring the cavity width at high and low trailing velocities? Is it more energy efficient to trail at low velocities? The latter is refuted by P. de Jong because at low trailing velocities, in the union-shaped cavity more turbulence would take place.

Supposing that the production decreases with increasing trailing velocities, the mass flux equation of Vlasblom no longer applies. Here the mass flux is independent of the trailing velocity. The value α , is not exactly the trailing velocity, there has to be a more accurate relation. According to van Rhee, the sand production can be approached with the empirical function below:

$$P_z = C * P_{sp}^\beta \quad (\text{eq. 184})$$

Where P_z is the sand production [m^3/s], C a coefficient with a value that depends on the nozzle and the soil characteristics, P_{sp} the jet capacity [Nm/s] and the exponent β , is a coefficient dependent on the trailing velocity. Beta is shown in Figure 86, as can be seen, its value slowly decreases with increasing trailing velocities (Jong, 1988).

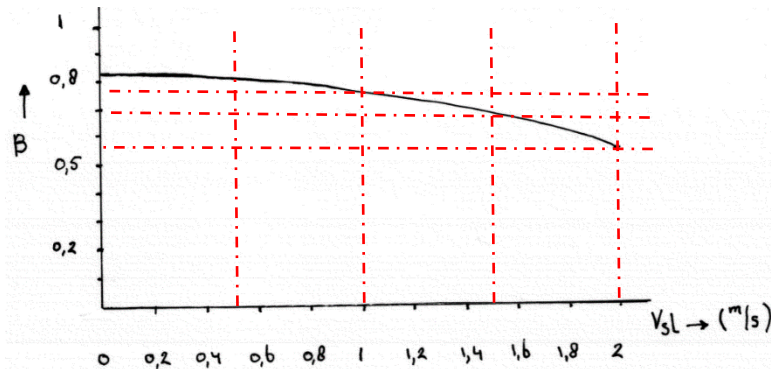


Figure 86: The production coefficient beta versus the trailing velocity

As can be seen in the graph, the coefficient beta remains almost equal until 1 m/s and then decreases faster. Up to 1 m/s, the production would therefore not decrease much because of the value beta.

In addition, van Rhee found an empirical relation for the penetration depth depending on the nozzle diameter, permeability and the trailing velocity (Jong, 1988). De Jong has described the jet production in a different way, where he equalled the cavity width and the penetration depth, resulting in:

$$h_{i,jet} = 291 * \Delta p^{0.59} * D_n^{0.49} * k^{0.369} * v_t^{-1} \quad [\text{mm}] \quad (\text{eq. 185})$$

$$P_z = \alpha * h_{i,jet}^2 * v_t \quad (\text{eq. 186})$$

Combining above equations results in:

$$P_z = \alpha * 0.0847 * \Delta p^{1.18} * D_n^{0.98} * k^{0.378} * v_t^{-1} \quad \left[\frac{\text{m}^3}{\text{s}} \right] \quad (\text{eq. 187})$$

$$\alpha = \frac{C * P_{sp}^\beta}{0.0847 * \Delta p^{1.18} * D_n^{0.98} * k^{0.378} * v_t^{-1}} \quad (\text{eq. 188})$$

The ratio α is now, among other variables, depending on the empirical coefficient C . As already mentioned at the beginning of this section, for every trailing velocity, soil characteristic and the jet settings, the value C has to be determined or calculated from the jet production. In the report of P. de Jong the values for C are given based on measurement of CBS. Because of a lack of data, there is no clear conclusion to be drawn. **For now, the assumption that $w_c = h_{i,jet}$, has therefore been used in the rest of the report for calculating the jet production, so it must be taken into account that this relation actually deviates at higher and lower velocities than 1 m/s.**

4.2.2.3 Overlapping scour holes

It is assumed that when the penetration depth and the cavity width are equal to each other, and become larger than $\frac{w}{n_n}$, the jet trenches will overlap (w is the width of the draghead visor). On both sides of the jet cavity, sand is diluted already, and a larger width will not contribute to a higher production anymore. A hypothesis is that the horizontal velocity components will work against each other while the vertical components, in upward direction, strengthen each other, Figure 87.

Furthermore, it is assumed that when the penetration depth is larger than $\frac{w}{n_n}$, the cavity width stays equal to $\frac{w}{n_n} = w_{c,max}$. This will be the case for low trailing velocities. When the trailing velocity is increased, the penetration depth and the cavity width will decrease again (Figure 88). The penetration depth does not necessarily have to reach its maximum when the cavity maximum is reached. In that case optimization of the distance between the nozzles should give a higher jet production.

Because the cavity width cannot increase more than $w_{c,max}$, for low trailing velocities, this results in a jet production decrease.

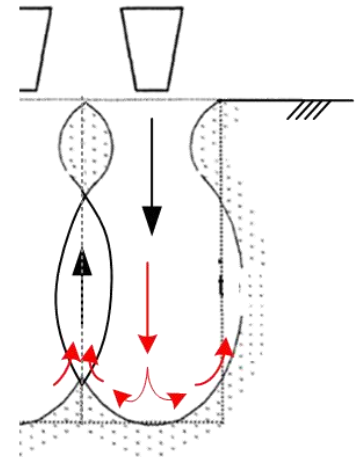


Figure 87: Interaction between the jets

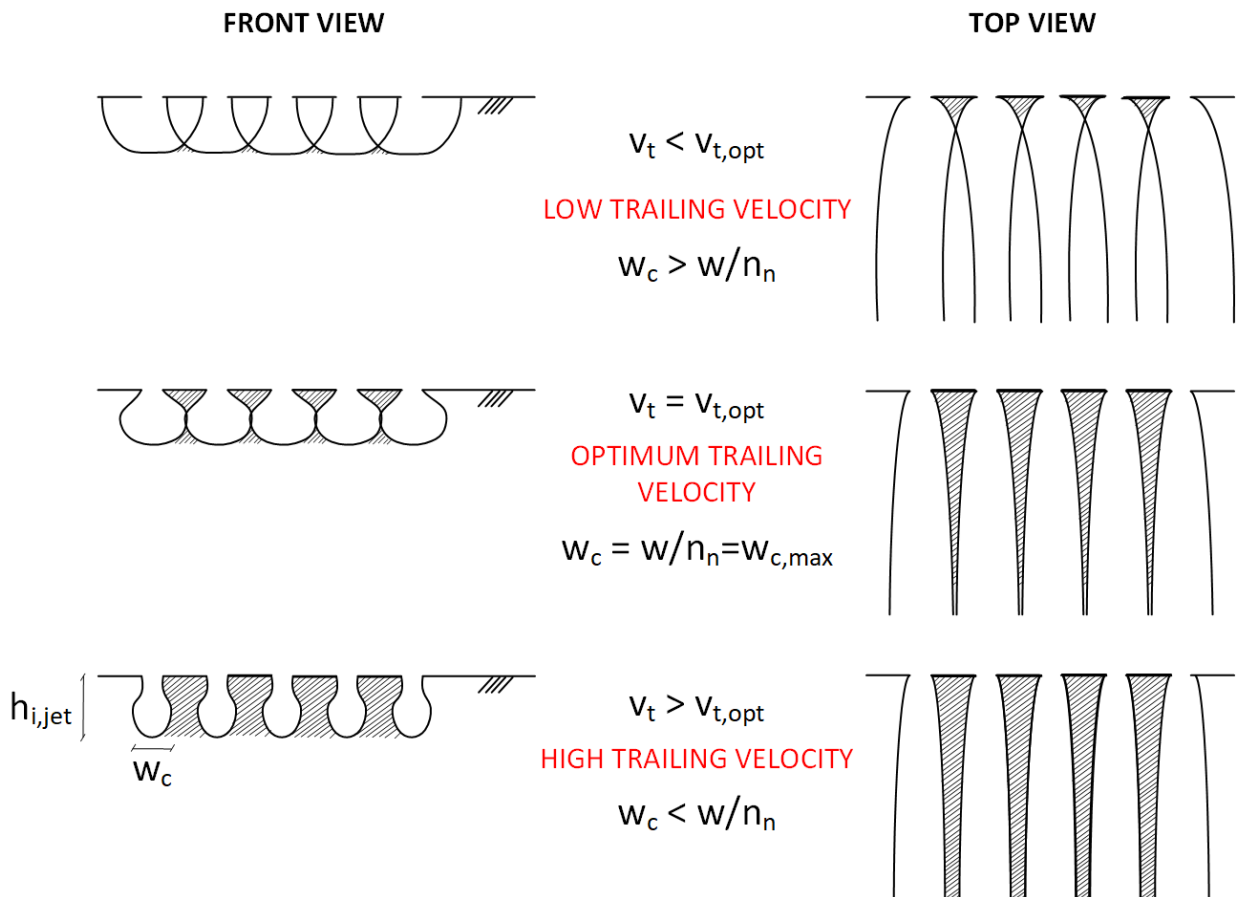


Figure 88: Influence trailing velocity on cavity width; front view and top view

4.2.2.4 Erosion distance

The last limit that has to be determined, to check whether it meets the dimensions of the draghead visor, is the erosion distance. The erosion distance is defined as the length at which the jets still have an eroding effect and is ensured that the sand particles are loosened and transported with the flow. When the strength of the flow has decreased, in the case there is no suction effect, the sand particles will settle again. The erosion distance needs to be sufficient enough so that the sand will not settle inside the draghead. From Wegenaar's erosion profile, visualized in Figure 80, and his test experiments can be concluded that the erosion distance is long enough. So that it can be assumed that no sedimentation occurs within the draghead. Besides that, the effect of the pump may cause that settling is not possible at all, and the sand particles are brought to the surface by the vacuum created by the pump. For this the capacity of the dredge pump needs to be sufficient so that spillage does not occur. This is discussed in chapter 5.

4.2.2.5 Volume flux

The total jet production is the amount of loosened in situ saturated soil plus the amount of jet water that is injected into the soil. Assumed is, that because of the small stand of distance between the jet and bed there is initially no entrainment of surrounding water in the jet flow. Another assumption is that there is no entrainment of water from the surrounding soil extra then what was already present in the soil eroded by the jet.

Vlasblom's mass flux production needs to be converted to volume per second, to compare the production and penetration depths with Miedema's estimation.

$$Q_s = \frac{M_s}{\rho_s} \quad (\text{eq. 189})$$

The total discharge of the jet and the jet production give the total jet production volume flux:

- In situ sand: $Q_s = \frac{M_s}{\rho_{soil}}$
- In situ water: $Q_w = \frac{Q_s}{(1-n)} * n$
- Jet discharge: Q_j

Because the soil is fully saturated there is already water present in the pores. The in situ mixture density can be determined by multiplying the in situ sand and water production with the porosity (eq. 3). The mixture density of the jet production is found by using the volume fluxes times the density and dividing it by the total volume flux. The mixture density follows by:

$$\rho_m = \frac{(Q_s + Q_w) * \rho_{insitu} + Q_j * \rho_w}{Q_s + Q_w + Q_j} \quad (\text{eq. 190})$$

4.2.2.6 Jet spillage

As already mentioned does the dredge pump needs to be strong enough to suck up the loosened mixture. If the dredge pump cannot handle to process the supply of sand by the jets, there is a chance spillage occurs. Secondly, it is possible that the jets penetrate deeper than the visor sinks into the bed. This happens when $h_{i,jet} > h_{visor}$. Part of the jet production will then get lost underneath the visor. For a free hanging visor this depends on the equilibrium position of the visor, which will be determined in the next chapter.

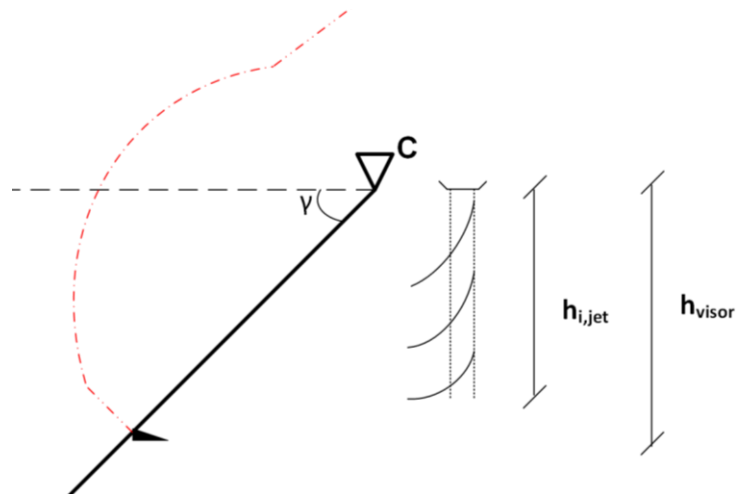


Figure 89: Jet spillage when penetration is too large

4.3 Model results & Discussion

In this paragraph, the theory described in the previous paragraph is used to calculate the jet production of the Damen draghead SLK600. The case study is worked out in the same order as the theory explained in the previous paragraph. The results are presented in this paragraph and throughout the paragraph the results are also already discussed.

4.3.1 Jet geometry

Damen uses a centrifugal water pump for the jet system which is built by the manufacturer Nijhuis. The pump capacity curve needs to be determined or delivered by the manufacturer. Then with the dimensions of the jet system the specific working point of the jet pump can be calculated. The original values for the Damen draghead are summed in the table below. For simplicity of the calculation further on, the design is slightly adjusted, $w_n = \frac{w}{n_n} = 0.25$ m and $w_e = \frac{1}{2} * w_n = 0.125$ m, see Figure 90.

Table 10: Draghead and suction pipe dimensions

Variable	Symbol	Value	Unit
Length suction pipe	L	30.75	m
Jet pipe diameter (inside)	D_j	0.31	m
Width draghead visor (outside)	w_{out}	2.272	m
Width draghead visor (inside)	w_{in}	2.037	m
Number of nozzles	n_n	8	-
Nozzle diameter	D_n	0.048	m
Distance between nozzles (heart)	w_n	0.225; (0.25)	m
Distance between nozzle and visor skirt inside (heart)	w_e	0.255; (0.125)	m
Contraction coefficient (theoretical)	c_d	0.85	-

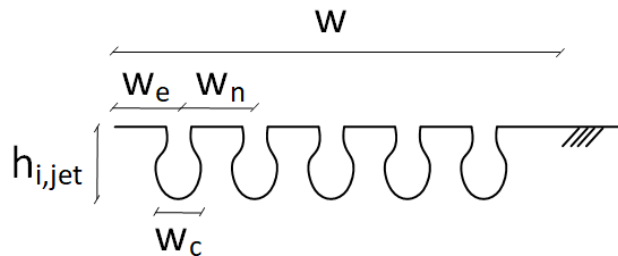


Figure 90: Jet position dimensions

4.3.2 Pump pressure, jet- velocity and discharge

With the pump curve estimation of Miedema, eq. 150 to eq. 152, the delivered pressure for the jet discharge can be approached for the jet pump. The resistance of the water in the jet pipe, expressed as a pressure loss, follows from Darcy-Weisbach and the Moody diagram, with eq. 153 to eq. 157:

$$R_{rel} = \frac{\varepsilon}{D_j * 1000} = \frac{0.000025}{0.31} = 8.0645 * 10^{-5} [-] \quad (\text{eq. 191})$$

The friction coefficient (f_d) derived from the Moody diagram is 0.0125 and follows from the Reynolds number and the relative roughness:

$$I_f = \frac{f_d * u_0^2}{2 * D_j * g} = \frac{0.0125 * u_0^2}{2 * 0.31 * 9.81} [m^{-1}] \quad (\text{eq. 192})$$

$$P_{pipe,loss} = I_f * \rho_w * g * L = I_f * 1025 * 9.81 * 30.75 \text{ [Pa]} \quad (\text{eq. 193})$$

With the theory of Bernoulli, the pressure drops over the nozzle is calculated. The contraction coefficient, c_d for the nozzle is theoretically 0.85, the number of nozzles is 8 and the nozzle diameter is 0.054 m.

$$P_{nozzle,loss} = \frac{1}{2} * \rho_w * \left(\frac{4 * Q_j}{c_d * \pi * D_n^2 * n_n} \right)^2 = \frac{1}{2} * 1025 * \left(\frac{4 * Q_j}{0.85 * \pi * 0.048^2 * 8} \right)^2 \text{ [Pa]} \quad (\text{eq. 194})$$

The only unknown is the jet discharge, by plotting the head of the pump and pressure losses, the specific working point is found. This allows the pressure over the nozzle to be calculated. With the equation below the pressure over the nozzle is used to calculate the nozzle exit velocity.

$$u_0 = \sqrt{\frac{2 * \Delta p}{\rho_w}} = \sqrt{\frac{2 * 7.77 * 10^5}{1025}} = 38.95 \left[\frac{m}{s} \right] \quad (\text{eq. 195})$$

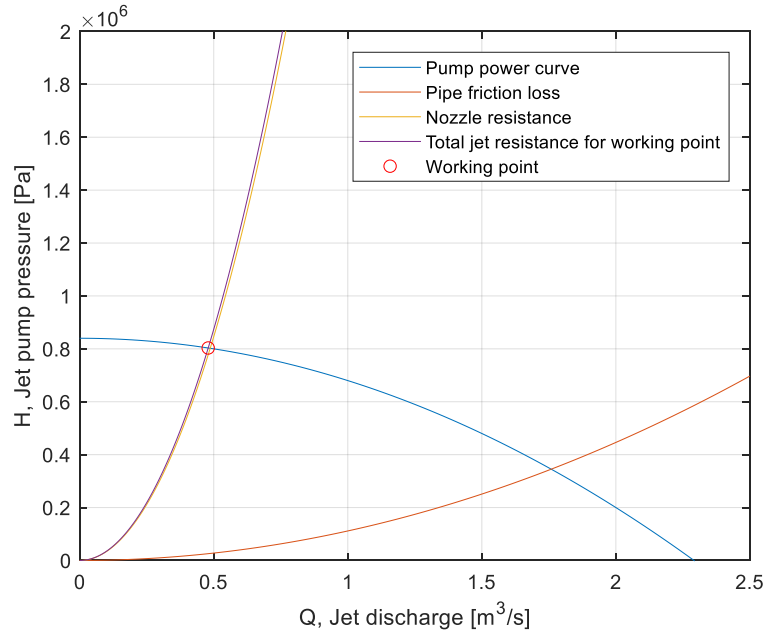


Figure 91: Working point jet pump

Table 11: Final values of the jet pump working point

Variable	Symbol	Value	Unit
Pump pressure	p_j	$8.032 * 10^5$	Pa
Jet pressure	Δp	$7.776 * 10^5$	Pa
Jet discharge	Q_j	0.479	m ³ /s
Jet velocity	u_0	38.95	m/s

4.3.3 Jet production

To determine the production the unknown variables, $h_{i,jet}$ and w_c , need to be calculated.

$$Q_s = h_{i,jet} * w_c * v_t * n_n \quad (\text{eq. 196})$$

The production estimation that is used to determine the penetration depth and cavity width is Vlasblom's and van Rhee's mass flux derivation. The jet production of eroded situ sand, the mass flux [kg/s], is according to Vlasblom given by eq. 197. For the variable α an initial value of 0.1 is taken which is suggested by Vlasblom.

$$M_s = \alpha * I = \alpha * \rho_w * Q_j * \sqrt{\frac{2 * p_j}{\rho_w}} = 0.1 * 1025 * 0.479 * \sqrt{\frac{2 * 7.776 * 10^5}{1025}} = 1914 \left[\frac{kg}{m^3} \right] \quad (\text{eq. 197})$$

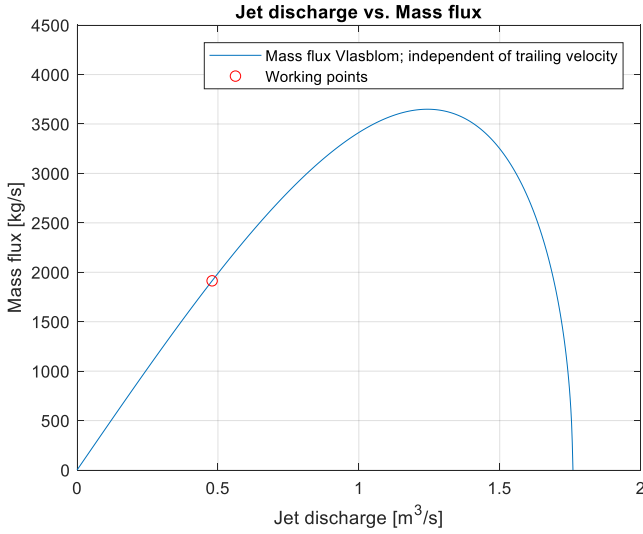


Figure 92: Jet production; situ sand

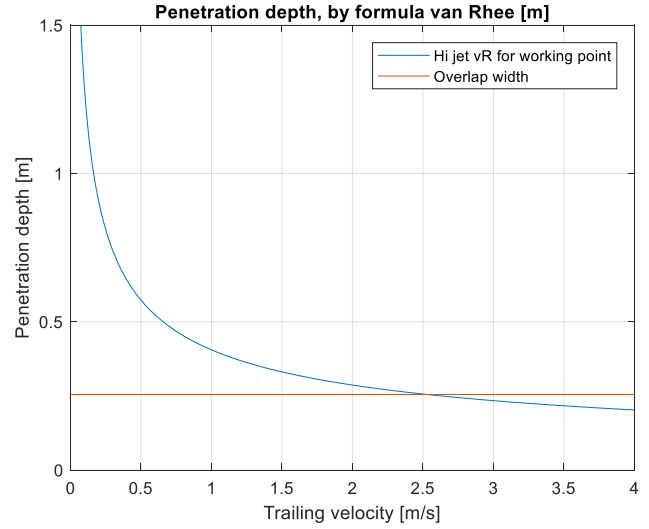


Figure 93: Penetration depth depending on the trailing velocity. Including the cavity width maximum

Penetration depth

By rewriting the formula (eq. 166), the jet penetration depth can be calculated with :

$$h_{i,jet} = \frac{M_s}{\rho_s * (1 - n_0) * w_c * v_t * n_n} = \frac{1914}{2650 * (1 - 0.45) * w_c * v_t * 8} [m] \quad (\text{eq. 198})$$

There is still one unknown, the cavity width. The suggested relation that the penetration depth is equal to the cavity width is used to solve the equation. This makes the cavity width also dependent of the trailing velocity and the porosity and the equation changes to eq. 199. The results are shown in Figure 93.

$$h_{i,jet} = w_c = \sqrt{\frac{M_s}{\rho_s * (1 - n_0) * v_t * n_n}} \quad (\text{eq. 199})$$

Because the cavity width cannot get wider than the maximum cavity width, it has a limited width of $w_{c,max} = \frac{w}{n_n}$. In the graph of Figure 93, this is indicated with the horizontal red line. For a trailing velocity lower than 2.53 m/s (4.9 knots) the cavity width stays equal to 0.25 m, in this case, and is not equal to the penetration depth. The jet production for trailing velocities lower than 2.53 m/s will differ.

The jet production, for trailing velocities higher than 2.53 m/s, is constant and consists of the excavated soil plus the injected jet discharge. The in situ density of the soil is:

$$\rho_{insitu} = 0,45 * 1025 + (1 - 0,45) * 2650 = 1919 \left[\frac{kg}{m^3} \right] \quad (\text{eq. 200})$$

$$Q_{s,situ} = \frac{M_s}{\rho_s} = \frac{1914}{2650} = 0.72 \left[\frac{m^3}{s} \right] \quad (\text{in situ sand}) \quad (\text{eq. 201})$$

$$Q_{w,situ} = \frac{Q_s}{(1 - n)} * n = \frac{0.72}{(1 - 0.45)} * 0.45 = 0.59 \left[\frac{m^3}{s} \right] \quad (\text{in situ water}) \quad (\text{eq. 202})$$

$$Q_j = 0.48 \left[\frac{m^3}{s} \right] \quad (\text{jet discharge}) \quad (\text{eq. 203})$$

The jet production mixture density follows by:

$$\rho_{m,jet} = \frac{(Q_s + Q_w) * \rho_{insitu} + Q_j * \rho_w}{Q_s + Q_w + Q_j} = \frac{(0.72 + 0.59) * 1919 + 0.48 * 1025}{0.72 + 0.59 + 0.48} = 1680 \left[\frac{kg}{m^3} \right] \quad (\text{eq. 204})$$

This looks like a high configuration for the production mixture density. However this is only the jet production, also the cut production and surrounding water have to be added to calculate the final mixture density which ends up in the hopper, this is done in chapter 5.

The mixture density depends on the amount of jet water that is injected, this is shown in Figure 94. The mixture density versus the trailing velocity is plotted in Figure 95. When the graph on the left is observed, it can be seen that the mixture density in the beginning slowly decreases with an increasing jet discharge. From a jet discharge of around 1.2 m³/s the mixture density drops faster to eventually the water density. This could be because with a low jet discharge the nozzle pressure is high and, in ratio with the jet discharge, the soil production is high. When the jet discharge increases the jet pressure will decrease. The jet pressure gets less and less powerful and is eventually not able to penetrate into the soil anymore to loosen the particles. Until the point there is no jet production anymore. Important to mention is that the jet mixture density is not directly affected by the amount of jet water that is injected but by the jet pressure that changes! The graph on the right side shows that the mixture density is constant for the trailing velocity except for the lower trailing velocities. This can be explained by the assumption that the cavity width is equal to the penetration depth. When the trailing velocity is lower than the switching point, the cavity width is wider than the maximum cavity width, and energy gets lost because the jets interfere with each other, turbulence.

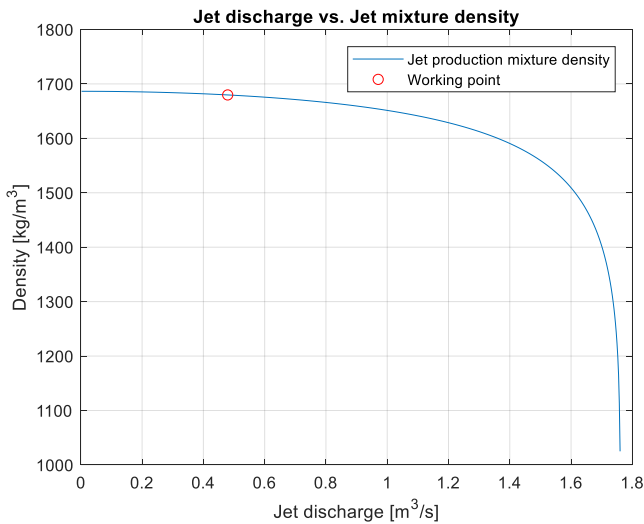


Figure 94: The jet mixture density depending on the discharge

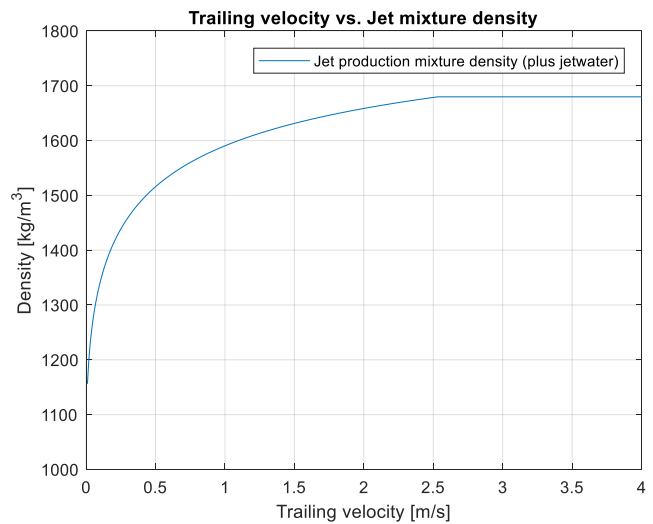


Figure 95: The jet mixture density depending on the trailing velocity

This gives the following final values for a common trailing speed of 1 m/s (1.94 knots).

Table 12: Final values case study; jet production

Variable	Symbol	Value	Unit
Penetration depth	$h_{i,jet}$	0.40	m
Cavity width	w_c	0.25 ($w_{c,max}$)	m
Jet pressure	Δp	$7.776 * 10^5$	Pa
Jet discharge	Q_j	0.479	m ³ /s
Production sand	Q_s	0.45	m ³ /s
Production total	Q_t	1.31	m ³ /s
Mixture density	$\rho_{m,jet}$	1590	kg/m ³

4.4 Optimization & Verification

4.4.1 Optimizing the jet settings

With the jet production model; the jet diameter, number of nozzles and the width between the nozzles can be optimized to the jet pump and draghead used. The jet production should be as high as possible while the trailing velocity should be minimized.

The parabola of Figure 92 suggests there is an optimum working point for a high jet production. The maximum jet power, of the jet pump in the case study, is 568.6 kW at a jet discharge of 1.02 m³/s and nozzle pressure of 5.6 bar (appendix 8.3.7). This is however not the maximum mass flux production point, which is 1.38 m³/s of situ sand by a jet discharge of 1.25 m³/s. The power of the jet and the amount soil that is loosened are closely related, the more power input the more jet production. For an optimum working point of the jet pump, the capacity of the dredge pump is needed. Because when too much sand is excavated, and the dredge pump cannot handle the supply anymore, spillage occurs. Besides that, the best efficiency point of the jet pump should be taken care of. This means the jet pump should be designed, on its best efficiency point, for the jet discharge wanted. This is however not taken into account in the scope of this research.

For now let's try to optimize the working point of the Damen SLK600. The maximum jet production density is reached at a trailing velocity of 2.53 m/s, which is too high. In case the trailing velocity is lowered to 1 m/s, the penetration depth will increase and more important, the cavity width start to overlap each other. This means the production will be lower and the mixture density will decrease.

An option to decrease the trailing speed and not lose potential production, is to lower the amount of nozzles by keeping the nozzle area equal. By doing this the jet discharge will slightly change but this is negligible. The distance between the nozzles will increase so there can be trailed with a lower trailing velocity. The results, for four different configuration are shown in the table below. The trailing velocity for the fourth configuration comes close to the wanted 1 m/s. This is a theoretical optimization, further investigation is needed to confirm this hypothesis.

Table 13: Amount of nozzles, equal nozzle area configurations

Variable	Configuration 1	Configuration 2	Configuration 3	Configuration 4
Amount of nozzles [-]	8	6	4	3
Nozzle diameter [m]	0.048	0.055	0.067	0.078
Distance between nozzle [m]	0.25	0.33	0.5	1
Trailing velocity [m/s]	2.53	1.87	1.24	0.94

Another option is to design a wider draghead so the optimum nozzle distance will fit. Due to dimension restrictions this is often not an option. For the SLK600 with 8 nozzles, the nozzles should be placed 0.4 m apart to dredge at 1 m/s. The total draghead width then becomes 3.2 meters, which is 1.2 meters wider than the original design.

4.4.2 Vlasblom's coefficient: alfa

The coefficient alfa is used in this study as an empirical coefficient in Vlasblom's equation and in P. de Jong study for the ratio between the penetration depth and the cavity width. In this subparagraph, first the empirical coefficient of Vlasblom is discussed with the conclusions from Wegenaar's study, after that the value is verified to see the influence on the jet production (mass flux). Finally, a relation between the ratio and empirical coefficient is shown.

Wegenaar compared the production results of his research with Vlasblom's equation (Wegenaar, 2014). For the experiments, Wegenaar found a value α of 0.14±0.034 (d50: 284 μ m) and 0.13±0.037 (d50: 142 μ m) (Wegenaar, 2014). His conclusion was that the variable α is related to the soil type and that Vlasblom underestimates the coefficient with an average factor of 1.3-1.4 depending on the soil type. Although the values found by Wegenaar are fairly close to the value given by Vlasblom this results in a serious larger production. From Wegenaar's research also not a clear relation can be drawn while the influence of the factor α cannot be ignored, see Figure 96.

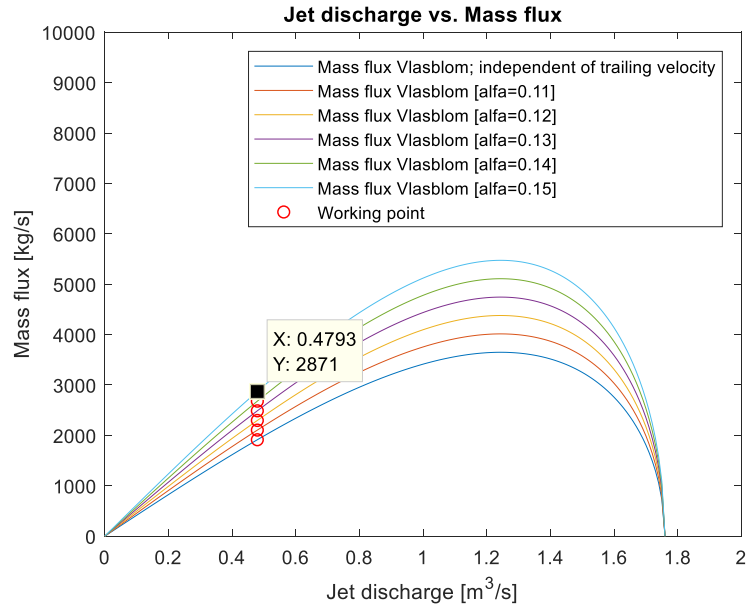


Figure 96: Mass flux comparison for different values of α

From the analysis of the study of P. de Jong appears that the coefficient of Vlasblom, α , and the ratio between the penetration depth and the cavity width are related to each other. This suggests that Vlasblom's coefficient α therefore applies for a certain trailing velocity, nozzle area, jet discharge and sand characteristics.

This is verified with the jet penetration and production data in the report of P. de Jong and the following equations:

$$\begin{aligned}
 M_s &= \alpha_{vlasblom} * I = \alpha_{vlasblom} * \rho_w * Q_j * u_0 = \alpha_{vlasblom} * \rho_w * Q_j * \sqrt{\frac{2 * p_j}{\rho_w}} \\
 &= \alpha_{vlasblom} * \rho_w * P_j * \sqrt{\frac{2}{\rho_w * p_j}} \left[\frac{kg}{s} \right]
 \end{aligned}
 \tag{eq. 205}$$

$$P_z = C * P_{sp}^\beta \left[\frac{m^3}{s} \right]
 \tag{eq. 206}$$

Equation 205 and 206 can be equated by:

$$P_z * \rho_s * (1 - n_0) = M_s = \alpha_{vlasblom} * \rho_w * P_j * \sqrt{\frac{2}{\rho_w * p_j}} \left[\frac{kg}{s} \right]
 \tag{eq. 207}$$

$$\alpha_{vlasblom} = \frac{P_z * \rho_s * (1 - n_0)}{\rho_w * P_j * \sqrt{\frac{2}{\rho_w * p_j}}} [-]
 \tag{eq. 208}$$

Now with the production data from the tables in P. de Jong's study the value for $\alpha_{vlasblom}$ can be determined. Assuming a porosity of 0.4, ρ_s of 2650 kg/m³, ρ_w of 1025 kg/m³, this gives the following results, shown in Table 14 and Table 15.

Table 14: Production data, $k=0.0024$ cm/s, $p_j=7.5$ bar, $d_{50}=105$ μ m, $D_n=14$ mm, $P_j=4471$ Nm/s (Jong, 1988)

Trailing velocity [m/s]	Production [m ³ /s]	$\alpha_{vlasblom}$
0.5	0.0131	0.089
1	0.0112	0.076
1.5	0.00996	0.0677
2	0.0093	0.0632

Table 15: Production data, $k=0.0062$ cm/s, $p_j=7.5$ bar, $d_{50}=105$ μ m, $D_n=14$ mm, $P_j=4471$ Nm/s (Jong, 1988)

Trailing velocity [m/s]	Production [m ³ /s]	$\alpha_{vlasblom}$
0.5	0.0263	0.179
1	0.0226	0.154
1.5	0.0201	0.137
2	0.0188	0.128

It appears that $\alpha_{vlasblom}$ actually also changes with the trailing velocity and that the calculated value seems close to the value, 0.1, given by Vlasblom.

4.5 Conclusion

The aim of this chapter was to determine the jet production of the draghead. The jet penetration and cavity width, depend on many variables of which the most important are: the permeability, jet pressure, nozzle diameter and the trailing velocity. Current relations are all based on data from experiments conducted in the lab. When the soil characteristics change, the coefficients have to be adjusted accordingly. Due to lack of experimental data, the choice was made to use Vlasblom's widely used jet production relationship with an empirical coefficient, α , of 0.1.

The results show that the penetration depth decreases for increasing trailing velocities and then levels out somewhat. Furthermore, from the measurement data it can be concluded that the cavity width also decreases with increasing trailing velocities. Therefore, it is assumed that the penetration depth is equal to the cavity width. Although it must be taken into account that this underestimates the production at low trailing velocities (<1 m/s) and overestimates at higher velocities (> 1 m/s).

With this assumption, overlap of the scour holes takes place at low trailing velocities when the nozzles are positioned too close together. By increasing the trailing velocity, the penetration depth and thus the cavity width decreases. The optimum trailing velocity for jetting, is found when the cavity width is equal to the optimal cavity width ($w_c = w/n_n$). At velocities higher than the optimum, the production and jet mixture density are constant. At velocities below the optimum, the density increases steadily when the velocity is increased.

Results showed that by decreasing the number of nozzles and keeping the nozzles surface equal, the distance between the jets can be enlarged so that no potential production loss occurs. In addition, it has been seen that the jet production is strongly related to the jet power of the pump. Briefly put, the more jet power used, the higher the jet production.

5 Cutting production

The purpose of this chapter is to describe how the cutting production of the draghead and the corresponding draghead trailing forces can be determined in relation with the trailing velocity. The cutting production is defined as the amount of in situ soil that is excavated by the cutting teeth. The draghead trailing forces are the forces which the draghead (including the visor) experiences while moving through the bed. To determine the cutting production first the layer thickness that is going to be excavated needs to be estimated. With a given trailing velocity and visor width then follows the situ cutting production.

The cutting teeth are attached to the visor of the draghead. When the visor is dragged through the soil, horizontal- and vertical reaction forces arise on the cutting teeth. Depending on the angle between the blade and the soil layer (the blade angle) in a different force magnitude ratio as discussed in chapter 3. The other forces that are working on the visor have also already been discussed in chapter 3 and will be applied in this chapter. These are the vacuum force, the sled force, the friction force and the gravity force of the submerged weight of the visor itself.

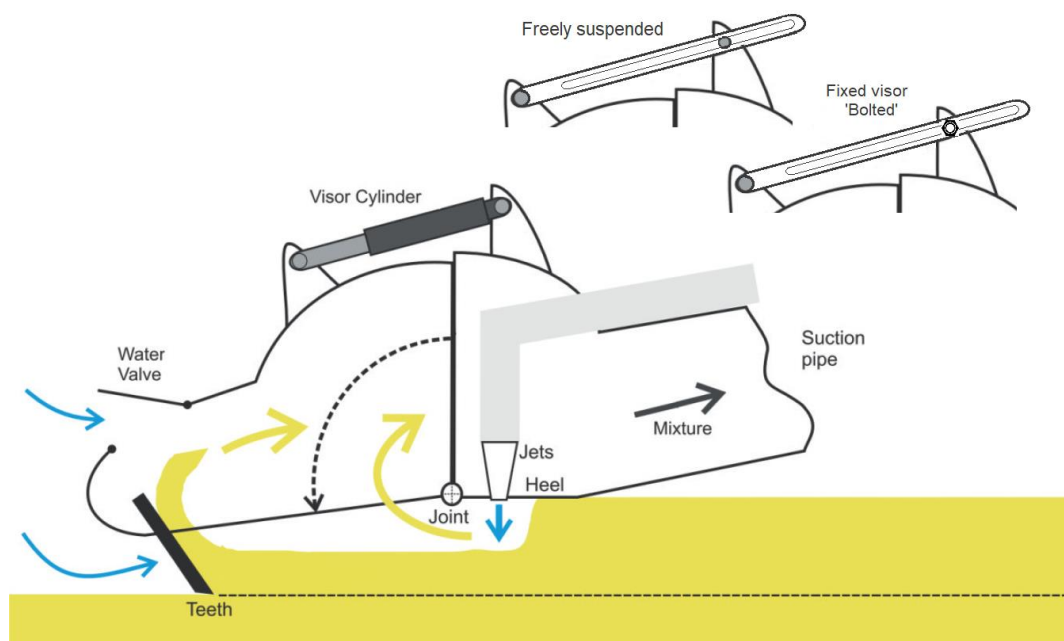


Figure 97: Cutting production visualization, with different visor suspension types. Source: (Bergh, Osnabrugge, & Keizer, 2015), modified

The visor is attached to the heel of the draghead by a hinge. The hinge ensures, besides the force transfer from the visor to the draghead, that the visor is able to rotate. In addition to the hinge attachment point, is the visor guided or secured at the top. Different options are used: The first option is a freely suspended visor, whereby the visor is able to move up and down in a slot. The length of the slot then determines the degrees of movement of the visor. Another option is to fix the visor on a certain position in the slot. The bar is then bolted on the draghead side of the slot. In this way the total layer thickness is fixed. The last option is to insert a cylinder between the visor and the draghead. The cylinder pressure can be regulated to give a certain counter force to push the visor downwards. In practice, most of the time is dredged with a freely suspended visor. The standard version of the Damen SLK600 is also of this type and therefore further analysed in this chapter in section 3.3.

In the previous chapter the working principle of the jets and the jet production is estimated. For a freely suspended visor, the jets are of big influence on the working principle of the visor and with that the cutting production. Because the jets have a certain penetration depth, the soil loses its strength in this layer and the resulting mixture can easily be pumped upwards. The visor will drop till a solid bed layer is reached which lead to a cutting layer when penetration of the teeth is deep enough. This is visualized in Figure 97, where also the three most common suspension possibilities are clarified.

The different forces on the visor cause a moment around the hinge of the visor. When this moment is equal to zero it means the visor is in an equilibrium position. The equilibrium position of the visor is the position in which the visor is in a static position. The equilibrium depends on many different factors and to take all factors into account, the system is modelled. When the trailing speed is increased, the equilibrium position changes, because the different forces on the visor change and the jet layer thickness decreases as was shown in paragraph 4.2.2.1. By looking at what the cutting layer thickness is at each equilibrium position, the cutting production can be determined per trailing velocity. This is a brief explanation of the entire cutting production model, but will be clarified in more detail in section 5.2 with the aid of visualizations and the force- and momentum balance in the model description.

In the literature section, the basic cutting production model will be described shortly. In section 5.3, the case study for the Damen SLK600 draghead visor is performed for the method described in section 5.2. Here the estimated production and trailing forces of the visor are calculated. The results from the calculations can be used in the fourth paragraph for the optimization of the cutting production. The cutting forces are one of the larger contributors to the total resistance that have to be overcome by the propulsion system. With the acquired cutting knowledge, in future design considerations, the trailing forces could be reduced and the control of the draghead can be adjusted to optimize the production.

Notation

Latin		
h_b	Blade height	m
$h_{i,cut}$	Cutting layer thickness	m
$h_{i,jet}$	Jet layer thickness	m
$h_{i,sled}$	Sled layer thickness	m
$h_{i,total}$	Total layer thickness / settlement visor	m
l_3	Visor length	m
$l_{3,a}$	Length visor hinge - application point vacuum force	m
$l_{3,b}$	Length visor hinge - application point gravity	m
$l_{3,c}$	Length visor hinge - application point cutting force	m
$l_{3,d}$	Length visor hinge - application point sled force	m
P_{cut}	Cutting production	m ³ /s
v_t	Trailing velocity	m/s
w	Draghead width	m
w_{in}	Visor opening width	m
$w_{wearing}$	Wearing piece width (one side)	m
Greek		
α_{blade}	Blade angle	°
β	Shear angle	°
γ	Visor angle	°
γ_2	Angle between visor and blade	°
ξ	Correction opening visor geometry	-

5.1 Literature

In literature, the cutting production is often described by the following formula:

$$P_{cut} = w * h_{i,cut} * v_t \quad (\text{eq. 209})$$

Where $h_{i,cut}$ is the cutting layer thickness, w is the width of the draghead and v_t the trailing velocity of the vessel. The question is how large this cutting layer thickness is and how it relates to the trailing velocity for a freely suspended visor.

P. de Jong has done extensive research into the jet and cutting production of a draghead (Jong, 1988). The production calculations are however based on a lot of basic assumptions for the layer thicknesses. For example he worked with a fixed visor with a constant layer thickness. Depending on the penetration depth of the jets, the cutting layer thickness decreased. The general conclusion from the research is that with a combination of jets and cutting, a higher production is achieved than when only jets are used. In addition, the needed power to overcome the trailing forces and to keep the vessel on the corresponding trailing velocity, is calculated for both cases. The production/ power ratios between cutting and jetting and only jets are similar according to de Jong. His results are shown in Figure 98.

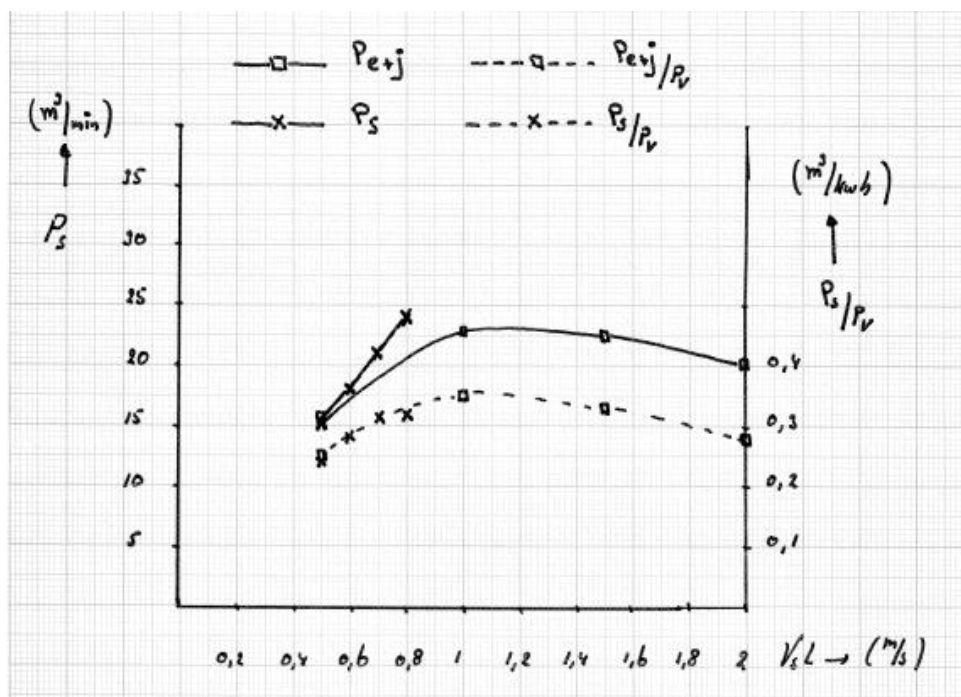


Figure 98: Production with teeth (P_s) and the combination of teeth and jets (P_{e+j}). On the right hand side of the graph the production and power ratio's for different trailing velocities. Source: (Jong, 1988)

5.2 Model description

In the introduction of this chapter has already been explained globally how the visor works and what the cutting layer thickness and production is. In this section, this story will be elaborated on in more detail and will go deeper into the theory of how an estimation of the cutting layer thickness can be determined, and thus the cutting production and associated trailing forces can be calculated.

First will be explained in sub-section 5.2.1, how the visor is schematized. Below, a cross section of the draghead is shown. On the left side of the dotted line, the visor is shown, on the right the 'fixed' part of the draghead. The schematisation is used to simplify the forces and momentum balances. The assumptions used for this will be named here. The biggest assumption is that it is a 2D model that is applied across the entire width of the visor. This is assumed because the visor moves in the x-z plane and pivots around the y-axis (2D). In addition, all the forces described in chapter 3 are an approximation of the 3D forces in 2D.

In 5.2.2 the equilibrium-moment method is explained and how this method can be used to determine the cutting layer thickness. In 5.2.3 the approach of the cutting production estimation is explained and its interaction with the jet production. In the final sub-section, 5.2.4, the method to calculate the resultant force in the visor hinge by the forces on the visor is described.

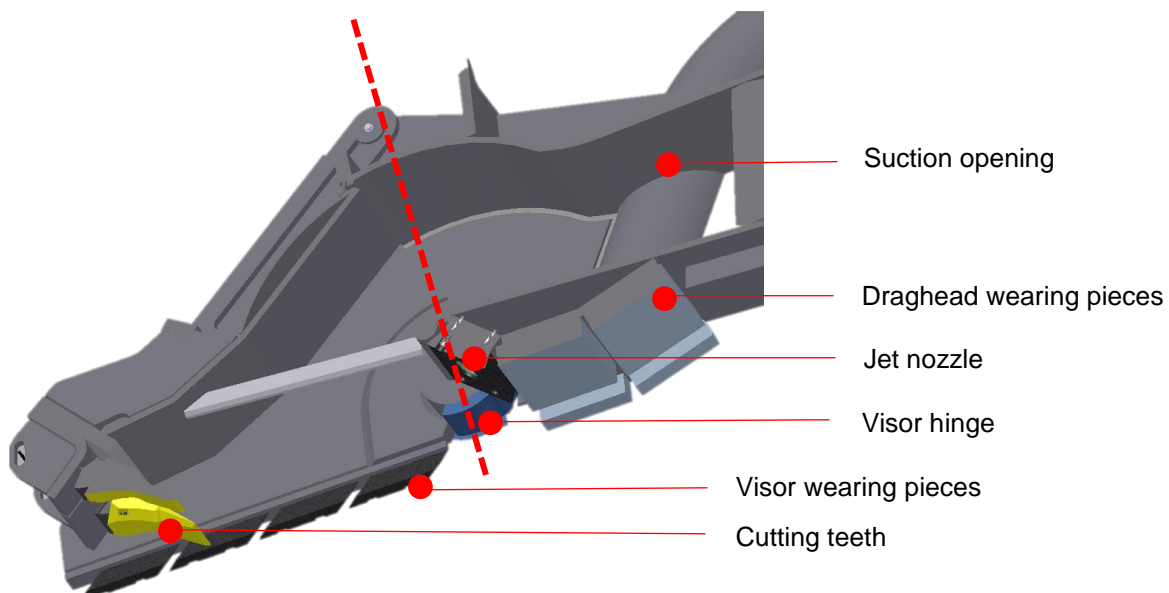


Figure 99: Draghead cross section, movable visor part on the left of the dotted line

5.2.1 Visor geometry

The visor is schematized as a long arm that is connected with a hinge to the draghead in point C, see Figure 100. The angle of the arm with respect to the x-axis, is the visor angle, γ . The layer thicknesses increase as the angle increases. As shown in the figure, is assumed that all forces of the visor, apply on this arm, which can be compared with the visor wearing pieces. Just in front of the hinge are the jet nozzles located, which inject water with high velocity, vertically into the soil. Because of the forward speed of the draghead, it seems as if this volume flow is deflected in the opposite direction of the trailing speed, and moves straight into the visor.

The jets significantly influence the behaviour of the visor. The maximum jet penetration depth, $h_{i,jet}$, and jet production are calculated in the previous chapter. It has been assumed that the depth of the soil layer that is reached is removed in its entirety by the jets. It is also assumed that the ground layer underneath the jet layer, is not affected by the jet. Grain stresses that change due to under pressure in the pores that will arise due to high speed erosion, as described in chapter 4, are not included. The soil layer that is cut has the initial situ soil properties. The situ soil layer that is excavated by the teeth in this model, is equal to the length from the tip of the teeth to the bottom layer, reached by the jets. Shortened to $h_{i,cut}$.

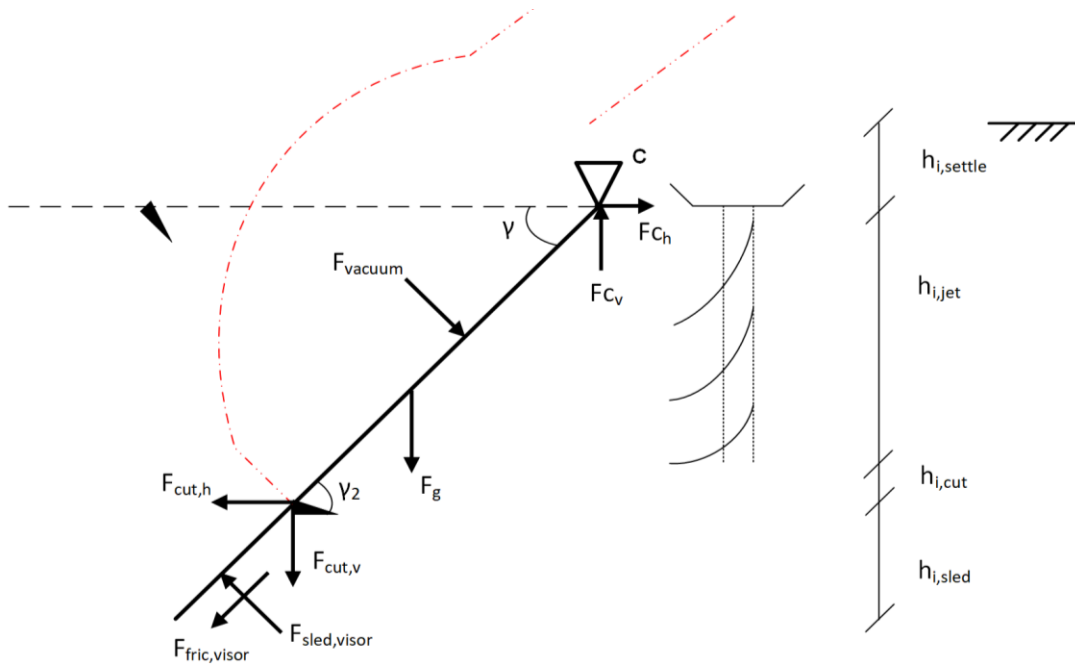


Figure 100: Schematization of the visor geometry, forces and layer thicknesses

The cutting teeth that are aligned in the direction of the y-axis, are slightly apart from each other. The idea behind this is that water can flow more easily to the shear plane to avoid under pressure in the sand layer and to allow cavitation to take place less quickly. In the cutting model of Miedema in chapter 3, this 3D effect is not included. A downside of the space between the teeth, is that this may cause spillage of the cutted layer. Assumed is that this does not happen.

Another factor that is important to mention is that for some dragheads, the teeth are not fixed at the end of the visor but there is still a relatively long wearing piece behind the teeth row. When the visor is positioned under an angle, this part makes contact with the sand rather than the teeth. This is clearly visible in the schematic representation where this layer thickness is indicated with $h_{i,sled}$. This causes a similar force as described in chapter 3 for the draghead moving through a soil layer.

5.2.1.1 Visor forces and points of application

Figure 102 shows once again where the force on the visor engage, and in addition the names of the lengths. The total length of the visor arm is L_3 . Gravity force, due to the submerged weight of the visor, engages in the centre of gravity of the visor and is always directed in the vertical direction and not depended on the visor angle. The length from the centre of gravity to the hinge is named with $l_{3,b}$.

Closer to the hinge applies the resultant force of the vacuum force. The vacuum force is a consequence of the under pressure in the draghead that is created by 'pushing away' the mixture by the dredge pump. The opening of the draghead determines the magnitude of the force but also where the resultant force engages. There is assumed that the surface area of the visor opening is equal to: the length of the tip of the cutting teeth up to the hinge of the visor, times the width of the inside of the visor. For the vacuum force it is assumed that it engages in the middle of the vacuum opening. This means that this arm is equal to half the length of the point where the cutting teeth are attached to the hinge. The length becomes:

$$l_{3,a} = \frac{l_{3,c}}{2} \quad (\text{eq. 210})$$

The cutting forces on the teeth can be estimated with the pore pressure cut theory model of Miedema, described in 3.3.1.7. The point where the cutting force engages is simply determined by the placement of the cutting teeth in the visor. The length of this application point to the visor is shortened to, $l_{3,c}$.

The cutting teeth are positioned under an angle in the visor, γ_2 . The ratio between the horizontal- and vertical forces will differ, depending on the blade angle. In some cases the vertical force is directed downwards and

causes the visor to bury itself. When the opposite happens the visor will move upwards. The blade angle of the teeth are depended on the visor angle and can be calculated with the following relation:

$$\alpha_{blade} = \gamma_2 - \gamma \tag{eq. 211}$$

In Figure 101, this relation is illustrated and clarifies that is important under which angle the cutting teeth are positioned in the visor. When the blade-visor angle, γ_2 , is smaller than the visor angle the cutting theory is not applicable anymore. Instead the wedge theory should be used as described by Miedema for a blade with a large angle. This will be discussed later on in 5.4.

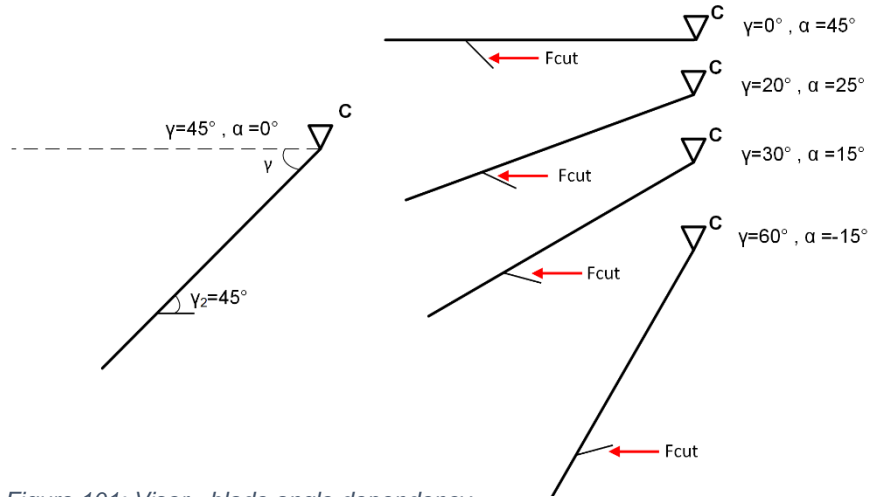


Figure 101: Visor - blade angle dependency

The sled force, resulting from the wearing pieces moving through the soil layer, are determined in the same way as the draghead sled forces in chapter 3. This is an assumption, because the soil could also behave as described in the wedge theory. The sled forces engage at the end of the wearing pieces. The length of this arm, from the engagement point to the hinge is $l_{3,d}$, and described with:

$$l_{3,d} = \frac{l_3 - l_{3,c}}{2} \tag{eq. 212}$$

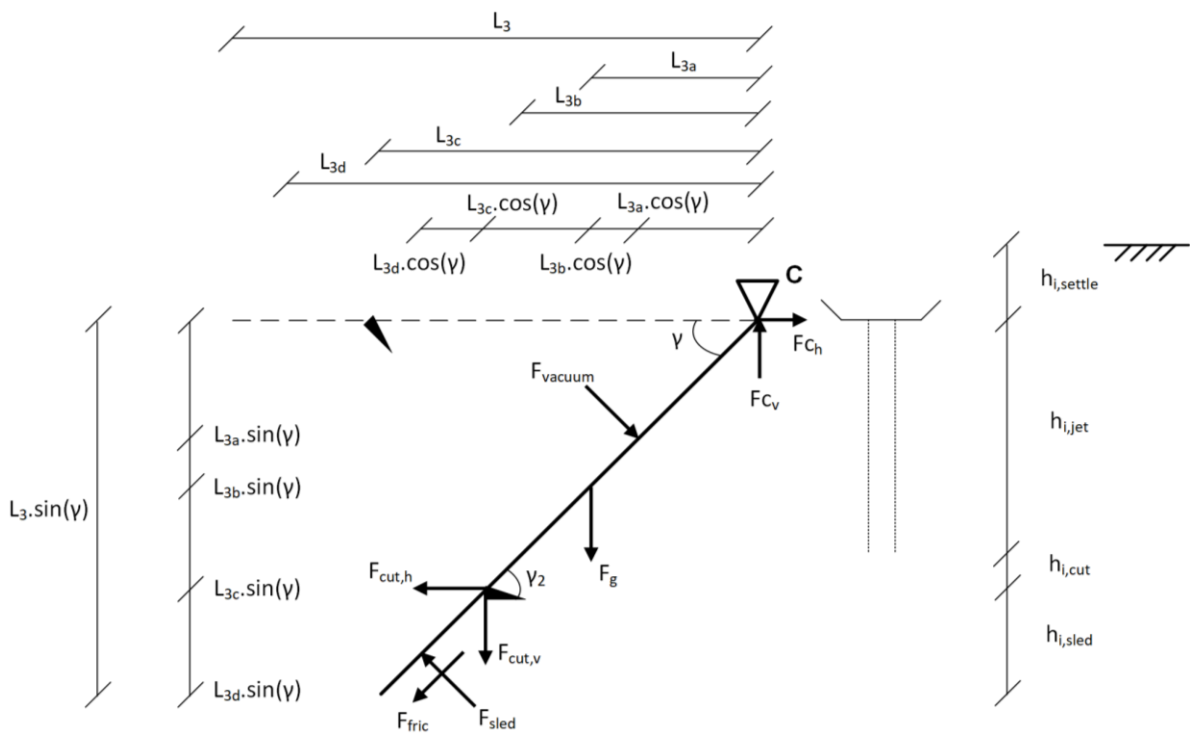


Figure 102: Visor forces and moment arm definitions

5.2.1.2 Determining the layer thicknesses

In order to calculate the cutting production, the cutting layer thickness must be known. The total layer thickness that affects the visor is defined as: $h_{i,total} = l_3 * \sin(\gamma)$. The total layer thickness can be divided into three different parts, consisting of a sled layer, a cut layer and a jet layer. The ratio in which these layers take place depends on the angle of the visor, due to the geometric dependence of the layers. The jet layer does not depend on the visor angle, but it influences the other layer thicknesses. In chapter 4 is shown that the penetration depth of the jets differs per trailing velocity, the ratio of the three layers changes continuously. So the two main variables that determine the final layer thickness are: the visor angle and the trailing velocity. The sled layer thickness can be defined as: $h_{i,sled} = (l_3 - l_{3,c}) * \sin(\gamma)$. And the cutting layer thickness as:

$$h_{i,cut} = h_{i,total} - h_{i,jet} - h_{i,sled} = l_{3,c} * \sin(\gamma) - h_{i,jet} \quad (\text{eq. 213})$$

To show the effect of the trailing velocity on the layer thicknesses, the visor is set at a fixed angle of 20 degrees. Assuming the total length of the visor is 1,2 m, this brings the total layer thickness to $1,2 * \sin(20) = 0,41$ m. The jet layer thickness is, as already indicated, not dependent on the visor angle but on the trailing velocity and will be smaller or bigger than the total layer thickness. This results in two statements with different consequences:

- $h_{i,jet} > h_{i,total}$ (eq. 214)

This will result in, that a part of the jet flows underneath the visor, and so part of the jet production gets lost. The visor will not be in equilibrium yet and will probably sink down till a solid layer has been reached.

- $h_{i,jet} < h_{i,total}$ (eq. 215)

At this point, the visor has reached a solid layer. There are two new consequences that can occur:

- $h_{i,jet} > h_{i,total} - h_{i,sled}$ (eq. 216)

The jets are flowing underneath the cutting teeth. Still part of the jet production gets lost. The wearing pieces are currently resting on the bed. The sled layer thickness increases slowly as the trailing velocity increases. The sled layer thickness is defined with the following relation: $h_{i,sled} = h_{i,total} - h_{i,jet}$. This continuous by and increasing trailing velocity until the last statement:

- $h_{i,jet} < h_{i,total} - h_{i,sled}$ (eq. 217)

From this moment, $h_{i,sled}$ is maximum and equal to $h_{i,sled} = h_{i,total} - h_{i,jet}$. The cutting production also increases from this moment on, as the trailing velocity rises, and is equal to $h_{i,cut} = l_{3,c} * \sin(\gamma) - h_{i,jet}$. This layer thickness / trailing velocity dependence gives the following result for the settings of the jets, given in chapter 4:

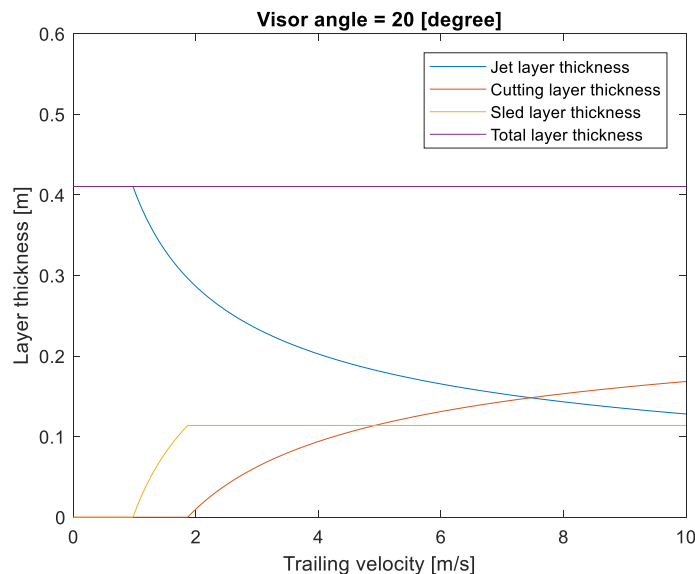


Figure 103: Layer thicknesses versus the trailing velocity for a fixed visor angle of 20 degrees

5.2.2 Visor equilibrium-moment method

In 5.2.1.2 is shown that for a fixed angle, the layer thickness can be calculated per trailing velocity. However this does not ensure that the visor is in balance. As indicated, the visor could sink through the fluidized mixture when the jets flow underneath the visor. The forces on the visor must be in balance in order to keep the visor in a stable position. The layer thicknesses are different at each trailing speed, but the layer thicknesses together with the trailing velocity, will ultimately determine the forces on the visor. When the moment around the hinge is calculated, it can be determined at which speed this moment becomes zero and the system is in equilibrium. The moment on the hinge is as follows:

$$\sum M_{c,visor} = F_{vac} * l_{3a} + F_{gravity} * l_{3,b} * \cos(\gamma) - F_{cut,h} * l_{3,c} * \sin(\gamma) + F_{cut,v} * l_{3,c} * \cos(\gamma) - F_{sled} * l_{3,d} = 0 \quad (\text{eq. 218})$$

Here a problem occurs, there is only one equation and there are two variables, namely: the trailing velocity and the visor angle. This is because the cutting and sled forces on the visor are dependent on the trailing velocity and the visor angle. This can be solved by determining for every position of the visor, so for every fixed angle, the equilibrium-moment. Then is known at what speed the position of the visor corresponds to a certain visor angle. The angle of the visor determines the layer thicknesses, together with the jet layer thickness is now known what the different layer thicknesses are at each speed, as was explained in 5.2.1.2. This relation is visualized in the red outlined part of the flow chart in Figure 104.

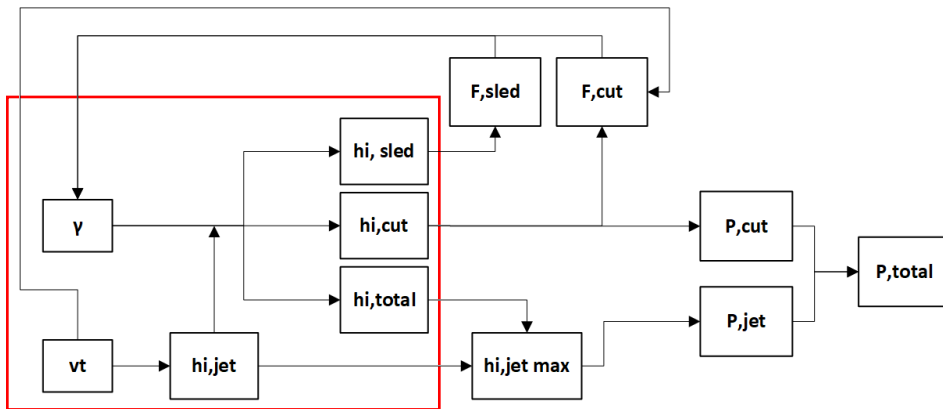


Figure 104: Flow chart of visor angle and trailing velocity influence on the layer thicknesses

When the momentum balance for a fixed visor angle of 20 degrees and a variable trailing velocity is solved, this gives the result as for example is displayed on the left side of Figure 105. With the calculated trailing velocity, from the point where the sum of the moment around C is equal to zero, and the corresponding jet layer thickness, $h_{i,jet}$, and visor angle, can the other layer thicknesses be calculated. By solving these momentum equations for more visor angles, an accurate curve of the layer thicknesses per trailing velocity is obtained, while the visor is constantly in balance. This curve is shown on the right-hand side of Figure 105. The calculated layer thicknesses can be used again to calculate the different forces on the visor with the corresponding trailing velocity and visor angle.

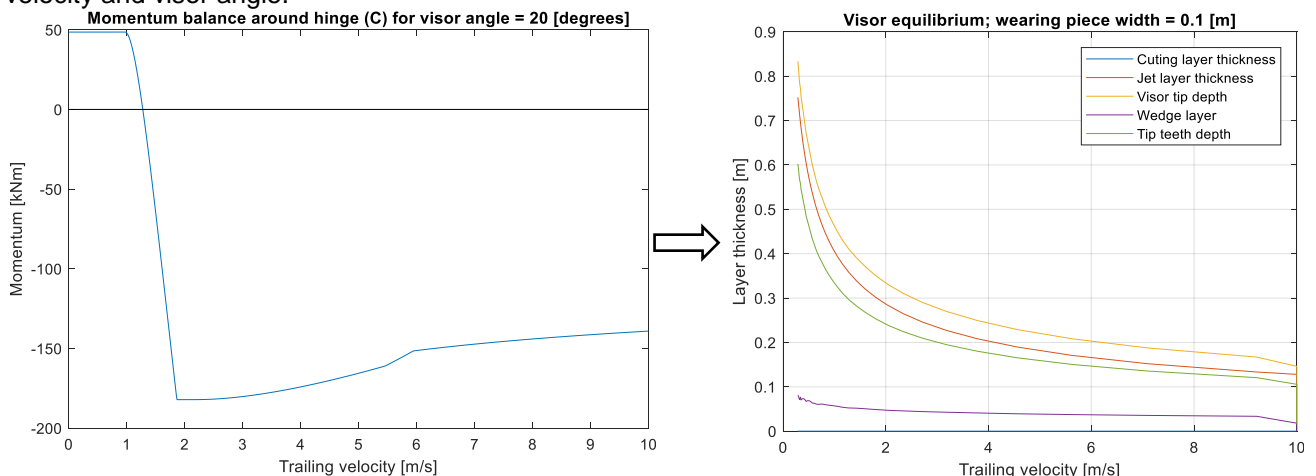


Figure 105: Momentum balance for a fixed visor angle in the left graph. In the right graph the calculated layer thicknesses for multiple solved momentum balances for different visor angles

5.2.3 Soil excavation forces of the visor

When the visor is in equilibrium, the forces for that equilibrium point can be determined. The layer thicknesses, visor angle and trailing velocity now determine the force on the visor. There are two force balances, one for the horizontal direction and one for the vertical direction:

$$\sum F_{v,visor} = 0 = F_{c,visor,v} - F_{vacuum,v} - F_{g,visor} - F_{cut,v} + F_{sled,v} - F_{fric,v} \quad (\text{eq. 219})$$

$$\sum F_{h,visor} = 0 = F_{c,visor,h} + F_{vacuum,h} - F_{cut,h} - F_{sled,h} - F_{fric,h} \quad (\text{eq. 220})$$

The horizontal and vertical components of the forces working in parallel or perpendicular direction on the visor follow from a force derivation that is included in the appendix. The resultant force in the visor hinge, $F_{c,v}$ en $F_{c,h}$, follow from the force balance and become:

$$F_{c,visor,v} = F_{vacuum,v} + F_{g,visor} + F_{cut,v} - F_{sled,v} + F_{fric,v} \quad (\text{eq. 221})$$

$$F_{c,visor,h} = -F_{vacuum,h} + F_{cut,h} + F_{sled,h} + F_{fric,h} \quad (\text{eq. 222})$$

5.2.4 Cutting production & jet dependency

In section 5.1 is the basic formula to calculate the cutting production given with equation 209. With the trailing velocity dependent cutting layer thickness, the cutting production can be determined per velocity step. As is shown in the flow chart of Figure 104.

Because it is known what the equilibrium position is per trailing velocity, a jet production limit can be calculated which may cause spillage. At the moment the jet flows underneath the cutting teeth, this will no longer be pumped into the draghead and this part will be lost. As a result, the maximum jet penetration depth the jets can have, depends on the visor angle and is equal to:

$$h_{visor} = h_{i,jet\ max} = l_{3,c} * \sin(\gamma) \quad (\text{eq. 223})$$

For $h_{i,jet\ max} > h_{i,jet}$, loss of the jet production occurs which is equal to

$$P_{jet,spillage} = (h_{i,jet\ max} - h_{i,jet}) * w_{c,jet} \quad (\text{eq. 224})$$

5.3 Model results & discussion

In order to determine the cutting production of the SLK 600, the method explained in 5.2 is again applied in a case study. This will give an impression of how the visor behaves depending on the trailing speed.

In the remainder of the paragraph, the calculated forces on the visor and the cutting layer thickness will be calculated with the equilibrium-moment method. Following with the production and its limits, to conclude with the total trailing forces of the visor and the draghead. The required dimensions of the SLK600 for the calculations, are shown in the table.

Table 16: Visor dimensions and variable values used in the case study

Variable	Symbol	Value	Unit
Surface area opening visor	$A_{suction}$	0.867	m ²
Standard gravity	g	9.81	m/s ²
Arm length visor	l_3	1.200	m
Arm vacuum force poa – hinge	$l_{3,a}$	0.434	m
Arm gravity force poa – hinge	$l_{3,b}$	0.675	m
Arm cutting force poa – hinge	$l_{3,c}$	0.867	m
Arm sled force poa – hinge	$l_{3,d}$	1.034	m
Blade length	l_b	0.128	m
Mass visor	m_{visor}	1800	kg
Number of cutting teeth	n_{teeth}	10	-
Specific compaction force	q_{sled}	6	kg/cm ³
Mixture velocity	v_m	5	m/s
Volume visor	V_{visor}	0.2186	m ³
Cutting teeth width	w_{teeth}	0.109	m
Width draghead (outside)	w_{out}	2.272	m
Width draghead (inside)	w_{in}	2.037	m
Width wearing piece	$w_{wearing}$	0.1	m
Dredging depth	z	16.9	m
Shear plane angle	β_{shear}	20	°
Dilatation	ε	0.12	-
Visor – blade angle	γ_2	45	°
Correction opening visor geometry	ξ	3	-
Water density	ρ_w	1025	kg/m ³
Mixture density	ρ_m	1350	kg/m ³

5.3.1 Visor forces

As explained in 5.2.2 are the layer thicknesses dependent of the visor angle and must be calculated per angle, using the moment equilibrium method, what the corresponding trailing velocity per equilibrium position is. To show the effect of the different forces on the visor, the forces in this subsection are calculated and plotted against the trailing velocity. **This is done, as an example, for a fixed visor angle, γ , of 20 degrees.**

5.3.1.1 Gravity force

The gravity force working on the visor is the submerged weight times the gravity constant. The total weight of the visor is, m_{visor} and its volume is, V_{visor} . Because of buoyancy this results in an effective mass, $m_{visor,eff}$, and a gravity force, $F_{g,visor}$, of:

$$m_{visor,eff} = m_{visor} - (V_{visor} * \rho_w) = 1800 - (0.2186 * 1025) = 1576 \text{ [kg]} \quad (\text{eq. 225})$$

$$F_{g,visor} = m_{visor,eff} * g = 1576 * 9.81 = 15.46 \text{ [kN]} \quad (\text{eq. 226})$$

5.3.1.2 Vacuum force

The vacuum force can be calculated with the method explained in chapter 3. The final equation is repeated here:

$$F_{vacuum,N} = \xi * \frac{1}{2} * \rho_m * v_m^2 * A_{suction} \quad (\text{eq. 227})$$

Assuming for the coefficient, ξ , a value of 3. The velocity of the mixture, v_m , depends on the total volume flow that is transported through the suction pipe with a density, ρ_m . These are calculated in chapter 5 and will be variable and depending on the trailing velocity. For simplicity, a constant speed of 5 m/s and a mixture density of 1350 kg/m³ has been chosen. This corresponds to the usual volume flows that are achieved with the SLK600. The opening of the visor has a width of, w_{visor} , and a length equal to, $l_{3,c}$. With this the vacuum force becomes:

$$A_{suction} = l_{visor,opening} * w_{in} = l_{3,c} * w_{in} = 0.867 * 2.037 = 1.77 \text{ [m}^2\text{]} \quad (\text{eq. 228})$$

$$F_{vacuum,N} = 3 * \frac{1}{2} * 1350 * 5^2 * 1.77 = 89.41 \text{ [kN]} \quad (\text{eq. 229})$$

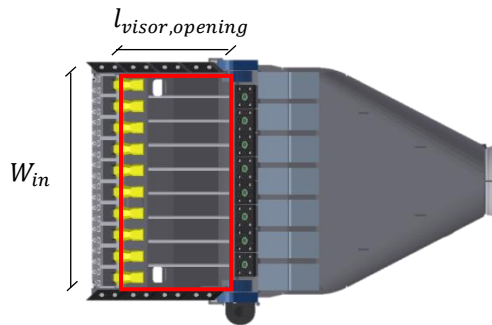


Figure 106: Visor vacuum opening surface

5.3.1.3 Cutting force

The cutting force on the teeth are estimated with the pore pressure model. The force is, among other things, depending on the trailing velocity, the visor angle and the cutting layer thickness. The calculation of the cutting forces are already explained in chapter 3. However in this section the pore pressure model calculations are the visor angle and the cutting layer thickness are variable!

For a visor angle of 20 degrees, a visor-blade angle, γ_2 , of 45 degrees, a variable layer thickness and variable trailing velocity, follows the next result for the SLK600:

Blade height / cutting thickness ratio

The blade height, h_b , is dependent on the blade angle and the blade length, l_b , which is 0.128 m. By repeating of equation 144:

$$h_b = l_b * \sin(\alpha_{blade}) = l_b * \sin(\gamma_2 - \gamma) = 0.128 * \sin(45 - 20) = 0.054 \text{ [m]} \quad (\text{eq. 230})$$

The ratio between the blade height and the cutting layer thickness is important factor of the cutting force, as can be seen in the equations 115 - 118. When the cutting layer thickness is too small the pore pressure model fails. Because the cutting layer thickness increases, as can be seen in Figure 103, the cutting layer thickness is small for lower velocities. By setting a limit for a minimum cutting layer thickness this can be solved. This can be done because for small cutting layers the cutting force is negligible. The ratio is given by:

$$\frac{h_b}{h_{i,cut}} = \frac{0.054}{h_{i,cut}} \quad (\text{eq. 231})$$

By setting a limit for $h_{i,cut}$, of 0.02 m, the ratio h_b/h_i versus the trailing velocity becomes:

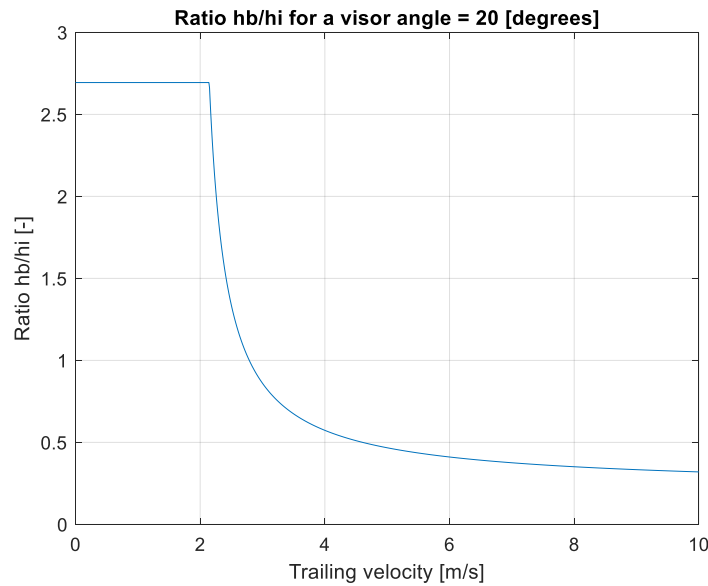


Figure 107: Ratio h_b/h_i for a blade height of 5.4 cm and a variable cutting layer thickness

Miedema showed in the 'Delft Sand, Clay & Rock Cutting Model', that the shear angle, β_{shear} , can be expressed in a formula when the internal friction angle, blade angle and h_b/h_i ratio is known (Miedema, The Delft Sand, Clay and Rock Cutting Model, 2014). This is however not taken into account in this calculation and the shear angle is assumed to be, constant, 20 degrees.

The length of the shear plane then follows by:

$$l_{max} = \frac{h_{i,cut}}{\sin(\beta_{shear})} \text{ [m]} \quad (\text{eq. 232})$$

Dimensionless pore pressure

The results of the pore pressure calculations show the dimensionless pore pressure in the shear and the blade in Figure 108 and Figure 109.

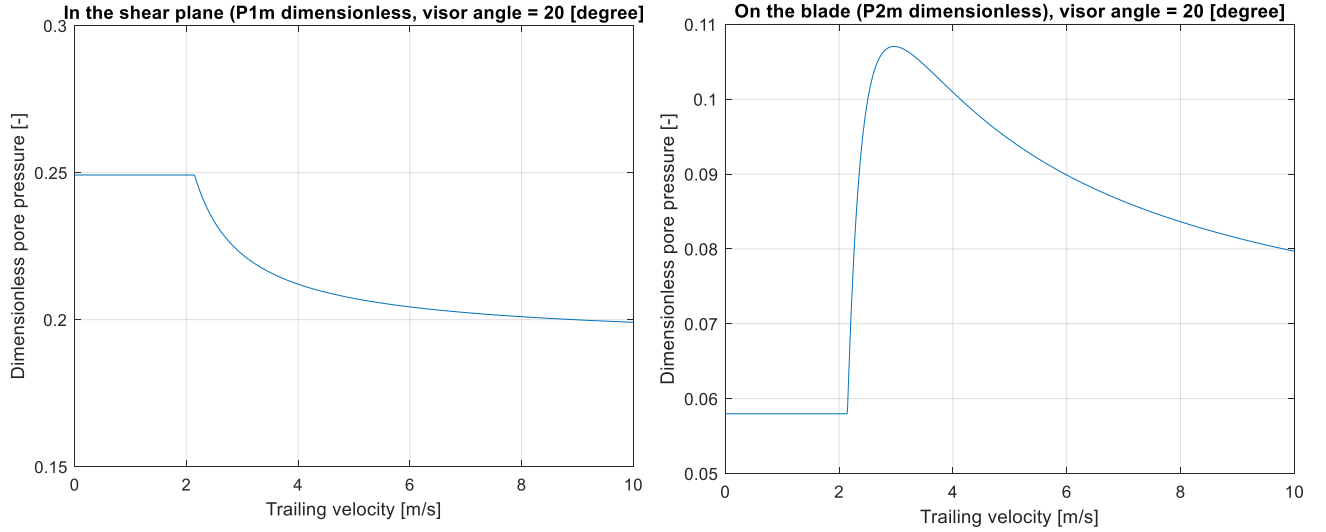


Figure 108: Dimensionless pore pressure in the shear plane Figure 109: Dimensionless pore pressure on the blade

With the dimensionless pore pressure the dimensionless cutting forces can be calculated. The dimensionless forces are not dependent on the trailing velocity but depend on the cutting layer thickness.

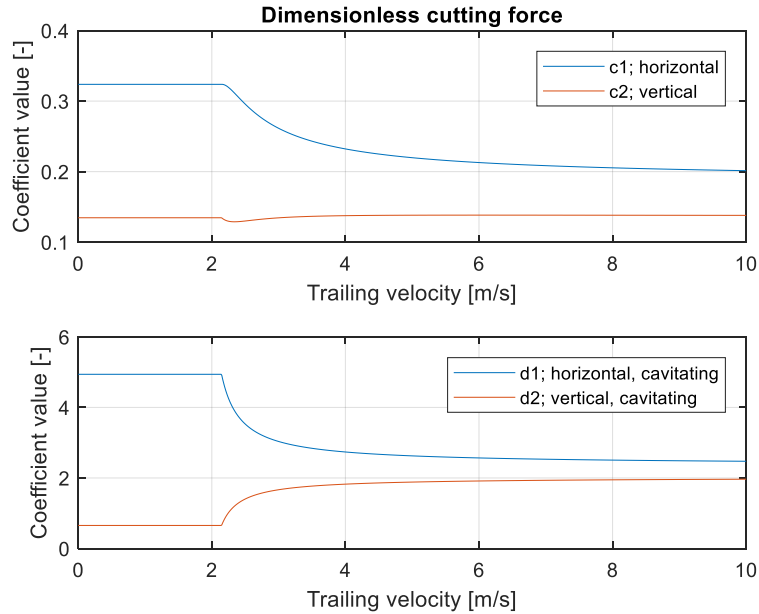


Figure 110: Dimensionless cutting force for a variable cutting layer thickness

For the non cavitating cutting force follows:

$$F_{ci} = \frac{c_i * \rho_w * g * v_c * h_{i,cut}^2 * \epsilon * w}{k_m} \quad (\text{eq. 233})$$

For the cavitating cutting force:

$$F_{ci} = d_i * \rho_w * g * (z + 10) * h_{i,cut} * w \quad (\text{eq. 234})$$

Where w is the total width of the cutting teeth which is equal to $w = w_{teeth} * n_{teeth} = 0.109 * 10 = 1.09$ m.

In Figure 111 and Figure 112, the horizontal and vertical cutting forces are shown. Because the cutting layer thickness is only present, in this case, the force will start to rise from a trailing velocity of around 2 m/s. Between 5 and 6 m/s, the cutting force will start to cavitate, which can be seen from kink in the line. The reason that both the horizontal and the vertical cutting force still increase, is because of the increasing cutting layer thickness.

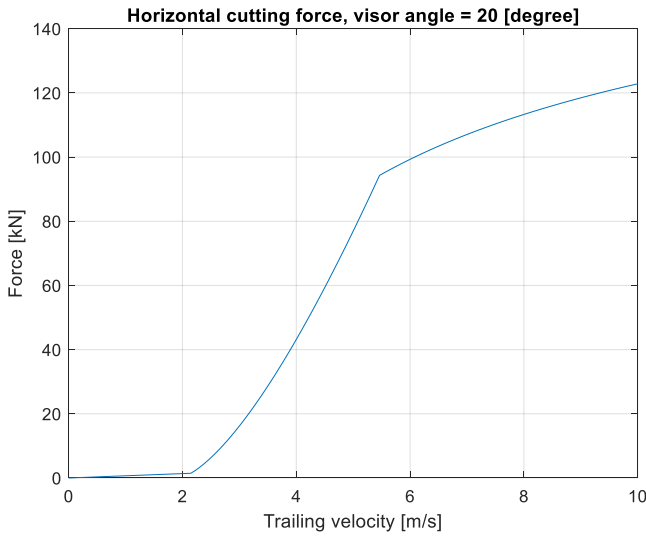


Figure 111: Horizontal cutting versus the trailing velocity

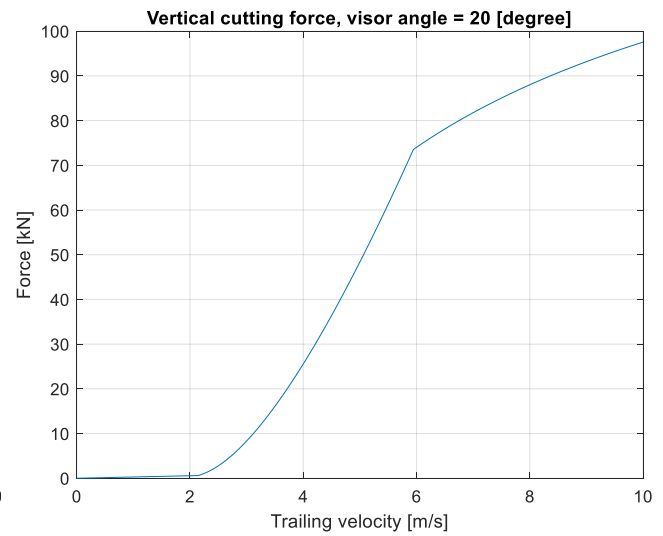


Figure 112: Vertical force versus the trailing velocity

5.3.1.4 Sled force

The sled forces are calculated with the compaction method shown in chapter 3. Knowing the 'settlement' of the visor, $h_{i,sled}$, because of a chosen visor angle and length of the visor, the force on the visor can be calculated. For a width of the wearing pieces on both sides and a specific compaction force of 6 kg/cm³. The sled force becomes:

$$F_{sled,N} = \frac{2 * w_{wearing} * h_{i,sled}^2 * q_{sled} * g}{2 * \sin(\gamma)} = \frac{2 * 0.1 * h_{i,sled}^2 * 6 * 9.81}{2 * \sin(\gamma)} = 5.89 * \frac{h_{i,sled}^2}{\sin(\gamma)} [kN] \quad (\text{eq. 235})$$

5.3.1.5 Friction force

The sled forces on the visor create a friction forces between the wearing piece surface and the bed layer.

$$\mu = \tan(\delta) = \tan(27) = 0.5 [-] \quad (\text{eq. 236})$$

$$F_{friction} = \mu * F_{sled,N} \quad (\text{eq. 237})$$

As was explained in 5.2.2 will the friction force not contribute to a moment around the visor hinge.

5.3.1.6 Total visor force overview

For a visor angle of 20 degrees, an overview of all the relative force working on the visor are shown in Figure 113. From the graph can be concluded that the sled force and vacuum force are dominant, in this case, for low trailing velocities and will determine in which position the visor will be.

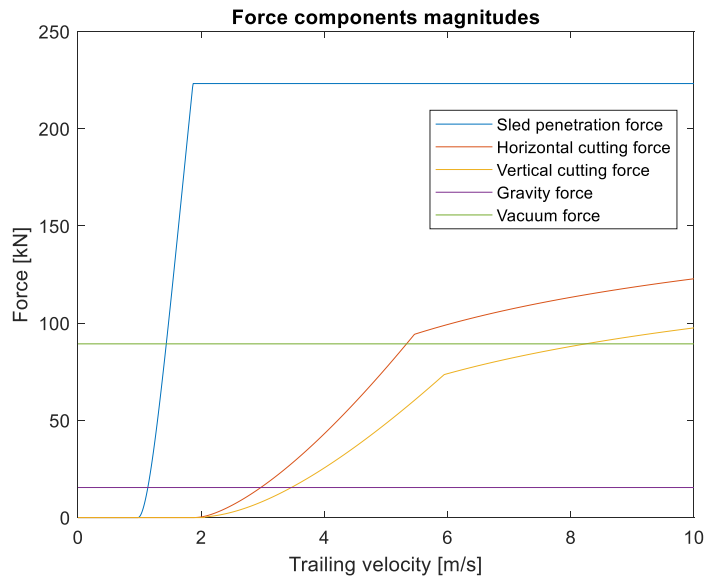


Figure 113: Overview forces on the visor, for a visor angle of 20 degrees

5.3.2 Visor equilibrium with variable layer thicknesses

The layer thicknesses at different visor angles and trailing velocities follow from the equilibrium moment method. For the results, of the equilibrium moment method for a visor angle of 20 degrees, first the effect of the different forces on the moment around C is shown. Then the equilibrium position is determined for all other angles from 0 to 44 degrees. Until a visor angle of 44 degrees, because when the blade angle becomes negative, the pore pressure model to determine the cutting force fails. The moment equation around the visor hinge was a follows:

$$\sum M_c = F_{vac} * l_{3a} + F_{gravity} * l_{3,b} * \cos(\gamma) - F_{cut,h} * l_{3,c} * \sin(\gamma) + F_{cut,v} * l_{3,c} * \cos(\gamma) - F_{sled} * l_{3,d} = 0 \quad (\text{eq. 238})$$

The layer thicknesses versus the trailing velocity are shown in Figure 114, the sum of the moments versus the trailing velocity in Figure 115.

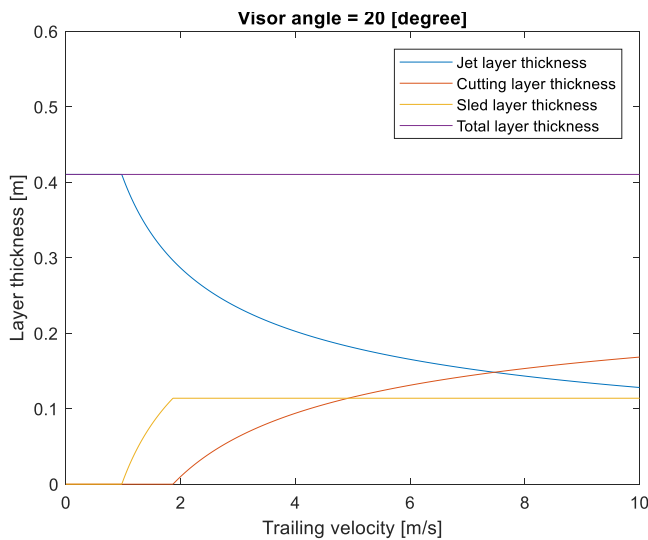


Figure 114: Layer thicknesses versus the trailing velocity for a free suspended visor; visor angle of 20 degrees

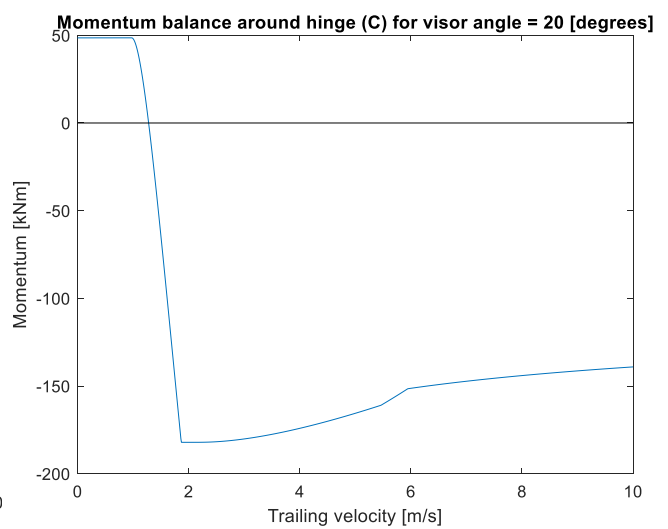


Figure 115: Moment balance around the visor hinge versus the trailing velocity, visor angle of 20 degrees

Because the jet penetration depth decreases, for increasing trailing velocities, the layer thicknesses change, as described in 5.2.1.2. When a trailing speed of 1 m/s is reached, the penetration depth of the jet drops and then becomes smaller than the total depth of the visor arm. From this point, the sled layer thickness, of the wearing pieces on the end of the visor, increases with the trailing velocity. This results in a big drop in the sum of the moments, because of the dominance of the sled forces. Until a trailing velocity of 2 m/s is reached, now the cutting layer thickness starts to increase and the belonging cutting forces have a positive effect on the moment around C.

Now the equilibrium position for a visor angle of 20 degrees is calculated and corresponds with a trailing velocity of 1.28 m/s. The cutting layer thickness for this speed is 0 m, the sled layer thickness 0.05 m and the jet layer thickness 0.36 m. This is repeated for visor angles of 0-44 degrees. Which delivers for each equilibrium point a corresponding layer thicknesses and velocity. The results for the layer thicknesses and corresponding visor angle are shown in Figure 116 and Figure 117.

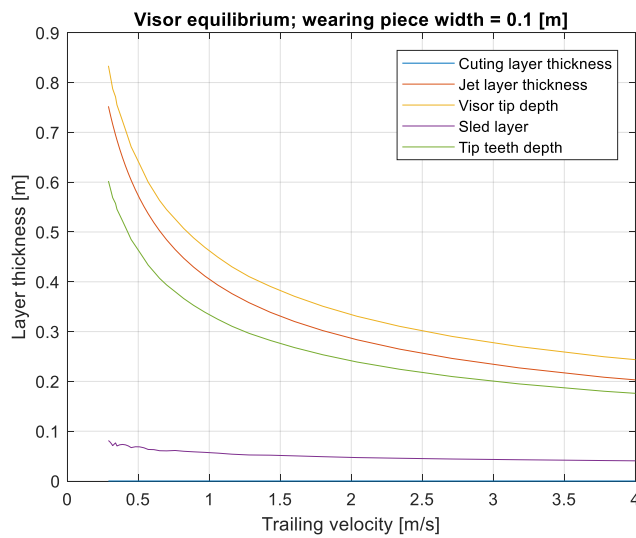


Figure 116: Layer thicknesses for a variable visor angle versus the trailing velocity

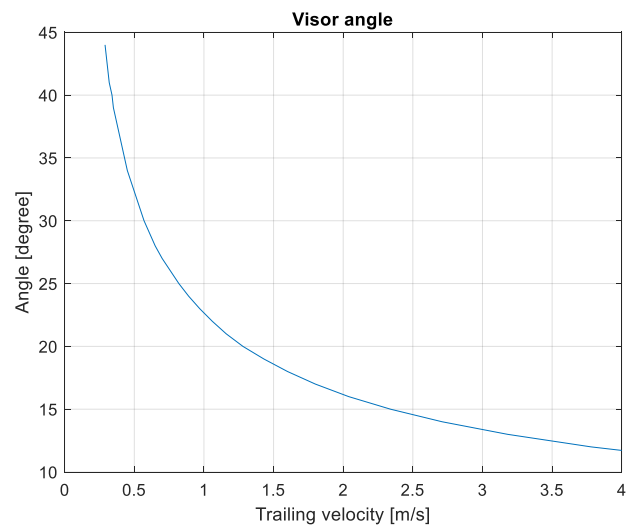


Figure 117: Visor angle equilibrium versus the trailing velocity

What is striking is that the jets have a very strong influence on the position of the visor and that the visor angle decreases steadily at an increasing velocity. Because the present wearing pieces, on the visor of the SLK600, are so wide, the sled forces are dominant, so that the cutting teeth are not able to dig into the soil. The calculations suggests that no sand is cut in this case and thus only jet production takes place.

These equilibrium layer thicknesses are used to calculate the force and eventually the production.

5.3.3 Soil excavation forces of the visor

The soil excavation forces are calculated by using the equilibrium layer thicknesses with the corresponding visor angle and trailing velocity. With the force balances from 5.2.3, the reaction force from the soil excavation forces in the hinge can be calculated. The trailing forces of the visor, depending on the trailing velocity, are shown in Figure 118 and Figure 119.

$$F_{c,visor,v} = F_{vacuum,v} + F_{g,visor} + F_{cut,v} - F_{sled,v} + F_{fric,v} \quad (\text{eq. 239})$$

$$F_{c,visor,h} = -F_{vacuum,h} + F_{cut,h} + F_{sled,h} + F_{fric,h} \quad (\text{eq. 240})$$

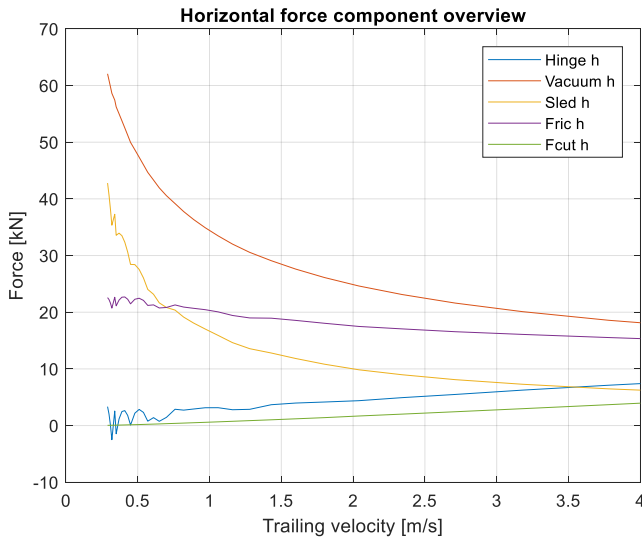


Figure 118: Force overview of the horizontal force components on the visor versus the trailing velocity

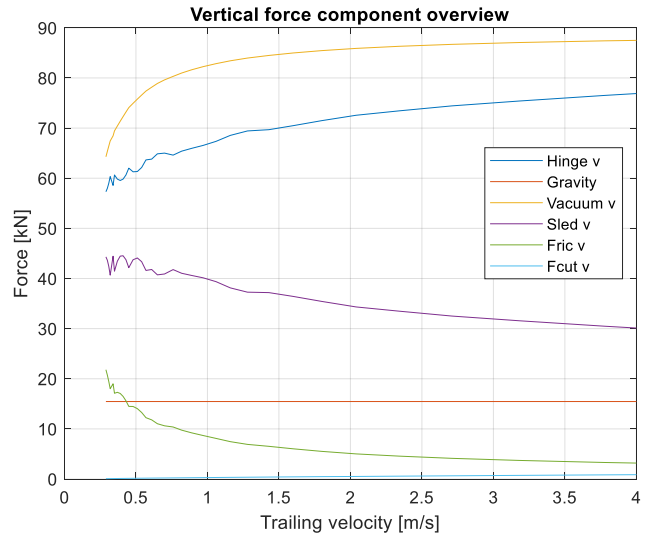


Figure 119: Force overview of the vertical force components on the visor versus the trailing velocity

Because the visor angle changes constantly for increasing trailing velocities, the direction of the resultant forces on the visor changes too. This can be seen in the graphs above, for example for the vacuum force. The vacuum force is assumed constant, but the horizontal component is decreasing for increasing trailing velocities and the opposite is happening for the vertical component of the vacuum force.

The horizontal reaction force in the hinge is small compared to the other forces, which suggests that the horizontal components outer balance each other. The vertical reaction force is substantial and increases slowly with an increasing trailing velocity.

5.3.4 Cutting production

The cutting production can be determined with equation 209. In Figure 120 and Figure 121 the cutting production for the SLK600 is shown, next to the jet production (calculated in the previous chapter) and the total situ production. The total situ production is in this case equal to the jet production, due to the absence of cutting production. At the moment the jet cavities are not connected to each other, as explained in 4.2.2.3, this causes an increased cutting layer thickness. The locally increased cutting layer thickness may cause a higher cutting force so that the visor angle will slightly decrease. This effect is not taken into account in the calculation for the cutting production. Therefore the production will be overestimated when the cavities are not connected, this happens for high trailing flow velocities.

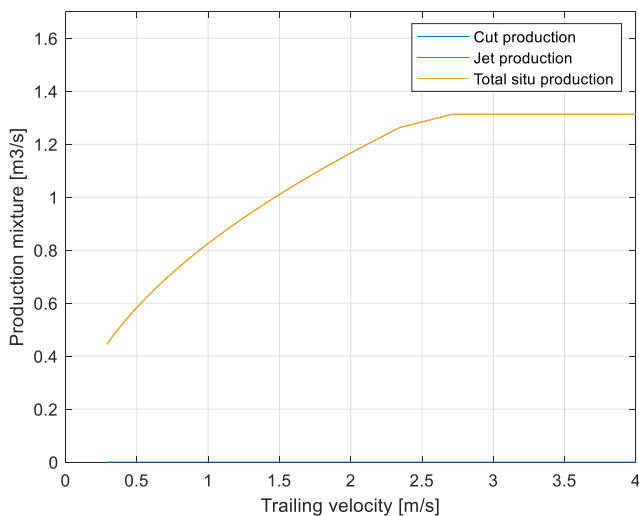


Figure 120: Volume production rate of the visor versus the trailing velocity

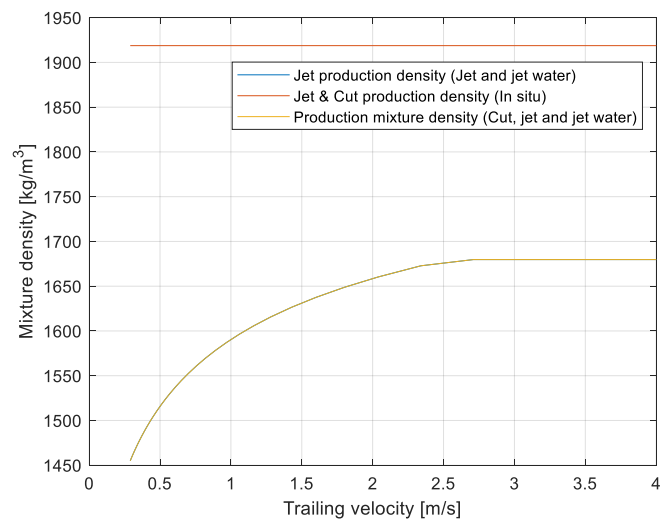


Figure 121: Production density versus the trailing velocity

5.4 Optimization & Verification

5.4.1 Narrowing of the wearing pieces

The Damen SLK600 draghead has wide wearing pieces on both sides of the visor. As a result, the outcomes suggests that there is no cutting production. This is because the sled forces are so large that the visor will never bury itself. The teeth are held above the solid sand layer and will not contribute to the cutting production.

By replacing the wearing pieces for narrower side skirts, in this way the sled forces will reduce, the teeth may penetrate into the solid sand layer. In addition, with a narrow side skirt it is more obvious that the sled theory can be applied instead of the wedge theory. The wearing pieces are then so narrow that the visor may slice through the sand, and sand compaction occurs as described in Agriculture soil mechanics (Koolen & Kuipers, 1983), instead of the wedge theory.

Therefore a new case study will be performed. For the new balance calculations the selected wearing piece width is set to 0.01 m. However, the new results show that there is no equilibrium and that the visor will never be in balance (see appendix 8.4.3). Due to the narrowing of the wearing pieces, the corresponding force, F_{sled} , has become so small that there is no negative moment that can neutralize the positive moment caused by the gravitation and vacuum force. The draghead will get sucked down into the soil.

The only force that can resolve this positive moment is the cutting force. Although the horizontal forces for a visor angle of 20 degrees and a visor-blade angle of 45 degrees are larger than the vertical forces, this difference is eliminated by the difference in length of the lever arm. For a visor angle of 20 degrees, the moment arm for the horizontal cutting force and the vertical cutting force is as follows:

$$\text{Horizontal cutting force, moment arm} = l_{3,c} * \sin(\gamma) = 0.867 * \sin(20) = 0.30 \text{ [m]}$$

$$\text{Vertical cutting force, moment arm} = l_{3,c} * \cos(\gamma) = 0.867 * \cos(20) = 0.81 \text{ [m]}$$

If the horizontal force is twice as large, it will still not be enough to neutralize the positive moment of the vertical force. The ratio between the horizontal- and vertical cutting force needs to be enlarged. The effect of the blade angle on the ratio between the horizontal and vertical cutting forces need to be checked.

By adjusting the visor-blade angle, the blade angle can be changed. With a blade angle larger than 45 degrees the vertical cutting force becomes 'negative' and will work in the direction of the negative momentum.

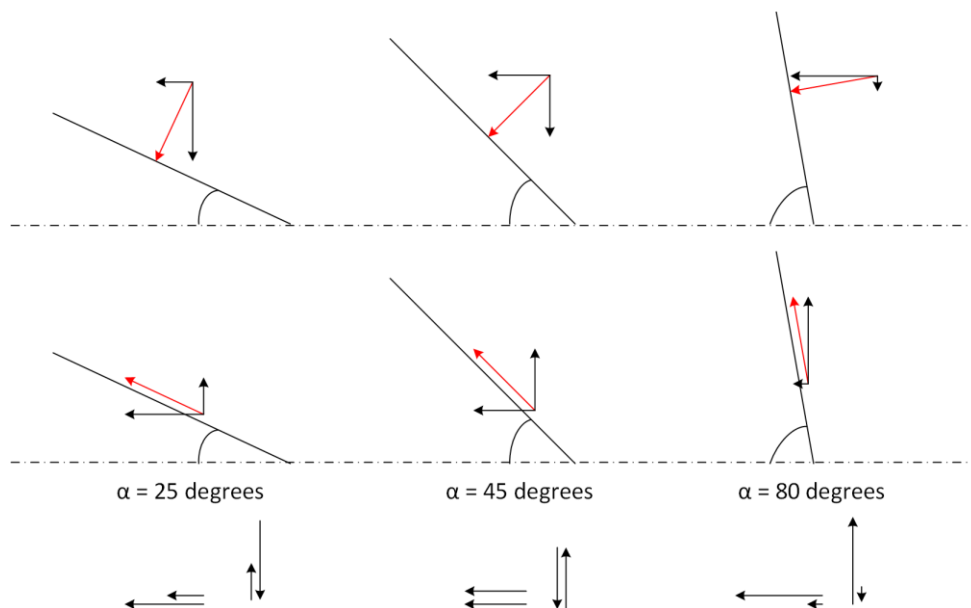


Figure 122: Blade angle effect, cutting force direction ratio. Attention: this is just an indication of the effect, the force components are not drawn to scale.

Although the vector analysis in Figure 122 will not completely match with the cutting forces calculated with the pore pressure model, the trend can be found with the model. By adjusting the visor-blade angle to 80 degrees, the blade angle becomes 60 degrees for a visor angle of 20 degrees. In this way the vertical force is slightly 'negative' and the horizontal cutting force is enlarged. Now an equilibrium for the visor should be found.

The question is whether the teeth will dig in at the beginning, when the visor angle is still zero degrees. Since the visor will 'fall' through the first layer section because of fluidization of the soil by the jets, the blade angle for a horizontal visor position will not matter. When the effect of the jets is reduced and the jet layer thickness decreases, this become dubious. Therefore, it will be necessary to look at the ideal visor-blade angle for each type of soil.

5.4.2 Cutting production for an optimized visor

In this section the new results for an optimized visor are shown. The wearing piece width is adjusted from 0.1 m to 0.01 m. And the visor-blade angle is enlarged to 80 degrees. The results are shown in Figure 123 - Figure 126.

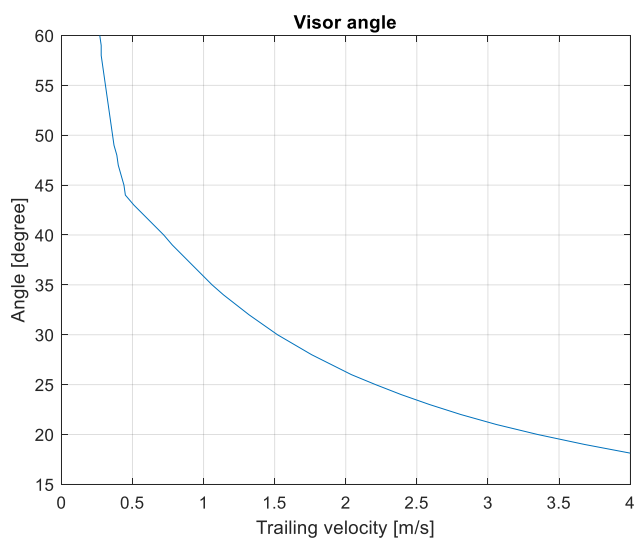


Figure 123: Visor angle equilibrium versus the trailing velocity, visor-blade angle = 80°

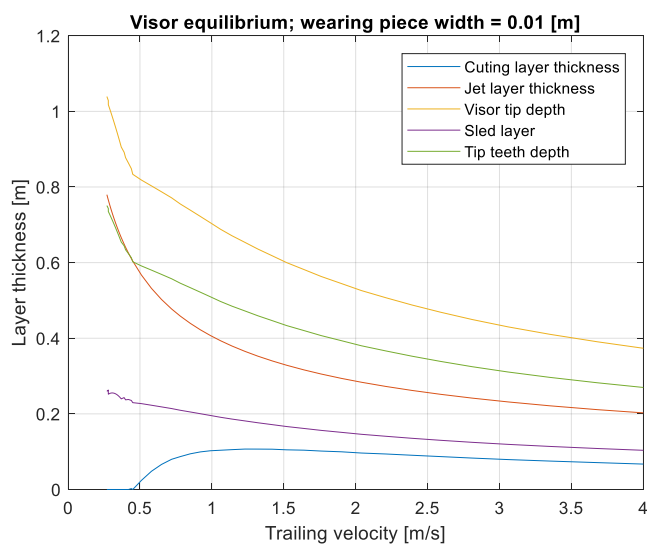


Figure 124: Layer thicknesses for a variable visor angle versus the trailing velocity, visor-blade angle = 80°

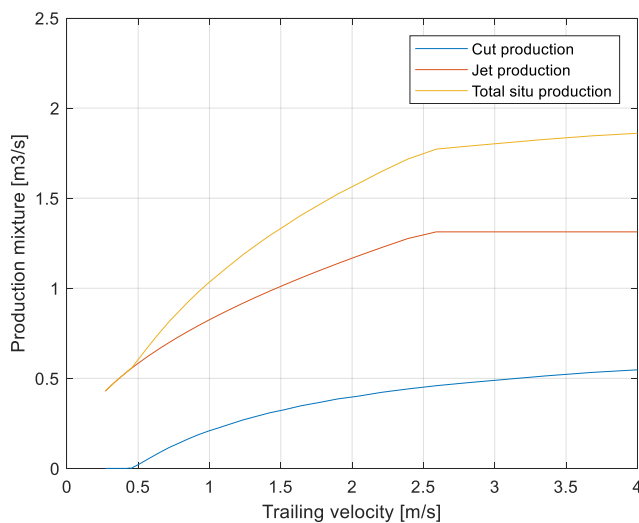


Figure 125: Volume production rate of the visor versus the trailing velocity, visor-blade angle = 80°

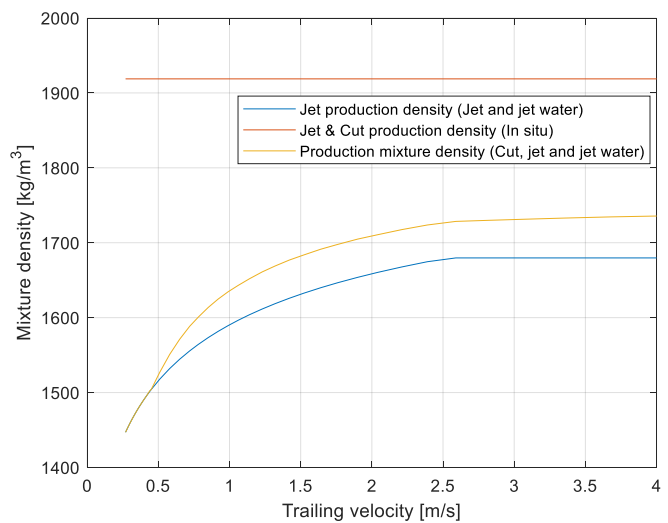


Figure 126: Production density versus the trailing velocity, visor-blade angle = 80°

It can be seen that an equilibrium is found. An almost constant cutting layer thickness, with only a small gradient, is present from a trailing velocity of 1 m/s, see Figure 124. This results in a cutting production which initially increases rapidly and then slowly flattens, as can be seen in Figure 125 and Figure 126. The cutting production contributes therefore in a positive way to the total situ production. For a velocity of 1 m/s, the cutting production is around 20% of the total situ production. For a velocity of 2 m/s this increases to 25%.

5.4.3 Vacuum force dominance

The vacuum force is very dominant as can be seen, in the results of the force components on the original visor in 5.3.3, and for the optimized visor with adjusted width and visor-blade angle too, see Figure 127 and Figure 128. This is in particular the force which holds the visor down to the bed.

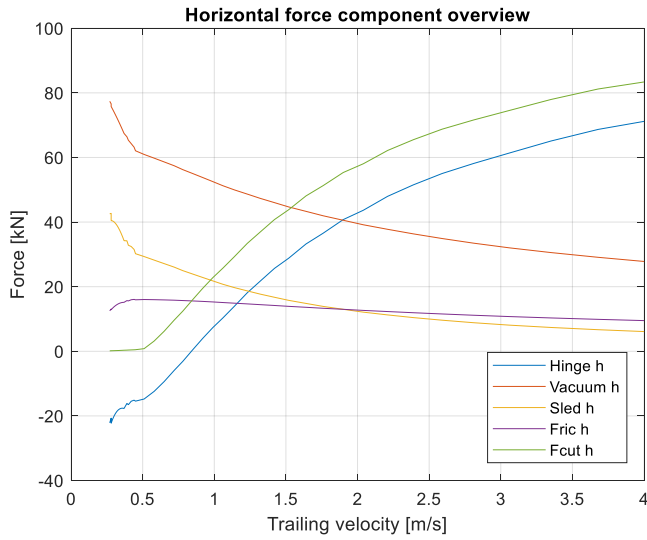


Figure 127: Force overview of the horizontal force components on the visor versus the trailing velocity

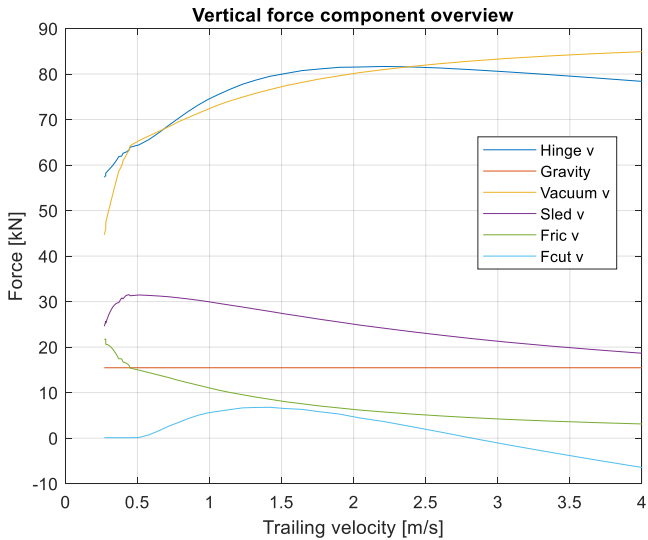


Figure 128: Force overview of the vertical force components on the visor versus the trailing velocity

For the coefficient, ξ , in equation 229, the value 3 is used in the case study. This coefficient may be chosen on the high side. Further investigation is needed to check whether the outcomes will change drastically when the vacuum force is lowered or increased.

5.4.4 Spillage

The aim of this subparagraph is to determine a quick first estimate of the spillage of the draghead. The composition of the sand-water mixture, i.e. the mixture density, which is pumped upwards depends on the amount of loosened situ sand and water, the amount of water that is injected and the extra amount of ambient water that is sucked (illustrated in Figure 129). When losses occur, the spillage must be subtracted. The total supply of situ sand and water, is the jet and cutting production. Another possible supply of sand could be the erosion production. However, this is not included in this study.

The dredging pump must be able to process the total production flow. When the pump limit is reached a certain amount of the mixture will be spilled. It should be avoided that energy, which is used to loosen the soil, is wasted.

In 5.4.4.2 will be indicated with the aid of Damen's pump performance data, what the capacity of the dredging pump is. This is used to determine the flow rate of surrounding water that is sucked and the amount of spillage that will occur.

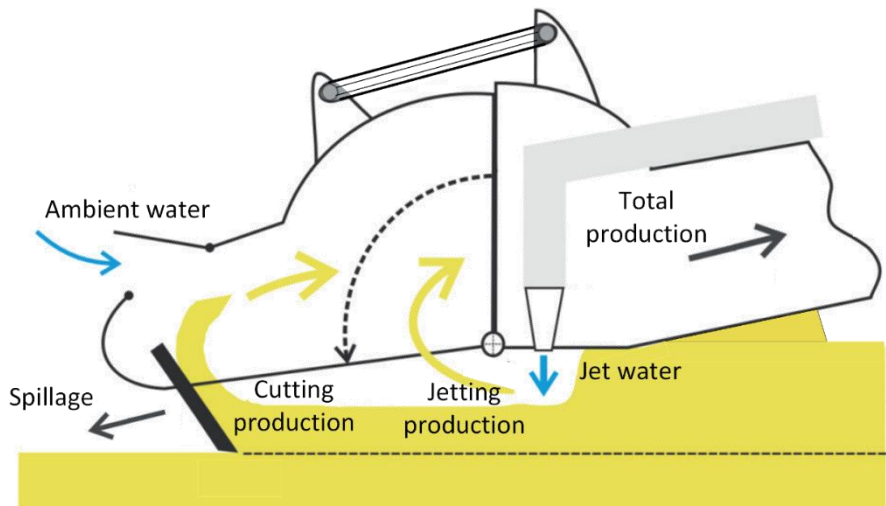


Figure 129: Overview of the flow contributions to the total production, source (modified): (Bergh, Osnabrugge, & Keizer, 2015)

5.4.4.1 Dredge pump capacity

The total production flow rate is limited by the capacity of the dredge pump. In order to achieve a high production, the pump capacity could be constantly increased. However, this also has adverse consequences, so it depends on the design considerations of the dredging pump. In this research a standard Damen dredge pump has been used. The rest of the suction pipe system is normally designed on the performance of the dredging pump. If the dredging pump can no longer process the amount of sand that is excavated, the production must be reduced. Otherwise, this could lead to spillage.

The following pump limits must be taken into account to make the right choice for the capacity of the pumps, and dimensions of the suction pipe and draghead. This is illustrated in Figure 130.

- The cavitation limit
- Friction losses
- Critical flow velocity in the pipe
- Density limit

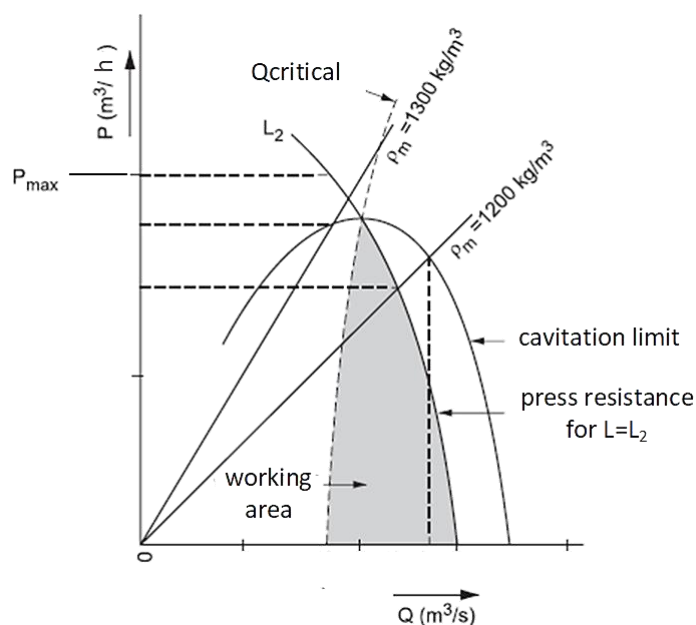


Figure 130: Dredge pump limits

5.4.4.2 Capacity pump

In Table 17 the pump performance of the dredging pump, which is used by Damen in combination with the TSP600, is shown. The pump has been chosen to achieve a pipe velocity of 5 m/s at a density, $\rho_{m,pump}$, of 1300 kg/m³. This results in a production rate of 1.41 m³/s. The variables used for the pump performance calculation are as following: a fine sand ($d_{50} = 0.2$ mm), dredging depth 20 m and assumed is that the inboard dredge pump is placed 1 m below the water surface. Variation of the position of the dredge pump depth are ignored.

Table 17: Dredge pump characteristics, TSP600 Damen; determined with ProDredge

Density [kg/m ³]	Rotations [rpm]	Production rate [m ³ /h]	Production rate [m ³ /s]	Pipe velocity [m/s]	NPSHr [kPa]	NPSHa [kPa]
1300	259	5053.66	1.40	4.96	25.5	29
1350	256	4636.44	1.29	4.56	22.8	23.2
1400	249	3982.99	1.11	3.91	18	20
1418	247	3763.74	1.05	3.68	17.6	17.8

By lowering the rpm, a higher mixture density can be pumped as can be seen in the table. A consequence is that the flow velocity in the pipe will decrease. In the two right columns of the table, the required Net Positive Suction Head (NPSHr) and the available Net Positive Suction Head (NPSHa) are shown. There must be ensured that the NPSHr is always smaller than the NPSHa, with a little safety margin, otherwise the production will decrease rapidly, and the pump could be damaged by cavitation. In this case, the maximum achievable mixture density is therefore 1400 kg/m³.

5.4.4.3 Spillage

The different volume flows of the draghead are indicated in Figure 129. In addition, the production capacity of the pump for a certain density and pipe mixture velocity is indicated in 5.4.4.2. This results in the following mass balance:

$$Q_{pump} * \rho_{m,pump} = Q_{situ} * \rho_{situ} + (Q_{ambient,water} + Q_{jet}) * \rho_w - Q_{spillage} * \rho_{spillage} \quad (\text{eq. 241})$$

The situ production is determined in the previous chapters and consists of the jet and cutting production. The jet flow is the amount of water that is inserted into the bed. To determine the spillage, two things are still missing: the ambient water flow, $Q_{ambient,water}$, and the density of the spillage, $\rho_{spillage}$. By assuming, the ambient water flow as a certain percentage of the situ production plus the inserted jet flow, the ambient water flow is known and the spillage can be determined. Another assumption is that the density of the spillage is equal to the density of the total production which ends up in the pump.

$$\rho_{spillage} = \rho_{m,pump} \quad (\text{eq. 242})$$

$$Q_{ambient,water} = x * (Q_{situ} + Q_{jet}) \quad (\text{eq. 243})$$

By substitution and rewriting of the assumptions mentioned above follows:

$$Q_{spillage} = \frac{Q_{situ} * \rho_{situ} + (x * (Q_{situ} + Q_{jet}) + Q_{jet}) * \rho_w - Q_{pump} * \rho_{m,pump}}{\rho_{m,pump}} \quad (\text{eq. 244})$$

The situ production increases with the trailing velocity, as determined and shown in Figure 120. When the supply of excavated sand increases, the amount of spillage will also increase. In Table 19, the spillage is determined for four different trailing velocities and three different pump mixture densities. The densities for the soil, water and situ density used in the calculation are stated in Table 18.

Table 18: Densities used for the calculation

Variable	Symbol	Value	Unit
Soil density	ρ_s	2650	kg/m ³
Water density	ρ_w	1025	kg/m ³
Situ density	ρ_{situ}	1918	kg/m ³

The results for an ambient water flow rate of 15% of the situ production plus the inserted jet flow are shown in Table 19.

Table 19: Overview of the pump capacity, the inflow of ambient water and the amount of spillage (for $x=0.15$)

Trailing velocity [m/s]	Pump mixture density [kg/m ³]	Q _{pump} [m ³ /s]	Q _{situ} [m ³ /s]	Q _{jet} [m ³ /s]	Q _{ambient} [m ³ /s]	Q _{spillage} [m ³ /s]
0.5	1300	1.40	0.61	0.48	0.09	0.01
0.5	1350	1.29	0.61	0.48	0.09	0.07
0.5	1400	1.11	0.61	0.48	0.09	0.20
1	1300	1.40	1	0.48	0.15	0.62
1	1350	1.29	1	0.48	0.15	0.66
1	1400	1.11	1	0.48	0.15	0.77
1.5	1300	1.40	1.34	0.48	0.20	1.17
1.5	1350	1.29	1.34	0.48	0.20	1.19
1.5	1400	1.11	1.34	0.48	0.20	1.27
2	1300	1.40	1.58	0.48	0.24	1.55
2	1350	1.29	1.58	0.48	0.24	1.55
2	1400	1.11	1.58	0.48	0.24	1.63

There is a significant amount of spillage which increases strongly when the trailing velocity is increased. This suggests that the determined amount of situ production is either overestimated or the jet production should be tuned so that not too much sand is excavated and less spillage will occur.

5.4.5 Cutting teeth holders and negative blade angle

An analysis of the visor shows that for the original draghead design under a visor angle of 22 degrees, the cutting teeth are exactly positioned in front of the cutting tooth holders. So, the tooth holders do not come into contact with the solid sand layer in this case, as seen on the left side of Figure 131. In this design, the angle between the visor angle and the blade is 45 degrees. When the visor moves deeper, these holders will start cutting/bulldozing through the sand layer, as shown on the right side of the figure. This may be avoided by adjusting the teeth length or placing the teeth holder in a different way.

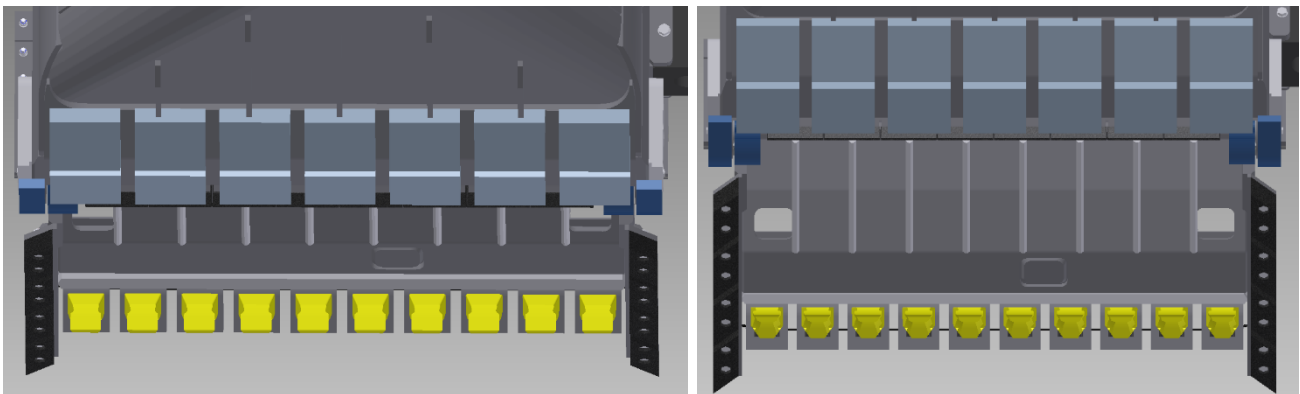


Figure 131: Front view draghead and draghead visor; left figure: visor angle of 22°, right figure: visor angle of 45° (suction pipe angle is in both cases: 45°)

Besides that, it can be seen that the blade angle is exactly 0 degrees, but the angle for the ‘under’ blade is already negative. For a negative blade angle, the pore pressure model, to calculate the cutting forces, does not work anymore. The sled theory, used for the sled forces of the wearing piece and visor house could be used in a follow-up research. This could improve the determination of the trailing force and the position of the visor. Next to the sled theory, the pore pressure model could also be improved with the wedge theory.

5.5 Conclusion

The aim of this chapter was to determine the cutting production and soil excavation force on the visor. Results showed that a freely suspended visor experiences several soil excavation forces during trailing, namely the gravitation force, vacuum force, cutting force, sled force and the friction force. Application of the equilibrium-moment showed that the visor changes position for different trailing velocities. It was shown that the position of the visor is strongly related to the penetration depth of the jets into the sand layer. Results showed that, at low speeds, the visor drops further down than at high velocities. This is possibly caused by the fact that penetration is high at low velocities. As the velocity increases, the penetration depth decreases and the visor moves slowly upwards.

The equilibrium-moment method was also applied to determine the forces on the visor. It was shown that the cutting and the vacuum force are dominant. The horizontal cutting force increases strongly with increasing trailing velocities and will change the sled forces and friction forces. With a decreasing visor angle, the vertical component of the vacuum force becomes larger and causes the draghead to be sucked down against the bed.

It was shown that the original Damen draghead visor does not produce any cutting production. However, cutting production could be achieved by narrowing the width of the wearing pieces and increasing the visor-blade angle. The results show that the cutting layer thickness remains almost constant with respect to the trailing velocity. This resulted in a linear increase of the cutting production with trailing velocity. It was shown that the cutting production contributes 20-25% of the total situ production.

In the rest of this report, the modified draghead visor with the narrowed wearing pieces and enlarged blade-visor angle is used, for the soil excavation forces and cutting production contribution.

6 Conclusion & Recommendations

The aim of this study was to determine the trailing forces and the production of the draghead. Both have been described as a function of the trailing velocity.

The aim of chapters 2 and 3 were to analyse the forces on the suction pipe and the draghead. It was shown that the horizontal excavation forces on the draghead are significant and increase strongly with the trailing velocity. This holds until the trailing forces become too high and consequently the draghead is lifted from the bed. From the results it can be observed that the drag forces at common trailing velocities of 1-2 m/s are relatively low compared to the soil excavation forces and therefore have a small share in the trailing forces. However, in case there is trailed against the current, the drag forces have a significant contribution to the total trailing force. Furthermore, it was shown that the behaviour of the suction pipe system is dependent on the dredging depth. Especially, the length of the horizontal and vertical lever arms have a significant influence on the draghead force equilibrium. Consequently, at lower dredging depths the trailing forces are larger and the draghead will be lifted at a higher trailing velocity and vice versa. The force distribution on the draghead is proportional to the trailing velocity, mainly caused by the cutting forces. Furthermore, it was shown that the soil reaction forces due to direct contact with the bed and the vacuum force are the dominant forces at conventional trailing velocities of 0.5 – 2 m/s.

The aim of chapter 4 was to determine the jet production. The results show that the penetration depth and cavity width decrease rapidly at low trailing velocities until approximately 1 m/s and slowly decreases for higher trailing velocities. When the nozzles are positioned too close together, at low trailing velocities overlap of the scour holes can take place. An optimum trailing velocity for jet production is found when the cavity width is equal to the optimal cavity width ($w_c = w/n_n$). It was shown that for velocities lower than the optimum, the jet production and mixture density increases. For higher trailing velocities the jet production is constant. In addition, the jet production is strongly related to the required jet power to loosen the sand. Thus, the more jet is power used, the higher the jet production.

The aim of chapter 5 was to calculate the cutting production. The analysis of the visor shows that the position of the visor is strongly related to the penetration depth of the jets into the sand layer. The freely suspended visor will sink into the fluidised jet layer until a balance is found. As the trailing velocity increases, the jet penetration depth decreases and the visor moves slowly upwards. The vacuum force and gravitational force push the visor against the bed while the cutting forces and sled forces push the visor upwards. Calculations predict that the original Damen draghead visor does not result in cutting production. However, cutting production could be achieved by narrowing the width of the wearing pieces and increasing the visor-blade angle. The results show that the cutting layer thickness remains almost constant with respect to the trailing velocity. This results in a linear increase of the cutting production with the trailing velocity. It was shown that the cutting production contributes 20-25% to the total situ production.

The capacity of the dredge pump sets a limit to the production. When too much sand is excavated by the jets and cutting teeth, spillage will occur. Spillage can be avoided by decreasing the jet power or reducing the trailing velocity.

Further research can be performed to improve the determination of the trailing forces and predict the production more accurately. Several recommendations are listed below:

- In this work, the assumption was made that the drag coefficient of the suction pipe is 0.9. In literature not a clear answer could be found about what the coefficient should be. To determine the drag forces on the suction pipe more accurately, this should be investigated.
- Moreover, in this research the bulldozing in front of the visor house is determined with the compaction method, while video images suggest that shearing of a sand layer takes place. The sled force could be replaced with the trailing forces resulting from the wedge theory. This force can be determined by extension of the pore pressure model with the wedge theory as shown by Miedema (Miedema, The Delft Sand, Clay and Rock Cutting Model, 2014).

- The pore pressure model is yet not able to handle negative blade angles, while it is seen that a negative blade angle can occur for the cutting teeth. This could also be solved with extension of the pore pressure model with the wedge theory.
- Extra research should be performed to find investigate the relation between the cavity width and the trailing velocity. It was found in literature that the assumption that the penetration depth is equal to the cavity width is not accurate enough.
- It should be researched if the jet production will decrease when two cavities overlap. This could be investigated by changing the distance between the nozzles while increasing or decreasing the trailing velocity.
- The coefficient used to determine the vacuum force in this research is uncertain. It is expected that the coefficient depends on the permeability of the soil and on how well the visor and the bed are sealed. It would be also interesting to research the contribution of the erosion production to the total production.
- In this study, it is assumed that the freely suspended visor experiences no resistance when moving through the fluidized jet layer. Therefore, the visor angle and consequently the production may be overestimated. Research could be performed to validate if this is the case.
- Lastly, it would be helpful to compare the results of this study to experimental data in order to validate the model. For this purpose, first contact is already made with dredging contractor Van Den Herik, who are open for cooperation.

7 References

- Bergh, P. v., Osnabrugge, J., & Keizer, C. d. (2015). An optimal dredging process by using draghead control concepts. *CEDA Dredging days 2015*. Rotterdam, the Netherlands: IHC.
- Braaksma, J. (2008). *Model-based control of hopper dredgers*.
- Damen Shipyards. (2018, March 1). *Damen; Dredging Equipment, company history*. Retrieved from <http://www.damen.com/en/companies/damen-dredging-equipment#history>
- Das, B. (2009). *Advance Soil Mechanics*. London & New York: Taylor & Francis.
- Dowling, D. (2015). *Fluid mechanics*. Amsterdam: Academic press.
- Jong, P. d. (1988). *Een productie optimalisatie van het gebruik van spuitende op de sleephopperzuiger "Volvox Delta"*. Delft: TU Delft.
- Journee, J. (2001). *Offshore Hydromechanics*. Delft.
- Koolen, A., & Kuipers, H. (1983). *Agricultural Soil Mechanics*. Wageningen: Springer-Verlag.
- Miedema, S. (1987). *The Calculation of the Cutting Forces when Cutting Water Saturated Sand, Basical Theory and Applications for 3-Dimensional Blade Movements with Periodically Varying Velocities for in Dredging Usual Excavating Elements*". Delft.
- Miedema, S. (2014). *The Delft Sand, Clay and Rock Cutting Model*. IOS Press BV.
- Miedema, S. (2016). *Introduction to Dredging Engineering [OE4607]*. Delft: TU Delft.
- Miedema, S. (2019). Production estimation of water jets in drag heads. *Proceedings of the Twenty- Second World Dredging Congress, WODCON XXII*. Shanghai, CHINA: TU Delft.
- Nobel, A. (2013). *On the excavation process of a moving vertical jet in cohesive soil*. Delft: TU Delft.
- Rhee, C. v. (2016). *Lecture notes Dredging Processes 2 [OE4727]*. Delft: TU Delft.
- Rhee, C. v. (april 1986). *De invloed van een waterstraal op een zandpakket*. Waterloopkundig Laboratorium.
- Rhee, C. v., & Bezuijen, A. (1998). *The breaching of sand investigated in large-scale model tests*. Delft: Coastal Engineering Proceedings.
- Sitanggang, A. P. (2017). *A Geo-Centrifuge Experiment of Spud Pole Anchoring in Sand*. Delft: TU Delft.
- Sloof, B. (2017). *Numerical modelling of sedimentation in trailing suction hopper dredgers*. TU Delft.
- Spaansen. (n.d.). *Draghead trailing at different velocities*. Dredging contractor.
- Vissers, B. (2018, March 1). *Dredgers by name*. Retrieved from Dredgers.nl: <http://www.dredgers.nl/default.htm?Dredgers/StGermain.html>
- Vlasblom. (2006). *Designing Dredging Equipment [OE4671]*. Delft: TU Delft.
- VOUW. (2010). 2. *Vloeistofmechanica*. Gouda: VOUW, Vereniging van waterbouwers.
- Wegenaar, R. (2014). *Sand erosion with a horizontally moving jet*. Delft: TU Delft.
- White, F. (2011). *Fluid Mechanics 7th edition*. New York: McGraw-Hill.
- Yeh, e. (2008). Large-scale laboratory experiment on erosion of sand beds by moving circular vertical jets. *Ocean Engineering* 36 (2009), 248-255.
- Zhi, L. (2002). *Dynamic behaviour of TSHD suction pipe system*. Delft: TU Delft.

8 Appendices

8.1 Appendices chapter 1

8.1.1 Detailed flow chart of the trailing force and production model

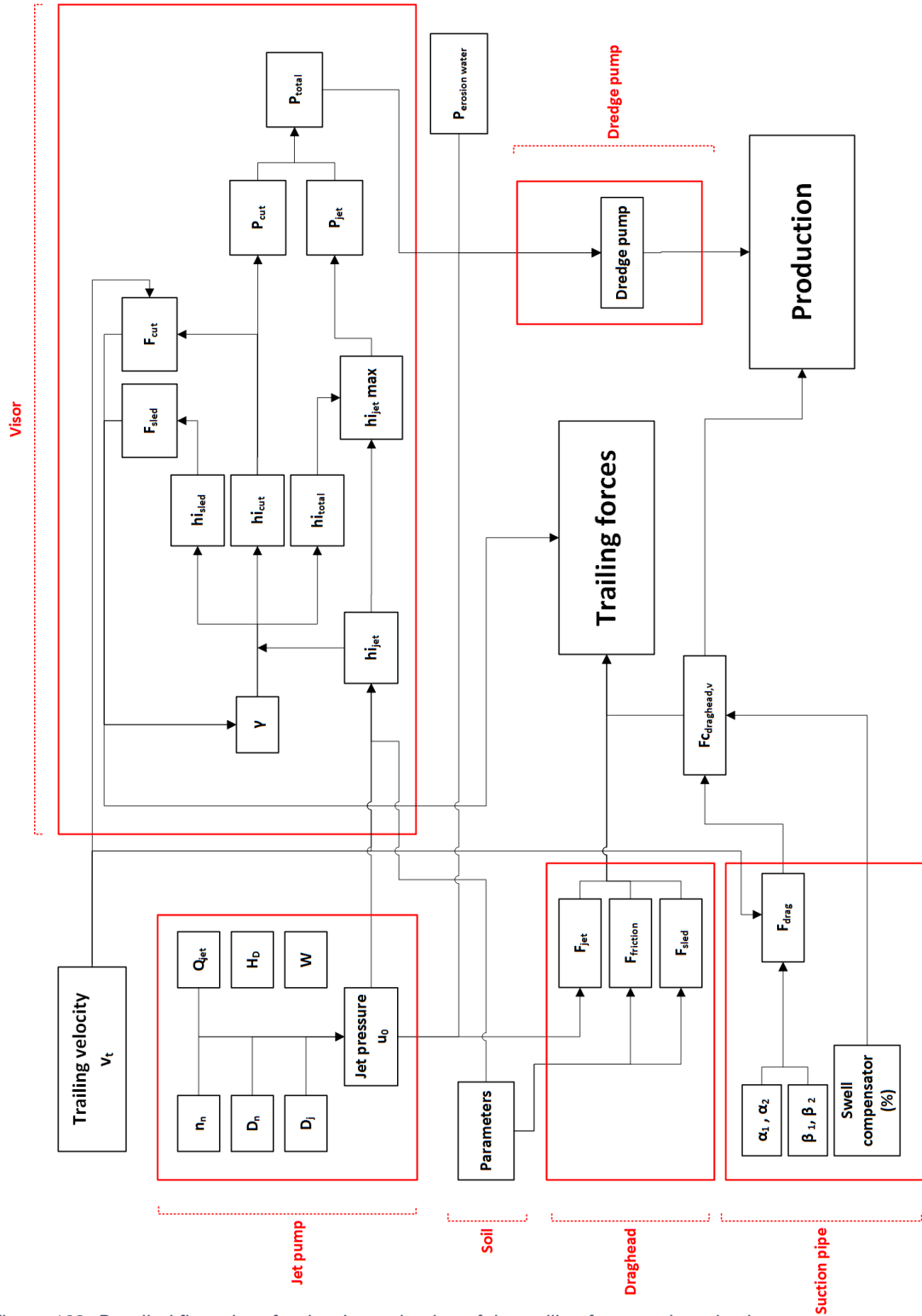


Figure 132: Detailed flow chart for the determination of the trailing force and production

8.2 Appendices chapter 2

8.2.1 Naming explanation of the suction pipe segments

Table 20: Abbreviations projection names lower pipe

Naming	Length
H2	$L2 \cdot \sin(\alpha_2)$
H2a	$L2a \cdot \sin(\alpha_2)$
H2b	$L2b \cdot \sin(\alpha_2)$
H2c	$L2c \cdot \sin(\alpha_2)$
H2d	$L2d \cdot \sin(\alpha_2)$
HC3	$LC3 \cdot \sin(\alpha_2)$
HD2	$LD2 \cdot \sin(\alpha_2)$
B2	$L2 \cdot \cos(\alpha_2)$
B2a	$L2a \cdot \cos(\alpha_2)$
B2b	$L2b \cdot \cos(\alpha_2)$
B2c	$L2c \cdot \cos(\alpha_2)$
B2d	$L2d \cdot \cos(\alpha_2)$
BC3	$LC3 \cdot \cos(\alpha_2)$
BD2	$LD2 \cdot \cos(\alpha_2)$

Table 21: Abbreviations projection names upper pipe

Naming	Length
H1	$L1 \cdot \sin(\alpha_1)$
H1a	$L1a \cdot \sin(\alpha_1)$
H1b	$L1b \cdot \sin(\alpha_1)$
H1c	$L1c \cdot \sin(\alpha_1)$
H1d	$L1d \cdot \sin(\alpha_1)$
H1e	$L1e \cdot \sin(\alpha_1)$
H1f	$L1f \cdot \sin(\alpha_1)$
H1g	$L1g \cdot \sin(\alpha_1)$
HC2	$LC2 \cdot \sin(\alpha_1)$
HD1	$LD2 \cdot \sin(\alpha_1)$
B1	$L1 \cdot \cos(\alpha_1)$
B1a	$L1a \cdot \cos(\alpha_1)$
B1b	$L1b \cdot \cos(\alpha_1)$
B1c	$L1c \cdot \cos(\alpha_1)$
B1d	$L1d \cdot \cos(\alpha_1)$
B1e	$L1e \cdot \cos(\alpha_1)$
B1f	$L1f \cdot \cos(\alpha_1)$
B1g	$L1g \cdot \cos(\alpha_1)$
BC2	$LC2 \cdot \cos(\alpha_1)$
BD1	$LD2 \cdot \cos(\alpha_1)$

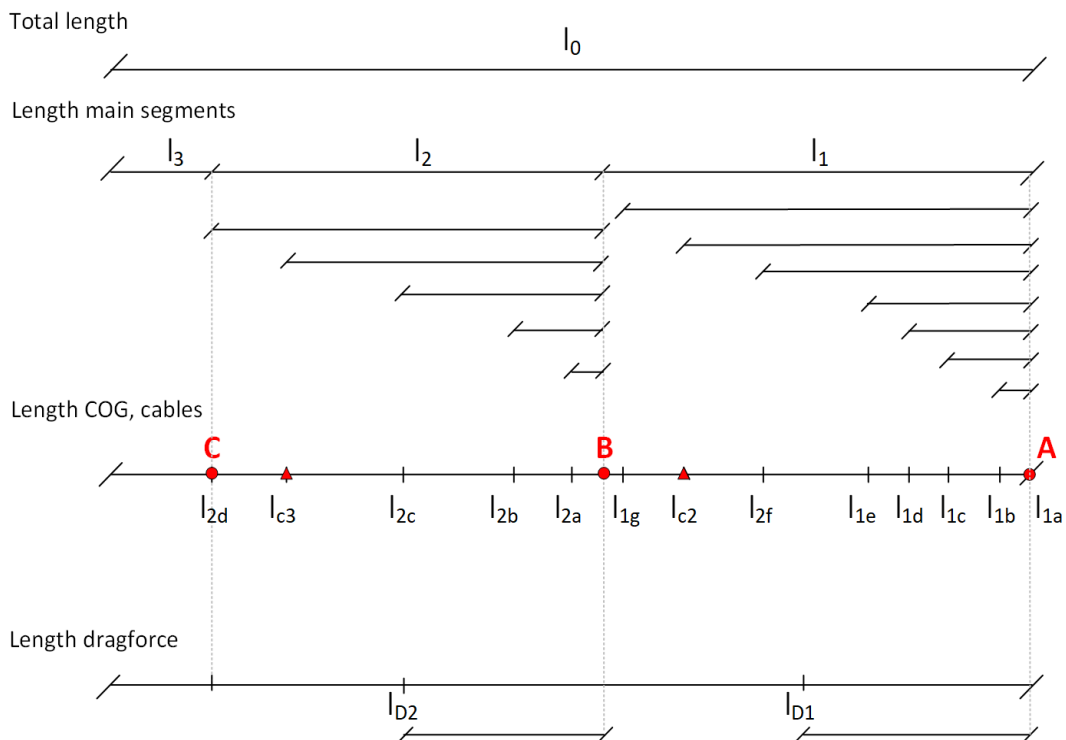


Figure 133: Naming lengths of the suction pipe and draghead, COG points of action, Cables suspension points and resultant drag force

8.2.2 Lengths suction pipe TSP600

Table 22: Lengths suction pipe TSP600 used in the case study

Length	Value [m]
L0	30.464
L1	15.560
L2	14.904
LC1	0
LC2	12.199
LC3	11.657
L3	1.200
LD1	7.780
LD2	7.748
L1a	0
L1b	0.42
L1c	1.30
L1d	3.01
L1e	4.07
L1f	9.40
L1g	14.66
L2a	0.45
L2b	2.13
L2c	7.75
L2d	14.90

8.2.3 Skin friction of the suction pipe

In the longitudinal direction of the pipe, the parallel component of the velocity causes mainly skin friction, as written in chapter 2. There is no frontal surface area, in the situation of an inclined pipe sticking out of the water, so the form drag for the parallel velocity component is therefore neglected. The friction force is the result of the skin resistance between the fluid and outside pipe wall. The skin friction will be negligible small in this case because of the high Reynolds number but for completeness explained and quantified. Theodore von Karman found an empirical relation for the skin friction coefficient C_f and is stated below. The Reynolds number is higher for this situation because of the change in the flow direction, longitudinal to the pipe.

$$R_{e,\parallel} = \frac{v * l}{\nu} = \frac{0.5144 * \cos(45) * 28.5}{1.05 * 10^{-6}} = 9.87 * 10^6 [-] \quad (\text{eq. 245})$$

$$C_{f,\parallel} = \frac{0.074}{R_{e,\parallel}^{0.2}} = \frac{0.074}{(9.87 * 10^6)^{0.2}} = 0.0030 \quad (\text{eq. 246})$$

$$C_{f,\perp} = \frac{0.074}{R_{e,\perp}^{0.2}} = \frac{0.074}{(2.165 * 10^5)^{0.2}} = 0.0063 \quad (\text{eq. 247})$$

$$F_f = \frac{1}{2} * \rho_w * (v * \cos(\alpha))^2 * C_f * A = \frac{1}{2} * \rho_w * (v * \cos(\alpha))^2 * C_f * l * \pi * D \quad (\text{eq. 248})$$

$$F_{f,\parallel} = \frac{1}{2} * 1025 * (0.5144 * \cos(45))^2 * 0.0030 * 28.5 * \pi * 0.625 = 11.37 \text{ N} \quad (\text{eq. 249})$$

$$F_{f,\perp} = \frac{1}{2} * 1025 * (0.5144 * \sin(45))^2 * 0.0063 * 28.5 * \pi * 0.625 = 23.91 \text{ N} \quad (\text{eq. 250})$$

As one can see in the formula, high Reynolds number causes a lower friction coefficient because the Reynolds number is positioned in the denominator. When the friction coefficient decreases the form drag becomes more dominant in the overall drag forces. The skin friction coefficient is in the case above, a factor 100 smaller than the drag coefficient, so its force contribution too.

8.3 Appendices chapter 4

8.3.1 Jetting theory

Free circular jet

The free circular jet theory can be used for the basic understanding of jets. When a free jet is dispersing into ambient water a large velocity difference is present. Because of the velocity difference, turbulence and viscous effects, the jet flow is decreased and the ambient water increased. At the shear zone, on the outside of the jet radius, water is entrained into the jet flow which enlarges the jet flow and the jet diameter becomes wider. The flow developing- and developed region can be distinguished from each other by the transition distance which is defined by $6.2 \cdot D_n$. In the developed region the velocity in axial direction is found by (Rhee, Lecture notes Dredging Processes 2 [OE4727], 2016):

$$u_{s,r} = \sqrt{\frac{k_1}{2}} * u_0 * \frac{D_n}{s} * e^{-k_2 \frac{r^2}{s^2}} \quad (\text{eq. 251})$$

Where k_1 and k_2 are entrainment coefficients, u_0 is the jet exit velocity, D_n is the jet diameter, r is the distance in radial direction from the centerline and s is the distance in axial direction from the nozzle.

The maximum velocity for the jet is in the center of the jet when $r=0$. The formula can then be reduced to:

$$\frac{u_{s,r}}{u_0} = \sqrt{\frac{k_1}{2}} * \frac{D_n}{s} \approx 6.2 \frac{D_n}{s} \quad (\text{eq. 252})$$

The jet nozzles are in most cases placed in the heel of the draghead. Because of the small stand of distance between the jet and the bed, the jet is still in the developing region and therefore the jet velocity is equal to u_0 at the centerline. The entrainment of water causes an increase in the total discharge which increases linearly with distance. In water the total discharge can be found with

$$\frac{dQ_s}{ds} = \sqrt{\frac{8}{k}} * \frac{Q_0}{D_n} = \frac{\pi}{4} * \sqrt{\frac{8}{k}} * u_0 * D_n = \frac{1}{\sqrt{2} * k} * \pi * u_0 * D_n \quad (\text{eq. 253})$$

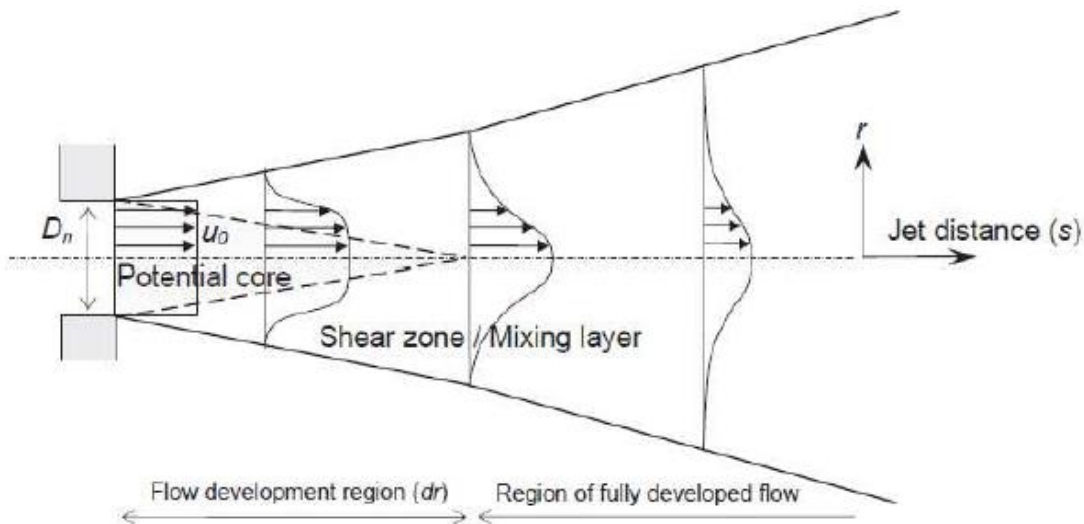


Figure 134: Schematic view of the jet velocity profile. Indicated is the developing region and the developed region.

Source: (Rhee, Lecture notes Dredging Processes 2 [OE4727], 2016).

8.3.2 Jet discharge (Bernoulli)

To calculate the jet pressure over the nozzle, the jet nozzle velocity and jet discharge should be calculated. This depends on the pump chosen and the available power. Starting from the top at the jet pump.

Bernoulli states:

$$p_1 + \frac{1}{2} * \rho_w * u_1^2 + \rho * g * \Delta h_1 = p_2 + \frac{1}{2} * \rho_w * u_2^2 \quad (\text{eq. 254})$$

p_0 = relative ambient fluid pressure [Pa]

p_1 = pressure jet chamber [Pa]

p_2 = pressure jet pipe [Pa]

u_0 = nozzle exit velocity [m/s]

u_1 = jet chamber flow velocity [m/s]

u_2 = jet flow velocity [m/s]

Assumptions:

- The jet chamber flow velocity is small compared to nozzle exit velocity ($u_1^2 \ll u_0^2$)
- The jet chamber flow velocity is small compared to the jet flow velocity ($u_1^2 \ll u_2^2$)
- Geodetic height difference between pressure sensor and water level is zero (Δh_1)
- Geodetic height difference between nozzle exit and jet chamber is zero (Δh_2)
- Relative ambient fluid pressure is zero (p_0)

With the assumption the Bernoulli's equation can be reduced to:

$$p_j = p_2 - p_{\text{loss, jetpipe}} + p_{\Delta h} \quad (\text{eq. 255})$$

In the assumptions above is mentioned that the velocity in the jet chamber is much lower than the nozzle exit velocity and can therefore be neglected.

The geodetic height difference can be neglected because the pressure sensor is placed behind the jet pump. The jet pump itself is located at the same height as the water level. The height difference between the water level and pressure sensor is negligible. The distance will vary depending on the draught of the vessel and is assumed to be on average close to zero.

With Bernoulli and the assumptions follows:

$$p_1 + \frac{1}{2} * \rho_w * u_1^2 + \rho * g * 0 = p_0 + \frac{1}{2} * \rho_w * u_0^2 \quad (\text{eq. 256})$$

$$p_j = p_1 - p_0 = p_1 \quad (\text{eq. 257})$$

$$p_j = \frac{1}{2} * \rho_w * u_0^2 \quad (\text{eq. 258})$$

By rewriting follows:

$$u_0 = \sqrt{\frac{2 * \Delta p}{\rho_w}} \quad (\text{eq. 259})$$

$$Q_j = C_d * \frac{\pi * D_n^2}{4} * \sqrt{\frac{2 * \Delta p}{\rho_w}} \quad (\text{eq. 260})$$

Source: (Rhee, Lecture notes Dredging Processes 2 [OE4727], 2016), (Wegenaar, 2014).

8.3.3 Cavitation

When the pressure drops to below the vapor pressure cavitation can occur. Along the streamline the water pressure drops due to an acceleration of the flow. The turning point when cavitation occurs is defined as the cavitation number:

$$\sigma_d = \frac{p_{a0} - p_{va}}{p_{cav}} \approx \frac{p_{a0}}{p_{cav}} \quad (\text{eq. 261})$$

Because the water vapor pressure (p_{va}) at room temperature (20 degrees Celsius) is negligible small this can be neglected. Nobel, 2013 found experimentally a value of 0,052 for the cavitation number.

Hence, cavitating jets occur when:

$$p_j > \frac{P_{a0}}{\sigma_d} \quad (\text{eq. 262})$$

Cavitation will not be a concern in practice because of the used pressures and especially the large operating depths. In research setups this is rather a concern because the hydrostatic pressure is low (At 20 m dredging depth and a jet pressure of 8 bar, jet cavitation does not occur. With jet pressure of 8 bar, jet cavitation occurs when there is dredged at lower than 4 m water depth; at 20 m depth, jet cavitation occurs at a jet pressure of 38 bar.)

During cavitation a vapor cone forms around the jet flow which obstructs that water can be sucked up into the jet stream. This reduces the effect of the jet which can be expressed in a lower penetration of the jet by an adjusted penetration coefficient k .

$$k_{cav} = k * \sqrt{\sigma_d} * \sqrt{\frac{p_j}{p_{a0}}} \quad (\text{eq. 263})$$

This results in the following stagnation pressure:

$$\frac{p_{stag}}{p_j} = \frac{k}{2} * \sqrt{\sigma_d} * \sqrt{\frac{p_j}{p_{a0}}} * \left(\frac{D_n}{s}\right)^2 \quad (\text{eq. 264})$$

The theory only applies for the cavitating jets and because jet cavitation will not occur in most of the cases this is not further included in this research.

Source: (Rhee, Lecture notes Dredging Processes 2 [OE4727], 2016).

8.3.4 Dilatation and Erosion (high speed erosion)

When sand grains are subjected to low flow velocities, the sand particles are eroded one by one with the flow. During jetting the flow velocities are high and the water flow over the bed cause a shear stress between the particles (Rhee, Lecture notes Dredging Processes 2 [OE4727], 2016). Because of this, the particles shear over each other and loses its closely packed structure. The porosity increases causing an under pressure in the voids. Water will flow to this low pressure region to neutralize the pressure difference. In case the particles size is large, with a corresponding high permeability, the water is able to flow without too much resistance into the voids. However, when the particles are small, the under pressure can raise because the water is not able to flow into the resulting pore space. The pressure can drop so low that cavitation occurs.

Source: (Rhee, Lecture notes Dredging Processes 2 [OE4727], 2016).

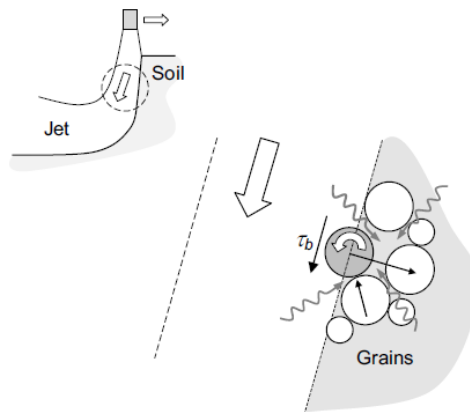


Figure 135: Erosion of sand particle out of the structure; Inflow of water into the pore, Animation: (Nobel, 2013).

8.3.5 Moody diagram

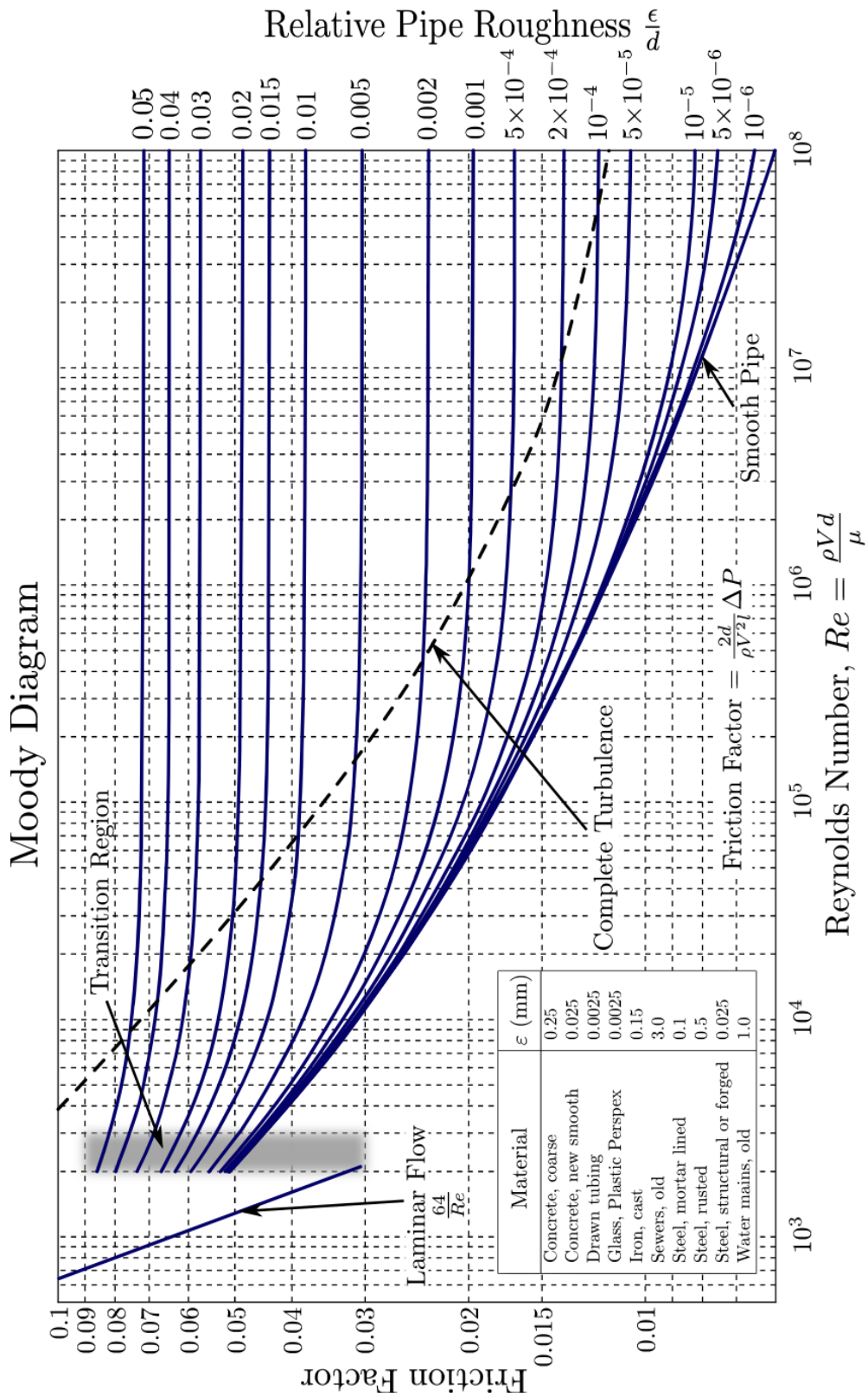


Figure 136: Moody diagram with an extra table with relative roughness indication

8.3.6 Results traversing jet experiment Wegenaar

Table 23: Sand types used in experiment Wegenaar (Wegenaar, 2014)

Sand type	1	2	Comments
D50 [μm]	284	142	Median grain size
Cu [-]	2.6	1.5	Coefficient of uniformity: D60/D10
n_m [-]	0.45	0.39	Porosity at maximum compaction
k [$*10^{-4}$ m/s]	1.08	4.16	Permeability

Table 24: Results from experiment Wegenaar (Wegenaar, 2014)

Sand type	1	2	Comments
Penetration depth	135%	100%	Equal D_n (9mm), P_j , v_t
Trail velocity [0.25 m/s]	165%	188%	Equal D_n (9mm) and P_j
Trail velocity [0.5 m/s]	100%	100%	Equal D_n (9mm) and P_j
Jet pressure [4 bar]	100%	100%	Equal D_n and v_t
Jet pressure [8 bar]	150%	150%	Average of sandtype 1 & 2 combined, equal D_n and v_t

8.3.7 Maximum jet power

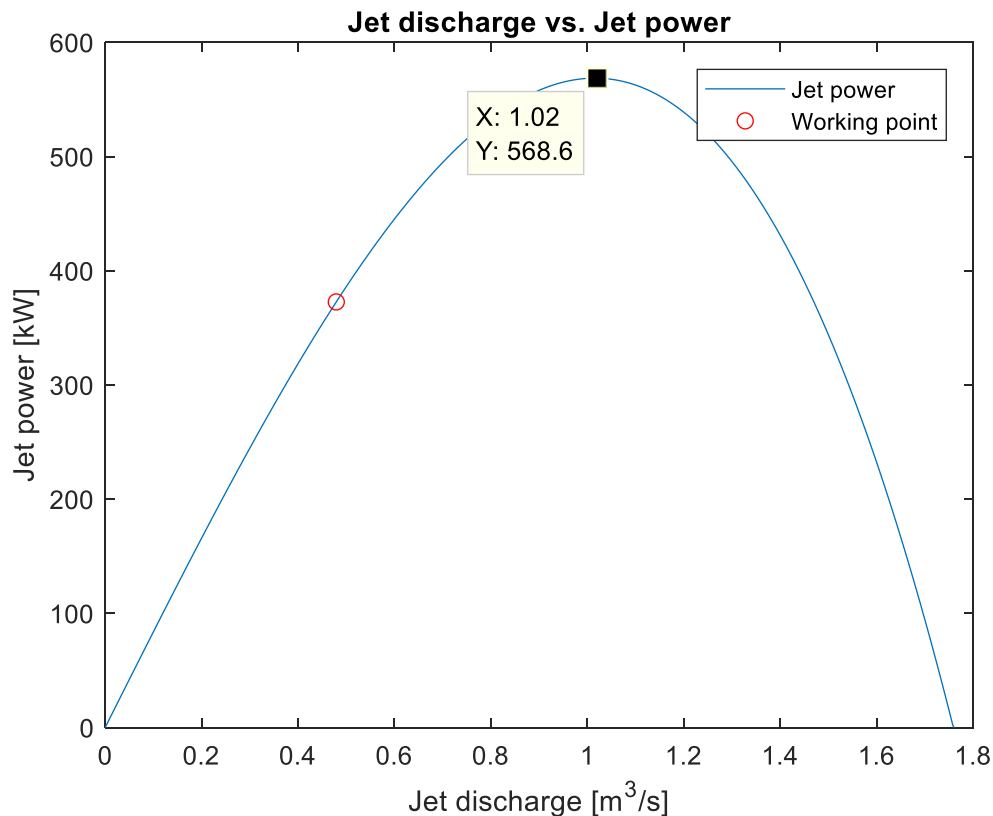


Figure 137: The maximum jet power for the pump in the case study

8.4 Appendices chapter 5

8.4.1 Resolution of forces working on the visor

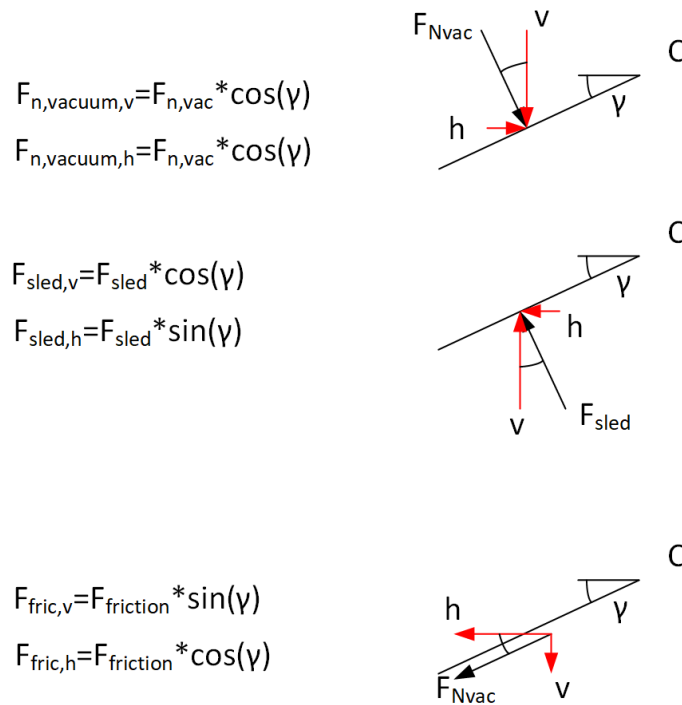


Figure 138: Resolution of the forces on the visor depending on the visor angle

8.4.2 Pore pressure distribution shear plane and blade

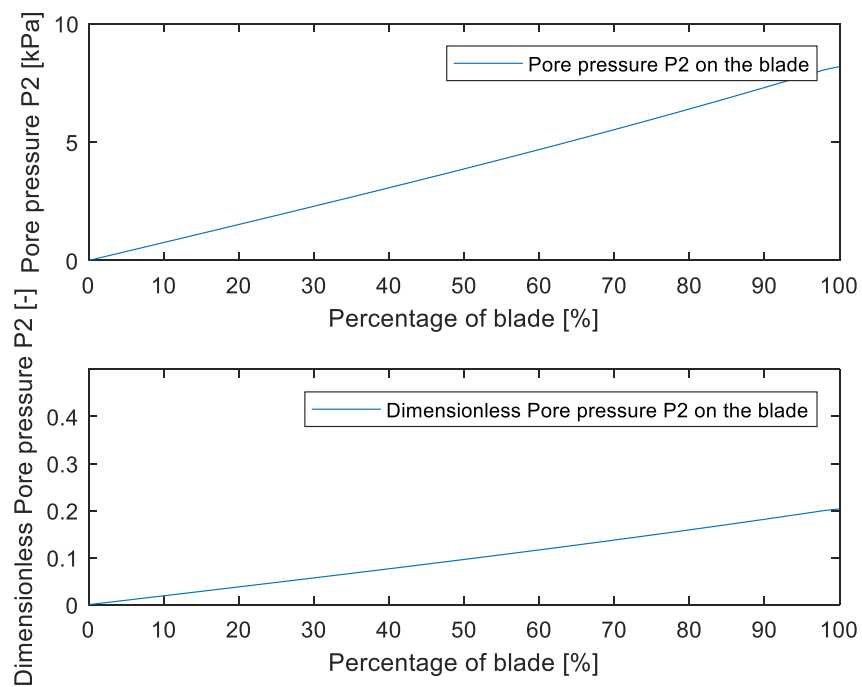


Figure 139: Pore pressure on the blade; situation for the variables in model results example, layer thickness 0.1 m, visor angle of 20 degrees.

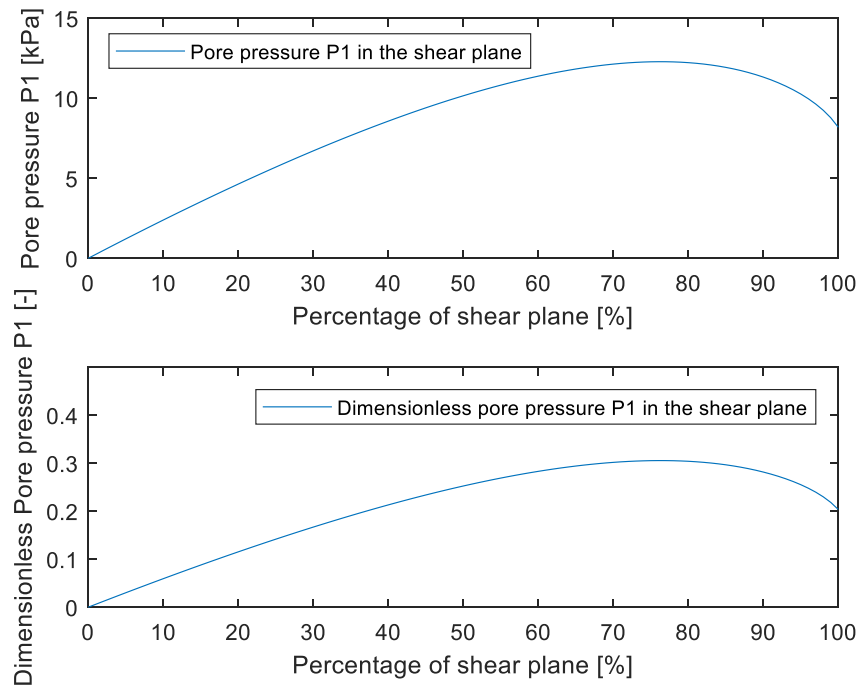


Figure 140: Pore pressure in the shear plane; situation for the variables in model results example, layer thickness 0.1 m, visor angle of 20 degrees.

8.4.3 Moment balance around the visor hinge

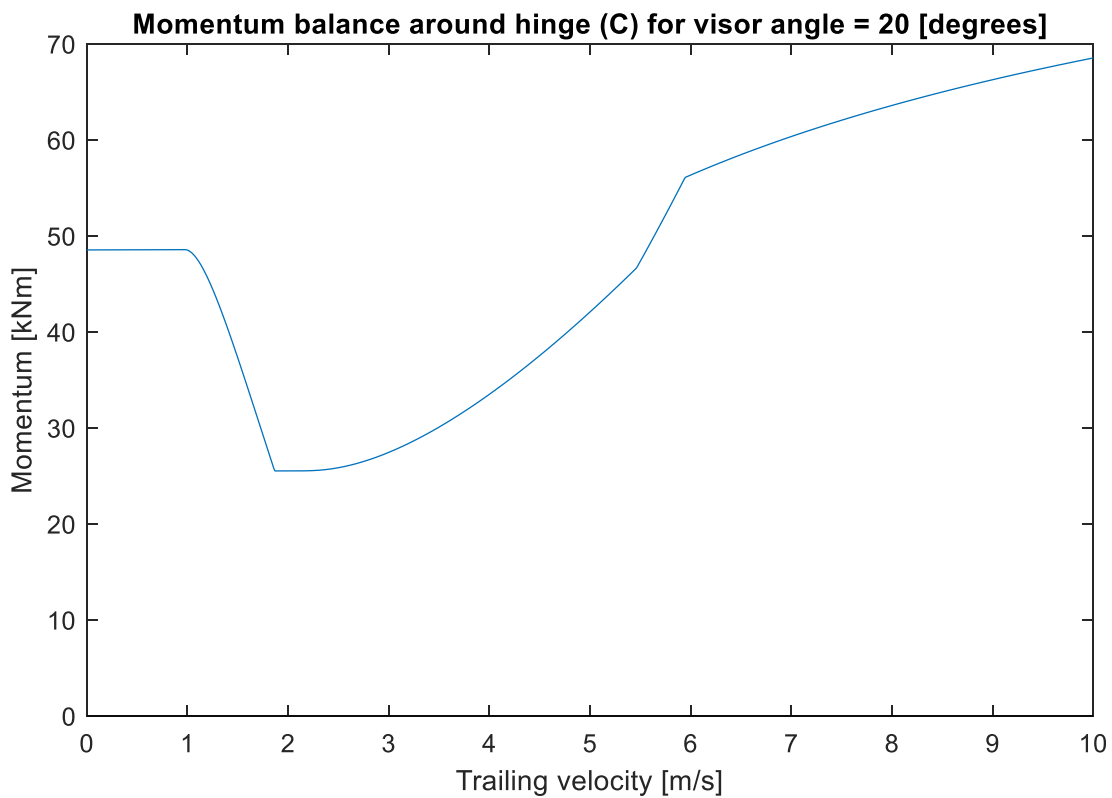


Figure 141: Situation for a visor angle of 20 degrees, visor-blade angle of 45 degrees, wearing piece width of 0.01 m.
